USING AVALANCHE STATISTICS TO FORECAST FAILURE IN MODELS OF EARTHQUAKE FAULTS AND MAGNETS

BY

BRADEN ANTHONY WIRUM BRINKMAN

DISSERTATION

Submitted in partial fulfillment of the requirements
for the degree of Doctor of Philosophy in Physics
in the Graduate College of the
University of Illinois at Urbana-Champaign, 2013

Urbana, Illinois

Doctoral Committee:

Professor Richard Weaver, Chair
Associate Professor K. A. Dahmen, Director of Research
Professor Emeritus Michael B. Weissman
Professor John Thaler

Abstract

Avalanches - bursts of activity spanning a vast range of sizes - occur in a wide variety of dynamical systems, such as magnets, granular matter, earthquake faults, neuronal networks, and of course the classic example of snow flows on mountains. By studying the statistics of avalanche sizes, we can understand the response of such systems to external driving forces, as well and their susceptibility to catastrophic failures. In this thesis, I present my work using models of avalanche statistics to study large failure avalanches. In particular, I use these avalanche models to explore statistical signals which can predict the likelihood of large earthquakes in a simple model of earthquake statistics. This analysis may also have applications to predicting seizures in neuronal networks. I also explore the effect that coupling has in models of disordered magnets which yield giant magnetization-reversal avalanches, which may have applications to predicting failures in power grid networks.

To Mom and Dad and my brother Matt,

for always supporting me,

even when you had no idea what in the world I was doing.

Acknowledgments

I saved writing the acknowledgments section of this thesis for last, and now I'm here, trying to come up with a clever way of starting this section, and thinking to myself that if I could somehow get away with not writing this section, well... I'd write it anyways. I am, as most scientists are, indebted to a network of colleagues, friends and family, all of whom have contributed to my development as a scientist and person, and deserve to be thanked here.

First, I give my thanks to my family, Mom, Dad, Matt, and Aunti Kristi, for all of your love and support. I am especially grateful to my Mom and Dad, for giving me the freedom to explore and learn and be myself, and for always encouraging me to do what made me happy, even if it meant moving a five hour plane ride away from home and dealing with an inferior health care insurance system!

Next, I have to thank my advisor, Karin Dahmen. Her limitless ability to see the silver linings in every new, annoyingly ambiguous result I obtained definitely gave me the motivation to soldier on every time I had worn out yet another desk by smashing my head into it repeatedly out of frustration. She always focused on developing physically intuitive explanations of our results, and trained me and my fellow group members to do the same. Karin is also by far one of the nicest people I have ever met, and I am not exaggerating!

I must also thank the Dahmen group members, with whom I have had countless conversations about physics and more. These members include Yang-Yu Liu, Georgios Tsekenis, Nir Friedman, Mike LeBlanc, Tyler Earnest, Matthew Wraith, Jim Antogonalia, Ryan Swindeman, and David Mertens (an honorary Dahmen group member!). You all definitely made working in the office interesting, albeit often at the cost of productivity!

Other people at the University of Illinois to whom I owe thanks include my prelim and thesis committee members, Richard Weaver, Mike Weissman, and Jon Thaler. Thank you for daring to read this thesis! Thanks also to Lance Cooper, who has been an excellent source of support, helping me (and many other students) acquire travel funding. He also taught an excellent writing course, the benefits of which will

hopefully be apparent in this thesis! I also thank Chilin Shih, my Chinese class professor, with whom my friend Tony and I had many interesting discussions about languages and language modeling, and Joseph Chen, another Chinese class teacher with whom Tony and I had many interesting conversations.

I thank also my collaborators, Yehuda Ben-Zion, Jonathan T. Uhl - without whom the first three chapters of this thesis would not exists - and John Beggs, with whom I got my foot in the door of research at the intersection of neuroscience and physics, which helped lead to the exciting postdoctoral position I will be taking up this fall!

No acknowledgments section would be complete without mentioning one's friends: the people who help preserve one's sanity as we grind away at our degrees. Or at least the people with whom we share our slow loss of sanity. For me, these people were Tony Hegg, Jess Vega, Tyler Naibert, Katie Crimmins, Phil Ansell, Umi Yamamoto, Yun Liu, Adam Weis, Yewon Gim, Cory Stephenson, Hamood Arham, Chris Nugroho, Cassi Hunt, Amanda Caringi and Johannes Strohle. Thank you all for your help and friendship! I also thank my friends from Chinese class, Brenna Williams, Jay Pahre, Ashley Chung and Tiffany Trinh. It was always nice to hang out with a group of people that weren't always talking about physics!

最後， 謝謝妳，陳瑞蕾。 妳鼓勵我做很多新事， 例如吃壽司，學中文， 去新地方，等等。 我教書到很晚的時後妳還有爲我煮飯。 一切妳爲我做的事,我都很感謝。 對我來說妳永遠會是特別的。

I very gratefully acknowledge funding from the University of Illinois physics department for teaching assistantships, the Drickamer Research Fellowship fund, summer research assistantships and travel funding; the National Science and Engineering Research Council of Canada (NSERC) for both a Postgraduate Master's Scholarship and a Postgraduate Doctoral Scholarship; the Southern California Earthquake Center (SCEC), based on NSF Cooperative Agreement EAR-0529922 and USGS Cooperative Agreement 07HQAC0026, and NSF grants NSF DMR 10-05209 and NSF DMS 10-69224.


此頁有意留為空白

Table of Contents

Chapter 1

Introduction

This thesis is not about snow. For most people, the notion of "avalanches" evokes images of runaway flows of snow on mountains. However, the dynamical processes that underlie these cascades are ubiquitous in nature and occur in a wide variety of systems [1, 2]. This thesis is about those ubiquitous underlying dynamical processes. More specifically, it is about developing powerful, yet simple, models of avalanche dynamics and applying these models to several problems of interest.

The basic features of avalanche processes can be illustrated using an analogy with falling dominoes. Dominoes, for the unfamiliar reader, are small 1" $\times$ 2" tiles. One mode of playing with dominoes is to stack the dominoes on their short side, close together, in interesting arrangements. Pushing over one domino generates an avalanche: the first domino knocks over one or two dominoes, which in turn knock over a few more dominoes, which in turn knock over even more dominoes in a process that continues to grow until most or all of the dominoes have fallen over.

There is an important difference between this analogy and the kinds of avalanching systems we study. Typically, dominoes are closely spaced and set up in a relatively ordered pattern, so that nothing interrupts the chain reaction once it starts. Real systems, in contrast, are very disordered. In our domino analogy, disorder can be introduced by removing dominoes randomly from our regular array of dominoes. In such a system, the size of an avalanche will depend on which domino(es) we knock over, resulting in a range of possible avalanche sizes. This leads to at least two important findings. One, similar set-ups differ only in their gaps (the "disorder"), so the avalanche sizes and durations that we observe will also differ from set-up to set-up. To form a general picture of the properties of avalanches, we should thus study the statistics of avalanches across different realizations of a system. Second, the range of avalanche can be divided into two kinds of avalanches: "small" avalanches, in which only a local section of the domino set-up is knocked over, and "large" avalanches, in which dominoes across the entire set-up are knocked over, in spite of any gaps. Large avalanches scale with the size of the system, whereas small avalanches do not scale with system size.

This distinction will be important when we discuss avalanches in real systems.

Barkhausen noise in magnets, earthquakes in fault zones and the firing of neurons in the brain are all examples of avalanche-like cascades [1, 2]. Allow me to use these systems to illustrate the basic features of these systems which give rise to avalanche behavior.

All three systems consist of individual subunits (the "dominoes"), which interact will one another. In magnetic systems, the dominoes would be magnetic domains, or "spins". When a spin changes its orientation (due to thermal noise or driving by an external magnetic field, interactions between it and its neighboring spins can cause those neighbors to flip as well, leading to a cascade of spin-flips – or Barkhausen noise. In earthquake faults the dominoes are pieces of granular material that slip past each other as the tectonic stresses drive the motion of the tectonic plates that form the fault. In brains, the dominoes are neurons. When one neuron fires, it sends electrical pulses to other neurons, causing some of those neurons to fire as well.

All three systems also have some kind of disorder or impurities. Disorder is important because it gives rise to non-trivial avalanche behavior. Again, we can understand this by analogy to dominoes: if we set up our dominoes so that they are all very close together and there are no gaps, then if we knock a domino over, it is very likely to knock over most, if not all, of the other dominoes. However, if our setup has many randomly-distributed gaps, then the size of the an avalanche will depend strongly on which domino we knock over first. It may only knock over five other dominoes, or two-hundred and eight, or seventeen. There is a wide distribution of possible avalanche sizes that would not exist if there were no randomness. In magnets, this randomness may be due to local non-magnetic impurities which effectively cause every spin to field a different local magnetic field. In the brain, every neuron has a different membrane voltage. If a firing neuron sends equally strong signals to several other neurons, only those with membrane potentials close to the firing-threshold voltage will fire. Similarly, the distribution of stresses along an earthquake fault is inhomogeneous, resulting in some patches of the fault slipping at different times than other patches.

Finally, all systems require some sort of driving in order to trigger avalanches. Just as we have to give one of the dominoes a kick to start the cascade, we drive magnetic systems with external magnetic fields, neurons are triggered to fire due to sensory inputs or environmental noise, and earthquake faults are driven by the motion of tectonic plates. These features of avalanching systems are summarized in Table 1.1.

It is important to point out that these features give rise to what I will refer to in this thesis as "small" avalanches. Small avalanches are local in space, and are characterized by having a wide distribution of

	Magnets	Brains	Earthquake Faults
"Domino"	Spins	Neurons	Fault Grains
Disorder	Magnetic impurities	Membrane voltage differences	Inhomogeneous stress distribution
Driving	External magnetic field	Sensory input or environment noise	Tectonic Driving

Table 1.1: Features which gives rise to avalanche-like behavior (left-most column). Specific examples for each of these features are given for magnetic systems, brain tissue and earthquake faults.

possible sizes an durations; for example, in the systems we investigate these distributions are typically power-laws. However, there also exist system-spanning or "large" avalanches. These large avalanches typically span from one side of a system to the other. The size of large avalanches scales with the sizes of the system, whereas small avalanches do not. Our example systems may also exhibit large avalanches. Magnets may undergo magnetic reversals, the flipping of the north and south poles of a bar magnet all at once, due to a large fraction of spins flipping in a single avalanche. A large avalanche in a brain may be akin to a seizure in which a large fraction of the neurons repeatedly fire. Large earthquakes are certainly familiar to anyone that has lived on the west coast of North America! It should be no surprise that large avalanches can have catastrophic consequences. Understanding them is thus of considerable importance. The major themes of the work I present in this thesis will be to use the statistics of these small avalanches to try and predict - and possibly prevent - when these large avalanches will occur.

Why are avalanches important?

What information do small avalanches provide us with that make them useful for trying to predict large avalanches or understand other features of a system under study?

Because avalanches are the response of a system to being driven, the distributions of the sizes or durations of these avalanches tell us something about the composition of the system. For instance, are interactions between the "dominoes" long or short ranged? How close is the system to a critical point? Such information is reflected in the statistics of avalanches.

The statistics of small avalanches may also yield important information about the strength or likelihood of large avalanches. My work on magnetic avalanches investigates how changing the coupling strengths between spins in magnets affects the statistics of the size of large, runaway avalanches in these magnetic systems. This study could lead to a better understanding of what measures to take to minimize power-grid failures, for example. Correlations between small avalanches and periodic driving forces may be viable signals for predicting *when* large avalanches will occur, as demonstrated in my work on earthquake statistics. This work

on predicting large earthquakes may also have applications to predicting seizures in the brain. The ability to predict when large, destructive events such as earthquakes, seizures or power-grid failures is naturally of great interest and importance!

Finally, avalanche statistics give us information about the *universality* of a system - the notion that certain properties of the macroscopic behaviors of a system (such as statistics) are independent of the microscopic details. This means that systems with very different microscopic origins - for example, earthquake faults versus neuronal networks - may have very similar, if not the same, avalanche statistics. This is an extremely important point from a model-building point of view. Universality means that no matter how detailed your model is, there are certain macroscopic features that are independent of these details (with some caveats). Suppose one has extensively studied a particular model and can show that another, less well-studied or harder-to-study model has the same universal macroscopic properties. We would then say both models are in the same "universality class". By showing that both models are in the same universality class, we gain a lot of information and intuition about the second, less-understood model's macroscopic behaviors or statistics. This is not only much easier than studying the second model entirely from scratch, but it also tells us about what kind of analyses of the first model will carry over to the second model! For example, it is conjectured that some models of earthquake faults yield the same statistics as models of neuronal firings, suggesting that we may be able to adapt the model I developed for predicting large earthquakes to trying to predict seizures! Though this is not yet a firmly established result, this direction may not have been obvious if not for the noted similarities between earthquake and neuron models.

This is of course not an exhaustive list of the benefits of studying avalanches in different models, but it gives a flavor of the possibilities and sets the stage for the specific problems that I investigated during the course of my Ph.D. research.

Organizing Principles

My Ph.D. research on avalanches consists of several different kinds of problems spanning the above-mentioned systems - primarily earthquake faults and magnets, with some recent ventures into avalanche statistics in rat brains. The recent work on neuronal avalanches has been done in collaboration with colleagues in my group and undergraduate students I have supervised; as I am not the lead author on these studies, this work will not be featured in this thesis. The focus of this thesis will thus be on my work on magnetic systems and earthquake faults or granular media. For organizational convenience, I will divide my work into two broad

categories: Part I on "Earthquake faults, Frictional Media and Granular matter", and Part II on "Magnets".

Part I consists of three chapters. In chapter 2 I present a new model which predicts the distribution of inter-event times of large stick-slip events in frictional systems, such as granular matter or earthquake faults. In chapter 3, I use this model to analyze correlations between large slips and in frictional media under a shear which includes a perturbative periodic component. In chapter 4, I extend this analysis to look at correlations between small slips and periodic shear stresses as predictors of large slips, with an explicit focus on applications to earthquake faults. Appendices A to C contain the technical details of the work presented in Part I.

Part II consists of one chapter. In chapter 5, I discuss an analysis of the mean field random field Ising model, in which I investigate the statistics of changes in the size of large magnetic avalanches as the coupling between magnetic spins is varied. There are also three appendices related to magnet models. I do not focus on the large failure avalanche in the RFIM in these appendices. Instead, I focus on other aspects of the model, such as how the dynamics change if thermal or quantum fluctuations are introduced. Appendix D contains a new, exact derivation of the avalanche size distribution in the zero-temperature, classical mean field random field Ising model. In Appendix E, I present work on a phenomenological model of the effects of thermal or quantum fluctuations in magnetic systems driven by an external field that changes non-adiabatically. Appendices F and G present some preliminary work developing random field Ising models with thermal and quantum fluctuations. This work compliments the phenomenological model presented in Appendix E.

Part I

地震

Earthquake faults, Frictional media and Granular Matter

Chapter 2

A probabilistic model for the distribution of waiting times between large slips in frictional media

2.1 Introduction

Failure in sheared frictional media is unpredictable. Despite much work towards understanding the failure dynamics of frictional media, including stick-slip behavior [3–8], jamming [8, 9], crack formation [10], and fracturing [11], we cannot reliably predict when a material will break. A prominent cause of our inability to predict failure is the high degree of variability individual frictional systems can possess. Impurities in frictional media can easily change the structural properties of a given sample [12]. Accordingly, theoretical studies of fracture mechanics in frictional media are often done at a statistical level. This may allow us to make statistical statements about the likelihood that a given sample will break, given the expected average properties across similar frictional systems. One example of a statistical quantity of interest is the distribution of times between large failure slips, in media where the system can sustain multiple failures. Knowledge of the distribution of times between large failure events - henceforth called "inter-event times" - could potentially be used to predict the likelihood of failure given that it has not yet occurred [13].

One particularly important example of a kind of frictional system which can sustain multiple failure events is an earthquake fault. Developing reliable methods for forecasting when the next big earthquake is going to occur is one of the greatest open problems in earthquake science. Earthquake prediction is of such great importance because successful prediction has the potential to save millions of lives around the globe. Knowing the typical distributions of times between large earthquake events would be extremely useful for estimating the risk of a large earthquake occurring some time in the future. However, due to the wide degree of variability between earthquake faults across the globe [14,15], predicting the actual form of an earthquake inter-event time distribution is quite difficult.

Many different models have been proposed for the distributions of waiting times between earthquakes [16–21]. Presently, a variety of distributions are used to empirically fit data. Some examples include the Weibull

distribution [18, 19, 21] and the Brownian passage-time distribution [20], which I will discuss specifically in Sec. 2.4. Other examples include the Weibull-log [18], Gamma [17], or even power-law distributions [18]. Some of these models are phenomenological. A connection to the underlying physics of frictional slip is thus not always made when choosing these distributions to fit data. Assumptions of different functional forms of stress accumulation with time can lead to related but different distributions [19]. As a result, it is not always clear how different stresses on the systems can impact the distributions of inter-event times or other earthquake statistics.

In this thesis, I present a new model of failure statistics in frictional media, designed to account for different external stresses exerted on the systems. This allows me to address not only the inter-event time distribution between large system failures, but also the predictability of such events. Rather than use a full microscopic statistical-mechanical model of frictional matter physics, I have taken an in-between phenomenological approach to the problem. I developed a probabilistic model of slip-statistics which can take as inputs macroscopic quantities calculated from microscopic models. In this way, I did not have to simulate a full microscopic model, but I was still able to make use of results from such models so as to maintain a connection to the actual physics of the problem.

2.1.1 Part I Overview

In this chapter, I introduce a probabilistic model of slip-statistics in frictional media. I use this model to derive the distribution of inter-event times between large failure events in these frictional systems. All three chapters presented in Part I of this thesis make use of this probabilistic model of frictional stick-slip statistics, and each will be the basis of a set of papers to be submitted for publication [22–24]. For simplicity, from here on I will primarily frame the discussion in terms of earthquakes, but we expect the results to apply to most frictional systems. In cases where there is a possible difference between earthquake faults and smaller frictional systems, I will note it explicitly.

The model is developed to accommodate different kinds of external stresses applied to earthquake faults. In this chapter I mainly consider a fault subjected to a constant compressive stress and a slow tectonic shear that increases linearly in time. However, as a prelude to the next two chapters, I also briefly consider the case of a fault subject to periodic stress perturbations. In this case I use the inter-event time distribution to derive the distributions of phases of the driving stress at which large earthquakes tend to occur.

The case of faults subjected to periodic stresses is explored in more detail in Chapters 3 and 4. In

these chapters I extend the investigation of the times between large events to include analyses of the correlations between when the timings of the large events and the phase of the periodic stress perturbations. In particular, in Chap. 3, I investigate correlations between the timings of large slips and the phase of the periodic component of the driving stress. I find a non-trivial relationship between the driving amplitude, driving frequency, and the degree of correlation observed. For the case of earthquakes, it will turn out to be impractical to use correlations between large earthquakes and the tidal or annual stress variations to predict future large quakes. However, the results prove to be applicable to materials testing applications, for which it is indeed practical to detect significant correlations between slips and periodic driving stresses. In particular, by studying the amplitude- and frequency-dependence of the mean inter-event time between slips and standard deviation, I predict how to exert some control over when failure will occur in material systems.

Though the model indicates we cannot reasonably detect correlations between large earthquakes and tidal stresses, there is a possibility that correlations between *small* earthquakes and tidal stresses may be possible to detect. In Chap. 4, I use the model presented here to study these small earthquake-tidal correlations, and indeed find that it may be possible to predict large earthquakes using small quake statistics. Though in this chapter I focus explicitly on the case of earthquake faults, I expect similar results to hold for material systems.

Because of the general applicability of the model, many more situations could be explored, including investigations of the effect of random seismic waves from other faults, or the effects of spatial variations in the total fault stress. In fact, models of earthquake statistics are similar to the integrate-and-fire models of neuron dynamics [25]. It could thus be possible that earthquake-prediction methods could have applications to neuroscience, such as developing similar methods for seizure-prediction. These situations will be left for future work. The development of the model and comparison to other inter-event time distributions, along with the effects of periodic driving on the earthquake- or slip-timing statistics, are the only situations I that I consider in this thesis.

I begin the discussion in this chapter by outlining the assumptions of our probabilistic model of slip-statistics, in Sec. 2.2. In the model assumptions, the functional forms of the small earthquake rate and the large earthquake triggering probabilities are arbitrary. For the analyses discussed in this thesis, I choose specific forms for these functions, which are derived from a phenomenological statistical-mechanical model of earthquake statistics, the Ben-Zion/Rice model, which has been used to model failure in many sheared

frictional systems [4–6, 26–28]. I briefly review this model and discuss the functional forms of the small event rate and large quake triggering probability in Sec. 2.3. In Sec. 2.4, I present the inter-event time distribution using the probabilistic model and the inputs from the Ben-Zion/Rice earthquake model. In Sec. 2.5, I discuss some other distributions currently used to model earthquake inter-event times, and I compare them with our model. Because there is not much empirical data on the inter-event times of characteristic earthquakes, comparison to other models of earthquake statistics will serve to demonstrate that our model is a viable candidate for modeling earthquake statistics. Finally, in Sec. 2.7, I present an analysis of the distributions of phases at which large earthquakes tend to occur in periodically-stressed earthquake faults, as an example of the applicability of the model to different stressing conditions.

2.2 Model assumptions

Our model for earthquake statistics[1], from which the inter-event time distribution is derived, obeys the following assumptions:

1. The earthquake fault exhibits small earthquake events which occur via a Poisson process, which is in general non-homogeneous; i.e., the attempt rate, $\lambda(F)$, at which earthquakes occur is a function of the overall stress on the fault, $F = F(t)$, which changes over time.

2. There is a stress-dependent probability, $P(F(t))$, that a small event will trigger a large event. This probability rapidly increases towards 1 near a critical stress value, F_c

3. After a large earthquake occurs, the stress relaxes to a baseline stress level f. We assume the timescale on which this relaxation occurs is much faster than any other relevant timescale, and so we treat the relaxation as occurring immediately.

In addition to these assumptions, we will also adopt a mean-field-like approximation: the stress on the fault, $F(t)$, is taken to be the average stress across the fault. This means we ignore spatially local stress fluctuations in our presentation here, which includes stress drops from the small, local earthquakes. Extensions of the model could include such spatial variations, for which the size of the small earthquakes would be important.

[1]The work in this chapter is to be submitted for publication as: B.A.W. Brinkman, M.P. LeBlanc, Y. Ben-Zion, J.T. Uhl and K.A. Dahmen, "A probabilistic model for the distribution of waiting times between large slips in frictional media" (2013). [22]

From these assumptions, we can derive the cumulative distribution function for the inter-event times of the large events. The derivation is given in Appendix A; here I quote the result,

$$\Phi\left(t|\{F(t)\}\right) = 1 - \exp\left(-\int_0^t d\tau\ \lambda(F(\tau))P(F(\tau))\right). \tag{2.1}$$

Here, I use the notation $\{F(t)\}$ to denote explicitly that the probability $\Phi\left(t|\{F(t)\}\right)$ is conditional on parameters in the total fault stress. For example, in the case of a periodically-stressed fault, discussed in Sec. 2.7 and the next two chapters, the probability is conditional on the phase of the stress.

Eq. (2.1) holds for arbitrary attempt rate $\lambda(F)$ and triggering probability $P(F)$, subject to the restriction that the integral over $\lambda(F(t))P(F(t))$ diverges at infinite times (such that $\Phi(t \to \infty|\{F(t)\}) \to 1$). Different choices for $\lambda(F)$ or $P(F)$ can reflect differences between different fault zones, or even other frictional systems, such as granular matter or rock interfaces.

For the purposes of the work presented in this chapter, I will restrict our attention to the case of constant attempt rate, $\lambda(F) = \lambda_0$. Qualitatively, we expect the restriction to constant attempt rate to have no major effect on the results presented in this chapter. Part of the reason for this is mathematical interpretation: for constant λ_0, we can always re-interpret $P(F)$ as containing the functional form of $\lambda(F)$. See Appendix A for further details. I will use this re-interpretation in Chap. 3. In Chap. 4, however, the stress-dependence of the small event rate is important, and so I will treat the case of non-constant $\lambda(F)$ explicitly in that chapter.

For the present discussion, however, let $\lambda(F) = \lambda_0$. Eq. (2.1) then reduces to

$$\Phi\left(t|\{F(t)\}\right) \equiv \text{Prob}(0 < \tau \leq t) = 1 - \exp\left(-\lambda_0 \int_0^t d\tau P\left(F(\tau)\right)\right). \tag{2.2}$$

The probability density of inter-event times follows from differentiating Eq. (2.2) with respect to time. The probability density is

$$\rho_T\left(t|\{F(t)\}\right) = \Theta(t)\lambda_0 P(F(t)) \exp\left(-\lambda_0 \int_0^t d\tau\ P(F(\tau))\right). \tag{2.3}$$

I have included a step function $\Theta(t)$ in the definition of $\rho_T(t|\{F(t)\})$ to enforce the fact that inter-event times must be positive.

To make specific predictions, we must choose a definite form for the triggering probability, $P(F)$. The form I will choose in this thesis is derived from a microscopic earthquake model, the Ben-Zion/Rice earthquake

model. I will present the functional form of $P(F)$ in the next section, along with a brief discussion of the physics of this model.

2.3 Ben-Zion/Rice earthquake model for the triggering probability $P(F)$

The Ben-Zion/Rice model captures the physics of both Gutenberg-Richter and "characteristic" earthquake faults. The difference between the two kinds of faults can be characterized by the distributions of earthquake sizes, $D(S, F)$, as shown schematically in Fig. 2.1. In Gutenberg-Richter faults, the small event sizes are power law distributed with a cutoff that depends on how close the fault stress is to some critical value F_c, while in characteristic faults this power law is cut off at a stress-independent critical earthquake size S_c. All small events above this critical size run away to become large earthquakes, the sizes of which are distributed about some characteristic earthquake size. The characteristic earthquakes are "large" in the sense that their size scales with the size of the fault, whereas the small earthquake sizes do not scale with the fault size. The characteristic earthquakes are the large slips in our probabilistic model.

The Ben-Zion/Rice earthquake model can produce both kinds of earthquake statistics by tuning the amount of dynamical weakening in the fault zone. Dynamical weakening is the tendency for patches of the fault to keep slipping after they have already slipped, akin to static versus dynamic friction. It is this effect that enables small earthquakes to become runaway large earthquakes. Accordingly, in the absence of weakening, the Ben-Zion/Rice model exhibits regular Gutenberg-Richter statistics. When weakening is present, the model exhibits characteristic earthquake statistics.

Weakening is characterized by a dimensionless parameter, ϵ, which represents the fraction by which a patch's stress threshold level decreases after the patch slips. The absence of weakening corresponds to $\epsilon = 0$. For small ϵ, one finds that the critical small event size above which the events runaway to become large events is $S_c \sim 1/\epsilon^2$. [6]

Because all small earthquakes with size greater than S_c run away to become large earthquakes when dynamical weakening is "turned on" in the Ben-Zion/Rice model, the probability that a small earthquake triggers a large earthquake is equivalent to the probability that a small earthquake has size $S > S_c$ when weakening is absent. The triggering probably $P(F)$ can thus be obtained by integrating the Gutenberg-Richter distribution $D(S, F)$ from S_c to ∞:

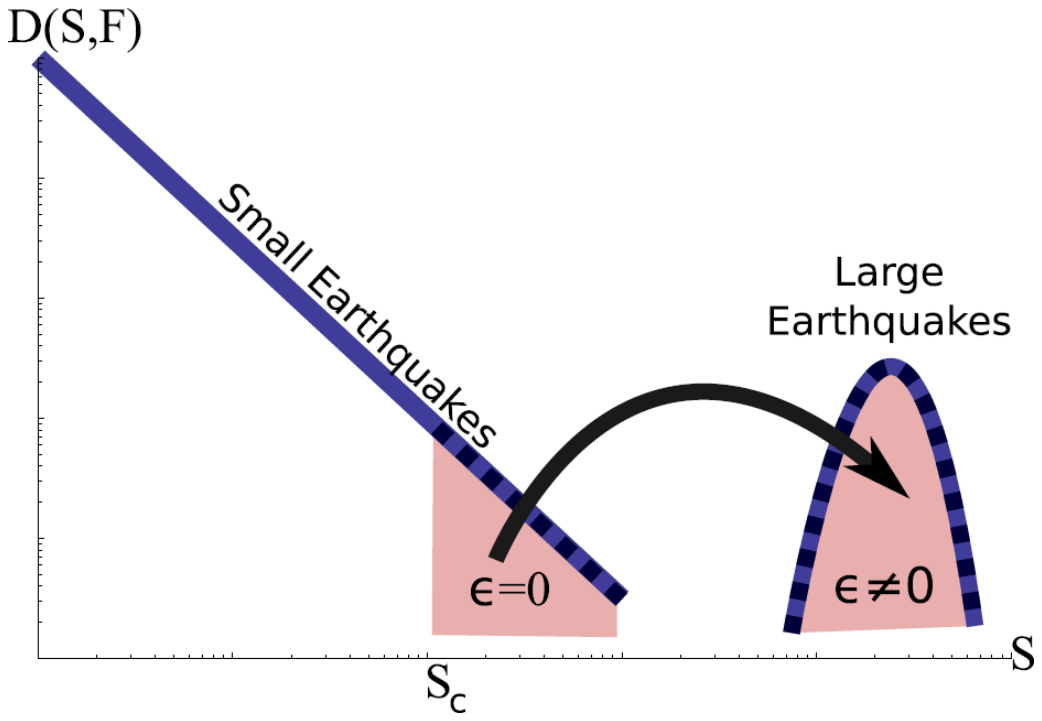

Figure 2.1: Statistics of earthquake sizes, S, in the Ben-Zion/Rice earthquake model. The sizes are dimensionless and represent, for example, the potency of a slip normalized by the minimum potency exhibited by the fault. In the absence of dynamical weakening ($\epsilon = 0$), the distribution is a power law, and only small earthquakes are produced. When dynamical weakening is present ($\epsilon \neq 0$), small earthquakes above a certain size S_c will run away to become large earthquakes, producing the characteristic earthquake distribution: a power-law with a cut-off at a critical earthquake size S_c, followed by a peak centered on a characteristic large earthquake size [6]. The exact shape of the distribution depends on the external total stress on the fault.

$$P(F) = \int_{S_c}^{\infty} dS\ D(S,F) = \frac{1}{\sqrt{S_c}} \frac{g\left(\sqrt{S_c}\frac{1-F/F_c}{b}\right)}{g(\frac{1-F/F_c}{b})}, \tag{2.4}$$

where S_c is the critical earthquake size above which small events run away to become larger events, F is the total external stress, F_c is a critical stress, b is a constant (related to the size of the precursor-cutoff in the Gutenberg-Richter fault) and

$$g(x) = \exp(-x^2) - \sqrt{\pi}x\ \mathrm{erfc}(x). \tag{2.5}$$

Here, $\mathrm{erfc}(x)$ is the complementary error function $\mathrm{erfc}(x) = (2/\sqrt{\pi}) \int_x^{\infty} dt\ \exp(-t^2)$. The derivation of these equations is given in Appendix A.

As stated, for small ϵ, $S_c \sim 1/\epsilon^2$. From this relation and Eq. (2.4), it follows that increased weakening results in a broader inter-event time distribution, effectively smearing out the spread of stresses at which a

large event may occur. Similarly, b, which is related to the amount of heterogeneities (or "disorder") in the fault, will also result in a broader distribution as it is increased.

Strictly speaking, Eq. (2.4) is valid only for an infinite system, and so this form for $P(F)$ is only valid for $F/F_c < 1$, above which $P(F)$ should be 1. However, most experimental systems designed to model earthquake faults, and perhaps even earthquake faults themselves, are not large enough to be suitably approximated as infinite, so we choose to account for the effects of a finite system size. We expect that in a finite system the sharp transition to $P(F) = 1$ at $F = F_c$ will be rounded off. Eq. 2.4 exhibits exactly this behavior for $F > F_c$. This effect is captured by Eq. (2.4) for $F > F_c$. We accordingly use Eq. (2.4) all stresses in the calculations and simulations presented in this chapter. The infinite and finite $P(F)$ curves are shown in Fig. 2.2 for comparison.

Lastly, I note that the Ben-Zion/Rice earthquake model assumes that the shear stress increase $F(t)$ is slow compared to the timescale on which earthquakes occur. This assumption is reflected in our model by the fact that large slip events and earthquakes occur instantaneously, leading to immediate drops in stress.

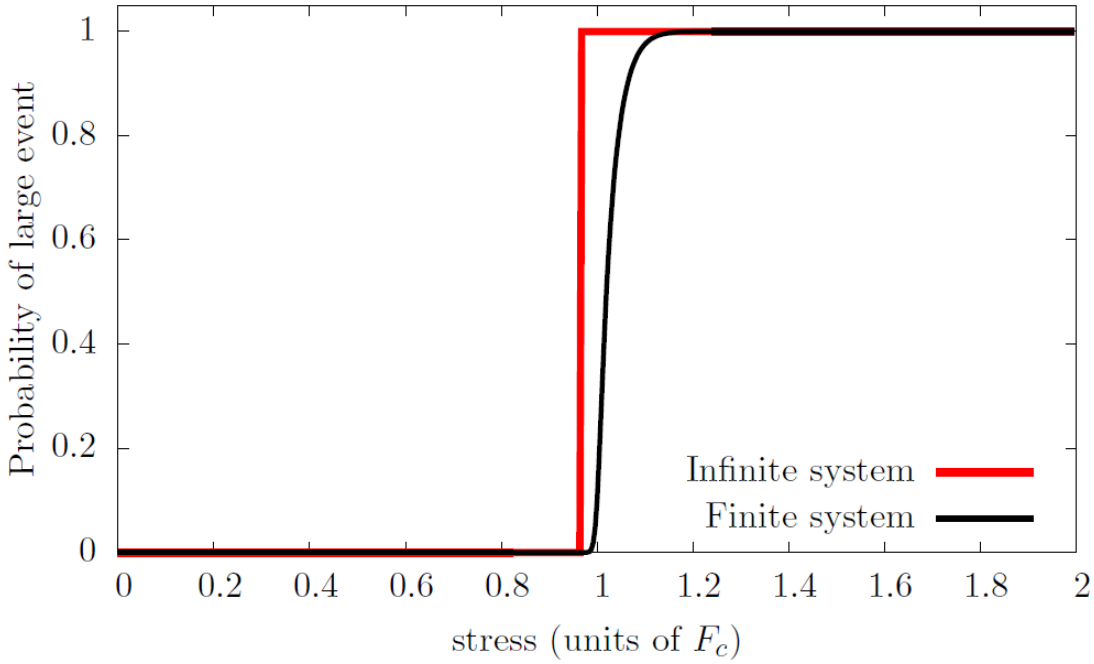

Figure 2.2: Probability of triggering a large event as a function of stress. For an infinite system, the probability abruptly becomes 1 at a stress close to the critical stress. For finite system, we expect the transition to be smoothed out. Our model results correspond to the finite system curve, as we expect it to be applicable to granular and rock friction experiments, which are not typically large in size.

2.4 Large earthquake inter-event time distribution

Having chosen a form for $P(F)$, we can now compute the inter-event time distribution for any $F(t)$ we desire. I will assume that the shear stresses on the fault are due mainly to compressive stresses and tectonic shear stresses which increase linearly in time: $F(t) = f + \Gamma t$, where f is the stress that the fault relaxes to after each large earthquake, Γ is the slow tectonic stress increase of a fault. The time since the last large earthquakes is t. A plot of the density for this choice of stress on the fault is shown in Fig. 2.3, below.

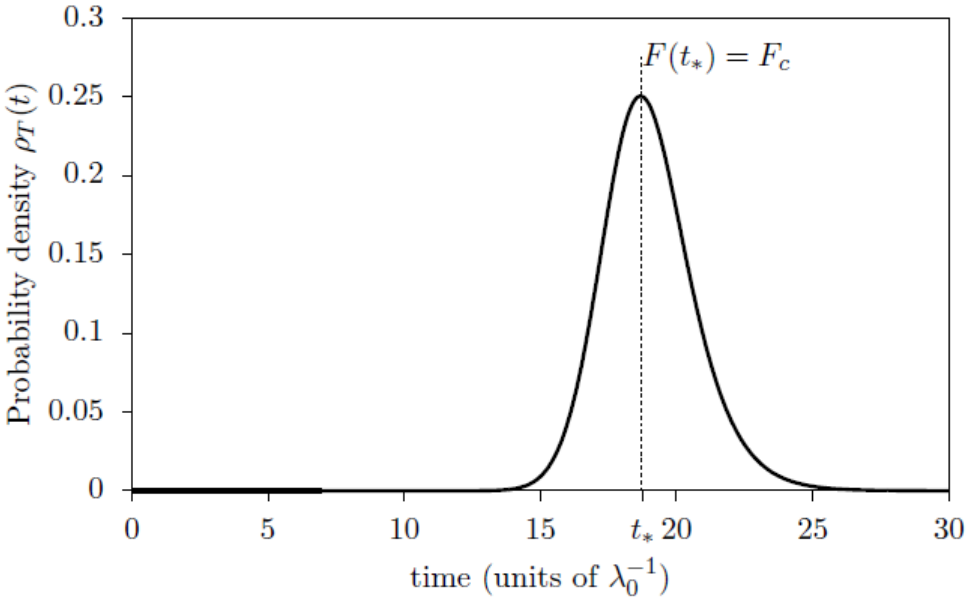

Figure 2.3: Plot of inter-event time distribution, $\rho_T(t)$, for an external stress $F(t)/F_c = 0.73{+}0.015t$. Because the parameters are fixed and do not change between earthquake events, the times are not conditional on any other events, so I drop the conditional in the notation in this plot. As expected, the most likely inter-event time is the time for which $F(t) = F_c$. The density drops off quickly for large inter-event times, and is similarly small for very short inter-event times.

This result agrees with simulations of the inter-event time distribution between large slips in the Ben-Zion/Rice earthquake model, as expected (see Appendix A). The simulations were performed by my collaborator Michael LeBlanc.

The shape of this distribution agrees qualitatively with the distribution observed in some recent granular matter experiments in which large stick-slips occur [7]. Unfortunately, there is presently not much other data on inter-event time distributions in granular matter or friction experiments. This is due to the fact that stick-slip events in such systems are often unrealistically periodic [2], and the distributions are effectively

[2] Y. Ben-Zion, Private Communication (2013).

Dirac delta functions. Future experiments designed to increase the aperiodicity between stick-slip events will provide opportunities to test our distribution against real data in materials. I discuss the case of earthquake faults in the next section.

2.5 Comparison to current models of earthquake inter-event time distributions

Ultimately, we would like to compare our distribution to real data on the inter-event times between large characteristic earthquakes. However, this is made difficult by the fact that there is little data available for characteristic events [21]. In lieu of real data to test our model against, I will instead compare our distribution to some distributions currently used to model earthquake statistics. The goal of this approach is to establish similarity between our model and currently employed models, demonstrating that our model is a viable candidate for modeling earthquake statistics.

Before I present this comparison, it is important to note that many distributions used in the earthquake literature are applied to earthquakes of all magnitudes above a specified cutoff [16–19, 21, 29–32]. This is quite different from the case of characteristic earthquakes, which have a narrow distribution of magnitudes. As we will see, distributions used to fit a wide range of magnitudes do not compare well with our distribution.

Common distributions used to model earthquake inter-event times include the Weibull distribution [18, 19, 21] and the Brownian passage-time distribution [20], which I will discuss specifically in Sec. 2.4. Other examples include the Weibull-log [18], Gamma [17], or even power-law distributions [18]. Some models and analyses have also demonstrated that some earthquake inter-event time distributions have universal scaling forms [16, 17, 29–32]. The universal scaling forms, however, are only expected to apply to earthquakes having sizes that follow the Gutenberg-Richter law. The sizes of large characteristic earthquakes do not follow a power-law distribution, and so we expect that our distribution of times between large events will not exhibit scaling.

Here, I will focus on two distributions: the Weibull distribution and the Brownian passage-time distribution. The Weibull distribution is often used to model the inter-event times between all earthquakes above a specified magnitude. While I am only modeling the inter-event times between characteristic earthquakes, the Weibull distribution can have a qualitatively similar shape to the one displayed in Fig. 2.3, and so I will check how well it compares to our distribution. The Brownian-passage time distribution is used to model

the times between large ruptures, and so we expect it to compare well with our distribution.

The Weibull distribution is a common phenomenological fit to earthquake inter-event time data [12, 19]. The Weibull distribution arises in some models of brittle materials [19, 33], often as a limiting distribution of an extreme value statistic [12, 19, 33]. Some studies have also attempted to derive the distribution from statistical mechanical models that assume power-law dependence on stress, which is assumed to increase linearly with time [19]. If the accumulation of stress proceeds logarithmically in time, these same models predict Weibull-log distributions of earthquake inter-event times.

The probability density function of the Weibull distribution has a relatively simple form,

$$\rho_{\text{Weibull}}(t) = k\lambda_w(\lambda_w t)^{k-1} \exp\left(-(\lambda_w t)^k\right),$$

where λ_w is a characteristic event rate and k is the "shape-parameter". The shape parameter controls the shape of the distribution - as suggested by its name. For $k < 1$, the probability density diverges as $t \to 0$, but otherwise looks roughly exponential (and is exactly exponential for $k = 1$). Accordingly, most inter-event times are relatively short. For values of $k > 1$, the probability density is finite at $t = 0$ and exhibits a peak at some time $t > 0$. Mathematically, the Weibull distribution is a special case of our distribution for $P(F(t)) \propto t^{k-1}$ (even for $k < 1$). Physically, if a fault had a triggering probability $P(F) \approx F^{k-1}$, then for $F(t) = f + \Gamma t$, we would expect our model to approximate a Weibull distribution. However, our chosen form of $P(F)$, derived from the Ben-Zion/Rice earthquake model (Eq. (2.4)), cannot be simply approximated as a power-law, and we will find our distribution is not well-described by the Weibull distribution, despite the qualitative similarity for $k > 1$.

The Brownian passage-time distribution is derived from a stochastic process called the Brownian relaxation oscillator process [20]. The model assumes a linear accumulation of stress on a fault, which results in a rupture when the fault stress reaches some critical amount. Furthermore, the model is characterized by two parameters: μ, the mean inter-event time, and α, the "aperiodicity", which characterizes the spread of the inter-event time distribution. The assumptions of this model are thus similar to the assumptions of our model, in the case for which the stress on the fault increases as $F(t) = \Gamma t$. In particular, the distribution models the inter-event times of large ruptures, not all earthquake events, as the Weibull distribution does. Qualitatively, the Brownian passage-time distribution indeed looks like our distribution. The analytical form of the distribution (particularly the cumulative distribution function) bears little resemblance to our

Distribution	Probability density function	Cumulative distribution Function
Our distribution	$\lambda_0 P(F(t)) \exp(-\lambda_0 \int_0^t d\tau\ P(F(\tau)))$	$1 - \exp\left(-\lambda_0 \int_0^t d\tau P(F(\tau))\right)$
Weibull distribution	$k\lambda_w(\lambda_w t)^{k-1} \exp(-(\lambda_w t)^k)$	$1 - \exp\left(-(\lambda_w t)^k\right)$
Brownian passage time distribution	$(\mu/2\pi\alpha^2 t^3)^{1/2} \exp(-(t-\mu)^2/(2\mu\alpha^2 t))$	See Ref [20].

Table 2.1: Comparison of the different candidate inter-event time distribution density functions: our distribution, the Weibull distribution and the Brownian passage time distribution. In our model, λ_0 is the constant small event rate and $P(F)$ is given by Eq. (2.2) or Eq. (2.1). In the Weibull distribution, k is a positive real number and λ_w is the characteristic failure rate. In the Brownian passage time distribution, α is the "aperiodicity" and μ is the mean inter-event time.

Distribution	Parameter	Fit value $\pm$95% confidence bounds
Weibull distribution	λ_w	0.0521 ± 0.002
Weibull distribution	k	13.0 ± 0.6
Brownian passage time distribution	α	0.084 ± 0.001
Brownian passage time distribution	μ	18.91 ± 0.02

Table 2.2: We fit Weibull and Brownian passage time distribution to a simulated distribution of earthquake inter-event times, where the times are drawn from Eq. (2.2), for $F = f + \Gamma t$. The fit parameters are given in this table. We set $\lambda_0 = 1$ in our simulation, so λ_w and μ are in units of λ_0 and λ_0^{-1}, respectively.

distribution for any choice of $P(F)$. However, as I will show below, the Brownian passage-time distribution fits our model much better than the Weibull distribution.

To provide a rough quantitative comparison between our distribution and the Weibull and Brownian passage-time distributions, I generate a set of random inter-event times drawn from our inter-event time distribution (Eq. 2.3)) and fit it with both a Weibull distribution and a Brownian passage time distribution. The fits are shown in Fig. 2.4, and the fit parameters are given in Table 2.2.

As seen in Fig. 2.4, I found that the Brownian passage-time distribution fits our own quite well. The Weibull distribution does not fit our distribution quite as well, even though it has a qualitatively similar shape to our distribution and the Brownian passage-time distribution. Clear systematic variations are visible in the residuals of the fit (the difference between the fit-curve and the actual data points). Furthermore, the fit parameters are not in the range that we might have expected. The mean rate λ_w is quite small compared to $\lambda_0 = 1$, the characteristic rate in our simulation. Furthermore, the shape parameter is quite large. We should expect a value of $k > 1$ due to the peaked shape of the histogram, but I have not observed any values of k as high as 13 in literature using Weibull distributions to model earthquake statistics.

To further investigate the issue, I calculated the empirical cumulative distribution function, denoted $\hat{\Phi}(t)$, of the random times drawn from Eq. (2.4) and plotted $\ln\left[\ln\left[((1-\hat{\Phi}(t))^{-1}\right]\right]$ versus $\ln t$. For a Weibull distribution, this plot should be a line with slope k. As seen in Fig. 2.5, the plot is non-linear, indicating

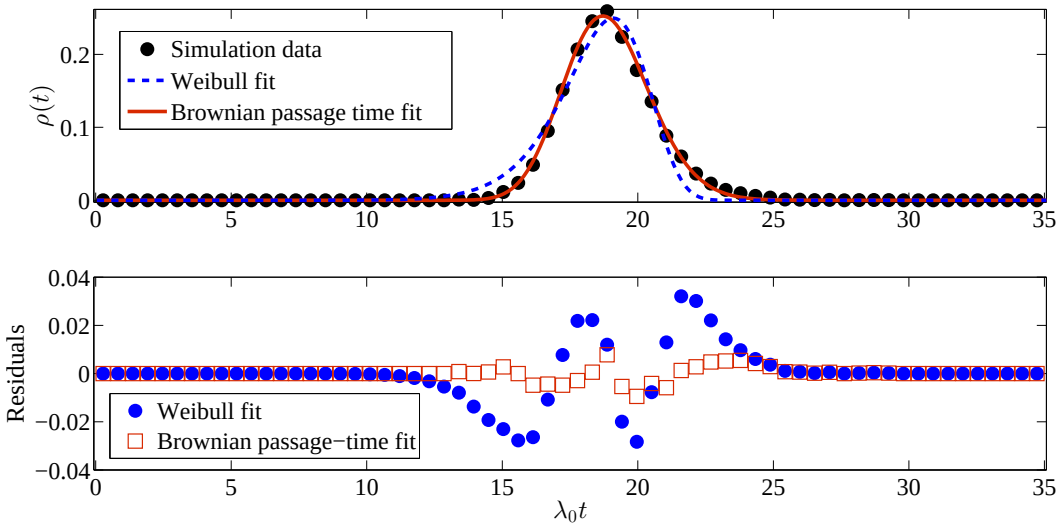

Figure 2.4: Fitting Weibull and Brownian passage-time distributions to a histogram generated by our distribution. The Brownian passage-time distribution fits quite well, while the Weibull distribution does not fit very well, despite having a qualitatively similar shape. Fitting was performed with MATLAB's curve-fitting toolbox, which performed non-linear regression on the simulation data.

that the Weibull distribution is a poor fit to the simulation data from our inter-event time distribution. As a test, I fitted a line to the data with a linear regression in MATLAB. The fit, of course, was poor, but the slope of the "best-fit" line was $k = 13.92$, as given by the non-linear fit. Linear fits to segments of the curve are possible, which could indicate Weibull-like behavior over certain time periods. Performing a linear regression for small times yields an even larger shape parameter $k \simeq 25$. Performing a linear regression for large times near the large event yields a more reasonable slope of $k \simeq 5$. However, the regimes of these linear fits correspond to the tails of the distribution (for which the residuals of the fit in Fig. 2.4 already suggest the fit is good), so all this analysis really suggests is that our distribution has similar asymptotic decay as the Weibull distribution. Otherwise, it is thus more appropriate to conclude that for our particular choice of $P(F)$, the Weibull distribution does not satisfactorily describe our simulation data.

I discuss the implications of these results in Sec. 2.6, below.

2.6 Discussion

As remarked earlier, the Weibull distribution is used to fit the inter-event times between earthquakes having a range of magnitudes above a chosen cutoff. Our distribution is meant only to model times between

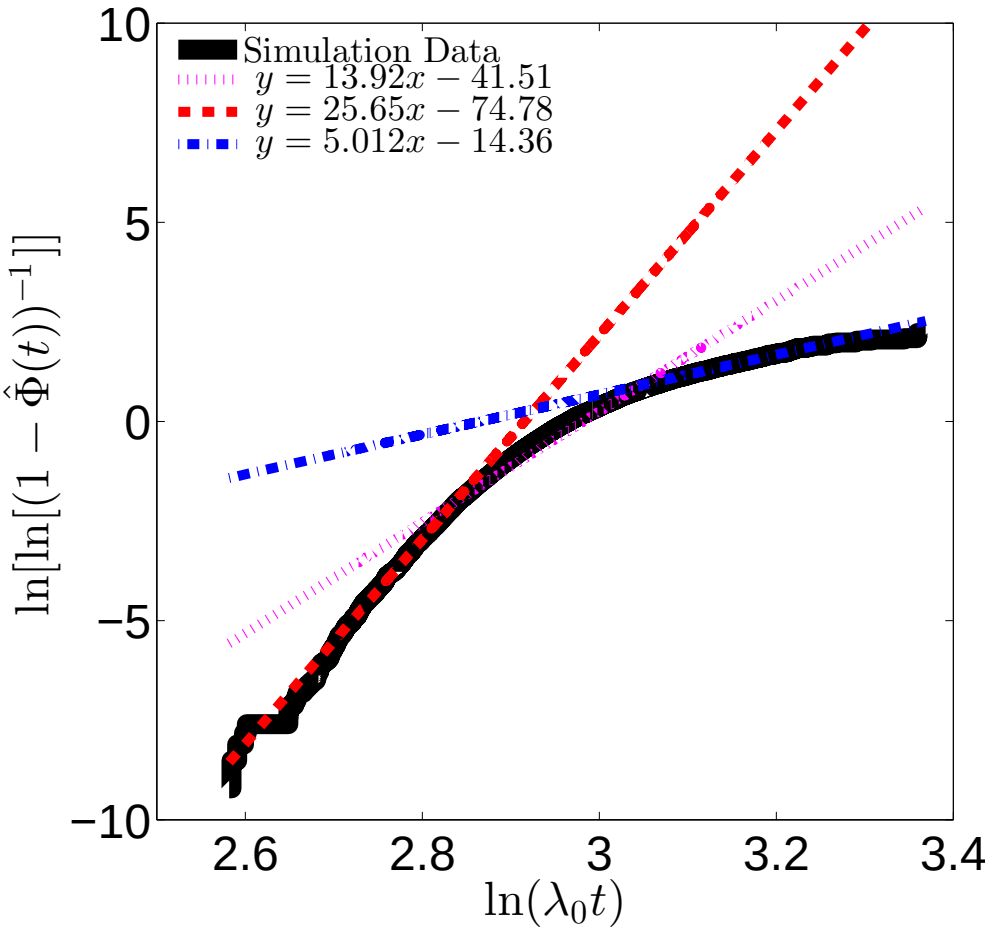

Figure 2.5: A Weibull plot of the cumulative distribution function of simulated inter-event times drawn from Eq. (2.3) using $P(F)$ as given in Eq. (2.4). The axes are chosen to be $\ln(\lambda_0 t)$ and $\ln\left[\ln\left[\left(1-\hat{\Phi}(t)\right)^{-1}\right]\right]$ because a Weibull distribution of shape parameter k will be a straight line with slope k on these axes. The nonlinear shape of our simulated data on this plot indicates that our simulation data is not well-modeled by a Weibull distribution. A linear regression to the entire data yields a line of slope $k = 13.92$, close to the value in Table 2.2. Restricting the linear regression to small $\ln t$ yields a better fit, but an even higher shape parameter of $k = 25.65$. Restricting the linear regression to larger $\ln t$ again yields a better fit, with a more reasonable shape parameter of $k = 5.012$.

characteristic large events, which have a narrow range of magnitudes. It is thus not surprising that the Weibull distribution results in a poor fit to an inter-event time distribution simulated using our model. In fact, for fits which include these low-magnitude earthquakes, the shape parameter has been observed to be $k = 0.66 < 1$. This is not only much lower than our fitted value of $k = 13$, but it corresponds to the $k < 1$ regime where the distribution is not peaked, but rather predicts most events occur at short inter-event times.

The derivation of the Brownian passage-time distribution, on the other hand, assumes that jump processes occur in the stochastic model, and the inter-event time distribution represents the times between these jumps [20]. These jumps represent large ruptures in the fault - i.e., large earthquakes. The fact that we observe excellent agreement between the Brownian passage-time distribution and ours supports the conclusion that the source of disagreement between our model and the Weibull distribution is that the Weibull distribution is used to model the inter-event time distribution of all earthquakes large than some magnitude threshold, not just large earthquakes. The sizes of the small events are outside of the scope of our model, so a future extension of our model will be necessary to address the question of the inter-event times of small earthquakes of different sizes.

Based on the agreement between our model and the Brownian passage-time distribution, we argue that our model is a viable candidate for modeling the statistics of the times between large characteristic earthquakes. For frictional experiments which observe non-periodic stick-slip behavior, we expect our model will also describe the statistics of times between large stick-slip events.

What advantage does our model have over the Brownian passage-time distribution or other models of the time between large earthquakes? The primary advantage is that it is quite easy to investigate different fault-stress conditions - i.e., different small event rate $\lambda(F)$, triggering probability $P(F)$, and fault stress $F(t)$. The inter-event time distribution does not need to be re-derived for different choices of these functions, which is not the case for the Brownian passage-time derivation.

Another advantage of our model is that it can be used to simulate the time-series statistics of more complicated microscopic models of earthquakes. Instead of repeatedly simulating a large microscopic model, which could be computationally expensive, one would only need to compute the small event rate $\lambda(F)$ and the triggering probability $P(F)$. These functions could then be used in our probabilistic model to generate a time series of events, which would be more efficient than a full microscopic simulation. This would allow for faster studies of the time series statistics of the microscopic model.

Our model will thus be useful for investigating a wide variety of interesting fault conditions. As an example of the flexibility of our model in analyzing different fault stresses, I end this chapter with a brief consideration of periodic fault stress perturbations[3], in Sec. 2.7, below.

[3]Detailed investigations of the effects of periodic fault perturbations are considered in chapters 3 and 4.

2.7 Application: Phase distributions in periodically-stressed faults

I now consider the case of an external stress with a periodic component:

$$F(t) = f + \Gamma t + F_0(\sin(\omega t + \phi) - \sin\phi). \tag{2.6}$$

The periodic component of this stress could represent tidal or seasonal stress variations. As before, f is the baseline stress level the fault relaxes to after a large earthquake, Γ is the slow tectonic shear stress, and t is the time since the last large earthquake. The periodic stress has amplitude F_0, frequency ω, and phase ϕ.

Using our inter-event time distribution, Eq. (2.3), we can derive the distribution of phases at which large earthquakes tend to occur. The probability density that a large earthquake will occur at phase φ given that the last large earthquake occurred at a phase ϕ is

$$\rho_\Phi(\varphi|\phi) = \omega^{-1} \sum_{k=-\infty}^{\infty} \rho_T\left(\frac{\varphi - \phi + 2\pi k}{\omega} \mid \phi\right). \tag{2.7}$$

This equation is derived in Appendix A. It is easy to show that this is periodic φ by setting $\varphi \to \varphi + 2\pi$ and re-indexing k to eliminate the extra factor of 2π. For our form of $P(F)$ from the Ben-Zion/Rice model, this sum cannot be evaluated in closed form. However, contributions from large k decay quickly, and contributions from negative k are canceled out by the step function $\Theta(t) \to \Theta(\varphi - \phi + 2\pi k)$ from the definition of $\rho_T(t|\{F(t)\})$ in Eq. (2.3). We can thus numerically evaluate Eq. (2.7) quickly.

More interesting than the conditional distribution, however, is the steady-state phase distribution which the system achieves after a large number of earthquakes has occurred. For earthquake faults whose properties are not changing significantly over time, we expect most earthquake faults to have achieved such a steady state. The steady-state distribution, $\varrho^*_\Phi(\varphi)$, is independent of the previous history of the fault (see Appendix A), hence why the conditional distribution is not as interesting if an earthquake fault has reached a steady-state. The steady-state distribution is given by solving the integral equation

$$\varrho^*_\Phi(\varphi) = \int_0^{2\pi} d\phi\ \rho_\Phi(\varphi|\phi)\varrho^*_\Phi(\phi). \tag{2.8}$$

Solving this equation analytically is quite difficult [4], but it can be solved numerically with relative ease by discretizing the integral [5], which reduces the problem to an eigenvalue equation. Details are given in Appendix A. Here, I will simply plot the results of numerically solving of Eq. (2.8) for some different frequencies ω and amplitudes F_0. I plot the numerical solutions against phase histograms generated by drawing random earthquake inter-event times from Eq. (2.3) and computing the nth phase via $\phi_n = \omega t_n + \phi_{n-1}$. I ran the simulation for several thousand events to allow the simulation to reach a steady state before collecting phases to form the histograms.

As shown in Fig. 2.6, the numerical solution agrees perfectly with the simulated steady-state phase distributions.

[4]Note that $\rho_\Phi(\varphi|\phi)$ is *not* a function of $\varphi - \phi$; after changing variables from t to φ, the stress contains a term $\sin\varphi - \sin\phi$. This prevents a simple Fourier series-type solution of Eq. (2.8).

[5]However, for low frequencies, the discretization of $\rho_\Phi(\varphi|\phi)$ is extremely sparse. It thus requires a large number of discretization points to attain a satisfactory resolution. Because the solution of the integral equation involves finding the eigenvalues of this matrix, computing the solution for very small frequencies can be time-consuming.

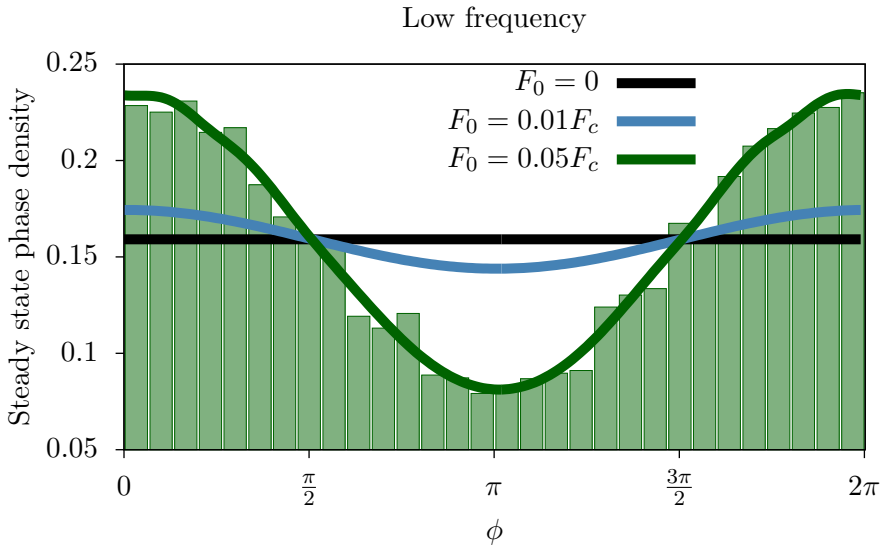

(a)

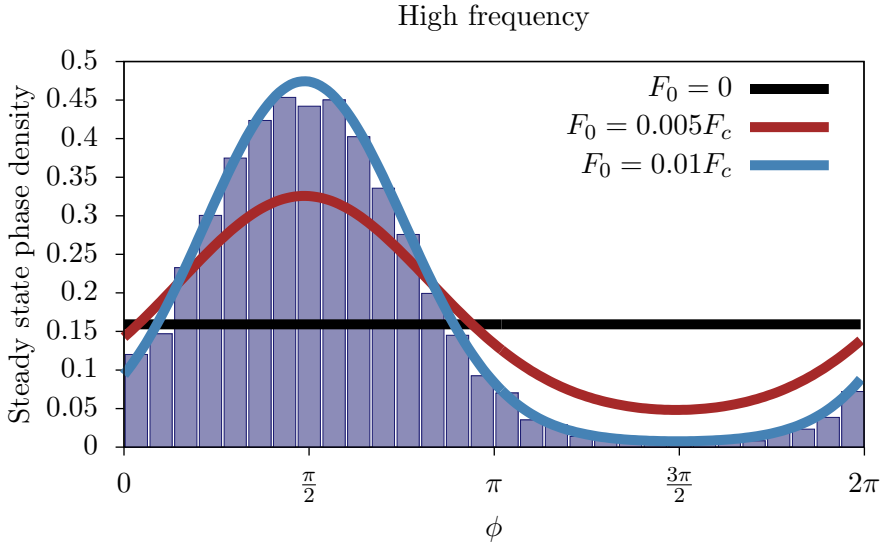

(b)

Figure 2.6: Numerical solutions for the steady-state phase distribution $\varrho^*_\Phi(\varphi)$ (solid curves) for different frequencies and amplitudes. Histograms are simulations generated by drawing random earthquake inter-event times from Eq. (2.3) and computing the n^{th} phase via $\phi_n = \omega t_n + \phi_{n-1}$. I ran the simulation for several thousand events to allow the simulation to reach a steady state before collecting phases to form the histograms.

Chapter 3

Control of large failures in frictional stick-slip systems subjected to periodic shear stresses

3.1 Introduction

With knowledge of the inter-event time distribution of large failure-slips in sheared frictional media, we can estimate the probability that a large system failure will occur in the future. However, the spread in the expected time we must wait until the next failure can still be quite large, so ideally we would like to develop even better methods of event prediction - or even control.

The application of periodic stresses to shear frictional matter has been studied as a possible tool for both predicting future large slips and for control. Work within the past decade or so includes studies of correlations between periodic driving and stick-slip behavior in rock interfaces [34,35] and granular matter [36,37], as well as studies of phase-locking in sheared plexiglass interfaces [38]. Studies of correlations with external stresses could reveal signals which may be used to better predict when failure is going to occur. Studies of phase-locking under periodic shear could reveal methods which enable us to *control* when failure is going to occur. These techniques could be readily applicable to material systems used for construction and engineering.

In addition, the stick-slip behavior of these experimental systems is also believed to mimic the behavior of earthquake faults. Earthquake faults are subjected to a variety of periodically varying stresses, including tidal stresses and seasonal or annual rainfall (or ice-load) variations. The impact of periodic stresses on these laboratory-scale systems could thus have implications for control or prediction of earthquakes. However, whether or not these laboratory experiments accurately capture the behavior of earthquake faults is controversial. Predictions based on rate-state frictional models of earthquake dynamics [34,35,39–42] predict the amplitude-dependence of the strength of correlations between earthquakes and periodic stresses should be constant at high oscillation-frequencies. In contrast, the laboratory experiments indicate a non-trivial amplitude-dependence at high frequencies. Until now, it has not been clear if the discrepancy between experiment and theory is due to a failure of the small-scale frictional media to mimic earthquake fault behavior,

or if previous theoretical models are missing some physics which would otherwise describe both systems.

In this chapter, I use the model presented in Chap. 2, which is designed to apply to both small-scale frictional systems and earthquake faults, to establish several results of relevance to shear frictional systems subjected to perturbative periodic stresses: (1) the model describes the experimental results which contradict previous theories. This indicates that the previous models are missing some physics which our model captures. (2) In relatively undisordered systems, correlations between stick-slip events and periodic driving are most easily detected when the system is driven at integer multiples of its natural failure frequency. For driving near these frequencies, we can reduce the uncertainty in the time between failures. (3) Our model reveals that the experiments are not being done at high-enough frequencies to properly describe correlations between large earthquakes and perturbative periodic stresses, such as tidal stresses. (4) For the frequency-regime of our model which is applicable to earthquakes, we predict that hundreds of thousands of earthquakes must be recorded (requiring a catalog of millions of years) to detect significant correlations between *large* earthquakes and tides.

In the following section, I discuss the application of the model of Chap. 2 to frictional systems undergoing slow shear with an additional perturbative periodic component. In Sec. 3.3, I discuss the analysis of the earthquake time series generated from the model. In Sec. 3.4, I present the results of the correlation analysis, and in Sec. 3.5 I investigate the amplitude and frequency dependence of the mean inter-event time and standard deviation. Finally, in Sec. 3.6, I discuss the implications of our results for earthquake prediction, before providing a summary in Sec. 3.7.

3.2 The earthquake statistics model for periodically-stressed systems

In this work[1], I will use the model of Chap. 2 to study the statistics of slowly-sheared frictional systems subjected to additional periodic perturbative stresses. In the experimental systems of Refs. [34–37], small slip events are not typically observed[2]. This suggests small slips events are either too small to observe in these experiments, or that all small slips trigger large slips. In the former case, it is possible that both the small-event rate $\lambda(F)$ and the large slip triggering probability $P(F)$ are stress-dependent, while in the

[1]This work is to be submitted for publication as: B.A.W. Brinkman, M.P. LeBlanc, Y. Ben-Zion, J.T. Uhl and K.A. Dahmen, "Control of large failures in frictional stick-slip systems subjected to periodic shear stresses" (2013). [23]

[2]Some experimental systems are reported to exhibit small slips. (P. A. Johnson, *Private communication*, 2012)

latter case the small event rate is stress-dependent and the triggering probability is $P(F) = 1$. Because the statistics of the large slips depend only on the overall functional form of the product $\lambda(F)P(F)$, we expect only quantitative differences in our results if we set either of $\lambda(F)$ or $P(F)$ to a constant. Thus, for simplicity, I assume that small events in the experiments are simply hard to observe, and they occur at a constant rate $\lambda(F) = \lambda_0$. I then assume that the triggering probability $P(F)$ is given by Eq. (2.4), which I remind the reader is derived from the Ben-Zion/Rice model of earthquake physics, which has also been applied to sheared granular systems [4–6, 26–28].

As in Sec. 2.7, I assume the total (average) shear-stress on the fault, $F(t)$, consists of two contributions: a slowly, linearly increasing component Γt, where the slow rate Γ is imposed, for example, by a slowly moving system boundary, and an external oscillatory stress $F_0 \sin(\omega t + \phi)$ of frequency ω, amplitude F_0 and phase ϕ. When the total stress exceeds a critical value F_c, the system almost certainly triggers a large slip, which relaxes the stress, until it reaches a much lower arrest stress, f. That is, the total fault stress is

$$F(t) = f + \Gamma t + F_0(\sin(\omega t + \phi) - \sin\phi). \tag{3.1}$$

Fig. 3.1 schematically depicts the time evolution of the total fault stress $F(t)$ relative to the applied periodic driving stress.

In this chapter, I will simulate a time series of large slips (or earthquakes), and analyze that time series for correlations between the timing of the slips and the phase of the periodic driving stress. I will also numerically calculate the mean inter-event times and standard deviations as a function of amplitude F_0 and frequency ω, which will give us information about how to try and exert some control over the timing of slip-events.

In the next section, I will briefly describe how we analyze the time series for correlations between the slips and the driving stress.

3.3 Time series analysis for correlations between stick-slip failure events and periodic driving

I generated a time series of large slips by drawing 100,000 random inter-event times from a random number generator which returns numbers distributed according to Eq. (2.3). Because t in Eq. (4.1) represents the

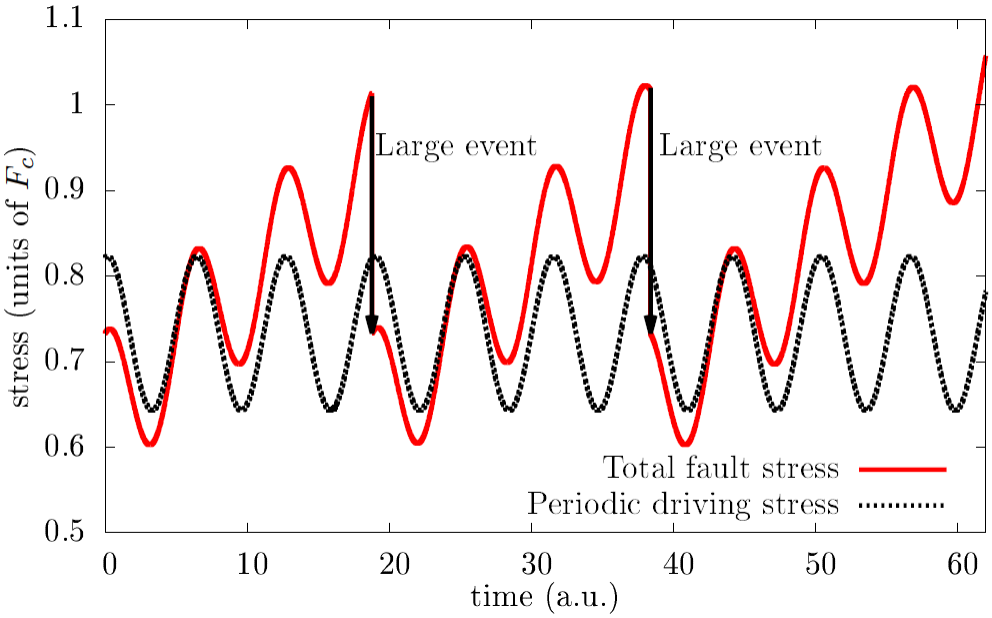

Figure 3.1: Total external stress on system (solid red line) compared to the small periodic driving stress (dashed line). We analyze correlations using a Schuster test, described briefly in Sec. 3.3 and in more detail in Appendix B. The correlations depend on the frequency ω and the amplitude F_0 of the periodic driving stress, as well as the number of events observed for the Schuster test. For clarity, we have exaggerated the amplitude of the oscillations. Realistic amplitudes are much smaller than the failure stress $F_c = 1$.

time *between* large slips, it resets to $t = 0$ whenever a large slip occurs. This also requires us to update the phase, $\phi \to \omega t_{\text{event}} + \phi$, where t_{event} is the time at which a slip event occurs. As a result, the phase is different for every slip event. As shown in the previous chapter (Sec. 2.7), there is a distribution of phases at which the large slips tend to occur. If the correlations in the system were weak, we expect a histogram of the phases at large slips occur to be roughly uniform. For strong correlations, the histogram of the phases is very non-uniform. This suggests that we can use the phase-histogram as a measure of correlations. To be precise, we will calculate the probability that a histogram of n recorded phases is non-uniform due only to statistical fluctuations. This is called a Schuster test, which I describe below.

3.3.1 Schuster test analysis

The Schuster test [34–36, 43] is a statistical hypothesis-testing technique used to quantify the strength of correlations between the timing of events and phases of a periodic driving signal. It quantifies the correlations by calculating the probability that a distribution of phases at which the earthquakes occur is at least as

extreme as the one we observe, given that the null hypothesis,

The histogram of phases at which n large stick-slip events occurs is uniform,

is true. If we map the phases at which the large slips occur to steps in a 2d random walk with unit steps (see Appendix B), the probability that the walker will have traveled a distance of D_n or greater is given, in the limit of large n, by

$$p_n = \exp\left(-\frac{D_n^2}{n}\right), \tag{3.2}$$

where D_n is the distance the random walk has traveled from the origin after n steps,

$$D_n^2 = \left(\sum_{k=1}^{n} \cos\phi_k\right)^2 + \left(\sum_{k=1}^{n} \sin\phi_k\right)^2, \tag{3.3}$$

and ϕ_k are the phases at which the large slips occur.

This is equivalent to the probability that the periodic motion of the measured phase distribution is greater than a threshold value, if it is in fact purely random. We thus identify p_n as the "p-value" for the null hypothesis that there is no systematic connection between the driving and the earthquake timing. The p-value quantifies the probability that we would observe the measured phase distribution or one with even stronger correlation if the null hypothesis were true. So, if D_n exceeds $\sqrt{n}$ by a significant amount, p_n is accordingly small, suggesting that it is unlikely that the observed phase distribution would be produced, assuming the earthquakes are triggered completely randomly. The p-value will thus be our benchmark to quantify how strongly the slip events in our model correlate with the periodic component of the driving stress.

Because even random fluctuations can cause the p-value to reach low values, a p-value of $p_n = 10\%$ or less is often chosen as a threshold for statistical significance. The experimental analysis in Refs. [34–36] choose a threshold of 0.5%, corresponding to a confidence threshold of 99.5%. We follow the experimentalists in choosing this as our significance threshold as well.

To evaluate the correlations in our model, I compute the root-mean-square value of D_n in my simulations for $19,200$ frequency-amplitude pairs, (ω, F_0). If the root-mean-square distance exceeds the distance expected for a purely random walk (obtained by solving Eq. (3.2) for D_n for a threshold of $p_n = 0.005$), I consider the

large slips to be correlated with the periodic component of the driving. See Appendix B for more details.

The results of this analysis are given below.

3.4 Amplitude and frequency dependence of correlations

The experiments on sheared granular matter and rock interfaces [34–36], to which we compare our model, interpret their correlation measurements in terms of a "threshold" amplitude, $F_{0\min}(\omega)$. That is, for a given frequency at which the systems are driven, there is a particular value of the amplitude F_0 for which p_n is less than 0.5% and the stick-slip events are considered correlated with the periodic driving stress. We similarly calculate $F_{0\min}(\omega)$ in our simulations. The resulting threshold curve is shown in Fig. 3.2, below. Points (ω, F_0) above the $F_{0\min}(\omega)$ curve correspond to values for which correlations are detected with 99.5% confidence.

The data points plotted in Fig. 3.2 correspond to re-scaled data from the granular matter experiments (diamond symbols) [36] and the rock-friction experiments (x symbols) [34, 35]. The agreement between our simulation results and the experimental data suggests that our model is indeed capturing the physics of the experimental systems! The qualitative agreement is particularly important, because the minimum that the rock interface data forms is not predicted by previous frictional models, indicating that our model captures some physics that the rate-state friction models do not seem to describe well.

In full disclosure, I should stress the data points in Fig. 3.2 do not represent a fit, only a qualitative agreement between observed behaviors and behaviors predicted by our model. The experimental data has been rescaled and overlaid on our plot. Many parameters of the experimental systems must be measured or characterized more precisely before we can make a quantitative comparison between the model and the experiments.

With that noted, there are several interesting features of the threshold amplitude $F_{0\min}(\omega)$. The physical origin of these features warrants further explanation, and I will now discuss them one by one, below.

3.4.1 Low frequency behavior: $\omega \ll 2\pi/\tau_0$

Our model predicts $F_{0\min}(\omega) \sim 1/\omega$ at small frequencies $\omega < 2\pi/\tau_0$, where τ_0 is the mean inter-event time in the absence of periodic stresses ($F_0 = 0$). This agrees with experiments on sheared granular materials [36]. The intuitive explanation behind this results is as follows: The $1/\omega$ decay reflects a competition between

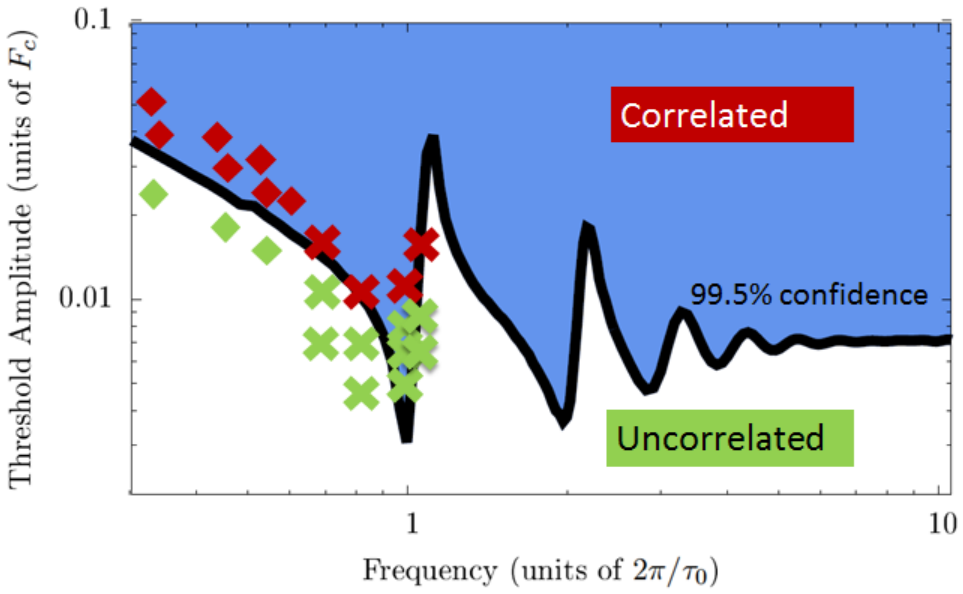

Figure 3.2: Minimum ("threshold") amplitude $F_{0,\min}$ required for detecting a correlation between the periodic driving stress and large events as a function of frequency, on a log-log plot. The curve represents the minimum amplitude required to detect a correlation at 99.5% confidence for $n = 500$ recorded events: in the shaded region above the curve we detect significant correlations, while below the curve the correlations do not meet our 99.5% threshold (and are labeled "uncorrelated"). As expected, the minimum required amplitude decreases as more events are recorded (see Appendix B). The frequency axis is plotted in units of the average failure rate $2\pi/\tau_0$, where τ_0 is the average time between sequential large events in the absence of oscillatory stresses ($F_0 = 0$). The diamond symbols represent rescaled data from the granular experiments of Ref. [36] and the crosses represent rescaled data from the rock-friction experiments of Refs. [34, 35]. Green symbols below the threshold curve represent experimental runs for which no correlations were detected, while red symbols above the threshold curve represent experimental runs for which correlations were detected. The correlation threshold for both experimental systems was 99.5%.

the slow loading rate, Γ, and the maximum oscillatory loading rate, ωF_0. At low frequencies, most large slips (per unit time) are triggered during periods of high stress rate. To detect correlations between large slips and the periodic driving stress, the periodic driving stress rate, ωF_0, must thus exceed the background stress rate, Γ. Hence, correlations with the oscillating stress are seen when $\omega F_0/\Gamma \gg 1$ and consequently $F_{0\min}(\omega) \sim \Gamma/\omega$.

3.4.2 First Minimum in $F_{0\min}(\omega)$

Following the power-law region is a minimum in $F_{0\min}(\omega)$. The existence of this minimum agrees with experiments on rocks [34, 35]. This minimum occurs when ω is equal to the natural characteristic failure

rate, $2\pi/\tau_0$. The model predicts that the frequency of the minimum $\omega = 2\pi/\tau_0$, with $\tau_0 \sim 1/\Gamma$, shifts to higher frequencies when the loading rate Γ is increased (see Appendix B for plots and more details). This, too, is observed in the rock experiments [34, 35].

The low-frequency power-law behavior and the existence of a minimum thus indicate that our model correctly predicts the observations of experiments on rocks and granular materials. In contrast, traditional friction models [34,35,39–42] predict no minima in $F_{0\min}(\omega)$. Instead, in these previous models, there is only a monotonic transition from the low frequency power-law behavior into a constant.

3.4.3 Multiple peaks at intermediate frequencies

At intermediate frequencies $2\pi/\tau_0 < \omega \lesssim 6(2\pi/\tau_0)$, our model predicts a series of valleys and peaks of decaying height in $F_{0\min}(\omega)$. We find the height of the peaks depends on the spread $\sigma_{0,\tau}$, of the distribution of inter-event times at $F_0 = 0$. The spread is an effective measure of the disorder in the system. Systems with large $\sigma_{0,\tau}$ exhibit smaller peaks. For large enough $\sigma_{0,\tau}$ the peaks are no longer visible and only the minimum at $\omega = 2\pi/\tau_0$ persists (see Fig. B.4 in Appendix B) [3].

The origin of the peaks and valleys is a resonance-like effect: when the driving frequency matches the system's natural failure frequency $2\pi/\tau_0$ (or an integer multiple of it), it is relatively easy for the additional oscillatory stress to trigger large slips so $F_{0\min}(\omega)$ is small. When the frequency is detuned from the natural failure frequencies, it becomes harder for the oscillatory stress to trigger events and $F_{0\min}(\omega)$ is larger.

3.4.4 High frequency behavior, $\omega \gg 2\pi/\tau_0$

Our model also predicts that $F_{0\min}(\omega)$ tends to a constant at high frequencies $\omega \gg 2\pi/\tau_0$, similar to traditional friction model predictions [34,35,39–42]. This regime corresponds to frequencies higher than have previously been tested in experiments. The asymptotically constant behavior of $F_{0\min}(\omega)$ is a consequence of the fast oscillations causing the driving stress to reach its critical value F_c at a "failure time" that is roughly a time F_0/Γ earlier than in the absence of oscillations. To observe a correlation, we must be able to distinguish this time-shift from statistical fluctuations in the average failure time when $F_0 = 0$; i.e., F_0/Γ must be greater than the statistical spread $\Delta t \simeq \sigma_{0,\tau}/\sqrt{n}$ (the standard deviation of the mean) of average

[3] It is possible that the experimental systems would not see subsequent peaks at high frequencies, and the data in Fig. 3.2 are better compared to the disordered threshold curve shown in Fig. B.4. However, without more experimental evidence, we cannot distinguish between the two plots. Here, we choose to highlight the non-disordered plots so that we can discuss potential applications for control in Sec. 3.5.

inter-event times of the oscillation-free ($F_0 = 0$) system. Here $\sigma_{0,\tau}$ is the standard deviation of inter-event times in the absence of periodic driving and n is the number of measured events. For a 99.5% confidence interval, corresponding to 3 standard deviations, we thus need $F_{0\min}(\omega)/\Gamma > 3\sigma_{0,\tau}/\sqrt{n}$, giving a constant high-frequency threshold

$$F_{0\min}(\omega) \sim \frac{3\sigma_{0,\tau}\Gamma}{\sqrt{n}}, \text{ for } \omega \gg \frac{2\pi}{\tau_0}. \tag{3.4}$$

The dependence on the number n of events is a general feature of $F_{0\min}(\omega)$, which scales as $F_{0\min}(\omega) \sim F_0/\sqrt{n}$ due to statistical fluctuations (see Appendix B).

3.5 Application of results: Control of frictional systems via small amplitude driving

Now that I have characterized the correlations in these different frequency regimes, we would like to know how these correlations relate to prediction or control of slips in this systems. The minima in $F_{0,\min}(\omega)$ suggests that the system is particularly susceptible to external periodic stressing at the resonant frequencies at which the minima occur. This suggests we may be able to trigger large slips in frictional systems by driving the system at the resonant frequencies. Perhaps by slightly detuning the driving away from the resonant frequencies we can even advance or delay failure.

To investigate this issue further, I computed the average inter-event time, $\langle t \rangle = \tau(F_0, \omega)$, and the standard deviation of the inter-event times, $\sigma(F_0, \omega)$, as functions of the amplitude and frequency of the periodic driving. Figs. 3.3 and 3.4 present plots of these functions for amplitudes $F_0 \ll F_c$.

At the "resonant" frequencies, $\omega_{\text{res}} = 2\pi m/\tau_0$, with m a small integer, $\sigma(F_0, \omega)$ has a local minimum and $\tau(F_0, \omega_{\text{res}}) \approx \tau(F_0 = 0, \omega) = \tau_0$. Recall that these resonant frequencies coincide with the minima in $F_{0\min}(\omega)$. Detuning the frequency just below (above) a resonant frequency increases (decreases) $\tau(F_0, \omega)$. Thus, on average, it is possible to delay or advance the timing of large slips by applying oscillatory stresses of the right amplitude and frequency. In this way one may be able to control the failure times. Notably, at the resonant frequencies, the standard deviation is smaller than it would be in the absence of periodic driving ($F_0 = 0$). By driving the system at a frequency corresponding to its natural failure rate, we can thus trigger failure with greater regularity than the undriven system. If the disorder in the system is not too large, one can also drive the system at integer multiples of the natural failure rate to achieve this effect; however, the

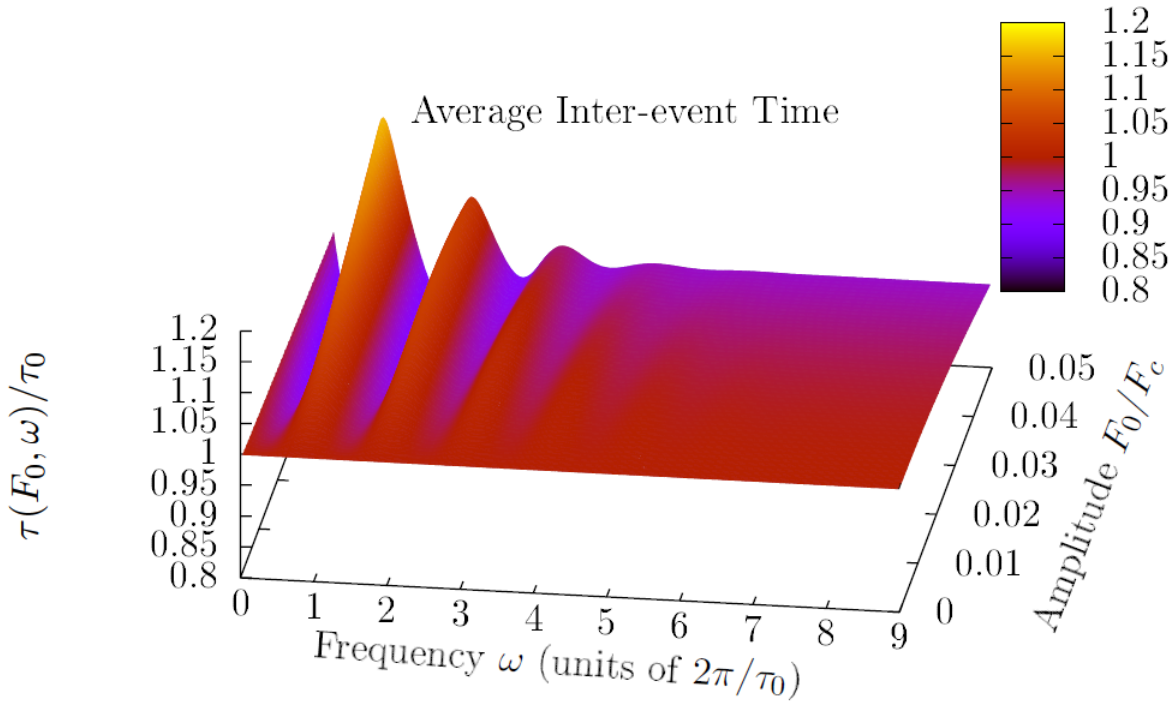

Figure 3.3: Average time between large slips, $\tau(F_0, \omega)$, as a function of frequency and amplitude, measured relative to the natural mean failure time in the absence of oscillations, τ_0. We find that when the driving frequency of the periodic stress is tuned just below or above the "resonant" frequencies at $\omega = 2\pi m/\tau_0$, m an integer, $\tau(F_0, \omega)$ increases or decreases relative to τ_0, respectively. At the resonant frequencies we find $\tau(F_0, \omega) \approx \tau_0$. Hence, on average it may be possible to delay, advance, or trigger system failure by applying oscillatory waves of the appropriate amplitudes and frequencies.

amount by which the standard deviation is reduced relative to the $F_0 = 0$ value, $\sigma_{0,\tau}$ diminishes at larger resonant frequencies. Between resonant frequencies, the standard deviation achieves a maximum value larger than the undriven standard deviation due to anti-resonant effects, so tuning the average inter-event times away from τ_0 also leads to wider spreads of failure times.

At amplitudes larger than a few tenths of the critical stress F_c, the average inter-event time drops below τ_0 (except at frequencies $\omega \ll 2\pi/\tau_0$) because the stress reaches its critical value much sooner than at lower amplitudes or in the absence of oscillatory stresses. The standard deviation is about the same as in the absence of oscillations at these larger amplitudes (except at some frequencies $\omega < 2\pi/\tau_0$, for which the standard deviation remains smaller than in the absence of periodic driving (see Appendix B for details)). Driving the system at large amplitudes thus offers little practical advantage compared to low-amplitude driving.

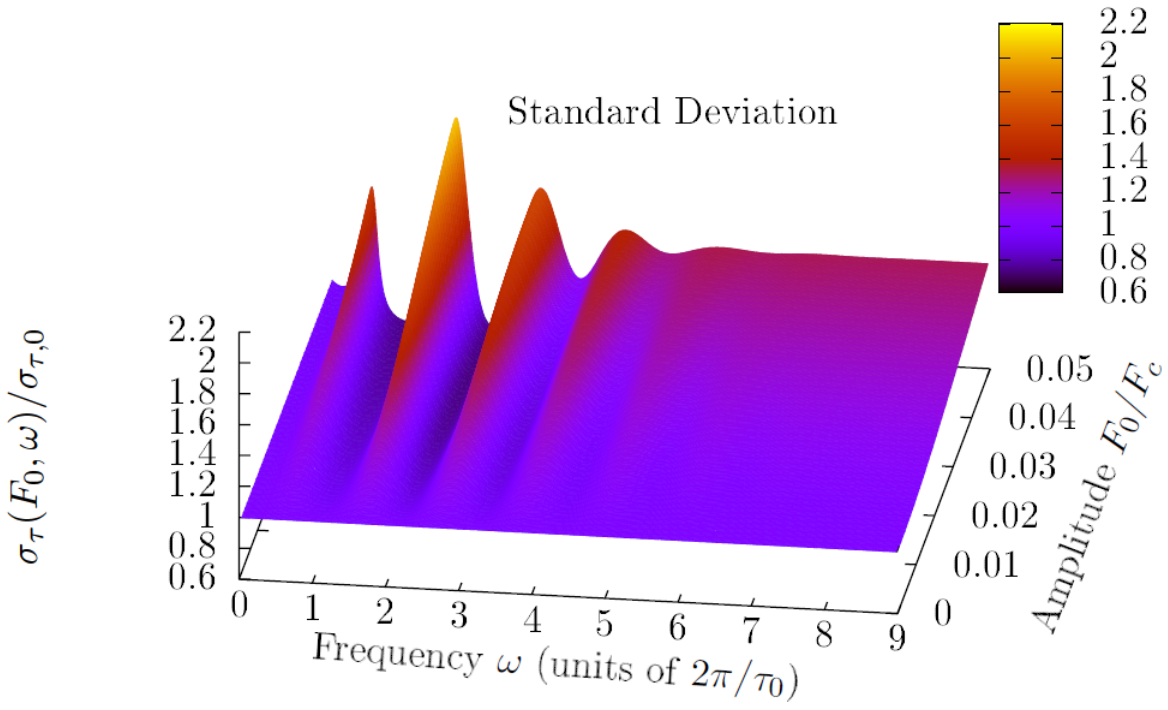

Figure 3.4: The standard deviation of inter-event times, $\sigma_\tau(F_0, \omega)$, as a function of frequency and amplitude, measured relative to the natural standard deviation in the absence of oscillations, $\sigma_{0,\tau}$. The standard deviation is not only smallest at the resonant frequencies, but smaller than the standard deviation in the absence of periodic driving. This implies we can trigger failure more reliably by driving frictional systems at these "resonant" frequencies. At frequencies away from the resonant frequencies, the standard deviation grows. As a result, there a trade-off between maximizing or minimizing the average inter-event failure times and the spread in failure times.

3.6 Implications for earthquake faults

If we want to use the model to study correlations between large earthquake timings and tidal or seasonal stresses, a comparison of typical earthquake inter-event times to tidal or seasonal frequencies reveals that earthquakes belong in the high-frequency regime, $\omega \gg 2\pi/\tau_0$. Tidal effects on earthquakes correspond to lab experiments at much higher frequencies than previously probed. This implies that experiments on lab-sized rocks and granular materials [34–37] must be done at larger frequencies in order to mimic the correlation-behavior of earthquake faults.

Because comparing earthquake timings to tidal or season stress variations corresponds to the high frequency regime of Fig. 3.2, Eq. (3.4) applies. We can use this equation to estimate the number of earthquake events we need to record in order to detect significant correlations.

Estimated solid tide amplitudes are on the order of $F_0 \sim 5$ kPa while typical model estimates of the shear stress rate Γ for tectonic loading are in the range of around 1-10 MPa/(100 years) [44]. We use an order-of-magnitude estimate of the standard deviation of inter-event times on the fault, $\sigma_{0,\tau}$, of 100 years. From Eq. (3.4) above, we then estimate that on the order of $n \sim 10^4 - 10^7$ large events are needed to detect statistically significant correlations between tides and large earthquake in faults like the San Andreas Fault. Thousands of large earthquakes (i.e., millions of years) are needed to observe statistically significant correlations with tidal or seasonal stress oscillations. This agrees with conclusions drawn by Beeler and Lockner [34, 35].

While it may be impractical to detect correlations between tides and large earthquakes due to the number of events needed, it may be easier to acquire good statistics for small earthquakes. Furthermore, by studying correlations between small slips and tidal or seasonal stress variations, we may be able to develop signals useful for forecasting large earthquakes. This work is the subject of the next chapter.

3.7 Conclusions

The results in this chapter demonstrate that our model explains prior experimental data on large-slip-correlations in many different materials, ranging from rock interfaces to granular matter. The model also predicts experimental results at higher oscillation frequencies than previously tested and suggests new methods of controlling the average failure time between large slips. By applying periodic stresses of the appropriate (near-resonant) frequencies and amplitudes to frictional systems with stick-slip behavior, we can predict

failure times more accurately and trigger failure with more certainty than in a system without additional periodic loading. We can also increase or decrease the average inter-event time by detuning the driving frequency just below or above the resonant frequencies, respectively. Engineering applications of these results could form the basis of new hazard prevention methods; for example, by delaying material failures so that reinforcements can be added.

Extensions of this work focus on the effects of microscopically small slips that occur between large slips, present in some rock-friction experiments[4] and earthquake faults [45]. Such small slip-events are local and do not affect the entire system. We find that our large slip results for $F_{0\min}(\omega)$ are qualitatively unaltered by the presence of small slips (see Appendix B for details).

For the applicability of the experiments to earthquakes, we draw two main conclusions:

(1) Our model predicts that tidal and seasonal frequencies for earthquakes are in the high frequency regime where $F_{0\min}(\omega) =$ constant. Experiments designed to mimic the effect of tides on earthquake faults must probe frequencies that are much higher than the natural failure repeat frequency $2\pi/\tau_0$ of the experimental system. This is a higher frequency range than was explored in the previous experiments on lab-sized rocks and granular materials [34–37].

(2) On the question of whether we can predict large earthquakes from their correlations with tidal or seasonal stress variations, our model predicts that it is not practical to extract such correlations from large earthquakes alone. The reason is that tens of thousands of large earthquakes (i.e., millions of years) are needed to extract statistically significant correlations. However, it may be easier to acquire good statistics for small events. By studying correlations between small earthquakes and tidal or seasonal stress variations, we may be able to develop signals useful for forecasting large earthquakes. This problem is addressed in the next chapter.

In summary, our model provides a new framework for understanding the effects of periodic stresses on large failure events in stick-slip systems such as rocks, granular matter, or earthquake faults, like the San Andreas fault, that show recurring large characteristic earthquakes [6]. We predict an interesting frequency-dependence of the minimum amplitude, $F_{0\min}(\omega)$, required to detect correlations between periodic stresses and large slips. Our model results not only explain recent experimental observations [34–37], but also provide new predictions for experiments at higher frequencies than previously tested. An analysis of the frequency- and amplitude-dependent mean inter-event times predicts new ways to use oscillatory stresses to control the

[4] P. A. Johnson, *Private Communication* (2012).

failure times in experimental stick-slip systems. The model also predicts the oscillation-frequency regime for which future experiments may mimic the effect of tidal and seasonal stresses on earthquakes. Finally, the model resolves the long-standing debate about the connection between friction experiments on rocks and granular materials and the observability of real earthquake-tide correlations. The results demonstrate the usefulness of our simple model as a starting point for phenomenological studies of non-destructive, correlation-based prediction of material failures, bolstering hope that we may one day be able to control - and perhaps prevent - such destructive events in frictional systems.

Chapter 4

Forecasting large earthquakes using small-quake tidal correlations

4.1 Introduction

It has been speculated that correlations between tidal stresses and large earthquakes could be useful for forecasting future events [46–48]. However, only 1% of large earthquakes are found to significantly correlate with tides [34, 48], suggesting that such correlations may not be so useful for earthquake prediction. The results of Chap. 3 support the claim that detecting correlations between earthquakes and tidal stresses is impractical.

On the other hand, recent analyses by Tanaka [49, 50] indicate significant correlations exist between tidal stresses and *small* earthquakes preceding large earthquakes. This suggests correlations between small quakes and tidal stresses may be useful for predicting impending large earthquakes. To test the effectiveness of these correlations, I used the simple probabilistic model of frictional slip-statistics introduced in Chap. 2 to compute the probability that a large earthquake will occur just after a time period of significant correlations between small earthquakes and tidal stresses. This allows us to study what earthquake-tide correlation analyses may optimize our assessments of earthquake risk. For example, I found that correlations with annual stress variations may be stronger than tidal correlations.

Small earthquakes are much more numerous than large earthquakes, and generally increase in number as the total stress on a fault increases [45]. Unlike detecting correlations between large earthquakes and tides, the relatively large numbers of small earthquakes suggest that detecting significant correlations between small earthquakes and periodic stresses may be feasible. Furthermore, the strength of the correlations should increase just prior to a large earthquake, when the fault stress is highest. Small-quake correlations with tidal stresses or other periodic stresses, such as annual stress variations, could thus signal an increased probability of an impending large earthquake.

Tanaka's recent analyses of small-quake correlations with tidal stresses, prior to three magnitude 9.0

earthquakes near Indonesia and the 2011 Tōhoku earthquake in Japan [49,50], support the plausibility of this idea. Tanaka found that correlations increased just prior to the large earthquakes. However, the correlations did not always achieve standard levels of statistical significance. We thus evaluate the effectiveness of small quake-tidal correlations as indicators of future large earthquakes.

To this end, I applied the earthquake time-statistics model presented in Chap. 2 to the case of a fault subjected to perturbative periodic stress variations. I pursued two primary goals in this work: (1) Determine which essential features of earthquake faults and small earthquake statistics lead to correlation signals like those observed by Tanaka and (2) Evaluate the correlations as a predictor of large earthquakes; e.g., I developed an analysis of the correlation-signal that estimates the probability that a large earthquake will occur within in the next ten years. I also studied whether other periodic stresses, such as annual stress variations, result in stronger signals than tidal stresses. I found that the model assumptions presented in Chap. 2 were sufficient to reproduce the correlation behaviors observed by Tanaka. Furthermore, I found that in our model, correlations between small earthquakes and tides *can* be used to estimate the risk of an impending large earthquake. These results open the door to the development of more advanced analyses of earthquake correlations, which may ultimately lead to early warning signals for impending large earthquakes[1].

4.2 Small earthquake event rate

In contrast to the previous chapters in which I assumed the small event rate $\lambda(F)$ was constant, in this chapter the stress-dependence of $\lambda(F)$ on $F(t)$ is important. If $\lambda(F)$ were stress-independent, the model would yield no significant correlations between small earthquakes and external stresses. Instead, we assume that $\lambda(F)$ is small for fault stresses much less than F_c, and rises rapidly to a larger rate as $F \to F_c$. This behavior, shown in Fig. 4.1, is verified by simulations of the Ben-Zion/Rice earthquake model, as shown in Appendix A. The exact form of the small earthquake rate I used is given in Appendix C. The stress dependence of $P(F)$ is again taken to be given by the Ben-Zion/Rice model, Eq. (2.4).

As in the previous chapter, the fault stress $F(t)$ is given by

$$F(t) = f + \Gamma t + F_0(\sin(\omega t + \phi) - \sin\phi), \tag{4.1}$$

[1] This work is to be submitted for publication as: B.A.W. Brinkman, M.P. LeBlanc, Y. Ben-Zion, J.T. Uhl and K.A. Dahmen, "Forecasting large earthquakes using small-quake correlations" (2013). [24]

where the slow rate Γ is the slow tectonic shear rate and the periodic component of the stress has frequency ω, amplitude F_0 and phase ϕ. When the total stress exceeds a critical value F_c, the system immediately relaxes to the arrest stress, f.

In this work, our goal is to detect correlations between the small earthquakes and the periodic component of $F(t)$. I also compare the strength of correlations between tidal stress variations and annual stress variations (e.g., annual rainfall load cycles). Below, I briefly outline the methods I used to generate and analyze the small earthquake time series data, before presenting the results in Sec. 4.4.

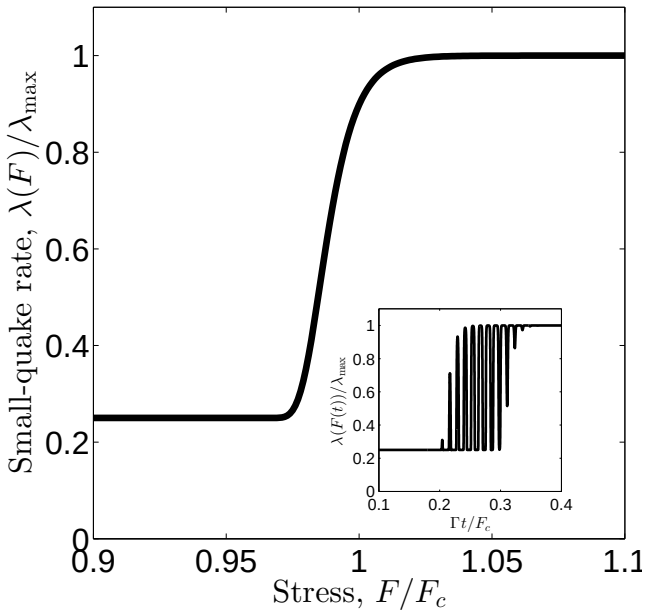

Figure 4.1: Small earthquake rate as a function of stress. For stresses much less than the critical stress of the fault, F_c, the rate of small earthquake occurrences is very low, rising quickly as the stress on the fault approaches F_c, before leveling off at higher stresses. The stress-dependent probability that a small event triggers a large event has a qualitatively similar shape. Inset: If the fault is subjected to periodically varying stresses in addition to regular slow tectonic shear, the small event rate will exhibit oscillations in time. By analyzing the effects these oscillations have on observed small-earthquake time series we can detect statistical signals that measure how likely it is that the fault is close to its yield stress, and in doing so predict large earthquake events. The oscillation frequency in this plot is reduced relative to actual tidal or annual stress variation frequencies so that oscillations can be clearly seen.

4.3 Methods

4.3.1 Time series simulation

I generated a time series of small earthquake events, generated by a non-homogeneous Poisson process with a stress-dependent rate, $\lambda(F)$. Again, see Appendix C for the exact form. Each small earthquake can trigger a large earthquake with a stress-dependent probability $P(F)$. After a large earthquake, I reset the average fault stress $F(t)$ to a constant arrest stress level and repeat the process. For each small earthquake, I recorded the effective phase at which it occurred, $\omega t_{\text{quake}} + \phi$, where t_{quake} is the time at which the earthquake occurred and ϕ is again the relative phase of the oscillatory stress at $t = 0$. I generated a time series for the p-value for 5000 large earthquake events.

4.3.2 Correlation analysis

I analyzed this time series for correlations using similar methods as Tanaka [49, 50]. The methods Tanaka used are similar to those of our analysis in Chap. 3: I identify correlations by recording at which phase of the periodic stress each small earthquake occurs. If most earthquakes occur near a preferred phase, the correlation is strong. I again quantify the correlations using the p-value. However, in this analysis, I update the p-value as more small earthquakes occur (see Appendix C for details). The p-value thus varies with time and depends on the number of earthquakes recorded per unit time. As the fault stress nears the critical stress, the p-value tends to drop, indicating the fault' s increased susceptibility to external stress changes.

To evaluate the effectiveness of the p-value as a predictor of large earthquakes, I performed two analyses. (1) I computed the distribution of values the p-value attains when a large earthquake occurs, at both tidal and annual stress variations, for tidal and annual stress amplitudes up to 5% of the critical stress. (2) I smoothed the p-value curve to eliminate noise, then computed the probability that a large earthquake occurs within a specified amount of time after the smoothed p-value dips below a desired threshold value.

(1) To compare the effectiveness of tidal correlations compared to annual-stress correlations, we recorded the values of p(t) when the large earthquakes occurred. I then computed the cumulative distribution (Fig. 4.3) of these values for several different amplitudes from 0-5% of the critical stress. I chose this amplitude range based on estimates of typical local average stress drops on faults, compared to typical tidal or seasonal amplitudes. I performed this analysis for two frequencies: one corresponding to a diurnal tidal stress frequency of $2\pi/(24 \text{ hours})$ (Fig. 4.3(a)), and one corresponding to an annual stress frequency of $2\pi/(1 \text{ year})$ (Fig. 4.3(b)).

Semi-diurnal tidal stresses alternate between two different amplitudes, whereas diurnal tidal stresses only have a single amplitude. We hence used diurnal tidal stresses for simplicity, but we expect similar results for semi-diurnal tidal stresses.

(2) The raw p-value curve, $p(t)$, exhibits many fast fluctuations, so to compute the data in Fig. 4.4, I first smoothed the curve with a window of 500 days to obtain the trend-line. The routine I used to smooth over our non-uniformly spaced data was written by Andreas Eckner and is available online at `www.eckner.com`. The routine uses a constant-value interpolation between data points and integrates over the curve to perform the smoothing.

I then analyzed how often a large earthquake occurs when the smoothed p-value, $\bar{p}(t)$, dipped below some specified threshold P. I recorded the length of the continuous duration, Δt, for which $\bar{p}(t)$ was less than P before the large earthquake occurred, or before $\bar{p}(t)$ rose above P again. I used this data to compute Prob (large event, $\Delta t < T \mid \bar{p}(t) < P$), the probability that a large earthquake occurs within a time $\Delta t < T$ since the smoothed p-value dips below the threshold P. This is shown in Fig. 4.4.

A detailed discussion of the simulation, including functional forms of $\lambda(F)$ and $P(F)$, as well as specific parameter values used for the various stress and time scales, is included in Appendix C.

4.4 Results

An exemplary plot of the p-value versus time between two large earthquakes is presented in Fig. 4.2. The smoothed curve is statistically similar to p-values observed by Tanaka [49,50], demonstrating that our model assumptions indeed capture the statistical physics of the earthquake faults.

For diurnal tidal and annual stress variations with amplitudes less than 1% of the critical stress F_c, the distributions of the p-value when the large earthquake occurs are all statistically similar to p-values observed in faults with no periodic stressing; see Fig. 4.3. The p-value may not be a useful predictor of large earthquakes in such faults, unless additional analyses (e.g., Bayesian inference) can boost the signal. However, for faults for which tidal or annual stress amplitudes are 3-5% of the critical fault stress, correlations are readily apparent, and the p-value could be a useful predictor of large quakes. Furthermore, comparing Figs. 4.3(a) and 4.3(b), we see that annual stress variations result in lower observed p-values (stronger correlations) when the large quake occurs. This suggests that, if the tidal and annual stress amplitudes are comparable, annual stress correlations may be better at predicting large earthquakes. The maximum

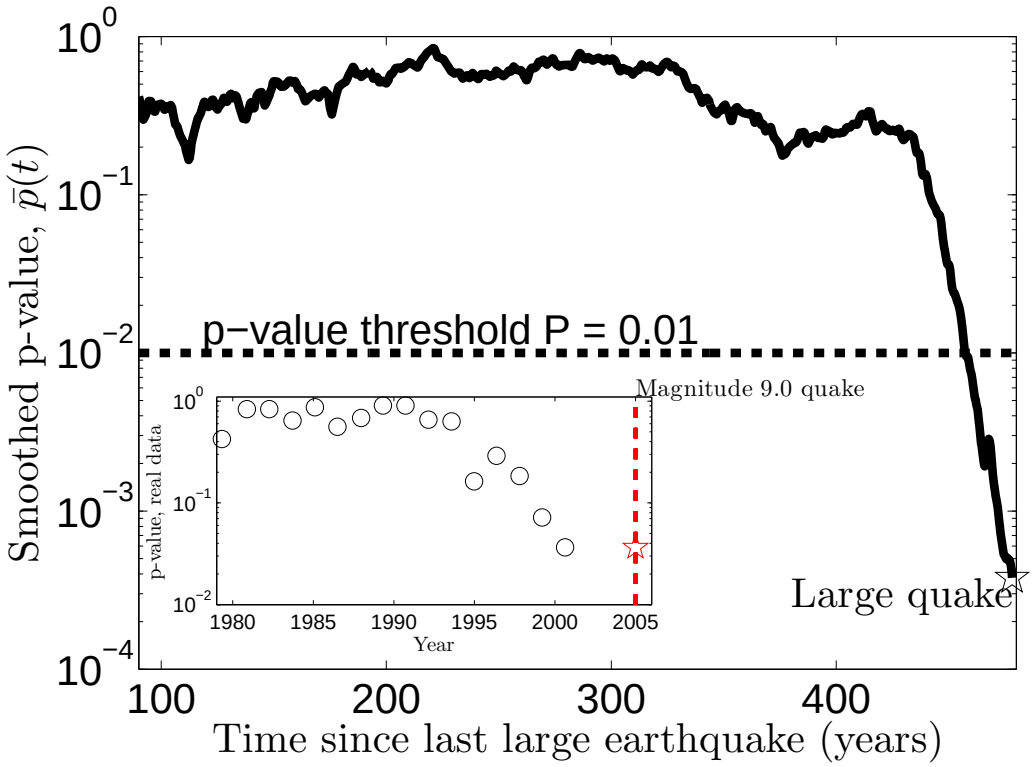

Figure 4.2: The smoothed p-value curve, $\bar{p}(t)$, as it varies between two large earthquakes. Small values of the p-value indicate strong correlations between small earthquakes and the periodic component of the fault stress. As the second earthquake is approached, the p-value drops significantly, indicating strong correlations between the timing of small earthquakes and tidal stresses. To evaluate the strength of correlations in our model, we performed two analyses: (1) we computed the distribution of p-values at which large earthquakes occurred (using the raw, non-smoothed p-value curve, not shown) and (2) we recorded how often a large earthquake occurred after $\bar{p}(t)$ descended below a chosen threshold level, and the distribution of times it took for failure to occur after descending below the threshold. An example threshold of $P = 0.01$ is shown in the plot (dashed line). Some instances of $\bar{p}(t)$ may dip below the threshold P and rise above it again without a large earthquake occurring. We also recorded these events in order to calculate the probabilities plotted in Fig. 4.4. The simulation shown here was done for a tidal stress with an amplitude of $F_0 = 0.05F_c$. The raw curve (not shown) was smoothed with a moving-average box window of 500 days. This simulation data qualitatively agrees with the observational data analyses performed by Tanaka [49,50], as shown in the inset. **Inset**: The p-value in the inset is computed from real earthquake data in the Sumatra region [49]. The p-value is initially close to 1, until it drops down to a value less than 0.1 over the course of fifteen to twenty years prior to a magnitude 9.0 earthquake which occurred in 2005. The timescale over which the observed p-value drops is less than the approximately fifty-year timescale over which our simulated p-value drops. This could be due to a variety of factors, such as statistical fluctuations or differences between the model parameters (such as time- or stress-scales) and the physical parameter values in the real fault. The physical parameter values are difficult or presently impossible to measure, so we use order-of-magnitude estimates here (see Appendix C for details).

small-event rate exceeds annual stress frequencies, but is less than tidal frequencies; i.e., for most faults typically more than one small earthquake is triggered per year, but not per day. Our model predicts that events triggered by annual stresses occur most often during stress *rate* maxima, whereas events triggered by tidal stresses occur most often during stress maxima (see Appendix B). Because large earthquakes are much less frequent than either tidal or annual stress variations, our model predicts they are similarly most likely triggered at stress maxima. We hypothesize an increase of small quakes triggered by annual stresses just prior to a large quake gives a "last-minute" boost to correlations between small earthquakes and annual stresses. Because most tidally-triggered small earthquakes occur when the large earthquake is also most likely to occur, they have less of a chance to register a last-minute increase in correlations.

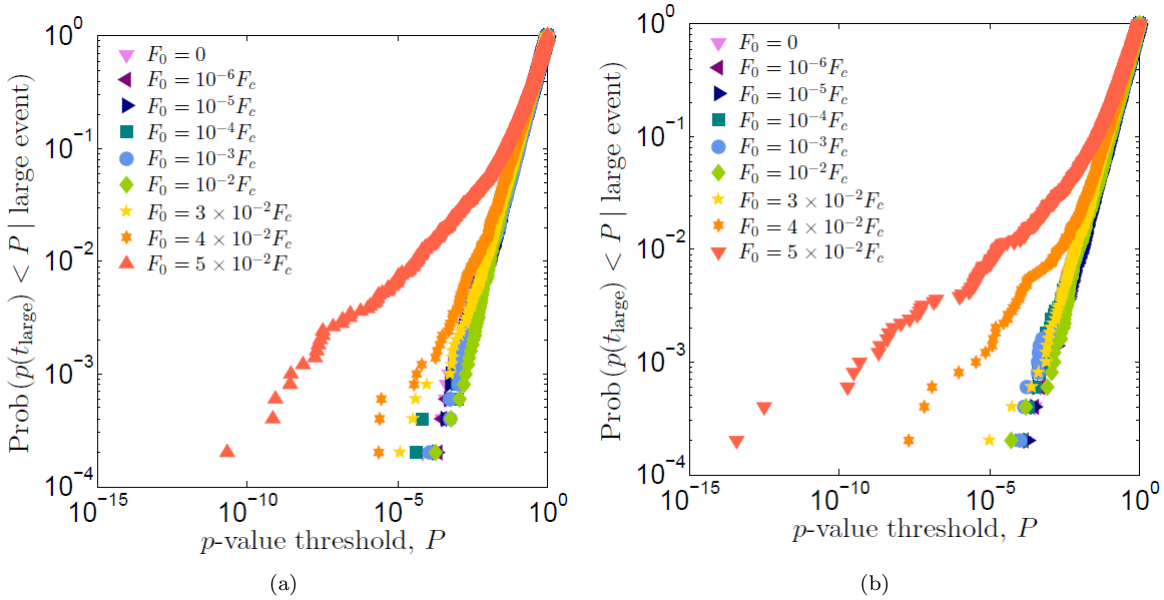

(a) (b)

Figure 4.3: Simulations of the distributions of the values the (raw) p-value $p(t)$ achieved when a large earthquake occurred, for (a) tidal stress driving and (b) annual stress driving. The simulation data demonstrates that annual stress variations results in smaller values of $p(t)$ when the large earthquake occurs, suggesting that correlations between annual stress variations and small earthquake timings may be more effective at predicting large earthquakes than tidal stress correlations. We hypothesize that the reason annual stress variations are more effective is because most annual-stress-triggered events will occur at stress rate maxima (because annual driving frequencies are less than the maximum small event rate), whereas tidal-triggered events will most likely occur at stress maxima, which is when the large quakes are also most likely to occur (because tidal driving frequencies are greater than the maximum small event rate). As a result, annual stress variations have a "last-minute" chance to triggers events that boost correlations before the large earthquake occurs.

Fig. 4.4 presents the probability that a large earthquake occurs within a time T after the p-value dips

below a threshold value P. For example, if we observe that the (smoothed) p-value dips below $P = 10^{-4}$ (light blue curve), Fig. 4.4 tells us there is a 60% chance that a large earthquake will occur within twenty years (assuming the p-value does not increase above 10^{-4} before then). This suggests it is possible to estimate the risk of an impending large earthquake from observations of the statistical behavior of the p-value, at least in faults subject to tidal or annual stresses of amplitudes near 5% of the critical stress of the fault. This is at the upper end of the expected range of periodic stress amplitudes [51], but with more advanced statistical analysis techniques, the p-value analysis could even be a viable method for lesser amplitudes.

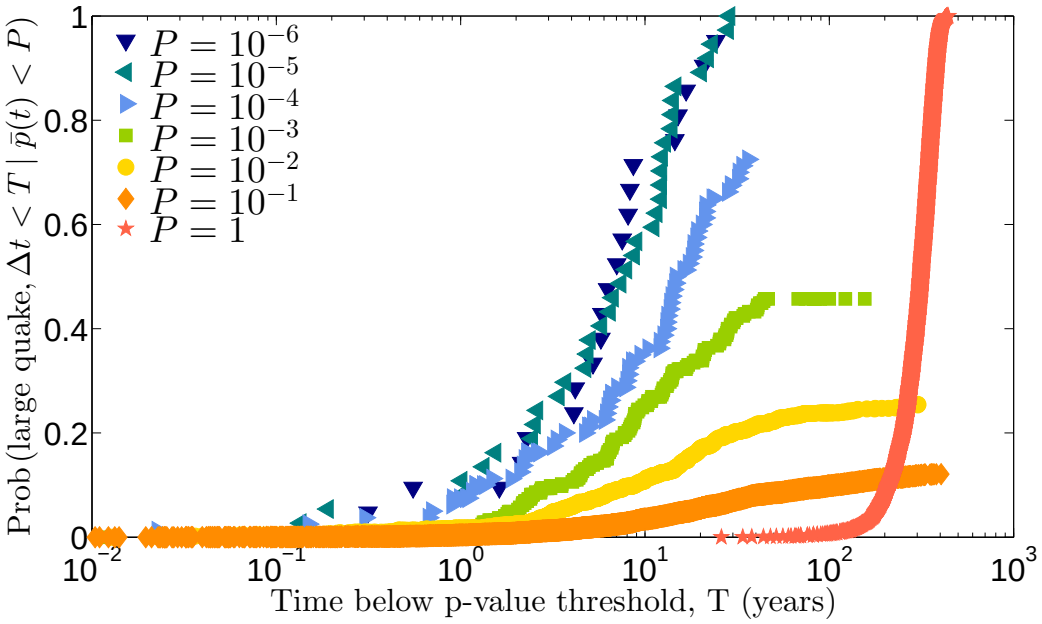

Figure 4.4: Probability that a large earthquake occurs within a time $\Delta t < T$ after the smoothed p-value curve, $\bar{p}(t)$, descends below a threshold level P. For example, if $\bar{p}(t)$ is observed to descend below $P = 10^{-4}$ (light blue right-facing triangles), there is a 60% chance that a large earthquake will occur within 20 years, assuming $\bar{p}(t)$ does not rise above the threshold level before the large quake occurs. This plot represents an assessment of the risk that a large earthquake is due to occur on this "fault", given observations of the behavior of the correlations between small earthquakes and external periodic stresses. These results suggest that with more advanced analysis techniques and models of the small earthquake rate an external stresses for specific real earthquake faults, combined with analysis of real earthquake data, it could one day be possible to assess the risk of large earthquakes in real faults. The simulation data shown here corresponds to tidal stresses of amplitude $F_0 = 0.05F_c$.

4.5 Conclusions

In summary, our model qualitatively captures the small quake-tidal correlations observed by Tanaka in real earthquake data, and provides a new framework for understanding the effects of oscillatory stresses on earthquake statistics. Within the model, we can compute the probability that a large earthquake will occur, given observations of the correlations. Extensions of the model can account for spatial variation in the fault stress, as well as other perturbations, such as seismic waves. Together with more advanced analyses of real data, we expect these tools to enable quantitative estimates the risk of a large earthquake on real faults. Finally, we note that our analysis should also apply to laboratory friction experiments [52, 53] and could be useful for hazard prediction and materials testing. Our results call for further analyses of periodic-stress correlations with small quakes in both geological faults and laboratory experiments.

4.6 End of Part I

With this, we come to the end of Part I of this thesis. In part II, I discuss some similar problems predicting large failures in a model of disordered magnets. Due to the last universality class this model belongs to (in the renormalization group sense), we expect this model is applicable to many other kinds of systems as well, including porous invasion systems and possibly power grids. Part II thus rounds out our discussion of models of forecasting failure in complex interacting systems. Some additional projects I have worked on, which are related to the model presented in the next chapter, but do not fit exactly into the theme of forecasting large failures, are presented in appendices at the end of this thesis.

Part II

磁鐵

Magnets

Chapter 5

Runaway avalanches in the random field Ising model

5.1 Introduction

Understanding avalanching systems is an extremely challenging problem. The most interesting avalanche phenomena occur in systems driven far from equilibrium. This renders statistical modeling a difficult task. The simple, general rules for developing statistical models of equilibrium systems do not apply. This would seem to leave us with the momentous task of modeling each system of interest separately! However, as explained in the introduction to this thesis, there is a saving grace to assist us with this task: the avalanche-propagation dynamics of many systems are the same, despite having different microscopic dynamics. As a result, we can begin our task by developing some prototypical models of avalanching systems, similar to the use of the Ising model as the prototype model in equilibrium statistical physics.

To this end, we begin our investigation of the statistical properties of large avalanches by studying the non-equilibrium random field Ising model (RFIM), a relatively simple model that exhibits both small and large avalanches. Beyond the direct applications of this model to magnetic materials, the model may also give us insight into porous fluid invasion, power grid networks, coupled oscillators, and more. Earthquakes are described more appropriately by a different class of models. This class of models includes the Ben-Zion/Rice earthquake model, which I will discussed in Part I of this thesis.

The numerous studies of the RFIM to be presented in this thesis are as follows. In this chapter, I present a study of the statistics of large avalanches in the model as the coupling strength between spins is adjusted. This work has been published previously[1]. In Appendix E, I present a model of the competition between thermal or quantum fluctuations and a non-adiabatic driving field rate in an RFIM-like magnet. This work will be submitted to Physical Review Letters. Finally, in appendices F and G, I present some preliminary

[1]This work has been published as: Braden A. W. Brinkman and Karin A. Dahmen, "Tuning coupling: Discrete changes in runaway avalanche sizes in disordered media", *Phys. Rev. E* **84**, 041129 (2011). [54]. It has been adapted with permission.

work related to developing a full statistical model of the random field Ising model coupled to a bath of thermal and quantum harmonic oscillators. The coupling to the bath introduces quantum fluctuations, which are absent in most studies of RFIM-like models. These microscopic models complement the phenomenological model presented in Appendix E.

I will begin this chapter with a general introduction of the random field Ising model, applicable to the material in all chapters of Part II, followed by a discussion of the mean field approximation of the model, relevant to the work in this chapter. Modifications to the model relevant to applications in subsequent chapters will be discussed in those chapters. Following this introduction of the RFIM, I will begin the discussion of the problem specific to this chapter, a study of the effects of tuning the coupling strength between spins on the statistics of large, runaway avalanches in the random field Ising model.

5.2 The Random Field Ising Model

The random field Ising model (RFIM) is a relatively simple model of interacting spins that has been used to study many driven, disordered, non-equilibrium systems with hysteresis and avalanches. [55–72] The model exhibits a second order phase transition as J/R is tuned. Above the critical ratio $(J/R)_c$ the magnetization of the system exhibits a runaway avalanche in which large numbers of spins collectively reverse orientation as an external longitudinal magnetic field H is swept from $-\infty$ to ∞. [55,56,58,59,62] The critical properties of the model near this transition will be universal for all models in the same universality class, [55] which is known to be quite large. [56] This means that many avalanche models may fall into this universality class, making the RFIM an excellent prototype model for studying avalanche dynamics.

The random field Ising model describes a collection of spins arranged on a hyper-cubic lattice. As in the regular Ising model, each spin can point up or down, and interacts with other spins in the lattice through some form of coupling - for example, short-range exchange couplings or long range dipolar couplings - and an external magnetic field felt equally by all spins. The difference between the regular Ising model and the random field Ising model is the introduction of random local magnetic fields at each lattice site. Each spin thus "feels" a different effective local field - the sum of the spin's interactions with other spins and the global and local random fields. The spins tend to align with their effective local field. By adjusting the global magnetic field, we can cause spins to flip from down to up (or vice versa), but due to the random local fields not all spins will flip at the same time. This results in a wide range of possible avalanche sizes. In the

absence of anisotropic dipolar interactions, there is the possibility that a small avalanche will runaway to become a large avalanche. Whether or not a large avalanche is possible depends on the size of the spread of random local fields.

We can formulate these dynamics mathematically by writing down the Hamiltonian, or energy functional, of the spin system. This is similar to the equilibrium Hamiltonian:

$$\mathcal{H} = -\sum_{i,j} J_{ij} s_i s_j - \sum_{i=1}^{N} (H + h_i) s_i. \tag{5.1}$$

The primary difference between the equilibrium and non-equilibrium Hamiltonians is that the system is driven by the global magnetic field $H = H(t)$, and there is no temperature. Due to the absence of temperature, the system will not relax to equilibrium and will instead remain in a metastable state as $H(t)$ changes. This gives rise to hysteresis, as shown schematically in Fig. (5.1).

The variables in the Hamiltonian are as follows: $s_i = \pm 1$ is the value of a classical spin located at site i. N is the total number of spins in the lattice, H, as already described, is a global magnetic field parallel to the spin axis. The h_i are random magnetic fields, different at each site, drawn from a peaked distribution with width R. The parameter R characterizes the amount of disorder in the system. We choose a Gaussian distribution for simplicity:

$$\rho(h_i) = \frac{1}{\sqrt{2\pi}R} \exp\left[-\frac{h_i^2}{2R^2}\right]. \tag{5.2}$$

The scaling properties should remain the same for similarly shaped distributions. [59]

The factor J_{ij} is the interaction between spins i and j. For the standard RFIM in finite dimensions, J_{ij} couples only nearest neighbor spins. One could also include long range, anisotropic dipolar interactions; however, these long range interactions work to cut off the propagation of large avalanches. For the purposes of our investigations of large avalanches we will consider only isotropic interactions, except in section E.3 of this chapter.

In general, even short-range interactions between spins render the RFIM difficult to solve analytically. Consequently, in this chapter we will focus on all-to-all (mean field) interactions, i.e., $J_{ij} = J/N$, for all i, j. The advantage of mean field theory is that it is often analytically tractable. The factor $1/N$ is required for

the model to be well defined in the thermodynamic limit. In mean field theory, the Hamiltonian becomes

$$\mathcal{H}_{MF} = -\sum_{i=1}^{N} h_i^{MF,eff} s_i, \tag{5.3}$$

where each spin experiences an effective *local field*

$$h_i^{MF,eff} = JM + H + h_i. \tag{5.4}$$

The net magnetization M is given by

$$M = \frac{1}{N}\sum_{j=1}^{N} s_j, \tag{5.5}$$

and must be determined self consistently. At zero temperature, each spin aligns with its local effective field. Spins hence flip when the sign of their effective field changes. Due to the random fields h_i, the effective fields do not all change sign simultaneously, as in the case of zero disorder. Hence, as H is tuned it can trigger a single spin to flip, which will change M, which can in turn then cause further spins to flip, which may then cause more spins to flip, and so on until the cascade of spin flips peters out. These cascades of spin flips are avalanches that are detected as Barkhausen noise in experimental systems [73]. In the thermodynamic limit, $N \to \infty$, and for $J > J_c$ there is an avalanche of size proportional to N in which a non-zero fraction of spins flips. This avalanche is referred to as the "runaway avalanche". The fraction of spins flipped in all other avalanches is zero in the thermodynamic limit. They fall into two groups: avalanches which occur prior to the runaway avalanche are dubbed "precursors" and those which follow the runaway avalanche are termed "aftershocks".

In mean field theory and in general, the runaway avalanche is detected experimentally as a discontinuous change, ΔM, in the magnetization as H is tuned. The size of the discontinuity depends on the coupling J. Fig. (5.2) shows the ΔM versus J curve which demonstrates a transition at $J = J_c$, where a runaway avalanche first appears and ΔM becomes non-zero. In the thermodynamic limit this curve is smooth. However, as shown in the figure, for finite N the curve has discrete jumps, which tend to zero as $N \to \infty$. These jumps in $\Delta M(J)$ are the central phenomenon that we study in this chapter: as J is tuned, the maximum avalanche size changes abruptly; the distribution of sizes of these changes is of interest as it has relevance to understanding - and potentially controlling - avalanches in many natural phenomena in systems such as power grids or magnetic materials. [55] Because the jumps in ΔM tend to zero in the thermodynamic

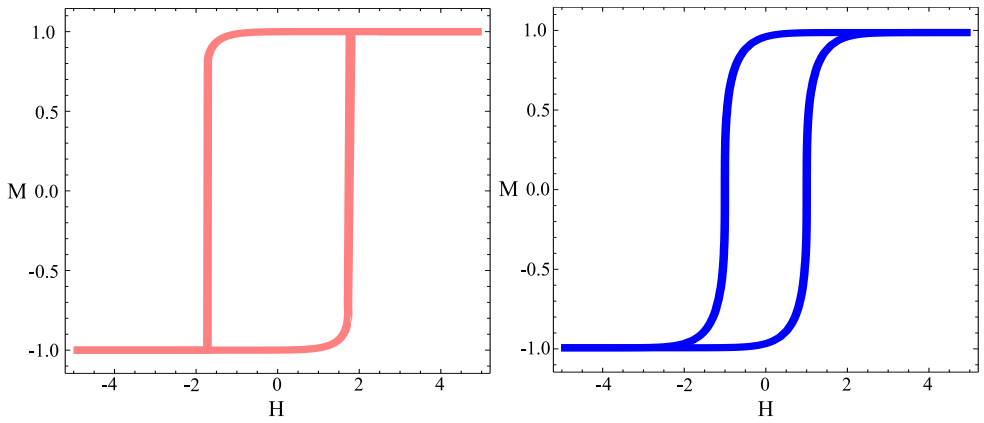

(a) $J < J_c$ (b) $J = J_c$

(c) $J > J_c$

Figure 5.1: (Color online) Plots of M versus H for the different coupling regimes. At $J = J_c$ the curve develops a discontinuity which grows with J. In mean field theory hysteresis only exists above J_c due to the simplicity of the hard spin model. The soft spin version of the mean field theory, however, displays hysteresis above and below R_c. It has the same critical exponents as the hard-spin mean field theory. [59]

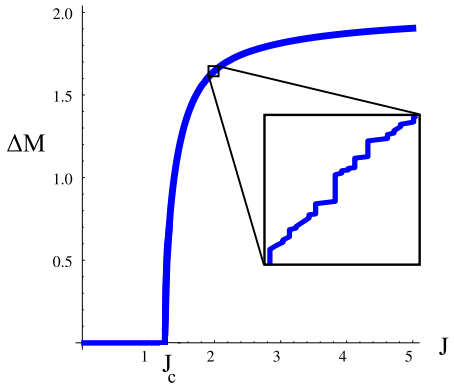

Figure 5.2: (Color online) Plot of the size of the runaway avalanche, ΔM, vs. J. In the thermodynamic limit the curve appears smooth, but for finite N there are discrete jumps in the runaway avalanche size. We study jumps in $S_m = N\Delta M/2$, the total number of spins that flip in the runaway avalanche. The S_m vs. J curve will always have discrete jumps as N is increased, making it the appropriate curve to study.

limit, it is better to study jumps in the number of spins that flipped in the runaway avalanche, S_m, versus J. Jumps in the S_m versus J curve do not tend to zero as $N \to \infty$. S_m is related to ΔM by $\Delta M = 2S_m/N$. Determination of the distribution, $P(S)$, of jump sizes, S, in S_m will be the main result of this chapter and a new prediction for experiments.

The remainder of this chapter will proceed as follows: In section 5.3 I sketch the derivation of the distribution of jumps in the runaway avalanche size as J/R is tuned. In section 5.4 I discuss numerical simulations performed to check our theoretical predictions. In section 5.5 I briefly discuss the three dimensional RFIM and I predict values for the critical exponents in three dimensions, and in section E.3 I briefly discuss avalanches in materials with dipolar forces, in which there are no runaway avalanches. In section 5.7 I discuss possibilities for experimentally measuring the critical exponents discussed in the text, and finally, in section 5.8 I summarize the work presented in this chapter and discuss directions for future studies.

5.3 Jump Size Distribution Derivation

We begin our analysis by carefully considering what happens when a spin flips. We consider finite N first, taking the $N \to \infty$ limit in the end. Before the limit is taken, we identify the runaway avalanche as the largest avalanche, S_m, for $J \geq J_c$.

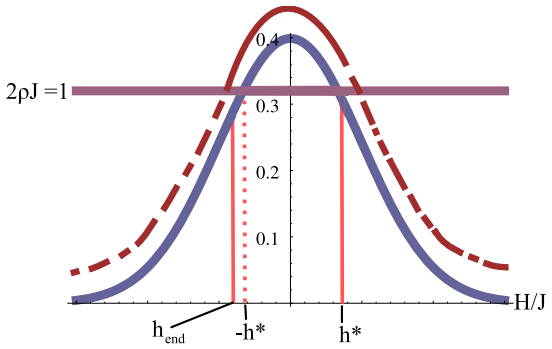

Figure 5.3: (Color online) Schematic plot of avalanches in the RFIM system. The solid curve is a Gaussian distribution of random fields and the straight line indicates the line $2J\rho = 1$. The dashed line represents avalanches; each dash corresponds to an avalanche consisting of spins with random fields in the segment of the distribution below the dash. As H increases, spins with fields on the far right of the distribution begin to flip when the sign of their local field changes. The resulting avalanches peter out quickly as $n_{\text{flip}} = 2J\rho(h_0) \ll 1$. When the spin with local field h^* (Eq. 5.4) flips it triggers an avalanche for which $n_{\text{flip}} = 1$, enabling the avalanche to run away and cause a finite fraction of the spins to flip. As the avalanche travels to the left on the curve, eventually n_{flip} falls below 1 again once the spin with local field $-h^*$ has flipped, but due to the increase in effective field built up from spin flips during the runaway avalanche the system overshoots $-h^*$ and the avalanche peters out at some local field $|h| > |h^*|$. For J close to J_c, the overshoot is very slight, and the distribution of aftershock sizes close to $-h^*$ is given by Eq. (5.8).

We initialize the system with $H = -\infty$. All spins initially point down as $h_i^{MF,eff}$ is dominated by H, and hence $M = -1$. The spins will flip in order of descending random fields, so we label the random fields $h_1 > h_2 > \cdots > h_N$. The spin with random local field h_1 is the first spin to flip. When the longitudinal field H is tuned such that it causes a spin with field h_i to flip it increases the effective field of all other spins by $2J/N$. The condition that this spin flip causes the next spin, h_{i+1}, to flip is $h_i - h_{i+1} \leq 2J/N$. If spin i causes several spins to flip, then each flip will increase the effective field of all spins by $2J/N$, which can in turn flip even more spins. If n_i spins have flipped in the avalanche started by spin i, then the condition that the $(n_i+1)^{th}$ spin flips is $h_i - h_{i+n_i} \leq 2Jn_i/N$. If the $(n_i+1)^{th}$ spin does not flip, then there remains a "gap" between spins i and $i+n_i$, $\Delta_{i,i+n_i}$. This gap is given by $h_i - h_{i+n_i} = 2Jn_i/N + \Delta_{i,i+n_i}$, or

$$\Delta_{i,i+n_i}(J) = h_i - h_{i+n_i} - n_i\frac{2J}{N}. \tag{5.6}$$

The gap is a function of the coupling J. When $\Delta_{i,1+n_i}$ is positive the global field H must be increased to cause spin $i+n_i$ to flip. When $\Delta_{i,j}$ is negative, it means that spin j is already part of an avalanche caused by spin i. When $\Delta_{i,j} = 0$ spin i changes the effective field just enough to trigger spin j to flip. Thus, when

studying changes in avalanche sizes as the coupling increases, we need only consider the gaps between pairs of spins for which $\Delta_{i,j}$ is positive, i.e., between the random fields of the initial spin of an avalanche and the initial spin of the avalanche that follows it. If we were to re-initialize the system with all spins pointing down, but with J adjusted so that the smallest positive $\Delta_{i,i+n_i}$ of the previous sweep of H vanishes, then when spin i flips, the resulting avalanche will now cause spin $i+n_i$ to flip. If spin i is the initial spin of an avalanche of size n_i with the smallest positive $\Delta_{i,i+n_i}$, then $J_{i,i+n_i}$, the value of J which will result in the avalanche flipping spin $i+n_i$, is given by

$$\frac{2J_{i,i+n_i}}{N} = \frac{h_i - h_{i+n_i}}{n_i}. \tag{5.7}$$

If during the previous sweep of H from $-\infty$ to $+\infty$ spin $i+n_i$, where n_i is the size of the avalanche started by spin i on the previous sweep, triggered an avalanche of size m_{i+n_i}, then spin i is now an avalanche of size $n_i + m_{i+n_i}$ on the current sweep (with coupling $J = J_{i,i+n_i}$). This is therefore how different avalanches join as J is increased. Because the gap $\Delta_{i,i+n_i}$ is now negative, for the next sweep we must look at the gap between spins i and $i+n_i+m_{i+n_i}$, $\Delta_{i,i+n_i+m_{i+n_i}}$, to determine if this gap or another one is the smallest gap on the current sweep of the system in order to determine what value to tune J to.

Although two avalanches have joined by increasing J, this has not necessarily caused a change in the runaway avalanche size S_m. To be precise, let $S_m^{(k)}$ denote the size of the largest avalanche on the k^{th} sweep of the system. We want to know which avalanche-joining processes will result in $S_m^{(k+1)} > S_m^{(k)}$ (as opposed to $S_m^{(k+1)} = S_m^{(k)}$). There are only three kinds of avalanche-joining processes which will increase S_m. The first process we label "PP/AA". In this process either two precursors have joined together or two aftershocks have joined together going from sweep k to sweep $k+1$. In this case $S_m^{(k+1)} > S_m^{(k)}$ only if the sum of the two precursors/aftershocks that joined is greater than $S_m^{(k)}$. In the second process, labeled "PR", spin i is the start of a precursor avalanche of size n_i and spin $i+n_i$ is the start of the runaway avalanche of size $S_m^{(k)}$. On the $(k+1)^{\text{th}}$ sweep the size of the largest avalanche is then $S_m^{(k+1)} = S_m^{(k)} + n_i > S_m^{(k)}$. The largest avalanche size has thus increased. In the last process, labeled "RA", spin i starts the largest avalanche of size $S_m^{(k)}$ and $i + S_m^{(k)}$ starts an aftershock, in which case $S_m^{(k+1)}$ is $S_m^{(k)} + n_{i+S_m^{(k)}} > S_m^{(k)}$ and the largest avalanche has increased between the k^{th} and $(k+1)^{\text{th}}$ sweeps.

Above J_c and in the thermodynamic limit process RA dominates and processes PP/AA and PR are negligible. Process PP/AA is negligible because in the thermodynamic limit the ratio of largest avalanche

size to the total number of spins, S_m/N, tends to a finite fraction $\Delta M/2$, whereas for a precursor/aftershock avalanche of size S, $S/N \to 0$ as $N \to \infty$. Thus, no two precursor/aftershock avalanches can ever join to become larger than the current S_m, and process PP/AA will not occur in the thermodynamic limit.

Process PR will not contribute in the thermodynamic limit because the gap between the runaway avalanche and the precursor avalanche preceding it will be larger than the gap between the runaway avalanche and the aftershock following it with probability 1 in the thermodynamic limit. The argument is as follows: Let $\Delta_{PR} = h_P - h_R - 2JS_P/N$ be the gap between the precursor to the runaway avalanche and the runaway avalanche, where h_P the field of the initial spin of the precursor avalanche, h_R the field at which the runaway avalanche starts and S_P the size of the precursor avalanche. Let $\Delta_{RA} = h_R - h_A - 2JS_m/N$ be the gap between the runaway avalanche and the aftershock following it, where h_A the field of the initial spin in the aftershock. On a given sweep of the system for which both gaps are positive, we want to know the values of J which will cause these gaps to vanishes. The gap with the smaller coupling will vanish first as we increase J. However, because the fields are random, we can only calculate the probability $\text{Prob}(0 < J_{PR} < J_{RA})$ that the coupling J_{RA}, which causes Δ_{RA} to vanish, is greater than the coupling J_{PR}, which causes Δ_{PR} to vanish. We show this probability is zero for arbitrary fields in the thermodynamic limit:

$$\begin{aligned}
& \text{Prob}(0 < J_{PR} < J_{RA}) \\
= \; & \text{Prob}\left(0 < \frac{2J_{PR}}{N} < \frac{2J_{RA}}{N}\right) \\
= \; & \text{Prob}\left(0 < \frac{h_P - h_R}{S_P} < \frac{h_R - h_A}{S_m}\right) \\
= \; & \text{Prob}\left(h_R < h_P < h_R + \frac{S_P}{S_m}(h_R - h_A)\right),
\end{aligned}$$

where in going to the third line we used the fact that $2J_{RA}/N = (h_R - h_A)/S_m$ and $2J_{PR}/N = (h_P - h_R)/S_P$, which come from the $\Delta_{RA}(J_{RA}) = 0$ and $\Delta_{PR}(J_{PR}) = 0$, respectively. Simple manipulations of the argument yield the last line above. Taking the thermodynamic limit, $S_m \to N\Delta M/2$, but $S_P/N \to 0$, hence $S_P/S_m \to 0$ in the thermodynamic limit, giving

$$\text{Prob}(0 < J_{PR} < J_{RA}) = \text{Prob}(h_R < h_P < h_R) = 0,$$

as the probability distribution is continuous. Hence, in the thermodynamic limit there is zero probability that $J_{PR} < J_{RA}$. Hence, the value of the coupling required to cause the runaway avalanche to absorb the aftershock following it will always be smaller than the value of the coupling required to cause the precursor to absorb the runaway avalanche, and thus on every sweep of the system it is the aftershock which is absorbed into the runaway avalanche, not the precursor.[2]

Because it is always an aftershock that is absorbed as $N \to \infty$, the distribution of jump sizes is identical to the distribution of aftershock avalanche sizes, which is [59]

$$P(S) \sim S^{-\tau} e^{-St^2/2}, \tag{5.8}$$

where $\tau = 3/2$ and $t = 2J\rho(h_0) - 1$, with h_0 the random local field of the spin which triggers the avalanche. At the critical point $J = J_c$, $t = 0$ and the distribution is a power law, $S^{-\tau}$, as expected at a continuous phase transition. An exact derivation of Eq. (5.8) is given in Appendix D.

The parameter t must be evaluated at the local field at which the aftershock to be absorbed begins. We now determine what the local field of the aftershock is. As $N \to \infty$, $S_m \to N\Delta M/2$. The value of J is tuned such that $2J/N = (h^* - h_{end})/S_m$, or $h_{end} = h^* - J\Delta M$ for $N \to \infty$, where h_{end} is the local field of the last spin in the avalanche. This determines the field of the last spin in the runaway avalanche in terms of the field of the first spin in the runaway avalanche, h^*, the current value of the coupling and the fraction of spins in the runaway avalanche, $\Delta M/2$. The fraction $\Delta M/2$ is determined implicitly by

$$\frac{\Delta M}{2} = \int_{h^* - J\Delta M}^{h^*} dh\ \rho(h). \tag{5.9}$$

Using the fact that $\rho(h)$ is Gaussian, we may write this integral in terms of error functions, $\mathrm{erf}(x) = 2/\sqrt{\pi}\int_0^x dt \exp(-t^2)$. We have

$$\begin{aligned} \Delta M &= \mathrm{erf}\left(\sqrt{\ln(1+j)}\right) \\ &- \mathrm{erf}\left(\sqrt{\ln(1+j)} - \frac{\sqrt{\pi}}{2}(1+j)\Delta M\right), \end{aligned} \tag{5.10}$$

where we define $j = J/J_c - 1$ for convenience. For $j = 0$ ($J = J_c$) the unique solution is $\Delta M = 0$. We thus

[2]Unless, of course, it were to happen that all of the aftershock avalanches were absorbed, in which case PR events would contribute to changes in S_m as there would be no more RA events. This can happen in finite systems for large J/R.

expect that for small j (J close to J_c) ΔM will be small, so we expand the right hand side for small $j > 0$ and ΔM (going to third order in ΔM, as the zeroth order vanishes and the first order cancels with the left hand side). We find

$$\Delta M \simeq \frac{6}{\sqrt{\pi}} j^{1/2}. \tag{5.11}$$

To lowest order in j, $h^* \simeq 2J_c j^{1/2}/\sqrt{\pi}$, [59] hence we find $h_{end} \simeq -4J_c j^{1/2}/\sqrt{\pi}$. Now that we have h_{end} we need only determine how far away the next spin is. In the thermodynamic limit the distance between spins tends to zero (as can be shown using the theory of order statistics. [74]) Hence, h_{end} will only be an infinitesimal distance from the field which begins the following aftershock, so we may evaluate t by inserting $h_0 \simeq h_{end}$. We find $t \simeq -3j$, and so

$$P(S) \sim S^{-\tau} \mathcal{D}(S^{\sigma} j), \tag{5.12}$$

with $\tau = 3/2$, $\sigma = 1/2$ and

$$\mathcal{D}(x) = \exp\left[-(ax)^{1/\sigma}/2\right], \tag{5.13}$$

where $a = 3$. While the parameter a is a non-universal quantity, $\mathcal{D}(x)$ is a universal scaling function and prediction for experiments.

5.4 Numerical Results

We test our prediction numerically by simulating the mean field model for many different configurations of spins. We set $R = 1$ in our simulations. Thus, all spins are drawn from a standard normal distribution in our simulations. We can turn the considerations at the beginning of the previous section into an algorithm to compute the jumps in S_m as a function of J. Some caution must be taken, however, as for a finite number of spins the processes PP/AA and PR will necessarily occur on occasion and contribute to jumps in S_m. Eq. (5.12) is valid only for RA processes in the thermodynamic limit, while the simulations have finite size effects. In order to compare the results of our simulations to the theoretical results, we record only jumps that occur due to RA processes, because that is the dominant process in the thermodynamic limit. Failing to remove the other processes distorts the histograms, resulting in bumps in the histograms at large S.

We ran simulations for 2000 configurations of both 10^4 and 10^5 spins and 400 configurations of 10^6 spins. Fig. (5.4) shows the results of the 10^6 run. The values of the critical exponents σ and τ are essentially indistinguishable from the theoretical values, with only the values of the non-universal quantities J_c and

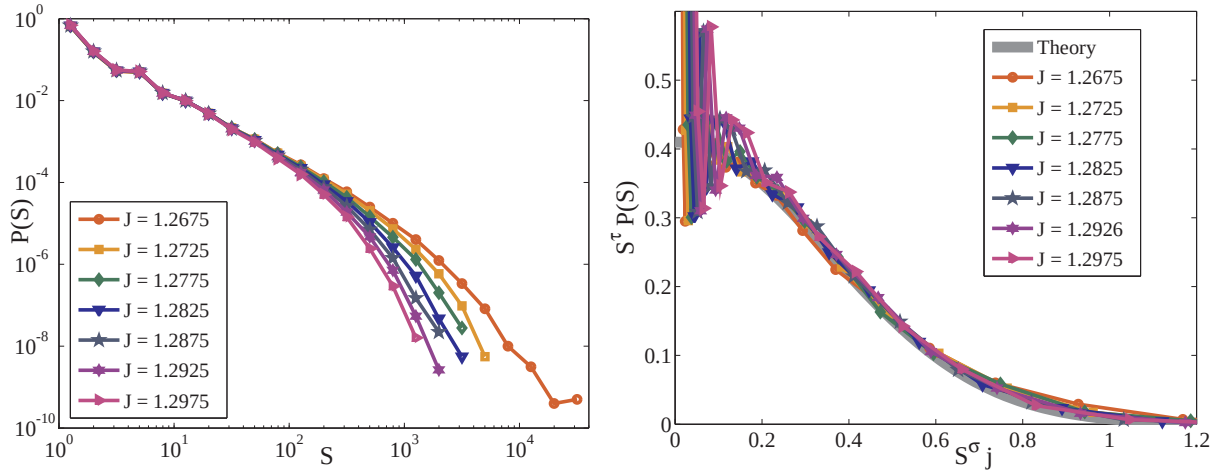

(a) Histogram of jump size S for various values of J.

(b) Collapsed Data.

Figure 5.4: (Color online) Simulation data. Fig. 5.4(a) (loglog scale) shows the normalized histograms for different values of J up to about 4% above the critical point. Fig. 5.4(b) (linear scale) is a collapse of the data, confirming the theoretical values of the universal quantities $\tau = 1.5$ and $\sigma = 0.5$, as well as giving estimates for the non-universal quantities, a and J_c, which are not far off from the predicted values. The discrepancy is due to finite size effects. Note that the data collapse falls almost completely on top of the scaling function, Eq. (5.13), confirming the scaling form, except near small S, where the scaling form does not apply and discreteness effects become visible.

a (the coefficient of x in Eq. (5.13), predicted to be 3) being smaller than theoretically predicted. These deviations from the theoretical results are expected to be due to finite size effects, as the values for both J_c and a increase toward the predicted values as N is increased. Table 5.1 compares the data for the two different values of N, revealing that as N increases the agreement between theory and simulation improves. Results for $N = 10^4$ are not given, as the data collapse was not satisfactory. However, this data is used in the finite size collapse, discussed below.

N	10^5	10^6	∞
τ	1.48(7)	1.50(6)	1.5
σ	0.50(3)	0.50(7)	1.5
J_c	1.244(3)	1.251(2)	1.253314
a	2.3(2)	2.8(3)	3

Table 5.1: Comparison of data collapses, such as in Fig. 5.4, for numbers of spins $N = 10^5$ and 10^6. We find the critical exponents τ and σ have the theoretical values within statistical error, and we obtain values for J_c and a, defined in Eq. (5.13), that are close to the theoretical values, and improve as N is increased. Parentheses indicate estimate error in last digit.

5.4.1 Finite Size Scaling Collapse

We also performed a finite-size scaling collapse to determine the critical exponents. By performing a data collapse using the number of spins as a tunable variable we can extract the value of the exponents and J_c in the thermodynamic limit, free of finite-size errors. This method is particularly useful for the analysis of experimental data. For a system of linear size L, we expect the scaling function of Eq. (5.12) to also depend on L/ξ, where ξ is the correlation length. For the infinite system $\xi \sim j^{-\nu}$; for a finite system ξ cannot exceed the linear system size L, and there are sub-dominant corrections that are negligible as the number of spins (and hence system size) grows large. We may write

$$P(S) \sim S^{-\tau}\ \mathcal{D}(S^{\sigma} j, L^{1/\nu} j),$$

If we now calculate the n^{th} moments of the jump sizes in S_m, $\langle S^n \rangle = \int dS S^n P(S)$, we find:

$$\langle S^n \rangle \sim L^{(n+1-\tau)/(\sigma\nu)} \mathcal{G}(L^{1/\nu} j), \tag{5.14}$$

where $\mathcal{G}$ is a new scaling function that depends only on $L^{1/\nu} j$. Using the fact that $N \sim L^d$ for a d-dimensional lattice we obtain

$$\langle S^n \rangle \sim N^{(n+1-\tau)/(\sigma d\nu)} \mathcal{G}(N^{1/(d\nu)} j). \tag{5.15}$$

In the mean field problem we assume d is effectively the upper critical dimension, d_c, above which mean field theory is exact. The critical dimension is $d_c = 6$ for the RFIM. [59] As d and ν only appear as $d\nu$, in a scaling collapse (as shown in Figs. (5.5) and Figs. (5.6)) we can only determine this combination from the collapse. We calculate $\langle S^n \rangle$ for $n = 1, 2$, and for system sizes of $N = 10^4,\ 10^5$ & 10^6. This allows us to determine the exponents $d\nu$ and $(n + 1 - \tau)/\sigma$, from which we calculate τ, σ, and ν, assuming we may set $d = d_c = 6$ for mean field theory. The results of the collapse are given in Table 5.2. Figs. (5.5) and Figs. (5.6) show plots of $\langle S \rangle$ and $\langle S^2 \rangle$, respectively, versus J, with their associated collapses.

5.5 Avalanches in Three Dimensions

The physical picture suggested by studying the mean field theory is that the runaway avalanche absorbs aftershock avalanches as J is increased. We expect this to be true in finite dimensions as well. Although

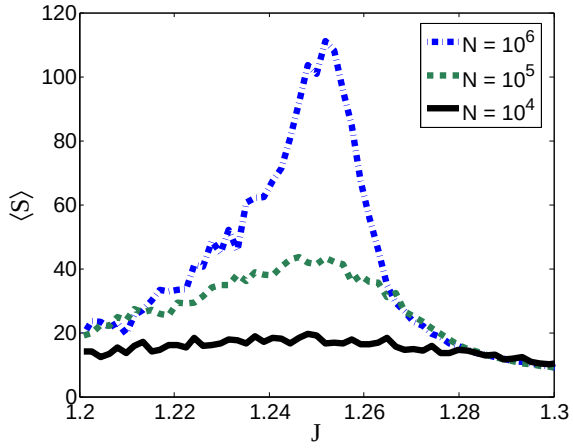

(a)

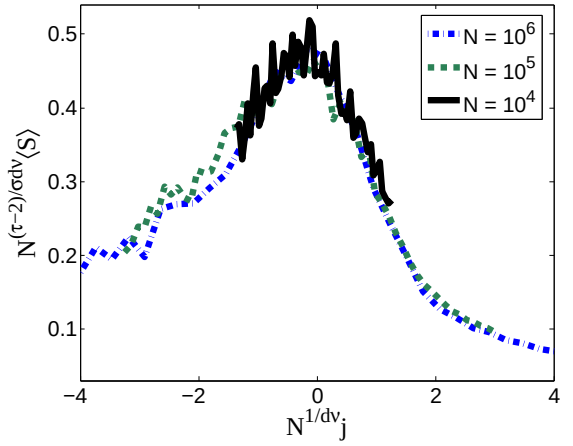

(b)

Figure 5.5: (Color Online) (a): $\langle S \rangle$ vs. J. (b): Finite-size scaling collapse. The $N = 10^4$ data appears noisy, but the general trend follows the 10^5 and 10^6 curves.

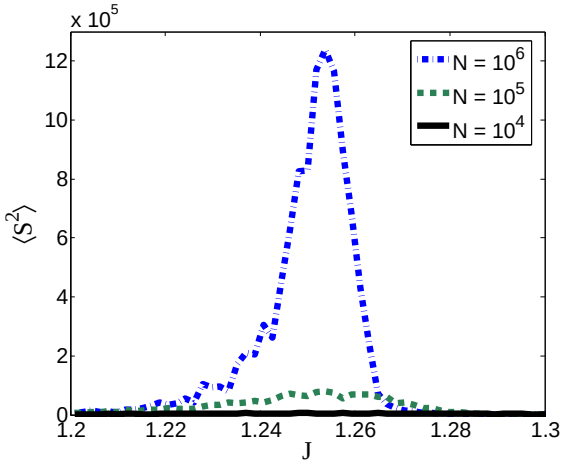

(a)

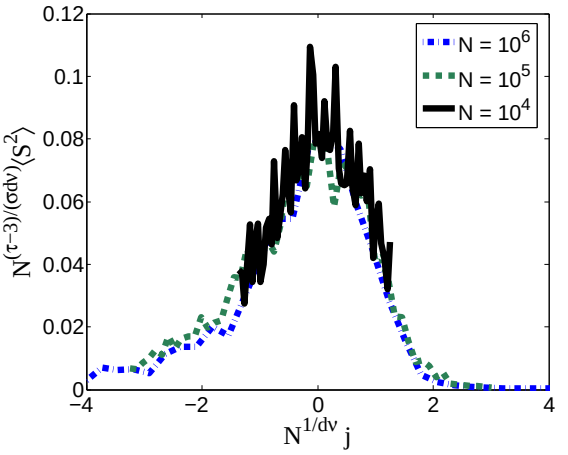

(b)

Figure 5.6: (Color online) (a): $\langle S^2 \rangle$ vs. J. (b): Finite-size scaling collapse. The $N = 10^4$ data appears noisy, but the general trend follows the 10^5 and 10^6 curves.

n	1	2
$d\nu$	2.6(6)	2.6(5)
$(n+1-\tau)/\sigma$	1.04(22)	3.2(4)
J_c	1.253(2)	1.2529(8)
Derived Exponents	Collapse	Theory
τ	1.5(2)	1.5
σ	0.5(3)	0.5
$d\nu$	2.6(6)	3
ν	0.4(1)	0.5

Table 5.2: Results of the finite-size scaling collapse shown in Figs. (5.5) and Figs. (5.6) of the n^{th} moments, $\langle S^n \rangle$, of $P(S)$ for $n = 1, 2$. The top table lists the combined exponent values obtained directly from the collapse. The lower table lists the individual exponents determined from these values. We assume $d_c = 6$, giving the estimate $\nu = 2.6/6 \approx 0.4$. The critical exponents are found to be quite close to the expected exponents. Statistical errors in the last digit reported are given in parentheses.

	τ	σ	ν
Mean Field Theory	1.5	0.5	0.5
Three Dimensions	1.60(6)	0.24(2)	1.4(2)

Table 5.3: Critical exponents τ, σ and ν in mean field theory and three dimensions. The results for mean field theory are those derived in this work. Those for three dimensions are argued to be the same exponents as those of the aftershock size distribution in three dimensions, reported in Ref. [62]. The exponents were determined numerically. Statistical errors in the last digit are given in parentheses.

the simulations of Ref. [75] find correlations between avalanche sizes and waiting times between avalanches at the 3D critical point, which could in principle affect scaling relations, no correlations appear to exist between avalanche sizes. As our arguments do not depend on the time between avalanches, we thus expect the distribution of changes in the runaway avalanche size will be equal to the distribution of aftershock sizes even in finite dimensions. The distribution of aftershock sizes in three dimensions has the same form as Eq. (5.12) with different values for the exponents τ and σ and a different scaling form $\mathcal{D}(x)$. In three dimensions the exponents are $\tau = 1.6 \pm 0.6$, $\sigma = 0.24 \pm 0.02$ and $\nu = 1.4 \pm 0.2$. [62] We summarize the derived results for mean field theory and three dimensions in Table 5.3.

5.6 Dipolar Interactions

We now briefly consider the effect of dipolar interactions between spins. Dipolar forces can give rise to demagnetizing fields which resist the propagation of large avalanches. [76] Most magnetization changes in the system are no longer due to nucleation of new domains, but due to motion of domain walls. [76–78] As a result,

the runaway avalanche is broken up into many small avalanches with size distribution $S^{-\tau'} f(S(k/R)^{1/\sigma'})$, with different critical exponents τ' and σ', and where k is the value of the effective demagnetizing field and $f(x)$ is a universal scaling function. [77–79] Over a large range of H, where the magnetization curve $M(H)$ has constant slope (dM/dH = constant) and is far from saturation. For disorders R less than some critical disorder $R_c^{dipolar}$, [80] the avalanche size distribution only depends on the ratio k/R and does not depend on H [77, 78]. This is quite different from the case analyzed above, and our previous results do not apply. However, it is interesting for the analysis of experiments on $LiHo_xY_{1-x}F_4$ and related materials. In these systems the disorder R can be tuned by tuning a transverse magnetic field applied to the sample. Thus, it may be possible to measure avalanches caused by tuning R using Barkhausen noise [73] or other techniques. Domain wall motion can be characterized by an equation of motion [77, 78]

$$\frac{du_i(t)}{dt} = H + \sum_j K_{ij}(u_j - u_i) + h_i, \tag{5.16}$$

where u is the height of the domain wall, K is an interaction kernel which contains the dipolar and exchange interactions, H is the global magnetic field and the h_i are the random local fields. In the $LiHo_xY_{1-x}F_4$ experiments tuning the transverse magnetic field amounts to tuning all of the h_i by the same factor. Suppose we tune R until a single spin flips and triggers an avalanche. Because the avalanche size distribution depends on R only through the ratio k/R (as long as $R < R_c^{dipolar}$), we expect the size statistics of avalanches triggered by tuning R to be given by the same distribution with a different cutoff that scales as $(k/R)^{-1/\sigma'}$, with $\sigma' = 1$ in three dimensions. [78]

5.7 Experimental Systems

Here we give a list of related experimental systems.

(1) As mentioned previously, the strength of the random local fields in $LiHo_xY_{1-x}F_4$ can be tuned by tuning an external magnetic field transverse to the orientation of the spins. In principle, this could be an excellent system to test the results of this work; however, the presence of dipolar forces in such materials changes the behavior of the system, resulting in domain wall motion, as opposed to domain nucleation. This renders such materials unsuitable for studying runaway avalanches. Although in some cases it is possible to minimize the dipolar forces by choosing a suitable sample geometry, such as a frame or thin wire, [77, 78]

the perturbative calculation of Ref. [81], which predicts that $LiHo_xY_{1-x}F_4$ becomes a dipolar-RFIM when a transverse field is applied, assumes the strength of the random local fields is less than the strength of the typical interactions between spins, suggesting that the strength of the random fields is at most comparable to the dipolar forces in this regime. In these materials, we expect domain wall propagation to dominate the dynamics. The results for this case are summarized in section E.3.

(2) It is possible to control the exchange interactions between spin-like states in atoms in optical lattice experiments [82]. This could allow for interesting experimental investigations of avalanches in RFIM-like systems and related systems modeled by the quantum mechanical transverse field RFIM [83–85], as the coupling is tuned.

(3) Experiments in systems of superfluid ^{4}He in Nuclepore show hysteretic and avalanching behavior in the amount of fluid trapped in the volume of the Nuclepore as the chemical potential is adjusted. [86–89] There are some qualitative differences between the hysteresis observed in these experiments and the RFIM. In particular, in fluid experiments the hysteresis curves are typically asymmetric, and do not seem to exhibit runaway avalanches. However, it may still be the case that the two systems are in the same universality class. A first attempt at a comparison between the statistics of the precursor avalanches in these experiments and in the RFIM has been done in Ref. [86]. The authors find that the experimental exponents are not inconsistent with the RFIM, but the error bars are not small enough to definitively conclude whether the universality classes are the same or different. Although the systems studied in Ref.'s [86–89] do not display runaway avalanches, this may be because the distribution of pore diameters is wide. A narrower range of pore diameters may allow for large runaway events. Additionally, some models of porous media develop a discontinuous jump in the hysteresis loop at sufficiently high porosity, [90, 91] providing another possible method to achieve runaway events. The group of Ref.'s [86–89] has also found that the coupling between different pores is mediated by a layer of superfluid helium, suggesting that perhaps the coupling can be tuned by adjusting the thickness of the fluid layer. However, the fluid layer thickness does change as the chemical potential is tuned, which may require modification of the results presented in this paper. If runaway avalanches can be triggered in superfluid ^{4}He in Nuclepore systems, then it may be possible to study changes in the runaway avalanche size as the coupling between pores is tuned, and the results could be compared to the predictions for the RFIM presented in this work, perhaps with some modifications to account for the coupling changing as the chemical potential is tuned.

(4) Preliminary studies of synchronization-avalanches in the Kuramoto model, a model of coupled oscilla-

tors, suggest that the Kuramoto model may also be in the same universality class as the RFIM [92]. Because the Kuramoto model is notorious difficult to study [93], relating it to the RFIM in some limit could greatly aid in our understanding of synchronization and avalanching phenomena. We hope that future studies will continue where these preliminary studies left off.

(5) The RFIM is applicable to a broad range of systems [55], ranging from magnets to decision making processes. We expect the results of this paper to be relevant to future studies of many of these systems if the coupling can be tuned.

5.8 Conclusion

In this chapter I have presented predictions for experiments which study the statistics of changes in the size of a runaway avalanche in a disordered system as the coupling between constituents in is tuned. To generate experimentally testable predictions I used the random field Ising model to derive the distribution of the size-changes in the runaway avalanche as the ratio J/R is slightly increased above a critical value $(J/R)_c$. We predict the values of the critical exponents in both mean field theory and three dimensions. The exponents found in mean field theory are likely to be those measured experimentally in systems with long range ferromagnetic interactions. For systems with short range interactions, simulations and a renormalization group calculation predict quantitatively accurate values for the exponents. [59] We argue that in finite dimensions the exponents of the jump in the runaway avalanche size will be equal to the exponents of the aftershock size distribution, which are already known. [62] Numerical simulations support our theoretical findings. We suggest possibilities for measuring these effects experimentally in ferromagnetic or fluid systems. Further studies could look at finite size effects in the system, such as how events due to processes PR or PP/AA affect the distribution of jump sizes S, or the relation of the random field Ising model to other systems which exhibit runaway avalanches[3].

5.9 Part II conclusions

This chapter ends Part II of this thesis, which focused on the random field Ising model of avalanches and hysteresis in magnets. The work presented in this chapter represents the completed work I have done on

[3]We have some results on this, which demonstrate that as J grows larges the distribution has a sharp decay followed by a small rebound which peaks quickly and then decays again. This occurs in a finite system when all aftershocks have been absorbed by the runaway avalanche and the system starts to absorb PR events.

studying the large spin-flip avalanche in the RFIM and related systems. However, I have done much more work on the RFIM and related models.

Notably, the model presented here assumes that temperature or other fluctuations in the magnet are negligible, such that spins flip deterministically according to their local random fields. However, this is often not the case. There are often thermal or even quantum fluctuations, both of which can trigger spin flips - and perhaps cause the system to equilibrate.

In the appendices, I present some work on projects which consider the effects of thermal or quantum fluctuations. In Appendix E, I present a phenomenological theory for the scaling of the hysteresis loop in the RFIM with thermal or quantum fluctuations. In Appendix F, I present a model of a single spin in contact with a thermal or quantum oscillator bath, to study the non-equilibrium dynamics in a simple microscopic model. In Appendix G, I present preliminary work developing a non-equilibrium thermal and quantum random field Ising model, from which I had hoped to derive the phenomenological theory presented in Appendix E.

As will become apparent in these appendices, developing such a thermal or quantum random field Ising model model is much easier said than done! One particularly difficult complication that quantum fluctuations give rise to is the generation of long-range temporal correlations between spins. This hinders both analytic and numerical treatments of the model. Nonetheless, it is an interesting model, and I hope to continue its development in the future.

Appendix A

Derivations of the earthquake inter-event time probabilities and steady-state phase distributions

A.1 Introduction

Chapter 2 introduced several probability formulas for earthquake statistics, many of which are also used in chapters 3 and 4. In this appendix, I present the derivations of some of these distributions.

A.2 Calculation of large event probability

The main equation presented in Chap. 2, Eq. (2.1), is the cumulative distribution function for the times between large earthquakes. The assumptions behind this expression, as given in Chap. 2.1, are

1. The earthquake fault exhibits small earthquake events which occur via a Poisson process, which is in general non-homogeneous; i.e., the attempt rate, $\lambda(F)$, at which earthquakes occur is a function of the overall stress on the fault, $F = F(t)$, which changes over time.

2. There is a stress-dependent probability, $P(F(t))$, that a small event will trigger a large event. This probability rapidly increases towards 1 near a critical stress value, F_c

3. After a large earthquake occurs, the stress relaxes to a baseline stress level f. We assume the timescale on which this relaxation occurs is much faster than any other relevant timescale, and so we treat the relaxation as occurring immediately.

Mathematically, assumption 1 can be expressed by saying the probability that $m(t_0, t_1)$, the number of small earthquakes which occur within a time window (t_0, t_1) , is equal to some non-negative integer number k, is

$$\text{Prob}_{\text{small}}(m(t_0, t_1) = k) = \frac{m(t_0, t_1)^k}{k!} \exp\left(-m(t_0, t_1)\right), \tag{A.1}$$

where

$$m(t_0, t_1) = \int_{t_0}^{t_1} dt\ \lambda(F(t)) \tag{A.2}$$

is the integrated rate of small earthquake attempts in the time window (t_0, t_1).

With these assumptions and Eqs. (A.1) and (A.2), we can derive the general distribution of large-earthquake inter-event times. To do so, it is easiest to consider the problem occurring in discrete time steps of size Δt. At the end of the calculation we can take the continuum limit.

Let's suppose we have k time bins of size Δt, and we want to calculate the probability that a large earthquake occurs in the kth time bin. Once a large earthquake occurs, our process stops, so in the previous $k-1$ time bins there can be no large earthquakes. This means that either no earthquake occurred in a time bin, or a small earthquake occurred, but it did not trigger a large earthquake. The probability that a large event occurs in the kth bin is then equal to the sum over all possible combinations of which bins small earthquakes occur in prior to the kth bin, times the probability that the large earthquake occurs in the kth bin.

From Eq. (A.1), the probability that no earthquake occurs in bin j is

$$\text{Prob(no quake in bin } j) = \exp(-m_j), \tag{A.3}$$

where $t_j = j\Delta t$ and m_j is given by

$$m_j = \int_{t_j - \Delta t/2}^{t_j + \Delta t/2} dt\ \lambda(F(t)) \approx \lambda(F(t_j))\Delta t \equiv \lambda_j \Delta t. \tag{A.4}$$

Similarly, the probability that one (and only one) earthquake occurs in the jth bin and does not trigger a large earthquake is

$$\text{Prob(one quake in bin } j \text{ and no large quake}) = m_j e^{-m_j}(1 - P_j), \tag{A.5}$$

where $P_j \equiv P(F(t_j))$.

Let us define binary variables $\epsilon_j = 0$ or 1, which denotes whether a small earthquake occurs in bin j ($\epsilon_j = 1$) or not ($\epsilon_j = 0$). With this, we can write the probability that a large earthquake occurs in bin k as

$$\text{Prob(large quake in bin } k) = \sum_{\{\epsilon_j\}} \prod_{j=1}^{k-1} \left[(1-\epsilon_j)e^{-\lambda_j \Delta t} + \epsilon_j \lambda_j \Delta t e^{-\lambda_j \Delta t}(1-P_j)\right] \lambda_k \Delta t e^{-\lambda_k \Delta t} P_k. \quad \text{(A.6)}$$

We can exchange the order of the product and the sum to get

$$\begin{aligned} \text{Prob(large quake in bin } k) &= \prod_{j=1}^{k-1} \sum_{\epsilon_j=0}^{1} \left[(1-\epsilon_j)e^{-\lambda_j \Delta t} + \epsilon_j \lambda_j \Delta t e^{-\lambda_j \Delta t}(1-P_j)\right] \lambda_k \Delta t e^{-\lambda_k \Delta t} P_k \\ &= \prod_{j=1}^{k-1} \left[e^{-\lambda_j \Delta t} + \lambda_j \Delta t e^{-\lambda_j \Delta t}(1-P_j)\right] \lambda_k \Delta t e^{-\lambda_k \Delta t} P_k. \quad \text{(A.7)} \end{aligned}$$

For the discrete time bin problem, this is the final result. However, we can take the continuum limit by setting $\Delta t \to 0$ and $k \to \infty$, while keeping the combination $k\Delta t = t$ finite. To take the continuum limit, it will be easiest if we first take the logarithm of Eq. (A.7). Doing so gives

$$\ln \text{Prob(large quake at time } t) = \sum_{j=1}^{k-1} \ln\left[e^{-\lambda_j \Delta t} + \lambda_j \Delta t e^{-\lambda_j \Delta t}(1-P_j)\right] + \ln\left[\lambda_k \Delta t e^{-\lambda_k \Delta t} P_k\right]. \quad \text{(A.8)}$$

Focusing on the first term, taking the continuum limit gives

$$\begin{aligned} \sum_{j=1}^{k-1} \ln\left[e^{-\lambda_j \Delta t} + \lambda_j \Delta t e^{-\lambda_j \Delta t}(1-P_j)\right] &\to \frac{1}{\Delta t}\int_0^t dt' \ \ln\left[e^{-\lambda(F(t'))\Delta t} + \lambda(F(t'))\Delta t e^{-\lambda(F(t'))\Delta t}(1-P(F(t')))\right] \\ &= \frac{1}{\Delta t}\int_0^t dt' \ \left(-\lambda(F(t'))\Delta t + \ln\left[1+\lambda(F(t'))\Delta t(1-P(F(t')))\right]\right) \\ &\approx \frac{1}{\Delta t}\int_0^t dt' \ \left(-\lambda(F(t'))\Delta t + \left\{\lambda(F(t'))\Delta t(1-P(F(t'))) + \mathcal{O}(\Delta t^2)\right\}\right) \\ &\approx \int_0^t dt' \ \left(-\lambda(F(t'))P(F(t')) + \mathcal{O}(\Delta t)\right). \quad \text{(A.9)} \end{aligned}$$

The second term in Eq. (A.8) is

$$\ln\left[\lambda(F(t))\Delta t e^{-\lambda(F(t))\Delta t} P(F(t))\right] \approx \ln\left[\lambda(F(t))P(F(t))\right] + \ln \Delta t + \mathcal{O}(\Delta t). \quad \text{(A.10)}$$

This expression appears as though it might be problematic because a $\ln \Delta t$ term survives; however, we recall at this point that for a short time window Δt, the probability Prob(large quake at time t) is equal to a probability density times the time window: Prob(large quake at time t) $= \rho_T(t|\{F(t)\})\Delta t$. The Δt term here will cancel with the surviving Δt term in Eq.(A.10). Putting together Eqs. (A.9) and (A.10) and re-exponentiating gives our final result for the inter-event time probability density,

$$\rho_T(t|F(t)) = \lambda(F(t))P(F(t)) \exp\left(-\int_0^t dt' \ \lambda(F(t'))P(F(t'))\right). \tag{A.11}$$

Integrating to get the cumulative distribution function gives

$$\text{Prob(large event within } T < t) = 1 - \exp\left(-\int_0^t dT \ \lambda(F(T))P(F(T))\right). \tag{A.12}$$

Note that this result is what we would have derived had we assumed that the large earthquakes occur via a non-homogeneous Poisson process with rate $\lambda(F(t))P(F(t))$. That is, the triggering probability $P(F)$ simply modulates the small earthquake rate $\lambda(F)$.

I have thus demonstrated Eq. (2.1) of Chap. 2 (equivalent to Eq. (A.12), above). Setting $\lambda(F) = \lambda_0 =$ constant similarly recovers Eq. (2.2).

A.2.1 Stress-dependent attempt rate versus constant attempt rate

Before I move on, I would like to comment on the choice of stress-dependent attempt rate $\lambda(F)$ versus a constant attempt rate λ_0. In typical earthquake faults, we expect that $\lambda(F)$ should typically have features similar to $P(F)$: it starts off at some relatively small, possibly constant value, and increases rapidly near the critical stress, F_c, before leveling off. Fig. A.1 shows a histogram of the number of small events in the Ben-Zion/Rice earthquake model as a function of stress. As expected, the rate is initially small and rises as it approaches the critical stress. The sudden drop-off in the number of small events is due to the fact that a large slip occurs. We assume that the rate would saturate beyond the critical stress. Lastly, I note that in the Ben-Zion/Rice model, the critical stress depends on the weakening ϵ. In Fig. A.1, I normalized the stress axis in terms of the critical stress at $\epsilon = 0$. However, in the work presented in this thesis, this shift is negligible.

Thus, the qualitative behaviors of the integrals of $P(F)$ and $\lambda(F)$ separately will be qualitatively similar

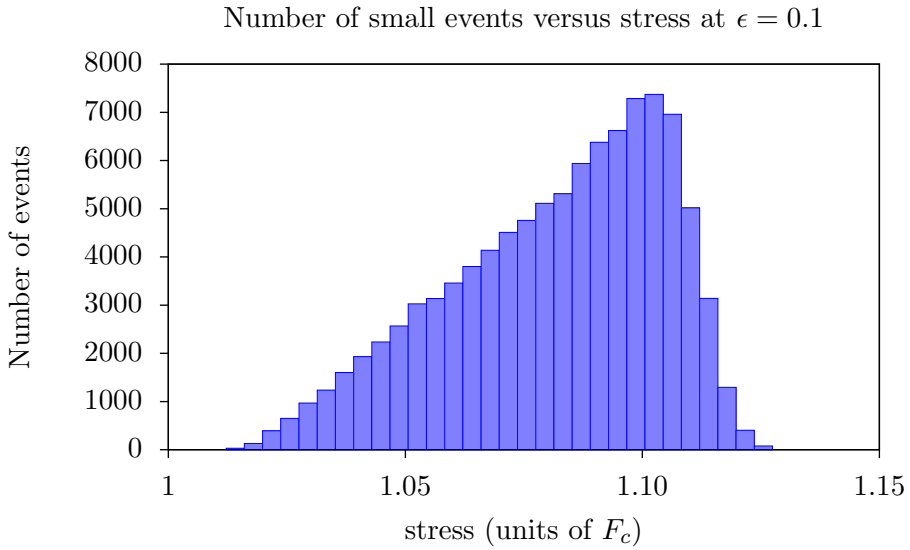

Figure A.1: Plot of the number of small events versus stress in a simulation of the Ben-Zion/Rice model with a small amount of dynamical weakening ($\epsilon = 0.1$). The x-axis is in units of the critical stress F_c. The shear zone is divided into 10000 patches in this simulation. For larger values of weakening the curve shifts to the right. Large events occur at stresses much greater than 1, so small events are not sampled in these regions. In simulations of the Ben-Zion/Rice model, the critical stress F_c varies with ϵ; we have normalized the x-axis in units of the critical stress in the Ben-Zion/Rice model at $\epsilon = 0$.

to the product $\lambda(F(t))P(F(t))$. We thus expect that setting $\lambda(F) = \lambda_0$ will only quantitatively affect the distribution Eq. (A.12). As long as we are only interested in the large earthquake inter-event times, and not the small earthquake time series, this will be a suitable approximation. Alternatively, a problem with constant small event rate and triggering probability $P(F)$ is equivalent to a problem with combined small-event rate and triggering probability $\lambda_0 P(F)$.

Accordingly, for simplicity of the following formulas and calculations, I will focus on the constant attempt rate case for the remainder of this appendix. Chap. 4 and the associated Appendix C discuss the case of non-trivial small earthquake attempt rates.

A.3 Derivation of $P(F)$ corresponding to the Ben-Zion/Rice earthquake model

In the previous section, the large earthquake triggering probability $P(F)$ was left arbitrary. In Sec. 2.3 of Chap. 2, I used a form for the function $P(F)$ that is derived from the Ben-Zion/Rice earthquake model. I present the derivation of this probability here.

For the derivation, we need the result that, in the absence of dynamic weakening, the distribution of earthquake sizes in the Ben-Zion/Rice model is given by [6]

$$D(S,F) \sim S^{-3/2} \exp\left(-S/S_{\max}\right), \tag{A.13}$$

where S is the dimensionless earthquake size (for example, potency over the minimum observed potency). The distribution is exponentially suppressed for earthquakes larger than $S_{\max} = b^2(1 - F/F_c)^{-2}$, where F_c is the critical stress of the fault, $F \leq F_c$ is the stress on the fault, b is a parameter that characterizes the amount of heterogeneity (disorder) in the system. At the critical point, $F = F_c$, $S_{\max} = \infty$, and $D(S, F_c)$ is a pure power-law distribution. In the thermodynamic limit of the Ben-Zion/Rice earthquake model, the system exhibits a single, never-ending avalanche for stresses $F > F_c$ [6]; hence the restriction to $F < F_c$ for Eq. (A.13).

When dynamic weakening is introduced to the model, all earthquakes greater than a critical size S_c run away to become large, "characteristic" earthquakes (see Fig. 2.1). However, probability must be conserved, so the probability that a small earthquake runs away to become a large earthquake in the Ben-Zion/Rice model must be equal to the probability of a small earthquake having size greater than S_c:

$$P(F) = \int_{S_c}^{\infty} dS \; D(S,F), \tag{A.14}$$

To properly interpret Eq. (A.14) as a probability, we need to use a normalized form for $D(S,F)$. Strictly speaking, the form of $D(S,F)$ given in Eq. (A.13) is an asymptotic formula, valid when S is large. However, so long as F is not drastically less than the critical stress F_c, we expect that deviations from the exact form should be relatively small, so we compute the normalization factor by integrating over $D(S,F)$ from $S = 1$ to ∞.

As we will have to compute similar integrals for the normalization factor and the probability $P(F)$, I will

just do the integral once, for an arbitrary lower limit, $a > 0$. We begin with

$$\int_a^\infty dS\ S^{-3/2} \exp\left(-S/S_{\max}\right) \tag{A.15}$$

and make the change of variables $y = \sqrt{S/S_{\max}}$, setting the new lower limit to $K = \sqrt{a/S_{\max}}$. The new integral is

$$\sqrt{K^2/a} \int_K^\infty dy\ \frac{\exp(-y^2)}{y^2}.$$

Integrating by parts:

$$\int_K^\infty dy\ \frac{\exp(-y^2)}{y^2} = -\left.\frac{1}{y} e^{-y^2}\right|_K^\infty - 2\int_K^\infty dy\ e^{-y^2} = \frac{e^{-K^2}}{K} - 2\int_K^\infty dy\ e^{-y^2}.$$

Identifying the remaining integral as the complementary error function, $\mathrm{erfc}(K) \equiv \frac{2}{\sqrt{\pi}} \int_K^\infty dy\ \exp(-y^2)$, I define the function

$$g(x) = \exp(-x^2) - \sqrt{\pi} x\ \mathrm{erfc}(x).$$

With this, we can write the integral Eq. (A.15) as

$$\int_a^\infty dS\ S^{-3/2} \exp(-S/S_{\max}) = \frac{1}{\sqrt{a}} g\left(\sqrt{a}\frac{1 - F/F_c}{b}\right). \tag{A.16}$$

Note that I have used the fact that $F < F_c$ to write $\sqrt{(1 - F/F_c)^2} = 1 - F/F_c$. The large earthquake probability can thus be written

$$P(F) = \frac{1}{\sqrt{S_c}} \frac{g\left(\sqrt{S_c}\frac{1-F/F_c}{b}\right)}{g(\frac{1-F/F_c}{b})}, \tag{A.17}$$

for $F < F_c$. For stresses $F > F_c$, we expect $P(F) = 1$ in an infinitely large system, as the large earthquake is guaranteed to trigger by the critical stress. However, in a finite system, we expect this sharp transition in $P(F)$ to be smoothed over, and F_c is only an average critical stress. To approximation the distribution for finite systems, we use $P(F)$ for $F > F_c$, as it reproduces the smooth transition to $P(F) = 1$ for $F > F_c$. See Fig. 2.2 in Chap. 2.

Distribution	Parameter	Fit value ±95% confidence bounds
Gaussian distribution	μ_G	0.1986 ± 0.0
Gaussian distribution	σ_G	0.00121 ± 0.00002
Brownian passage time distribution	α_B	0.00429 ± 0.00008
Brownian passage time distribution	μ_B	0.1986 ± 0.0

Table A.1: We fit Gaussian and Brownian passage time distribution to a distribution of earthquake inter-event times that was simulated using the Ben-Zion/Rice earthquake model. The fit parameters are given in this table. We fit a Gaussian with mean μ_G and standard deviation σ_G to the data, as well as a Brownian-passage time distribution of mean μ_B and aperiodicity α_B. All fit quantities have units of time, except for the aperiodicity α_B, which is dimensionless. The time is in units of an arbitrary time scale in the Ben-Zion/Rice model simulations.

A.4 Simulated distribution of times between large slips in the Ben-Zion/Rice model

The distribution of inter-event times between large slips can be simulated in the Ben-Zion/Rice earthquake model. Here, I give the results of this simulation, as performed by my collaborator Mike LeBlanc. As expected, the simulated inter-event time distribution agrees qualitatively with the results of the probabilistic model presented in Chap. 2. In the Ben-Zion/Rice model, the stress is actually swept adiabatically, so we cannot directly compare timescales between the simulation and the probabilistic model. We thus comment only on the similarity in shape between the model predictions.

In addition to simulating the inter-event time distribution, we fit Gaussian and Brownian passage-time distributions to the simulation data. The two fits are nearly indistinguishable, owing to the fact that the distribution is sharply peaked: accordingly, in the Brownian passage-time probability density function, $\rho_T(t) = (\mu/2\pi\alpha^2 t^3)^{1/2} \exp(-(t-\mu)^2/2\mu\alpha^2 t)$, the time dependence is controlled by the exponential term $(t-\mu)^2$; the other instances of t vary little over the region the distribution is peaked, and hence do not affect the fit prominently. The fits are shown in Fig. A.2. The fit parameters are given in Table A.1.

Fitting a Weibull distribution to the data was not successful using MATLAB's built-in fitting tools. I thus computed a Weibull plot of $\ln t$ versus $\ln[-\ln[1-\hat{\Phi}_{BZR}(t)]]$, where $\hat{\Phi}_{BZR}(t)$ is the empirical cumulative distribution function of the simulated Ben-Zion/Rice model data. The plot, as shown in Fig. A.3, is very nonlinear, demonstrating that the Weibull distribution is a poor fit to the simulation data.

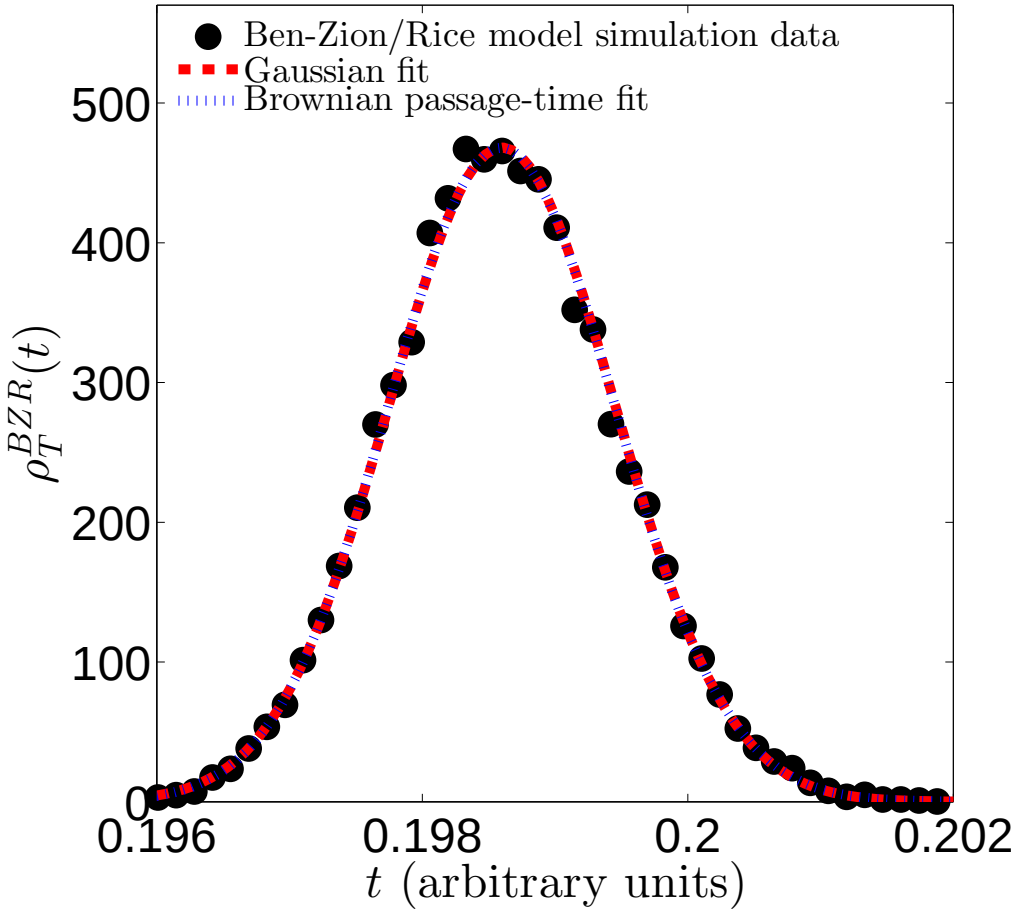

Figure A.2: Fitting Gaussian and Brownian passage-time distributions to a histogram of inter-event times simulated using the Ben-Zion/Rice earthquake model. Both distributions fit quite well, and the fits are nearly indistinguishable. The Weibull distribution does not fit our data at all using MATLAB's built-in fitting tools.

A.5 Derivation of probability distributions of phases for periodic stressed faults

For the case of an external stress on the fault which contains a periodic component, it is possible to consider the distribution of phases at which large earthquakes tend to occur, which can be useful for correlation analyses, as discussed in Chap. 3. Here I derive the form of the probability density for the phase of the next earthquake given the phase of the previous earthquake, as well as the integral equation for the steady-state phase distribution.

I remind the reader that for simplicity, I assume a constant small earthquake attempt rate in these

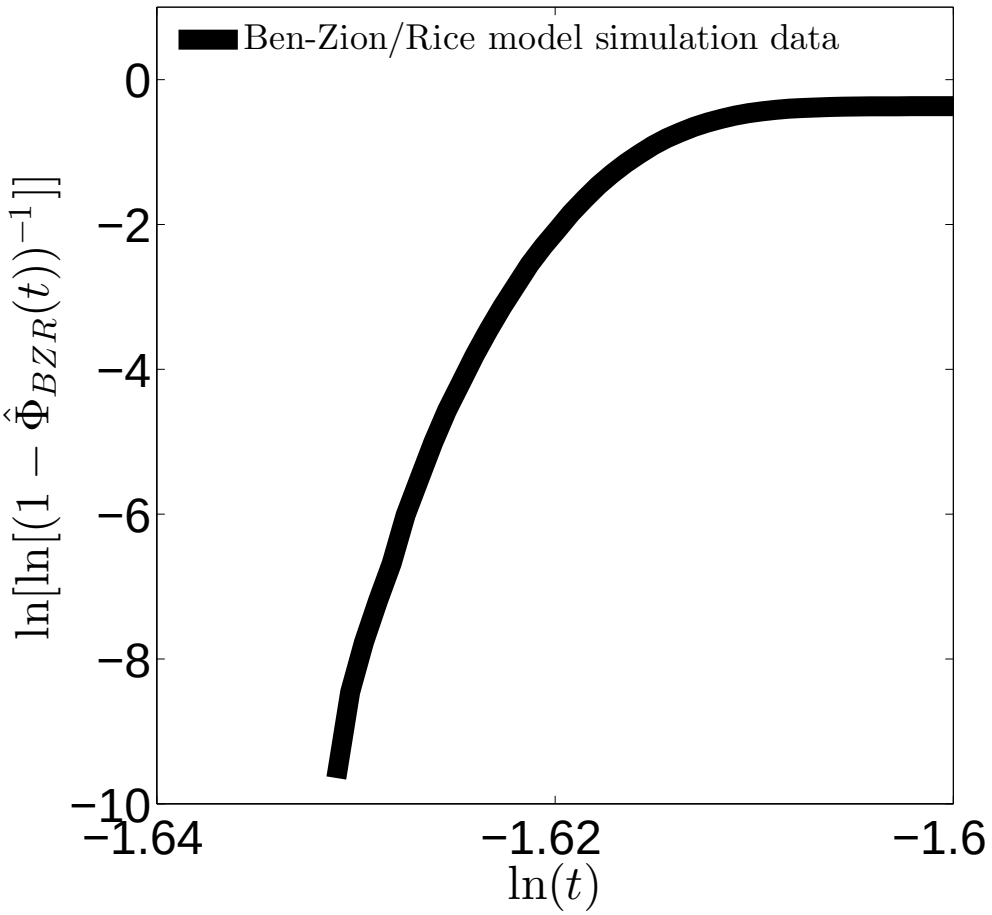

Figure A.3: A Weibull plot of the cumulative distribution function of simulated inter-event times between large slips in the Ben-Zion/Rice earthquake model. The axes are chosen to be $\ln(t)$ and $\ln\left[\ln\left[\left(1-\hat{\Phi}_{BZR}(t)\right)^{-1}\right]\right]$ because a Weibull distribution of shape parameter k will be a straight line with slope k on these axes. The nonlinear shape of our simulated data on this plot indicates that our simulation data is not well-modeled by a Weibull distribution.

derivations, $\lambda(F) = \lambda_0$. However, the results are fully applicable to the case of non-trivial small event rate if we set $\lambda_0 P(F) \to \lambda(F)P(F)$.

The probability density for the large earthquake inter-event times for constant small event rate is just

$$\rho_T(t|\phi) = \Theta(t)\lambda_0 P(F(t)) \exp\left(-\lambda_0 \int_0^t du\ P(F(u))\right), \tag{A.18}$$

where the external stress $F(t)$ has a periodic component of phase ϕ, and the density function is explicitly denoted as being conditional on the phase. This is important, as the phase changes every time a large

earthquake occurs. The update rule is $\phi_{k+1} = \omega t_{k+1} + \phi_k$, where ω is the angular frequency of the periodic stress component, t_k is the time of the $(k+1)$th event, and ϕ_k and ϕ_{k+1} are the phases of the stress following the k and $(k+1)$th events, respectively. Note that the probability of the $(k+1)$th inter-event time t_{k+1} is conditional on the set of all previous inter-event times. However, the distribution is conditional on only the most recent phase, which makes calculations of the phase distributions much nicer to work with.

The distribution is valid only for positive inter-event times $t > 0$. To ease with the follow calculations, I have explicitly enforced this condition by including a step function in the definition of ρ_T, which is convenient when deriving the phase distributions, as it allows us to let the time integrals run from $-\infty$ to ∞.

The exact form of the stress I choose to use is

$$F(t) = f + \Gamma t + F_0 \left(\sin(\omega t + \phi) - \sin\phi\right). \tag{A.19}$$

Here, t is the time since the previous large earthquake, such that $F(0) = f$, where f is the arrest stress that the fault relaxes to after a large earthquake. As previously mentioned, ω is the frequency of the periodic stress and ϕ is the phase. The amplitude of the periodic component is F_0. In addition to the periodic stress, there is a slow tectonic shear increase, Γ.

A.5.1 Conditional phase distribution

First, I will derive the distribution of the next phase that a large earthquake will occur at, denoted φ below, given the phase of the previous large earthquake, denoted ϕ. This conditional phase distribution will be denoted $\rho_\Phi(\varphi|\phi)$. I begin by changing variables from t to φ, and then taking care to reduce the domain of φ to $[0, 2\pi)$.

From the normalization condition I can write

$$1 = \int_{-\infty}^{\infty} dt\ \rho_T(t|\phi) = \omega^{-1} \int_{-\infty}^{\infty} d\varphi\ \rho_T\left(\frac{\varphi - \phi}{\omega} \mid \phi\right),$$

where I make the change of variables $\varphi = \omega t + \phi$. The negative inter-event times do not actually contribute to the integral due to a step function $\Theta(t)$ in the definition of ρ_T, but explicitly working with the infinite limits will make the following calculation easier. We want φ to take on values in $[0, 2\pi)$, so we split the integral up into infinitely many regions of width 2π. I then change variables to reduce the range of the integrals to $[0, 2\pi)$:

$$\omega^{-1} \sum_{k=-\infty}^{\infty} \int_{2\pi k}^{2\pi(k+1)} d\varphi \; \rho_T \left(\frac{\varphi - \phi}{\omega} \mid \phi \right) = \int_0^{2\pi} d\varphi \; \omega^{-1} \sum_{k=-\infty}^{\infty} \rho_T \left(\frac{\varphi - \phi + 2\pi k}{\omega} \mid \phi \right).$$

Because we want $1 = \int_0^{2\pi} d\varphi \; \rho_\Phi(\varphi|\phi)$, we identify

$$\rho_\Phi(\varphi|\phi) = \omega^{-1} \sum_{k=-\infty}^{\infty} \rho_T \left(\frac{\varphi - \phi + 2\pi k}{\omega} \mid \phi \right). \tag{A.20}$$

It is easy to prove this is 2π-periodic: shifting $\varphi \to \varphi + 2\pi$, the extra 2π can be absorbed into the $2\pi k$ and a redefinition of the k dummy index restores the original equation. The negative k terms are mostly zero due to the step function in ρ_T. The step function $\Theta(t) \to \Theta(\varphi - \phi + 2\pi k)$ will kill all k terms less than $(\phi - \varphi)/(2\pi)$. Given the ranges of the phases, this means the sum starts at either $k = 0$ or 1, depending on the values of φ and ϕ.

Unfortunately, this sum cannot be done analytically for our choice of $P(F)$ from the Ben-Zion/Rice earthquake model (Eq. (A.17)). However, the terms tend to decay quickly as k increases, and the distribution can be calculated relatively quickly numerically.

Steady-state phase distribution

Given the conditional phase distributions $\rho_\Phi(\varphi|\phi)$, we can derive an integral equation for the steady-state distribution of phases after a large number of earthquakes have occurred. Let $\varrho_\Phi^{(n+1)}(\phi_{n+1}|\phi_0)$ be the probability density of the $(n+1)$th phase of the system, given a starting phase of ϕ_0. This is distinct from $\rho_\Phi(\phi_{n+1}|\phi_n)$, which carries only information about the most recent phase. The density $\varrho_\Phi^{(n+1)}(\phi_{n+1}|\phi_0)$ can be calculated, in principle, from the multiple integral

$$\varrho_\Phi^{(n+1)}(\phi_{n+1}|\phi_0) = \int_0^{2\pi} d\phi_n d\phi_{n-1} \ldots d\phi_1 \; \rho_\Phi(\phi_{n+1}|\phi_n)\rho_\Phi(\phi_n|\phi_{n-1}) \ldots \rho_\Phi(\phi_1|\phi_0). \tag{A.21}$$

Recognize that we can rewrite this as

$$\varrho_\Phi^{(n+1)}(\phi_{n+1}|\phi_0) = \int_0^{2\pi} d\phi_n \; \rho_\Phi(\phi_{n+1}|\phi_n)\varrho_\Phi^{(n)}(\phi_n|\phi_0). \tag{A.22}$$

The importance of the fact that the conditional phase distributions $\rho_\Phi(\phi_k|\phi_{k-1})$ depend only on the most recent phase now comes into play. This fact is equivalent to saying the sequence of phases at which the large

earthquakes occur is described by a Markov process. A well-known result of Markov chain theory is that such a process has a well-defined limiting distribution [94–96]. Furthermore, this limiting distribution will be *independent* of the initial phase, ϕ_0. If we take the limit $n \to \infty$, $\varrho_\Phi^{(n+1)}(\varphi|\phi_0)$ will approach this limiting distribution, denoted $\varrho_\Phi^*(\varphi)$. The limiting distribution can thus be obtained by solving the integral equation

$$\varrho_\Phi^*(\varphi) = \int_0^{2\pi} d\phi \; \rho_\Phi(\varphi|\phi)\varrho_\Phi^*(\phi). \tag{A.23}$$

This is a homogeneous type 2 Fredholm equation [97] with a kernel $\rho_\Phi(\varphi|\phi)$. Unfortunately, solving this integral equation analytically is quite difficult, if not impossible. However, the equation is relatively easy to solve numerically. We can approximate the integral as an N-term sum:

$$\int_0^{2\pi} d\phi \rho_\Phi(\varphi|\phi)\varrho_\Phi^*(\phi) \to \sum_{j=0}^{N} w_j \rho_\Phi(\varphi|\phi_j)\varrho_\Phi^*(\phi_j), \tag{A.24}$$

where w_j is a quadrature weight evaluated at the discrete points ϕ_j. If we define $\varrho_i \equiv \varrho_\Phi^*(\phi_i)$, and $K_{ij} = w_j\rho_\Phi(\phi_i|\phi_j)$, then the numerical problem is reduced to solving the matrix equation

$$\sum_j K_{ij}\varrho_j = \varrho_i. \tag{A.25}$$

Solving this equation is an eigenvalue problem; hence, we need only find the eigenvalues and eigenvectors of K_{ij}, and choose the eigenvector corresponding to the eigenvalue of 1 [1]. After we solve for this eigenvector, we can write down an interpolating formula for ϱ^*:

$$\varrho_\Phi^*(\varphi) = \sum_{j=0}^{N} w_j \rho_\Phi(\varphi|\phi_j)\tilde{\varrho}_j, \tag{A.26}$$

where $\tilde{\varrho}_j$ denotes the eigenvector of K_{ij} corresponding to an eigenvalue of 1. Note that the kernel, $\rho_\Phi(\varphi|\phi_j)$ can be used with any phase φ; only the conditional phases must be the discretization points ϕ_j.

The distribution can be calculated quite accurately numerically, as seen in Fig. 2.6. However, there are a number of pitfalls with the numerical solution. In particular, the discretized kernel K_{ij} is quite sparse when $\Gamma/(\omega F_0) > 1$. As a result, a large number of discretization points is needed for the discretized matrix to have an eigenvalue very close to 1. Another problem that arises is that if we wish to change the frequency or

[1] To be more accurate, there is one eigenvalue that is real and close to 1. Increasing the number of discretization points (i.e., if we sample our kernel $\rho_\Phi(\phi_i|\phi_j)$ with more precision) increases the convergence of this eigenvalue to 1. The other eigenvalues are all complex numbers. These are spurious eigenvalues caused by the discretization scheme.

amplitude, it is necessary to re-generate the numerical kernel and re-solve the eigensystem, which can become rather time-consuming, even if an efficient eigensolver is used. As a result, for computing the $F_{0,min}(\omega)$ versus ω curves presented in Chap. 3, it proved to be far more efficient to simply simulate the phase distributions, rather than solve Eq. (A.23) for many different (F_0, ω) pairs.

A.6 Solution for $\varrho_\Phi(\varphi)$ when $F_0 = 0$

Lastly, although in general we must solve the integral equation numerically, we expect that in the case of $F_0 = 0$, $\varrho^*_\Phi(\varphi) = (2\pi)^{-1}$. I will show that this is indeed a solution to Eq. (A.23). If we insert $\varrho^*_\Phi(\varphi) = c$ into the integral equation, we see that we require $\int_0^{2\pi} d\phi \rho_\Phi(\varphi|\phi) = 1$. The integral is not necessarily 1 when done over the second variable, but when $F_0 = 0$ we can show it is. In the inter-event time distribution, when $F_0 = 0$, the distribution is independent of ϕ: i.e., we may write $\rho_T(t|\phi) = \rho_T(t|0)$. Then,

$$\int_0^{2\pi} d\phi\ \rho_\Phi(\varphi|\phi) = \int_0^{2\pi} d\phi\ \sum_{k=-\infty}^{\infty} \omega^{-1} \rho_T\left(\frac{\varphi - \phi + 2\pi k}{\omega} \mid 0\right).$$

We can then change variables $\varphi - \phi + 2\pi k \to \phi$. The limits of the integral are then $\varphi + 2\pi(k-1)$ to $\varphi + 2\pi k$:

$$\omega^{-1} \sum_{k=-\infty}^{\infty} \int_{\varphi+2\pi(k-1)}^{\varphi+2\pi k} d\phi\ \rho_T(\phi/\omega|0) = \omega^{-1} \int_{-\infty}^{\infty} d\phi\ \rho_T(\phi/\omega|0) = \int_{-\infty}^{\infty} dt\ \rho_T(t|0) = 1.$$

We have shown that the integral is 1, and hence that the solution to the equation is ϱ^*_Φ = constant. Normalization determines that the constant is $(2\pi)^{-1}$.

Appendix B

Technical details behind the probabilistic large-earthquake time-series model

B.1 Introduction

This appendix contains some technical details and additional results related to the study of correlations between large stick-slip events in frictional media and external periodic driving stresses.

B.2 Simulation of the slip time series data

Using the probability density Eq.(2.3), I generated a simulated time series of large events. Between large events the stress on the shear zone is

$$F(t) = f + \Gamma t + F_0(\sin(\omega t + \phi) - \sin\phi), \tag{B.1}$$

where as before, t is the time since the last event, f is the constant arrest stress following a large event, Γ is the slow monotonic stress increase rate, F_0 is the amplitude of the periodic driving force, ω is the oscillation frequency, and ϕ is the phase of the periodic stress following the last event. The form of the stress is chosen so that $F(0) = f$; i.e., after every large event the stress reduces back down to a constant value of f.

The time-series is generated by choosing a random inter-event time T from the probability density and letting the stress on the system evolve according to equation Eq. (B.1) until the time T, when the next large event takes place. The stress is then reduced back to the initial value f, the phase is updated to the phase of the sinusoidal driving stress at the time of the event, and a new inter-event time is drawn from the probability density distribution to determine when the next event will occur. This process continues until enough events have been generated to analyze the statistics of the time series and determine the steady-state phase distribution. The values of the stress between large events are not necessary for computing the steady-

state phase distribution; they merely provide a picture of the stress variations on the fault. An example plot of the stress versus time is shown in Fig. 3.1 in Chap. 3.

B.3 Analysis of time series data

The analysis of the simulated time series proceeds as described in Chap. 3. The phases at which the large earthquakes occur are mapped to the angles of steps in a 2d random walk, as depicted in Fig. B.1.

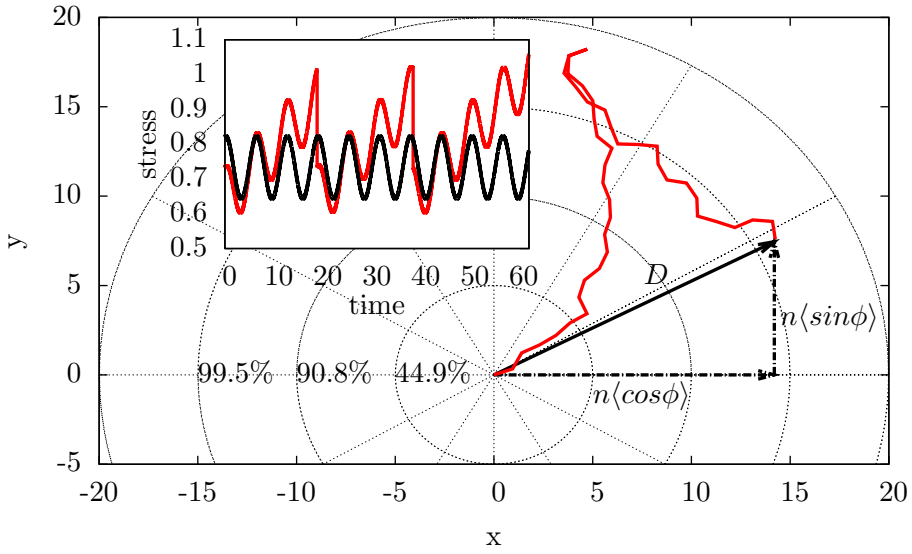

Figure B.1: Determining correlations between large slips and the periodic driving stress by comparison to a random walk. For each phase at which a large slip occurs, the random walker takes a step with an angle equal to that phase on a 2d plane. All steps are of equal length. After n steps, if the odds that the walker is at a distance D away from its starting position greater than what would be predicted if it moved completely randomly, we determine that there was some bias in the way it moved - i.e., there is a significant correlation between the driving stress and the large slips.

The theoretical root-mean-square distance the random walker travels after n steps is

$$\langle D^2 \rangle = n(n-1)(\langle \cos\phi \rangle^2 + \langle \sin\phi \rangle^2) - n, \tag{B.2}$$

which follows from noting that the squared distance is a Pythagorean sum over the resultant x and y directions of the random walk and averaging over the many runs, which amounts to an average over the (steady-state) phases.

If $\langle D^2 \rangle$ exceeds $(n - n\ln(p_n))/n(n-1)$ (i.e., the squared distance expected after n steps if the random walker were perfectly random), for a significance threshold of $p_n = 0.5\%$, we declare that a strong correlation exists between the stick-slip timings and the periodic driving.

The averages $\langle \cos\phi \rangle$ and $\langle \sin\phi \rangle$ are computed from our simulated time series, using data after allowing the system to reach a steady-state phase distribution (which we discuss in the next section). We calculate the averages for 19,200 pairs of amplitudes and frequencies, and use them in Eq. (B.2) to compute the threshold amplitude as a function of frequency and number of observed events, n. We have found numerically that the power-law $F_0 \sim 1/\omega$ holds down to at least frequencies of $0.01(2\pi/\tau_0)$, where τ_0 is the mean inter-event time in the absence of driving ($F_0 = 0$), and for amplitudes up to about $3.0F_c$.

B.4 Steady state phase distributions

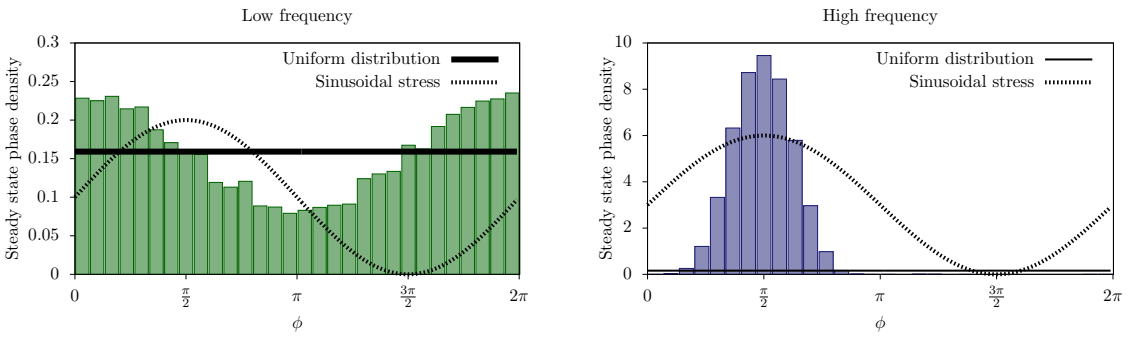

Figure B.2: Steady state phase distributions (histograms) at low (left figure) and high (right figure) frequencies ω (relative to the average inter-event rate $2\pi/\tau_0$). The dashed line is a guide to show to which part of the sinusoidal cycle the phase corresponds. For low amplitudes F_0, the distributions appear uniform (solid black line, obtained for $F_0 = 0$), as expected, since correlations with the oscillatory driving stress are practically undetectable in this case. As the amplitude F_0 is increased, the phase distributions become more sinusoidal. For low frequencies, the most likely phase is $\phi = 0$ (equivalent to 2π) for periodic driving of the form $F_0 \sin(\omega t + \phi)$. At higher frequencies the most likely phase approaches $\phi = \pi/2$. This is consistent with the experimental observation that at low frequencies large events occur near the maxima of the stress increase rate, while at high frequencies they occur near the maxima of the stress itself. Histograms were obtained numerically from runs with 10,000 large events. Note that at low frequencies a much larger amplitude F_0 is required to observe the same amount of correlations with the oscillatory stress (i.e., to observe the same deviation from a uniform phase distribution) than for high frequencies. Both histograms correspond to the same amplitude $F_0/F_c = 0.05$.

After enough recorded large-slip events, the system achieves a steady state phase distribution, as explained in Appendix A. The form of the distribution depends on the driving frequency and amplitude. The

distribution also encodes information about how strongly the fault is affected by the additional periodic stress. For small amplitudes, correlations are weak and consequently the distribution of phases is roughly uniform for $0 < \phi < 2\pi$, while for larger amplitudes, correlations are stronger and obvious sinusoidal variations appear in the distribution of phases, as seen in Fig. B.2. Additionally, the model predicts that at low frequencies the most likely phase at which a large event occurs is near the maximum of the stress rate, which we take to correspond to $\phi = 0$ (Fig. B.2, left). At higher frequencies they occur near the maximum stress, corresponding to $\phi = \pi/2$ (Fig. B.2, right). Here "low" or "high" frequency is measured relative to the average failure rate in the absence of periodic driving, $2\pi/\tau_0$, where, as before, τ_0 is the average inter-event time at $F_0 = 0$. This prediction agrees with experiments on sheared granular gauge material [36, 37]. Intuitively, one expects that large events are most likely to occur at stress maxima ($\phi = \pi/2$ in Fig. B.2), as observed at high frequencies. The reason this is not the case at low frequencies is because at low frequencies many slips occur per driving cycle: For $\omega \ll 2\pi/\tau_0$, large events occur during every part of the cycle (i.e., at any phase ϕ). Furthermore, the number of events observed per unit time is highest when the stress increase per unit time is highest. Consequently, at low frequencies most events occur when the stress rate is a maximum, which is at $\phi = 0$ or 2π, in Fig. B.2. In contrast, for $\omega \gg 2\pi/\tau_0$ the periodic stress oscillates through many cycles before a large event is triggered. In this case, most large events occur near a stress maximum; i.e., near $\phi = \pi/2$, as intuitively predicted and illustrated in Fig. 3.1. Based on a different model, Ref. [38] predicts that the phase $\phi_{\max}$ at which the maximum in the phase-distribution occurs scales as $\phi_{\max} - \phi/2 \sim -(\omega F_0/\Gamma)^{-1/2}$, for large values of $\omega F_0/\Gamma$. This is in agreement with our model for $\omega F_0/\Gamma \gg 1$, as shown in Fig. S5. We note that for low disorder (defined precisely in the next section), the phase $\phi_{\max}(\omega)$ has sharp peaks near frequencies that are integer multiples of $2\pi/\tau_0$ (where τ_0 is again the average inter-event time when $F_0 = 0$), just like the $F_{0\min}(\omega)$ curve discussed in the main paper. We find that the peaks sometimes overshoot the large-frequency asymptotic value of $\pi/2$, representing delays in triggering at these frequencies. This may be an artifact of the form of $\lambda(F)$ that we chose: the derivative of our sigmoidal function is approximately symmetric about the critical stress F_c. If the derivative instead dropped off sharply for $F > F_c$, corresponding to a fast saturation in the small event rate, we expect the events would not overshoot the stress maximum. The peaks do not appear at all if the disorder in the system is high. This is also true for the $F_{0\min}(\omega)$ curve. We discuss this in the next section.

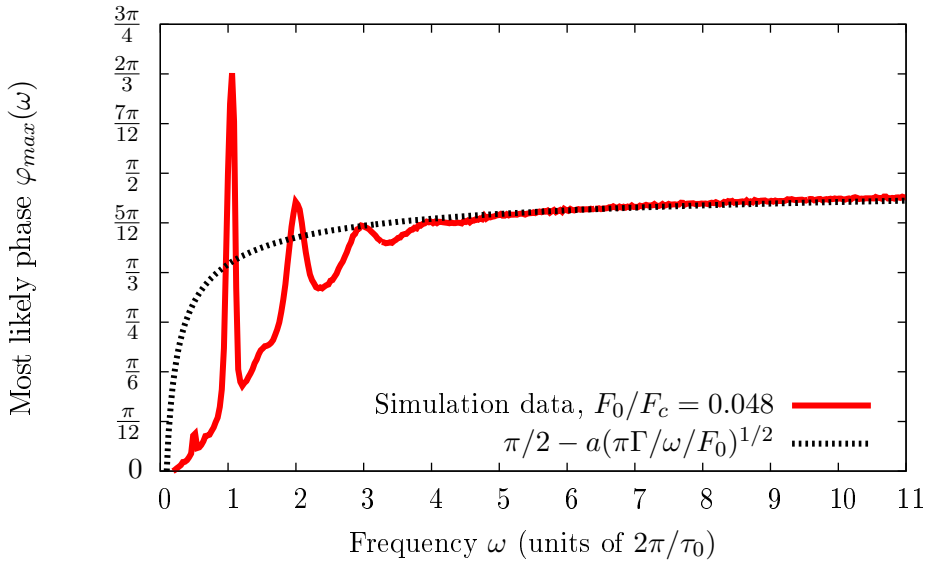

Figure B.3: Most likely phase $\phi_{\max}(\omega)$ as a function of frequency ω. For very low frequencies the most likely phase $\phi_{\max}$ is near zero, corresponding to the regime for which many large slip events occur per cycle. $\phi_{\max}$ implies that in this case most events are nucleated when the stress rate is maximized. At high frequencies the maximum phase approaches $\pi/2$, for which the events tend to occur at stress maxima. Peaks in $\phi_{\max}$ occur near frequencies for which ω is an integer multiple of $2\pi/\tau_0$, where τ_0 is the average inter-event time between large slips. The dashed line corresponds to the asymptotic form of the phase as predicted in Ref. [38], up to a parameter-dependent constant a, as labeled in the figure. Here, we find $a = 0.4$ gives the best fit to the high frequency tail of the curve. Finally, we note that if the spread in inter-event times is wide, as is expected for highly disordered frictional surfaces, the peaks are diminished in height. At very high disorders the peaks are not observable (see Fig. B.5).

B.5 Amplitude threshold versus frequency results at high disorder

In the BZR model, disorder is present in the random threshold stresses of the individual patches of the shear zone. Increasing the spread of possible patch-stress threshold values, which we refer to as "increasing the disorder", leads to a large spread in inter-event times between large events. To capture this in our probabilistic model, we include a parameter, which we call the "disorder parameter", in our functional form of $\lambda(F)$ which controls the sharpness of the increase in rate near the critical stress. Increasing the disorder parameter results in a more gradual increase of $\lambda(F)$, which in turn results in a larger spread in the inter-event time distribution. As mentioned in the main text, this has the effect of reducing the peaks in $F_{0\min}(\omega)$. For high enough disorders the peaks will be damped out completely, giving a power law decay at

low frequencies, which increases near the first resonant frequency, $\omega_{\text{res}} = 2\pi/\tau_0$, forming a minimum, before leveling off into a constant threshold. Plots for different n at low disorders are given in Fig. B.4.

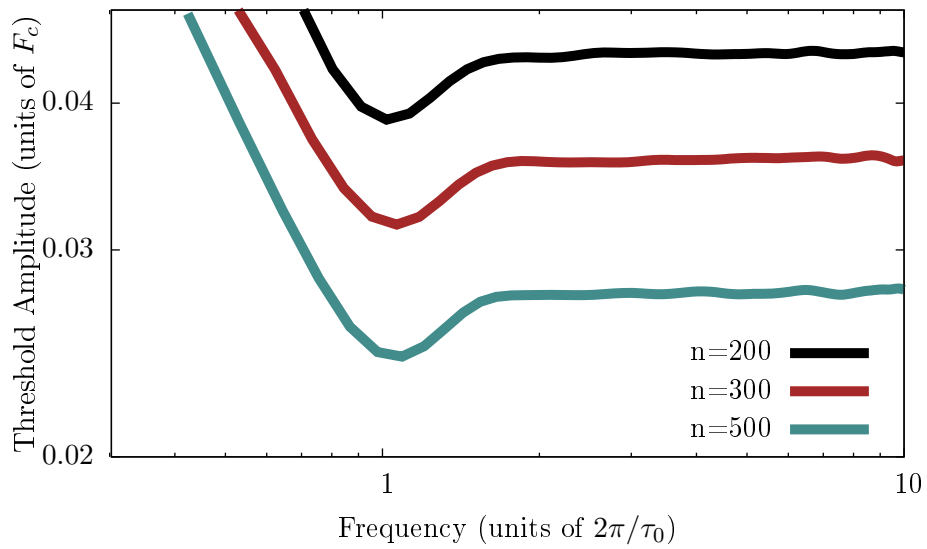

Figure B.4: Threshold amplitude versus frequency for different n with a higher value of disorder compared to the other plots. The peaks have been completely damped out; only the minimum at $\omega = 2\pi/\tau_0$ remains.

Similarly, the peaks which appear in $\phi_{\max}(\omega)$, the most likely phase at frequency ω, vanish for high disorder, as shown in Fig. B.5).

B.6 Amplitude threshold versus frequency results for different numbers of events

As mentioned in Chap. 3, the minimum amplitude needed to detect a correlation above a desired threshold decreases as the number of measured events increases, as is intuitively expected: the more events one measures, the better the statistics, and the less of an amplitude one needs to detect a correlation. We find that the amplitude scales as $F_{0\min}(\omega) \sim n^{-1/2}$, which is a consequence of the threshold amplitude being proportional to the statistical spread of the root-mean square distance $\sqrt{\langle D^2 \rangle}$). Fig. B.6 compares the minimum amplitude needed to observe a correlation with confidence 99.5% for different numbers of measured events. Fig. B.7 demonstrates that for large $n > 50$ all curves collapse onto the same curve by plotting the threshold amplitude times $n^{1/2}$ versus frequency.

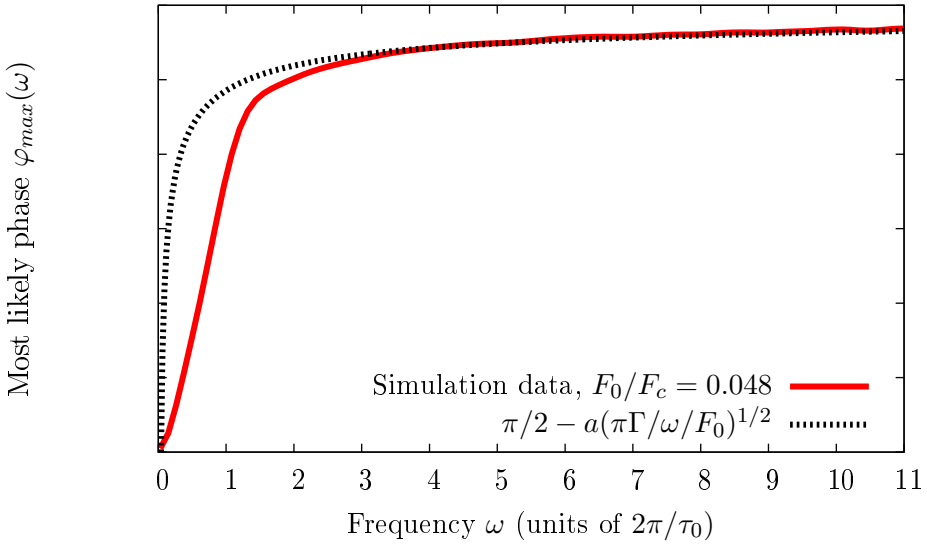

Figure B.5: Most likely phase $\phi_{\max}$, as a function of frequency ω, at high disorder. For very low frequencies the most likely phase $\phi_{\max}$ is near zero, corresponding to the regime for which many large slip events occur per cycle. $\phi_{\max} = 0$ implies that in this case most events are nucleated when the stress rate is maximized. At high frequencies the maximum phase approaches $\pi/2$, for which the events tend to occur at stress maxima. Unlike in the low disorder case, the phase increases monotonically towards $\pi/2$ as the frequency increases. There are no visible peaks at high disorder. The dashed line corresponds to the asymptotic form of the phase as predicted in Ref. [38], up to a parameter-dependent constant a, as labeled in the figure. Here, we find $a = 0.25$ gives the best fit to the high frequency tail of the curve.

B.7 Amplitude threshold versus frequency results for different slow monotonic shear rates Γ/F_c

When the slow monotonic shear stress rate Γ/F_c is changed, we find changes to the threshold curves that agree with observations in experiments [34,35]. In particular, we find that increasing Γ results in the minima of the curves, $\omega_{\min}$, being linearly shifted to higher frequencies, $\omega_{\min} \sim \Gamma/F_c$. However, this is not simply a rescaling of the frequency-axis: the threshold amplitudes also tend to increase as Γ increases. See Fig. B.8, below.

The fact that this is not a simple rescaling of the frequency axis is a consequence of our assumption that there is a time-scale λ_0^{-1}, which sets the timescale of $\lambda(F)$ (i.e., $\lambda(F) = \lambda_0 h(F)$, for some dimensionless sigmoidal function $h(F)$), which is independent of the frequency or loading rate. This gives three independent time scales: the driving stress frequency ω, the slow shear rate Γ/F_c, and the small event rate λ_0. Instead of λ_0 we could take the average inter-event time, τ_0, as our third independent timescale, as we have done in

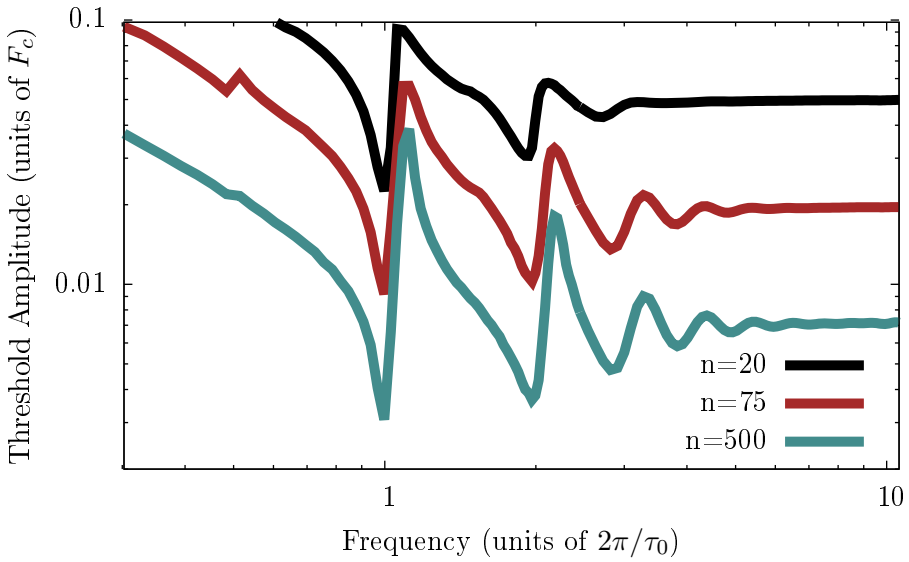

Figure B.6: Minimum amplitude required to detect a correlation versus frequency for different numbers of measured events. For each curve, any driving amplitude above the curve is sufficient to detect a correlation above 99.5% confidence. Below each curve the observed correlations do not meet the 99.5% confidence threshold. As intuitively expected, for smaller numbers of recorded events, larger amplitudes are needed to meet the confidence threshold. Note also that the oscillations appear to be damped out for very small numbers of measured events.

the rest of the paper; however, τ_0 changes with Γ, while the time-scale λ_0^{-1} does not, and hence is the more fundamental quantity. We choose τ_0 in favor of λ_0^{-1} in the rest of the paper simply because τ_0 is much easier to measure experimentally.

If the small event rate were determined by the frequency or slow shear rate, as could be the case experimentally, then there would only be two independent time scales and changing Γ/F_c would simply amount to a rescaling of the frequency axis. Systematic measurements of the small event rate for different oscillatory frequencies ω and loading rates Γ/F_c would be extremely useful to determine whether or not the small event rate depends strongly on the oscillatory or shear stress rates.

B.8 Average inter-event time and standard deviation at amplitudes comparable to the failure stress

In the Chap. 3, I showed that for small driving stresses one can trigger system failure with improved accuracy by driving the system near its "resonant" frequencies, integer multiples of $2\pi/\tau_0$. By detuning the frequency

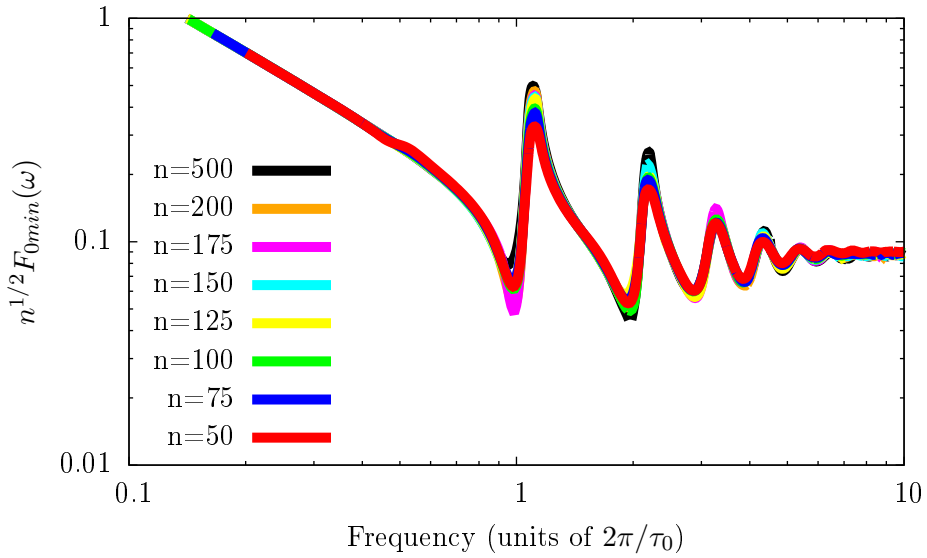

Figure B.7: Plot of threshold amplitude scaled by $n^{1/2}$ against frequency, which demonstrates that all curves for different numbers of measured events collapse approximately onto a single curve. The collapse is not as good near the minima and maxima due to limited data resolution in those regions. The curves have been smoothed to eliminate some numerical noise.

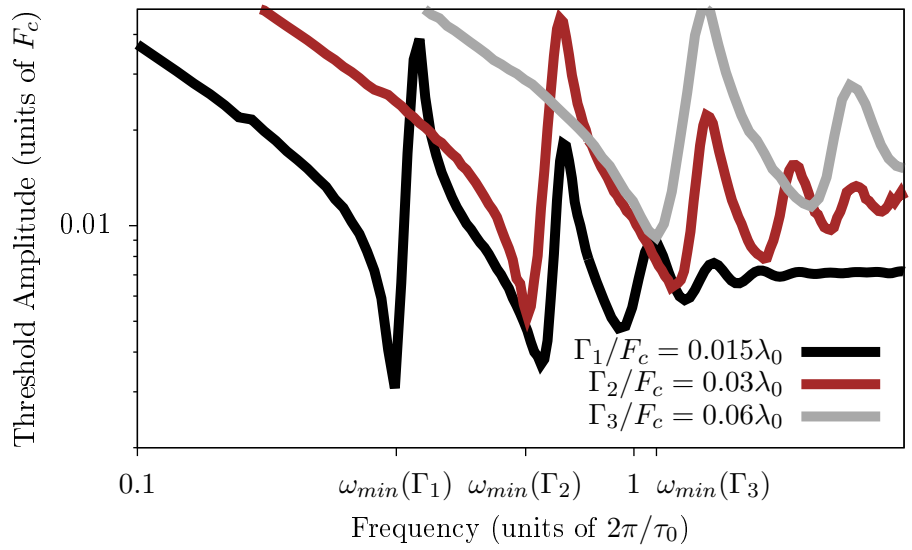

Figure B.8: Threshold amplitude vs. frequency for different slow shear rates Γ/F_c. As Γ is increased, the minima of the curves occur at higher frequencies and the required amplitude increases.

from these resonant values, one can also delay or advance failure, on average, albeit at the cost of an increased standard deviation. At larger amplitudes the average inter-event time drops, but this is merely because the

driving stress amplitude is large enough to push the total stress above the critical stress F_c and trigger failure. It is thus not as interesting for control of frictional systems. Furthermore, the standard deviation returns to its $F_0 = 0$ value at high amplitudes, so the certainty with which failure occurs is no better than the undriven system. For completeness we plot the high-amplitude range of the average inter-event time $\tau(F_0, \omega)$ in Fig. B.9 and the standard deviation $\sigma_\tau(F_0, \omega)$ in Fig. B.10. We find that at frequencies $\omega \ll 2\pi/\tau_0$, the average inter-event time does not drop dramatically, and the standard deviation is lower than its undriven value.

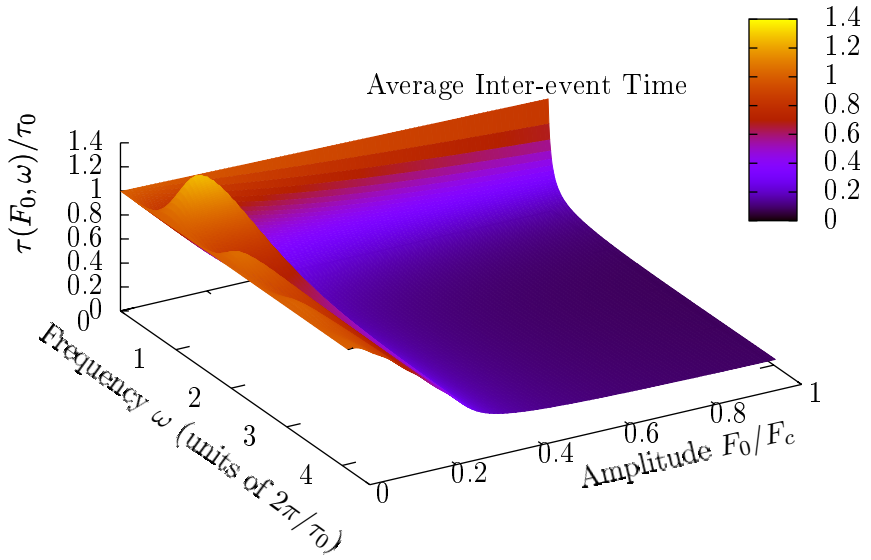

Figure B.9: The average inter-event time up to amplitudes of $F_0/F_c = 1$. As the amplitude becomes large, the stress oscillations are large enough to trigger failures simply by pushing the system above the critical stress F_c, except at the lowest frequencies $\omega \ll 2\pi/\tau_0$. The most interesting regime for controlling failure is thus at the lowest amplitudes, $F_0/F_c < 0.1$.

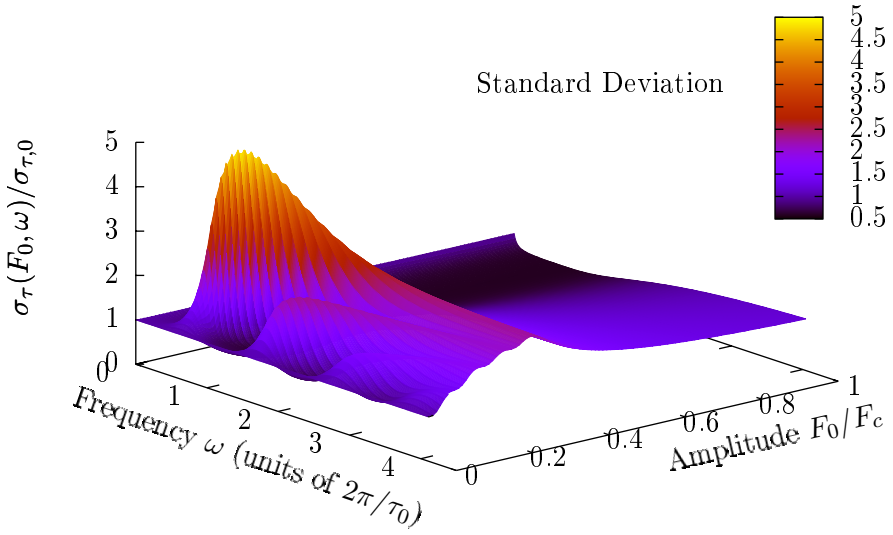

Figure B.10: The standard deviation for amplitudes up to $F_0/F_c = 1$. As the amplitude becomes large, the standard deviation returns to its undriven value, $\sigma_{0,\tau}$, at $F_0 = 0$, except at low frequencies $\omega \ll 2\pi/\tau_0$.

Appendix C

Technical details behind the small earthquake model correlation analysis

C.1 Introduction

In this appendix I go over some of the technical details behind the work presented in Chap. 4.

C.2 Mathematical details of the probabilistic model of earthquake triggering

The probabilistic process which generates the time series of small earthquake events is a non-homogeneous Poisson process. That is, the probability of k small earthquakes between times t_1 and t_2 is given by

$$\text{Prob}_{\text{small}}(k) = \frac{m(t_1,t_2)^k}{k!} \exp\left(-m(t_1,t_2)\right), \tag{C.1}$$

where

$$m(t_1,t_2) = \int_{t_1}^{t_2} dt\ \lambda(F(t)), \tag{C.2}$$

as in Appendix A. Again, $\lambda(F)$ is the small event rate as a function of total fault stress, $F(t)$, which in turn depends on time. As stated in assumption (3), we use the average total stress along the fault, which neglects possible spatial variations in the stress $F(t)$. We are thus treating the triggering probabilities in a mean-field manner, wherein the earthquakes are triggered by the mean shear stress on the fault. Future extensions of the model could take into account local stress variations. Such an extension would not be able to treat stress drops due to small earthquakes as negligible, as we have done in this work.

In chapters 2 and 3, I assumed a constant small event rate $\lambda(F) = \lambda_0$, as we expect a non-constant small event rate to produce only quantitative changes to the results of chapters 2 and 3 (see Appendix A). The

small event rate $\lambda(F)$ is an input to the model that can either be chosen on phenomenological grounds or calculated from microscopic models of earthquake statistics. Here, we choose a middle ground approach. We measured the number of small events as a function of stress in a microscopic earthquake model that has been studied previously [3–6, 26, 27]. We observed that the small event rate was low (or even zero) for stresses much less than the critical stress, and increased sharply near the critical stress. In the simulations, the small event rate is cutoff above the critical stress because a large earthquake is triggered. Here, we will assume that if a large earthquake were not triggered, the small event rate would saturate for stresses much larger than the critical stress [1]. To capture this behavior, we choose $\lambda(F)$ to be

$$\lambda(F(t)) = \lambda_{\max}\left[\frac{\lambda_{\min}}{\lambda_{\max}} + \left(1 - \frac{\lambda_{\min}}{\lambda_{\max}}\right)\exp\left(-A\exp\left(B\left[1 - \frac{F(t)}{F_c}\right]\right)\right)\right], \tag{C.3}$$

where $\lambda_{\max}$ and $\lambda_{\min}$ are the maximum and minimum small event rates, respectively. Here, $\lambda_{\min}$, can be interpreted as a small background small event rate at which earthquakes are triggered even when the stress on the fault is not close to the critical stress. In our simulations, I chose $\lambda_{\min}/\lambda_{\max} = 0.25$. The numerical values I chose for these rates will be given below. The parameters A and B are constants that set the scale of stresses over which the rate increases. We chose $A = 0.1454134$ and $B = 131.066$ to give an increase from $\lambda_{\min}$ to $\lambda_{\max}$ over a stress range from about $0.98F_c$ to F_c.

The stress-dependent probability, $P(F)$, that a small earthquake runs away to become a large earthquake was again chosen to be

$$P(F) = \frac{1}{\sqrt{S_c}}\frac{g\left(\sqrt{S_c}\frac{1-F/F_c}{b}\right)}{g(\frac{1-F/F_c}{b})}, \tag{C.4}$$

where S_c is a (dimensionless) critical small-earthquake size above which small earthquakes run away to become large earthquakes, and b is a phenomenological constant which parametrizes the amount of disorder in the fault. Large b implies larger disorder, which leads to wider spreads in large earthquake inter-event times. The function $g(x)$ is

$$g(x) = \exp(-x^2) - \sqrt{\pi}x\ \mathrm{erfc}(x).$$

where erfc(x) is the complementary error function, $\mathrm{erfc}(x) \equiv \frac{2}{\sqrt{\pi}}\int_x^\infty dy\ \exp(-y^2)$.

[1] Assuming that the small event rate saturates is not strictly necessary. The behavior of the small event rate for stresses much greater than F_c is not important for our applications, because the earthquake is very likely to occur before stresses exceed the critical stress. We thus simplify our problem by assuming the small event rate saturates. However, the behavior of the small event rate may be important for estimating the hazard function, which for our model is $\lambda(F)P(F)$. Because $P(F)$ must saturate to 1 at long times (large stresses), the long-time behavior of the hazard function will depend on the long-time behavior of $\lambda(F)$. However, the long-time behavior is not likely to be sampled, as a large earthquake is likely to have occurred.

Finally, the total fault stress is again chosen to be

$$F(t) = f + \Gamma t + F_0(\sin(\omega t + \phi) - \sin\phi).$$

The parameter Γ is the slow tectonic stress increase rate and ϕ is a phase difference which keeps track of the difference between the total stress on the fault and the external periodic stress. Because I reset the time to 0 after a large event, we must update the phase as $\phi \to \omega t_{\text{event}} + \phi$, with t_{event} the time since the previous event, in order to ensure the phase after the large earthquake is equivalent to the phase before the large earthquake. The parameters f, F_0 and ω are again the arrest stress after a large earthquake, oscillatory stress amplitude and the angular frequency of the oscillatory stress, respectively. I chose the values of the parameters to be $f = 0.724F_c$, $\lambda_{\max} = 20000\Gamma/F_c$, $1/\sqrt{S_c} = 0.1$ and $b = 0.1$. I chose the timescale $F_c/\Gamma = 2000$ years. For long simulation runs the results are independent of the initial phase. In units of Γ/F_c, a diurnal tidal frequency of 24 hours is $\omega_{\text{tidal}} = 4406748\Gamma/F_c$ and an annual frequency of one year is $\omega_{\text{annual}} = 12568\Gamma/F_c$. I varied the periodic stress amplitudes F_0/F_c in a range from 10^{-6} up to 0.05. Our choices of ω_{tidal}, ω_{annual} and F_0/F_c are motivated by estimates from observations, while our choices of f and S_c are motivated by estimates from experiments designed to mimic earthquake faults [34–36]. The parameters f and S_c are also constrained by microscopic earthquake models [3–6, 26, 27]. In particular, $1/\sqrt{S_c}$ must be much less than 1, and f is less than F_c by an amount of order $1/\sqrt{S_c}$. Varying f and S_c within these allowed ranges does not lead to qualitative changes to our results. Lastly, $\lambda_{\max}$ and b are chosen because we find these parameter choices produce physically relevant behaviors in our model, as well as the microscopic model from which $\lambda(F)$ and $P(F)$ were derived. A larger value of b corresponds to more disorder in the fault, and would, for example, increase the spread of inter-event times between the large earthquakes.

C.3 Details of the time-series analysis

C.3.1 Small earthquake correlations

As stated in Chap. 4, the measure we used to detect correlations in earthquake time series is the Schuster test [34–36, 49, 50]. In the Schuster test, we record the phases at which earthquakes occur and calculate the "p-value", $p(t)$, given by

$$p(t) = \exp\left(-\frac{D(t)^2}{n(t)}\right), \tag{C.5}$$

when $n(t) \gg 1$. Here, $n(t)$ is the number of events recorded at a time t since the previous large earthquake and

$$D(t)^2 = \left(\sum_{k=0}^{n(t)} \cos \phi_k \right)^2 + \left(\sum_{k=0}^{n(t)} \sin \phi_k \right)^2 , \tag{C.6}$$

where the ϕ_k are the phases of the periodic stress at which the recorded earthquakes occur. Formally, the p-value is the probability that we would that we would observe the measured phase distribution, or one with even stronger correlations, if the null hypothesis, "The distribution of phases at which $n(t)$ earthquakes occur is uniform", were true. Suppose we measure a set of phases at which earthquakes occur and find that the histogram of these phases is not uniform. The expression for $p(t)$ is calculated by mapping the phases at which earthquakes occur to the angles of steps of unit length in a 2d random walk. If we calculate $p(t)$ and find it to be more than 10% or so, we attribute the non-uniformity of the histogram to be a statistical fluctuation. However, a value of $p(t)$ less than 10% indicates that it is unlikely that we would observe such a phase distribution if the null hypothesis were true. The fact that this phase distribution is unlikely if the null hypothesize is true is taken to be indicative of a strong correlation between the periodic stresses and the earthquake timings, which generate a non-uniform distribution of phases at which the earthquakes occur.

In my analysis, I generated a time series of 5000 large earthquakes with numerous small earthquakes occurring in-between. I calculated $p(t)$ between each set of large earthquakes. I initialized $p(t) = 1$ after each large earthquake and held it at that value until 200 small earthquakes occurred, before updating the value of $p(t)$ according to Eq. (C.5) as small earthquakes accumulate. I fix $p(t) = 1$ for the first 200 small earthquakes after a large earthquake because Eq. (C.5) is an asymptotic expression that only applies for large $n(t)$. Though values of $n(t)$ greater than 10 are often considered large, I chose to be conservative and use $n(t) = 200$ as the cutoff before starting to calculate $p(t)$. I continuously updated $p(t)$ and $n(t)$ as small earthquakes arrived (until a large earthquake occurs, when I reset $n(t) = 0$ and $p(t) = 1$). Another possible analysis method would be to calculate $p(t)$, between large quakes, for subsets of events in (possibly overlapping) bins. In this analysis method, all bins have similar numbers of events, and the last bin, before the large earthquake occurs, has no events in common with the first bin. We find that in our model, the continuous accumulation is less noisy than the binned accumulation. It is accordingly more suitable for our analyses.

To determine if the periodic stress has an effect on the triggering of large earthquakes, I computed the cumulative distribution of values of $p(t_{\text{large}})$, the value that $p(t)$ takes when a large earthquake occurs (at

$t = t_{\text{large}}$). I computed this distribution for several logarithmically-spaced amplitudes from $F_0 = 10^{-6}F_c$ to $0.01F_c$, as well as $F_0 = 0.04F_c,\ 0.05F_c$ and 0 (no periodic driving). I performed the computation for both of the tidal and annual stress variation frequencies quoted in Chap. 4.

For each amplitude-frequency pair, I computed the cumulative distribution by counting the number of events less than each observed value of $p(t_{\text{large}})$. I then normalized the cumulative distribution so that it approaches 1 as the recorded values of $p(t_{\text{large}})$ approach 1. The results are plotted in Fig. 4.3 of Chap. 4. Because correlations are indicated by small p-values, I plotted the distributions on a logarithmic scale. Compared to a fault with no periodic driving, higher amplitude periodic stresses lead to lower p-values when the large earthquakes occur, indicating that the periodic stresses indeed have an effect on the triggering of earthquakes, as discussed in the Chap. 4. However, this analysis only tells us the distribution of p-values when the large earthquakes occur. It provides no advanced warning of large earthquake occurrences. To formulate a predictive measure, I analyzed the behavior of the entire p-value curve between large earthquakes, rather than its value when the large earthquakes occurred in the model.

For predicting large earthquakes, it would be ideal to assess the probability that a large earthquake is going to occur within a specified amount of time, given observations of the p-value. In Tanaka's analysis [49,50], the p-value did not always reach accepted levels of significance (less than 10%) when the large earthquake occurred. Furthermore, in our simulations, fluctuations in p(t) can drive it below 10%, but the p-value can quickly recover while no earthquake occurs. We thus want to assess how likely a large earthquake is to occur if we observe that the p-value dips below a certain value.

To do so, I analyzed $p(t)$ to determine: (1) how often our simulated p-values, $p(t)$, descended below a specified threshold level, P. I chose a logarithmically-spaced range of thresholds P from 10^{-10} or less up to 1. (2) When $p(t)$ dipped below the threshold P, I recorded how long it remained below the threshold, Δt, until either a large earthquake occurred or $p(t)$ climbed back above the threshold. From these measurements, I computed the probability that a large earthquake occurs within a time T since the p-value dips below a chosen threshold level P. The probability is calculated as

$$\begin{aligned} &\text{Prob}\left(\text{large event}, \Delta t < T \mid \bar{p}(t) < P\right) \qquad \text{(C.7)} \\ = \ &\frac{\text{Number of time periods during which a large event occurs\&}\Delta t < T, \text{ for which } \bar{p}(t) < P}{\text{Total number of periods for which } \bar{p}(t) < P}, \end{aligned}$$

where $\bar{p}(t)$ is a smoothed version of the p-value curve, $p(t)$, explained below. Eq (C.8) is not identically 1 because there are time periods for which $\bar{p}(t)$ dips below P, but no large quake occurs before $\bar{p}(t)$ rises above P again.

The data in Fig. 4.4 of Chap. 4 is calculated according to Eq. (C.8). Because we expect qualitatively similar results for both tidal and annual stress frequencies, I performed the following analysis only for tidal frequencies. Similarly, because correlations between the small earthquakes and the tides were strongest for an amplitude of $F_0 = 0.05F_c$, I used this value for the driven amplitude in the data presented in Fig. 4.4.

To perform the thresholding analysis used to compute Eq. (C.8), I first smoothed over the $p(t)$ curve using a 500 day box-window (which is much larger than tidal frequencies). This smoothing eliminates small, fast fluctuations in $p(t)$ that would otherwise interfere with our thresholding procedure and record many short dips below the thresholds P that offer no predictive power. The smoothing procedure leaves only the general trend, $\bar{p}(t)$, which is more appropriate to analyze.

To smooth over the $p(t)$ curve, we need to account for the fact that our time data is not uniformly spaced. I used a C routine developed by Andreas Eckner, available online at `www.eckner.com`, designed specifically to smooth over non-uniformly spaced data. The routine uses a constant-value interpolation between data points and integrates over the curve to perform the smoothing. We do not use a linear interpolation scheme because the p-value does not change between small earthquake events.

To find the times at which $\bar{p}(t)$ crosses the threshold level, P, we start at the 201st event (because we set $p(t) = 1$ for the first 200 events) and move along the curve until we find the times of the $(j-1)$th and jth events for which $\bar{p}(t_{j-1}) > P$ and $\bar{p}(t_j) < P$, respectively. We compute the time for which $\bar{p}(t_{\rm down}) = P$ by linear interpolation,

$$t_{\rm down} = t_{j-1} + (P - \bar{p}(t_{j-1})) \left[\frac{t_j - t_{j-1}}{\bar{p}(t_j) - \bar{p}(t_{j-1})} \right].$$

We continue moving along the curve until either a large earthquake occurs, for which the time $\bar{p}(t)$ spent below P is $\Delta t = t_{\rm large} - t_{\rm down}$. If no large quake occurs and $\bar{p}(t)$ instead rises back above P between times t_{k-1} and t_k, we compute the time at which it passed above the threshold by linear interpolation again,

$$t_{\rm up} = t_{k-1} + (P - \bar{p}(t_{k-1})) \left[\frac{t_k - t_{k-1}}{\bar{p}(t_k) - \bar{p}(t_{k-1})} \right],$$

which is formally the same as the equation for $t_{\rm down}$. The time for which $\bar{p}(t)$ was less than P is then $\Delta t = t_{\rm up} - t_{\rm down}$, and we make a note that no large earthquake occurred during this time period.

Appendix D

An exact derivation of the mean field random field Ising model avalanche size distribution

In this appendix, I give an exact calculation of the avalanche size distribution for the mean field random field Ising model (RFIM). This calculation follows the derivation in the Ph.D. thesis of Amit Mehta [98], which in turn follows a more general approach to calculating avalanche size distributions reported in [99]. The primary difference between the calculations is that the approximation of a transcendental equation that Mehta uses to derive the scaling function appears to give rise to a divergent (but constant) integral which is thrown out as an unimportant proportionality constant; in contrast, I use the properties of the Lambert-W function [100] to complete the derivation exactly and avoid this divergent integral.

D.1 Hamiltonian

We briefly review the random field Ising model (RFIM) Hamiltonian, introduced in Chapter 5. Consider an N spin system consisting of classical spins with nearest neighbor coupling J_{ij} between all spins. The Hamiltonian is

$$-\mathcal{H} = \sum_{\langle i,j \rangle} J_{ij} s_i s_j + \sum_i (H + h_i) s_i,$$

where $\langle i, j \rangle$ indicates a sum over nearest neighbor pairs only, H is a global magnetic field and h_i is the local magnetic field of spin i. To get the mean field version of this problem, we allow the first sum to run over all pairs, with $J_{ij} = J/N$. Defining the Magnetization to be $N^{-1} \sum_i s_i$, the Hamiltonian becomes

$$-\mathcal{H} = \sum_i (JM + H + h_i) s_i.$$

In the following, the avalanche size will be denoted by a capital letter S, not to be confused with the spin variable, a lowercase s_i.

D.2 Avalanche Distribution Derivation

An avalanche in the mean field theory consists of "shells" of flipped spins - one initial spin flips, increasing the overall field by $2J/N$ and causing a number of spins, n_1, around it (not physically nearby, but with random local fields within the increased field range) to flip, which in turn increase the field by $2Jn_1/N$, which will then cause n_2 spins with fields inside this new change to flip, and so on. The process is modeled in the $N \to \infty$ limit as a Poissonian process with the average number of spins flipped in shell t being $2J\rho(h_*)n_{t-1}$, where h_* is the field of the first spin in the avalanche. The fact that the probability at step t depends on the result of step $t-1$ makes this a conditional probability at each step. The probability that n_t spins flip given n_{t-1} spins flipped in the last step is then

$$P(n_t|n_{t-1}) = \frac{(2J\rho n_{t-1})^{n_t} \exp\left[-2J\rho n_{t-1}\right]}{n_t!}, \tag{D.1}$$

where $\rho \equiv \rho(h_*)$. The total probability for the distribution of the size of each shell is then

$$P(n_0 = 1, n_1, \ldots, n_T) = \frac{(2J\rho)^{n_1} e^{-2J\rho}}{n_1!} \prod_{t=2}^{T} \frac{(2J\rho n_{t-1})^{n_t} e^{-2J\rho n_{t-1}}}{n_t!} \tag{D.2}$$

We now define the characteristic function of the distribution,

$$\Gamma_T(\{\mu\}) = \left\langle \exp\left[i \sum_{t=0}^{T} \mu_t n_t \right] \right\rangle = \sum_{\{n_1, n_2, \ldots, n_T\}} e^{i \sum_{t=0}^{T} \mu_t n_t} P(n_0 = 1, n_1, \ldots, n_T). \tag{D.3}$$

We note that the n_T term in this expression is coupled only to the n_{T-1} term, so we may evaluate the n_T sum first:

$$\begin{aligned} \sum_{n_T=0}^{\infty} e^{i\mu_T n_T} \frac{(2J\rho n_{T-1})^{n_T} e^{-2J\rho n_{T-1}}}{n_T!} &= e^{-2J\rho n_{T-1}} \sum_{n_T=0}^{\infty} \frac{(2J\rho n_{t-1} e^{i\mu_T})^{n_T}}{n_T!} \\ &= e^{-2J\rho n_{T-1}} e^{-2J\rho n_{T-1} e^{i\mu_T}} \\ &= e^{-2J\rho n_{T-1}(e^{i\mu_t} - 1)} \end{aligned}$$

Hence,

$$\begin{aligned}\Gamma_T(\{\mu\}) &= \sum_{\{n_1,\ldots,n_{T-1}\}} e^{i\sum_{t=0}^{T-1}\mu_t n_t} e^{2J\rho(\exp[i\mu_T]-1)n_{T-1}} P(1,n_1,\ldots,n_{T-1}) \\ &= \Gamma_{T-1}(\mu_0,\mu_1,\ldots,\mu_{T-2},\lambda_{T-1}),\end{aligned}$$

where $\lambda_{T-1} = \mu_{T-1} - 2iJ\rho(e^{i\mu_T} - 1)$. This equation relates Γ_T to Γ_{T-1}. We could repeat this procedure for each n_t, but instead let us perform a slight cosmetic adjustment and write $\mu_T = \lambda_T$. Our relation then looks like

$$\Gamma_T(\mu_0,\mu_1,\ldots,\lambda_T) = \Gamma_{T-1}(\mu_0,\mu_1,\ldots,\mu_{T-2},\lambda_{T-1}), \tag{D.4}$$

where the left hand side has T arguments and the right hand side has $T-1$ arguments. This is now a recursion relation, and so through repeated use of it we can reduce Γ_T to

$$\begin{aligned}\Gamma_T(\{\mu\}) &= \Gamma_1(\mu_0,\lambda_1) \\ &= \sum_{n_1=0}^{\infty} e^{i\mu_0 n_0 + \lambda_1 n_1} P(1,n_1) \\ &= e^{i\lambda_0},\end{aligned}$$

where the λ_t are given by the recursion relation

$$\lambda_{t-1} = \mu_{t-1} - 2iJ\rho(e^{i\lambda_t} - 1), \tag{D.5}$$

with the initial condition $\lambda_T = \mu_T$. In principle we can solve this equation for the endpoint λ_0. We will not do this in general. Instead we will consider the case $\mu_t \equiv \mu$ for all t. We do this because in doing so Γ_T reduces to having one argument, and is given by

$$\Gamma_T(\mu) = \sum \exp\left[i\mu \sum_{t=0}^{T} n_t\right] P(1,\ldots,n_T) = \sum e^{i\mu S} P(1,\ldots,n_T),$$

where $S = \sum_{t=0}^{T} n_t$ is the total size of the avalanche, the distribution of which is what we are after. Also consider that for a general set of μ_t, if we inverse Fourier transform Γ_T, the result is proportional to the original probability $P(1,\ldots,n_T)$:

$$\begin{aligned}
\prod_{t=1}^{T}\left(\int_{-\pi}^{\pi}\frac{d\mu_t}{2\pi}\right)e^{-i\mu_t m_t}\Gamma_T(\{\mu\}) &= \prod_{t=1}^{T}\left(\int_{-\pi}^{\pi}\frac{d\mu_t}{2\pi}\right)e^{-i\mu_t m_t}\sum_{\{n_1,\ldots,n_T\}}e^{i\sum\mu_t n_t}P(1,\ldots,n_T)\\
&= \sum_{\{n_1,\ldots,n_T\}}\prod_{t=1}^{T}\left(\int_{-\pi}^{\pi}\frac{d\mu_t}{2\pi}\right)e^{-i\mu_t(m_t-n_t)}P(1,\ldots,n_T)\\
&= \sum_{\{n_1,\ldots,n_T\}}e^{i\mu_0}\prod_{t=1}^{T}(\delta_{m_t n_t})\,P(1,\ldots,n_T)\\
&= e^{i\mu_0}P(1,m_1,\ldots,m_T).
\end{aligned}$$

Following this, if we set all μ_t equal to one another, then

$$\int_{-\pi}^{\pi}\frac{d\mu}{2\pi}e^{-i\mu S}\Gamma_T(\mu)\propto P(S),$$

the distribution of avalanche sizes S. Setting all μ_t simplifies our recursion relation for λ_t:

$$\lambda_{t-1}=\mu-2iJ\rho(e^{i\lambda_t}-1). \tag{D.6}$$

We note that this equation has a fixed point λ^* such that if any $\lambda_t=\lambda^*$ for some t, then $\lambda_t=\lambda^*$ for all t, given by

$$\lambda^*=\mu-2iJ\rho(e^{i\lambda^*}-1). \tag{D.7}$$

This is a transcendental equation. In the previous work by Mehta [98], the exponential was expanded to second order to obtain an approximate relation for λ^*. Here we will instead use the properties of the Lambert-W function to obtain $P(S)$. The Lambert-W function [100], $W(z)$, is defined by the relation

$$z=W(z)e^{W(z)}; \tag{D.8}$$

for real z there are two branches of solution,labeled $W_0(x)$ and $W_{-1}(x)$. Analytically continuing to complex z introduces infinitely many branches, $W_k(z)$, where $W_0(z)$ is the only one analytic at the origin, and has a convergent Taylor series there, given by

$$W_0(z)=\sum_{k=1}^{\infty}\frac{(-k)^{k-1}}{k!}z^k. \tag{D.9}$$

There exists a branch point at $z = -1/e$, and by the ratio test one can show the radius of convergence of this series is $1/e$. Our fixed point solution λ^* can be expressed in terms of this function. It can be shown that for $p^{ax+b} = cx + d$, $p > 0$, $c, a \neq 0$,

$$x = -\frac{W_k\left(-\frac{a\ln p}{c}p^{b-ad/c}\right)}{a\ln p} - \frac{d}{c}.$$

At least for $p = e$ this holds for complex values of the parameters, as by the transformation $-t = ax+ad/c$ we can turn the equation into the form of $te^t = -a/ce^{b-ad/c}$, which requires no assumptions that the parameters be real, and hence identifying $a = i$, $b = 0$, $c = (-2Ji\rho)^{-1}$ and $d = (\mu + 2iJ\rho)/(2Ji\rho)$, we have

$$\lambda^* = iW_k\left(-2J\rho e^{-2J\rho}e^{i\mu}\right) + \mu + 2iJ\rho; \tag{D.10}$$

there are infinitely many fixed points for this equation, each corresponding to a branch of the Lambert-W function.

At this point we must ask which fixed point solution λ_0 flows to as $T \to \infty$, as the initial condition $\lambda_T = \mu$ is to be integrated over, and so we need to know there is a stable branch for any initial μ that λ_0 will tend to. If we can show there is a unique stable attracting fixed point independent of μ, then as $T \to \infty$ we λ_0 will converge to this λ^*. If we make a small change $\lambda_t \to \lambda_t + \epsilon_t$, for $|\epsilon_t| \ll 1$, we find

$$\epsilon_{t-1} = 2J\rho e^{i\lambda_t}\epsilon_t;$$

this is just a linear recurrence relation, which is easily solved to give

$$\epsilon_0 = (2J\rho)^T e^{i\sum_{t=1}^{T}\lambda_t}\epsilon_T. \tag{D.11}$$

If we set $\lambda_t = \lambda_k^*$, where the k refers to the branch of the Lambert-W function, we get

$$\epsilon_0 = (2J\rho e^{i\lambda})^T\epsilon_T. \tag{D.12}$$

A fixed point λ_k^* is stable if $|\epsilon_0|$ tends to zero as $T \to \infty$. We find $|\epsilon_0|^2 = (2J\rho)^{2T}(e^{i\lambda_k^*}e^{-i\overline{\lambda_k^*}})|\epsilon_T|^2$, and so

$$|\epsilon_0| = (2J\rho e^{-\mathbf{Im}\lambda_\mathbf{k}^*})^T|\epsilon_T|.$$

Using our solution for we see $\mathrm{Im}\lambda_k^* = 2J\rho + \mathrm{Im}\left(iW_k\left(-2J\rho e^{-2J\rho}e^{i\mu}\right)\right) = 2J\rho + \mathrm{Re}\left(W_k\left(-2J\rho e^{-2J\rho}e^{i\mu}\right)\right)$.

We can show the principal branch is stable for any value of μ as follows: Note that

$$\mathrm{Re}W_0(xe^{i\mu}) = \mathrm{Re}\sum_{k=1}^{\infty}\frac{(-k)^{k-1}z^k}{k!}e^{ik\mu} = \sum_{k=1}^{\infty}\frac{(-k)^{k-1}z^k}{k!}\cos(k\mu).$$

Because $\cos k\mu \leq 1$,

$$\sum_{k=1}^{\infty}\frac{(-k)^{k-1}z^k}{k!}\cos(k\mu) \leq \sum_{k=1}^{\infty}\frac{(-k)^{k-1}z^k}{k!} = W_0(x).$$

Hence,

$$\begin{aligned}|\epsilon_0| &\leq (2J\rho e^{-2J\rho}e^{-W_0(-2J\rho e^{-2J\rho})})^T|\epsilon_T| \\ &= \left[-W_0(-2J\rho e^{-2J\rho})\right]^T|\epsilon_T|.\end{aligned}$$

By the definition of the Lambert-W function, if $u = ve^v$, then $v(u) = W(u) = W(ve^v)$; hence, $-W_0(-2J\rho e^{-2J\rho}) = 2J\rho$ and so

$$|\epsilon_0| \leq (2J\rho)^T|\epsilon_T|.$$

$2J\rho$ is restricted to the range $[0,1]$ (zero corresponding to $J = 0$ and 1 corresponding to the criticality condition $2J\rho = 1$), and hence as $T \to \infty$, $(2J\rho)^T|\epsilon_T| \to 0$, $|\epsilon_0| \leq 0 \Rightarrow |\epsilon_0| = 0$, and thus the principal branch is a stable fixed point as $T \to \infty$.

For the other branches, we note that Eq. (D.12) may also be written (upon taking the modulus)

$$|\epsilon_0| = \left|W_k(-2J\rho e^{-2J\rho}e^{i\mu})\right|^T|\epsilon_T|.$$

Note that $|z| \geq |\mathrm{Im}(z)|$ for any complex number z. As can be seen in Fig. 4 in Ref. [100], $|\mathrm{Im}(W_k)| > 2\pi$ for $|k| > 1$, and hence $|\epsilon_0| > (2\pi)^T|\epsilon_T|$, which diverges as $T \to \infty$. It thus follows that for $|k| > 1$ all fixed points are unstable. All that remains now is the $|k| = 1$ branches. For these branches the imaginary part may be zero, but the real part is then strictly less than -1 (except when actually at the branch point), and so for this region $|W_{\pm 1}| \geq |\mathrm{Re}(W_{\pm 1}) \geq 1$, hence $|\epsilon_0| \to \infty$ and so for values of $-xe^{-x}e^{i\mu}$ such that we are

in this region of the complex plane the fixed point is unstable. For $\mathrm{Re}(W_{\pm 1}) > -1$ the smallest the values can be are those lying on the curve separating the ± 1 branches from the zero branch, which are given by $\eta \cot \eta + i\eta$, for $\eta \in (-\pi, \pi)$; hence $|W_{\pm 1}| \geq \eta^2 + \eta^2 \cot^2 \eta = (\eta / \sin \eta)^2$, which is strictly greater than 1 (except, again, at the branch point), and hence $|\epsilon_0| \to \infty$ as $T \to \infty$.

Thus, the principal branch is the only branch which corresponds to a stable fixed point of Eq. (D.7). We may now continue our derivation by inserting the principal branch solution into our integral:

$$P(S) = \int_{-\pi}^{\pi} \frac{d\mu}{2\pi} e^{-i\mu S} e^{i\lambda^*} = \int_{-\pi}^{\pi} \frac{d\mu}{2\pi} e^{-i\mu S} e^{-W(-2J\rho \exp[-2J\rho] \exp[i\mu])} e^{i\mu} e^{-2J\rho}.$$

From the definition of the Lambert-W function, $e^{-W(z)} = W(z)/z$, giving

$$\int_{-\pi}^{\pi} \frac{d\mu}{2\pi} e^{-i\mu S} e^{2J\rho} \frac{W(-2J\rho e^{-2J\rho} e^{i\mu})}{-2J\rho e^{i\mu} e^{-2J\rho}} e^{i\mu} e^{-2J\rho} = -\int_{-\pi}^{\pi} \frac{d\mu}{(2\pi)(2J\rho)} e^{-i\mu S} W(-2J\rho e^{-2J\rho} e^{i\mu}).$$

The (modulus of the) argument of W_0 has maximum value $1/e$; hence the series expansion for it will converge for all values of $2J\rho$. Inserting the series expansion into the integral we have

$$\begin{aligned} P(S) &= -\int_{-\pi}^{\pi} \frac{d\mu}{(2\pi)(2J\rho)} \, e^{-i\mu S} \sum_{k=1}^{\infty} \frac{(-k)^{k-1}}{k!} (-2J\rho^{-2J\rho})^k e^{ik\mu} \\ &= -\frac{1}{2J\rho} \sum_{k=1}^{\infty} \frac{(-k)^{k-1}}{k!} (-2J\rho^{-2J\rho})^k \int_{-\pi}^{\pi} \frac{d\mu}{2\pi} \, e^{-i\mu(S-k)}, \end{aligned}$$

where swapping the integral and summation will at worst leave us with an asymptotic series, but is in fact perfectly valid as the series is uniformly convergent on any disk within the radius of convergence of the series. This can be shown by the Weierstrass M-test:

Consider a disk in the complex plane of radius R, centered at the origin. We need to find an M_n such that each term in the series is less than or equal to it:

$$\left| \frac{(-n)^{n-1}}{n!} z^n \right| \leq M_n.$$

Because on the disk $|z| \leq R$ we may set

$$M_n = \frac{n^{n-1}}{n!} R^n.$$

The Weierstrass M-test then states that if $\sum_{n=0}^{\infty} M_n$ converges, the original series is uniformly convergent. We can show this is the case for $R < 1/e$ by the ratio test (essentially the same computation that shows the radius of convergence of the series is $1/e$:

$$\lim_{n\to\infty} \frac{M_{n+1}}{M_n} = \lim_{n\to\infty} R\left(1+\frac{1}{n}\right)^{n-1} \to Re.$$

This converges if $R < 1/e$, and hence because $|z| < R$, the series is uniformly convergent for any z arbitrarily close to $1/e$ (which means any value of $2J\rho$ arbitrarily close to 1).

Having established this fact, we now return to our calculation. The integral has reduced to a Kronecker $\delta_{S,k}$, and hence the sum collapses to

$$\begin{aligned} P(S) &= -\frac{1}{2J\rho}\frac{(-2J\rho e^{-2J\rho})^S(-S)^{S-1}}{S!} \\ &= \frac{1}{2J\rho S}\frac{(2J\rho S e^{-2J\rho})^S}{S!} \\ &= \frac{(2J\rho e^{-2J\rho})^S}{2J\rho S}\frac{S^S}{S!}. \end{aligned}$$

So far our calculation has been exact: what is written above is the exact distribution function (up to normalization). We know make use of an approximation. The last line is a cosmetic rewrite to facilitate this next step, the use of the asymptotic Stirling Formula, which states that for large S,

$$S! \simeq \sqrt{2\pi S}\frac{S^S}{e^S} \Rightarrow \frac{S^S}{S!} \simeq \frac{e^S}{\sqrt{2\pi S}},$$

and so

$$P(S) \simeq \frac{(2J\rho e^{-2J\rho})^S}{2J\rho S}\frac{e^S}{\sqrt{2\pi}S^{1/2}},$$

giving

$$P(S) \sim \frac{1}{S^{3/2}}(2J\rho)^{S-1}e^{-S(2J\rho-1)}. \tag{D.13}$$

The critical point is defined as being when $2J\rho = 1$, at which point we have a power law with exponent

$-3/2$. This expression also gives the scaling function close to the critical point. Let $t = 2J\rho - 1$. Then

$$(2J\rho)^{S-1}e^{-S(2J\rho-1)} = (t+1)^{S-1}e^{-St} = e^{-St+(S-1)\ln(1+t)}.$$

Because $S \gg 1$, $S-1 \simeq S$, and noting that near the critical point $t \ll 1$, we find $-St+S(t-t^2/2) \simeq -St^2/2$. Thus, close to the critical point,

$$P(S) \sim \frac{1}{S^{3/2}}e^{-St^2/2}, \tag{D.14}$$

a result previously obtained by other methods [59, 98, 99].

Appendix E

Thermal-dependence of magnetization hysteresis loop shapes

E.1 Introduction

In the previous chapter, I studied the non-equilibrium random field Ising model (RFIM) at zero temperature. The lack of thermal fluctuations prevents any spins from randomly flipping; the spin motion is entirely deterministic, and the only randomness is introduced via the local random fields, which are quenched in time. In a real magnet, experiments done at low enough temperatures, such that thermal fluctuations are very unlikely to cause any magnetic domain flips, are well described by the zero-temperature RFIM. However, it would of course also be interesting to study the hysteretic properties of magnets at higher temperatures. While experiments at higher temperatures are relatively easy to do, non-equilibrium models at non-zero temperatures are quite difficult!

Nonetheless, in this chapter we relax the zero-temperature approximation and consider the effects of fluctuations on a random field Ising magnet. Similarly, we might also consider the effects of quantum fluctuations, as might occur if our spins were true quantum spins. The introduction of fluctuations introduces an interesting competition into the model. The energy landscape of the RFIM contains many metastable states. In the zero-temperature RFIM, as the magnet is driven by an external magnetic field, the system will always remain in a local metastable. However, if fluctuations are present, the system can be "knocked" from one metastable state into another (either via thermal activation or quantum tunneling). Given a long enough time, the system could even reach the global metastable energy minimum - the ground state. That is to say, the system can *equilibrate*, which it cannot do at zero temperature (or without quantum fluctuations). If we sweep the magnetic field too slowly, we expect the fluctuations to have time to equilibrate the system, before it is driven out of equilibrium again by the external field. However, if we sweep the magnetic field quickly, the fluctuations will not have time to equilibrate the system. We anticipate that this competition between the magnetic field sweeprate and fluctuations will give rise to interesting scaling behavior in the magnetization

hysteresis loop in many RFIM-like systems. The work presented in this chapter is a phenomenological model of the scaling behavior of the magnetization in the presence of thermal fluctuations and a non-adiabatic sweeprate.

This work is based on some preliminary results developed by Robert White in his thesis [101]. I formalized some of his arguments and rough calculations, and introduced an analysis of quantum fluctuations to complement the analysis of thermal fluctuations. I also began developing a set of microscopic spin models which include thermal and quantum fluctuations. My preliminary work developing these quantum random field Ising models are presented in appendices F and G. The work presented in this chapter is to be submitted to Physical Review Letters[1].

I begin this chapter with a review of the equilibrium properties of the random field Ising model. In particular, we discuss how the energy barriers between metastable states scale in the model. I then review some surprising connections between the equilibrium and non-equilibrium avalanche statistics in the RFIM, and discuss the possibility of a crossover between equilibrium and out-of-equilibrium dynamics at the system is driven in the presence of an external magnetic field. Following this review, I present a set of arguments to derive a phenomenological scaling relation for the magnetization as a function of sweeprate and temperature (or transverse field strength, if we are considering quantum fluctuations).

E.2 Developing the scaling theory

The goal of the scaling theory is to describe the crossover from the strongly non-equilibrium regime to the fully equilibrated regime near the critical point. We will do so by introducing temperature (or quantum) fluctuations into the non-equilibrium calculation, and at the same time a finite sweeprate, Ω for the external driving force. For low sweeprates, the fluctuations will tend to cause the system to equilibrate, while high sweeprates will result in non-equilibrium and hysteretic behavior. By tuning Ω, we can explore the crossover between the two extremes, the pure equilibrium random field Ising model and the zero-temperature random field Ising model. At fixed temperature, but for progressively lower sweeprates, we expect the hysteresis loop to become smaller and smaller, asymptotically attaining a universal shape at low enough sweeprates. The tails of these hysteresis loops will match the equilibrium magnetization curve. In the limit of zero frequency, the hysteresis loop shrinks to a point, and equilibrium is expected at all values of the external magnetic field.

[1]This work is to be submitted for publication as: B.A.W. Brinkman, R.A. White, J.P. Sethna, J.T. Uhl, E. Carlson and K.A. Dahmen, "Temperature Effects on Hysteresis with Crackling Noise" (2013). [102]

On the other hand, if the temperature is taken to zero before the sweeprate is taken to zero, we will only observe non-equilibrium behavior.

E.2.1 Magnetization curves for finite field sweeprate

The Hamiltonian for the equilibrium random field Ising model is

$$\mathcal{H} = -\sum_{\langle i,j \rangle} J_{ij} s_i^z s_j^z - \sum_i (H + h_i) s_i^z. \tag{E.1}$$

This is largely the same at the non-equilibrium model: J_{ij} is a coupling between spins at sites i and j, s_i^z is the value of the z-component of the spin at site i, h_i is the local random magnetic field at site i, and H is a global magnetic field. The only difference between the equilibrium and non-equilibrium models is the field H, which is a function of time in the non-equilibrium model, which we take to be $H(t) = H_0 + \Omega t$. As $\Omega \to 0$, at a non-zero temperature T, we expect the non-equilibrium model to "equilibrate" to the equilibrium model.

As before, the random fields are assumed to be drawn from a Gaussian distribution $\rho(h_i)$ of variance R^2,

$$\rho(h_i) = \frac{1}{\sqrt{2\pi}R} \exp\left(-\frac{h_i^2}{2R^2}\right). \tag{E.2}$$

As in the regular Ising model, in equilibrium there is a ferromagnetic-paramagnetic transition at particular critical temperature. In the equilibrium random field Ising model, this temperature is a function of the disorder, R. In fact, one can view this transition as being disorder controlled: as the disorder is tuned, there is a phase transition at a temperature-dependent disorder, $R_c^{eq}(T)$. The fundamental features of the phase transition are actually controlled by a "zero-temperature" critical point. This means that the observed critical exponents and scaling functions are equal to those given by the zero-temperature theory. This also holds true for the phase transition that occurs in the non-equilibrium theory. In principle, the critical exponents in the equilibrium and non-equilibrium models could be different. Although it turns out that in the RFIM this is not the case [69], we will denote the non-equilibrium exponents with a subscript "n". Exponents lacking a subscript will refer to the equilibrium exponents. The phase diagrams for the equilibrium and zero-temperature non-equilibrium are given in Fig. E.1.

As the temperature T approaches the ferromagnetic transition temperature $T \to T_c(R)$ the correlation length ξ of the equilibrium state grows as $\xi \sim (T - T_c(R))^{-\nu} \Xi(H/(T - T_c(R))^{\beta\delta})$ [72], where Ξ is a universal

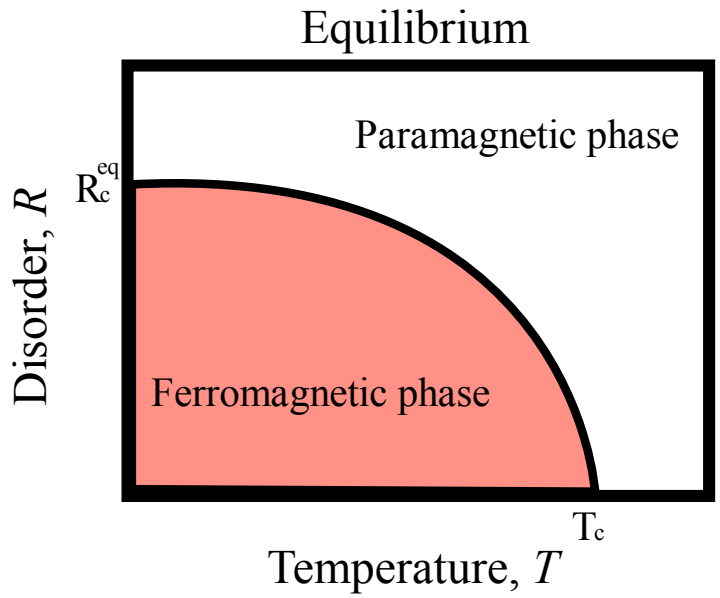

(a) Equilibrium phase diagram

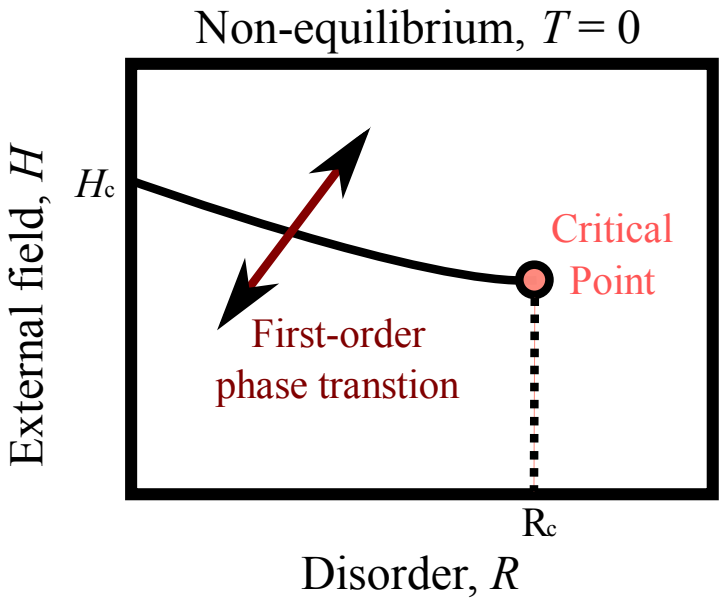

(b) Non-equilibrium phase diagram

Figure E.1: Phase diagrams of the equilibrium and non-equilibrium random field Ising models. (a) In the equilibrium model, a critical R-T curve separates a paramagnetic phase and a ferromagnetic phase. Near this curve, the critical behavior is controlled by a zero temperature fixed-point at R_c^{eq} with a critical external field $H_c = 0$ by symmetry. (b) In the zero-temperature, non-equilibrium model, there is a critical point at $R = R_c$ and field $H = H_c$ (not necessarily zero), which is characterized by scaling in the magnetization, for example. Below the critical disorder, the non-equilibrium model undergoes a first-order phase transition at $H_c(R)$.

scaling function. The energy barriers to equilibrium scale as $E \sim \xi^\theta$ [72], where θ is the violation of hyperscaling exponent [72, 103]. The time τ to get over these energy barriers by thermal activation is given by $\tau = \tau_0 \exp(cE/k_BT)$ where k_B is Boltzmann's constant, τ_0 is some characteristic activation time and c is some constant [72].

If the system is driven by an external magnetic field $H(t) = H_0 + \Omega t$, then in some small window of the magnetic field, ΔH, the system will equilibrate if the amount of time the system spends in that window is greater than the mean relaxation time during the window. That is, at a given field H_0, if

$$\frac{1}{\Delta H}\int_{H_0}^{H_0+\Delta H} dH\ \tau(H) \leq \int_{H_0}^{H_0+\Delta H} dH \frac{dt}{dH}, \tag{E.3}$$

then the system has enough time to equilibrate in the window $[H_0, H_0 + \Delta H]$. Here, we have used the fact that $\int dt = \int dH(dt/dH)$. The field at which the system no longer has enough time to equilibrate is when we have equality. In the limit $H_0 \gg \Delta H$, Eq. (E.3) reduces to $\tau(H_0) \approx \Delta H dt/dH$. Since $dH/dt = \Omega$, we thus find that

$$\tau(H_0) \approx \frac{\Delta H}{\Omega}. \tag{E.4}$$

If the system is initialized with $H(-\infty) = -\infty$, then the system will start near equilibrium at H is increased. Hence, until the field reaches the value at which it no longer has enough time to equilibrate in the small ΔH windows, the system is always close to equilibrium, and the energy barriers back into the equilibrium state scale as $E \sim \xi^\theta$. Since the system is close to equilibrium, the equilibrium scalings hold, hence for fields $H \to 0$, ξ scales as $|H|^{-\nu/(\beta\delta)}$. We thus have $\tau(H) \approx \tau_0 \exp(c|H|^{-\nu\theta/(\beta\delta)}/k_BT)$, and solving Eq. (E.4) for the field H_0 gives $|H_0|^{-\nu\theta/(\beta\delta)} \sim k_BT \log(\Delta H/(\Omega\tau_0))$, or

$$|H_{neq}| \sim (-k_BT \log(\Omega))^{-\frac{\beta\delta}{\nu\theta}}, \tag{E.5}$$

where we relabel H_0 by H_{neq}, the field at which the system falls out of equilibrium. We have also dropped the constant $\Delta H/\tau_0$ from this equation, as it does not contribute to the scaling[1]. This scaling is only valid when $|H_{neq}|$ is close to zero (otherwise $\xi \sim |H|^{-\nu(\beta/\delta)}$ does not hold); hence we see that for fixed T, we must have $\Omega \to 0$ in order for $|H_{neq}| \to 0$.

The analysis applies to increasing and decreasing external magnetic field $dH/dt = \pm\Omega$. As the field

[1]The argument of the logarithm should be $\Omega\tau_0/\Delta H$ in order to be dimensionless, but the constant is often dropped in scaling equations for convenience.

is increased (decreased) from $H = -\infty$ ($H = -\infty$), and falls out of equilibrium at $-|H_{neq}|$ ($+|H_{neq}|$), hysteresis develops and the magnetization changes sharply at a coercive field $+|H_c|$ ($-|H_c|$). The value of the coercive field depends on the history of the system. For the given initial conditions, the particular history is determined by the temperature and sweeprate, in addition to the disorder. Hence, $|H_c| = |H_c(R, T, \Omega)|$. The width of the hysteresis loop is thus approximately $2|H_c|$. As we will argue below, in the $\Omega \to 0$ limit, $|H_{neq}| \sim |H_c|$, so the loop scales as $2|H_{neq}|$.

E.2.2 Irrelevance of temperature in the hysteresis loop regime

At $T = 0$, the coercive field $|H_c|$ is a finite value for any Ω. However, at $T > 0$, it must be the case that $|H_c(R, T, \Omega)| \to 0$ as $\Omega \to 0$, as for very slow sweeprates the system has enough time to equilibrate, and in equilibrium $H_c = 0$. By time reversal symmetry of the system, we expect $|H_c| < |H_{neq}|$. We assume that as $\Omega \to 0$, $|H_{neq}| \approx c|H_c|$. Near $|H_c|$ the non-equilibrium statistics emerge, as the equilibration time near $|H_c|$ is much longer than Ω^{-1}. Because the system is controlled by a zero-temperature fixed point, we assume that in the non-equilibrium regime the statistics correspond to the previously studied zero temperature non-equilibrium RFIM. The magnetization in the zero temperature RFIM is

$$m \sim h^{1/\delta_n} \mathcal{M}\left(\frac{h}{|r|^{\beta_n \delta_n}}\right),$$

where $m = M(H, R) - M_c(H_c, R)$, $h = H - |H_c|$, and $|r| = |R - R_c|/R$. The subscript n on the critical exponents denotes that they are non-equilibrium exponents. As mentioned earlier, it turns out that they are equal to the equilibrium exponents in the RFIM [69], but this is not generally expected. To incorporate finite temperature into the scaling form for the magnetization, we note that when H is close to $|H_c| \sim |H_{neq}|$, it must scale as $(-k_B T \log \Omega)^{-\beta\delta/(\nu\theta)}$. We may hence generate a new Widom scaling form by adding $H/(-k_B T \log \Omega)^{-\beta\delta/(\nu\theta)}$ as an argument to the scaling function $\mathcal{M}$. For $|H| \gtrsim |H_c|$, we may set $|H_c| \approx 0$ in our scaling form. Noting that $M_c(|H_c| \approx 0, R) \approx 0$, we finally find the finite temperature, low sweeprate scaling for the magnetization to be

$$\begin{aligned} M(R, H, T, \Omega) \quad &\sim \quad (-k_B T \log \Omega)^{-\frac{\beta}{\nu\theta}\frac{\delta}{\delta_n}} \\ &\quad \times \widetilde{\mathcal{M}}\left(\frac{H}{(-k_B T \log \Omega)^{\beta\delta/(\nu\theta)}}, \frac{H}{r^{\beta_n \delta_n}}\right). \end{aligned} \tag{E.6}$$

where $\widetilde{\mathcal{M}}(x,y)$ is a new scaling function. Finally, we note that the discontinuous jump, ΔM, in the hysteresis loop scales the same way as the magnetization M.

E.2.3 Power spectra

We now consider the power spectrum of the Barkhausen noise that would be observed at finite temperatures and sweep-rates. The Barkhausen noise is the noise from induction voltage measurements of the system due to the change in magnetization as H increases. At finite temperatures the equilibrium noise and non-equilibrium noise contribute independently to the power spectrum:

$$\begin{aligned} P(\omega) &= \left(\int_{-\infty}^{-|H_{neq}|} + \int_{+|H_{neq}|}^{\infty}\right) dH\ P_{eq}(\omega, H) \\ &\quad + \int_{-|H_{neq}|}^{|H_{neq}|} dH\ P_{neq}(\omega, H). \end{aligned}$$

The equilibrium contribution to the power spectrum is approximately $P_{eq}(\omega)(1-2|H_{neq}|)$, where $P_{eq}(\omega) = \int_{-\infty}^{\infty} dH P_{eq}(\omega, H) \sim k_B T\omega$ [101]. The $-2|H_{neq}|P_{eq}(\omega)$ contribution comes from the missing H range of the integral, noting that $P_{eq}(\omega, H=0) \approx P_{eq}(\omega)$. We estimate the non-equilibrium contribution to the power spectrum as the power spectrum of the hysteresis loop for an adiabatic, zero temperature RFIM system scaled down to the size of the non-equilibrium portion of the loop in the power spectrum presently under consideration. The frequency, disorder and field dependence of the power spectrum is $\omega^{1/(\sigma_n\nu_n z_n)} f(\omega^{-1/(\nu_n z_n)}|r|, h/|r|^{\beta_n\delta_n})$, where $h = H - H_c$, for some scaling function $f(x)$. Using Parseval's theorem, we expect that the normalized power spectrum will scale as the square of the total change in magnetization over the hysteresis loop, $|\Delta M|^2$. Hence, putting everything together, we find

$$\begin{aligned} P(\omega) &\sim 2(-k_B T \log\Omega)^{-\frac{\beta\delta}{\nu\theta}\left(1+\frac{2}{\delta_n}\right)} \\ &\quad \times \omega^{-2/(\sigma_n\nu_n z_n)} f^2(\omega^{-1/(\nu_n z_n)}|r|) \\ &\quad + k_B T\omega(1 - 2(-k_B T\log\Omega)^{-\frac{\beta\delta}{\nu\theta}}). \end{aligned} \tag{E.7}$$

Because the non-equilibrium and equilibrium power spectra contribute separately to the overall power spectrum, Eq. (E.7), we expect the experimental observations will yield two frequency regimes, one when the non-equilibrium behavior dominates, and one when the equilibrium behavior dominates, with a cross-over

regime near some frequency ω_c corresponding to when the two contributions to $P(\omega)$ are roughly equal. We cannot in general solve for this frequency; however, if we approach the critical point $R = R_c$ (from above, as for $R < R_c$ the hysteresis loops are discontinuous and Eq. (E.7) does not apply), then the $f(r/\omega^{1/(\nu_n z_n)})$ term is just a constant, and we find

$$\omega_c(R = R_c) \sim \left[\frac{1}{k_B T} \frac{2(-k_B T \log \Omega)^{-\frac{\beta\delta}{\nu\theta}(1+\frac{2}{\delta_n})}}{1 - 2(-k_B T \log \Omega)^{-\frac{\beta\delta}{\nu\theta}}} \right]^{\frac{\sigma_n \nu_n z_n}{1+\sigma_n \nu_n z_n}} \tag{E.8}$$

E.3 Dipolar Fields

It is well known that existence of dipolar forces in Eq. (E.1) changes the dynamics (and hence the universality class) of the system [77, 78, 80]. Hysteresis is no longer due to domain nucleation, but domain wall motion. The scaling theory of this paper thus will not apply to systems in which dipolar forces are comparable to the exchange coupling between spins. However, a theory of hysteresis in magnets with dipolar interactions has previously been developed by Lyuksyutov *et al.* [104].

E.4 Transverse Quantum Field

Another interesting and important addition to Eq. (E.1) is a transverse field term $\Gamma \sum_i s_i^x$, which enables quantum tunneling between states. [83–85] Intuitively, one expects quantum tunneling to have similar effects to thermal activation: at zero temperature and finite sweep rate the system may equilibrate due to tunneling events between metastable states. We thus expect similar results to the scaling theory described above to hold at zero temperature, finite transverse field Γ and finite sweeprate. Studies of the equilibrium random field transverse Ising model (RFTIM) [83] suggest that relaxation from nearby metastable states to equilibrium scales roughly as $\exp(c\xi^{\psi_Q})$, for some exponent ψ_Q, which is not necessarily equal to θ. We thus conjecture that our results hold for the quantum case as well, with different quantum exponents β_Q, β_{nQ}, δ_Q, δ_{nQ}, etc, and making the replacements $k_B T \to \Gamma$ and $\theta \to \psi_Q$.

E.5 Experiments

The RFIM is applicable to many different systems [1], including ferromagnets, fluids, elastic charge density waves [105] nematics [106–108]. We thus expect our results to apply to all of these systems, as long as

there are no demagnetizing fields present (or as long as such fields are negligible). Previous experiments that measure disorder-induced transitions in hysteretic magnetic systems may be able to measure the scaling behavior predicted by the RFIM. [109, 110]

Some experimental systems, such as $LiHo_xY_{1-x}F_4$ have the convenient feature that the disorder R may be tuned by applying a transverse magnetic field [81,111]; however, such systems typically have strong dipolar interactions which cannot be eliminated using sample geometry. Accordingly, our theory is not expected to apply to such systems. It may be possible to experimentally test the dipolar scaling theory of Lyuksyutov *et al.* [104] using $LiHo_xY_{1-x}F_4$, an anisotropic ferromagnet that exhibits dipolar-RFIM behavior in the presence of a transverse magnetic field [81, 111]. Unfortunately, in the temperature and transverse field regimes for which $LiHo_xY_{1-x}F_4$ exhibits RFIM-like behavior, the dipolar interactions are necessarily stronger than the random fields, even in geometries which might otherwise minimize the dipolar interactions. Hence the RFIM without dipolar interactions cannot be used to study this material.

E.6 Conclusions

I have presented theoretical results for the scaling behavior of hysteretic systems in the RFIM universality class at finite temperatures. The scaling theory is valid at slow sweep-rates and non-zero temperatures, and presents a first look at the behavior of RFIM systems as they are driven out of thermal equilibrium. Analogies between thermal activation and quantum tunneling suggest that these results may also be applicable to the random field transverse Ising model.

Looking beyond the phenomenological scaling model proposed here, I have begun developing some microscopic models which capture the behavior of the RFIM in the presence of fluctuations. In Appendix F I present a model of a single spin coupled to a thermal bath, which qualitatively reproduces the expected competition between sweeprate and thermal fluctuations predicted by the scaling theory presented in this chapter. In Appendix G, I present the beginnings of a full lattice model which includes thermal and quantum fluctuations (at least to a semiclassical level). However, in the thermodynamic limit in which the number of spins in the lattice tends to infinite, the barriers to equilibrium become infinite. Studying the sweeprate competition in this lattice model at the mean field level will require a more complicated spin structure than has presently been studied.

Appendix F

The soft-spin boson model

F.1 Introduction

In Appendix E, we developed a phenomenological model of the competition between magnetic field sweeprate and thermal or quantum fluctuations in magnetic systems. If possible, we would like to develop an effective microscopic model in which we can study these same effects more thoroughly.

To this end, I developed some initial formulations of the random field Ising model with thermal or quantum fluctuations. These models are the focus of both this and the following appendix. In this appendix, to build our intuition and study sweeprate effects, we will study a single spin coupled to a bath of quantum harmonic oscillators in equilibrium at temperature T. The spin is driven by an external magnetic field and is not in a steady state. In the next appendix, Appendix G, I study a lattice of spins. However, as will be argued and explained later, sweeprate effects may not be observable in the $N \to \infty$ limit unless we consider spins with many components.

Both the single spin model and the lattice model are based off the soft-spin random field Ising model studied by Dahmen [56, 59]. In Dahmen's RFIM, the "hard" Ising spins, which take only values $s = \pm 1$, are replaced with "soft" spins, which take any value on the real line, $(-\infty, \infty)$. These soft spins can be thought of as effective coarse-grained hard spins. However, we would still like the soft-spins to retain an Ising-like character, so we introduce to the models a double-well potential $V[s]$ which constrains the soft-spins to taking values close to ± 1. The use of soft spins is much more amenable to a path-integral formulation than hard spins.

In this appendix, I introduce the single spin Hamiltonian and effective action. For clarity of presentation, the details of how to derive the effective action from the Hamiltonian will be reserved for Appendix G. The derivation in Appendix G is done for a lattice; the single spin action follows as a special case. I then show that the average spin dynamics can be found as the solution of a stochastic differential equation. In

the classical limit ($\hbar \to 0$), this equation can be mapped to a Fokker-Planck equation for the probability distribution of the values which the spin s takes, as a function of time. I will show that the average spin value as computed from this probability distribution exhibits hysteresis-loop shrinking as the temperature is increased, relative to the sweeprate. The quantum case is more challenging, and is yet to be solved.

F.2 The soft-spin boson model

The Hamiltonian for a single soft-spin in the presence of a bath of harmonic oscillators is

$$\mathcal{H} = \frac{\dot{\sigma}^2}{2g} - V[\sigma(t)] + H(t)\sigma(t) + \sigma(t)\sum_{i=1}^{N_b} C_i x_i + \sum_{i=1}^{N_b} \frac{1}{2} M_i \left[\dot{x}_i^2 + \omega_i^2 x_i^2\right]. \tag{F.1}$$

Here, $\sigma(t)$ is the value of our spin at time t and $\dot{\sigma}$ is its time derivative. The potential $V[\sigma]$ constrains σ's value to remain close to ± 1, and the external field $H(t)$ drives the spin. The spin is coupled to the harmonic oscillators, x_i, with coupling strength C_i. There are N_b harmonic oscillators, each with their own mass M_i and frequency ω_i.

The first term in Eq. F.1 is a kinetic term, which is not present in the classical soft-spin RFIM [56,59]. A kinetic term introduces inertia in the system, while we typically are only interested in over-damped dynamics. However, if are interested in quantum fluctuations, we need to introduce a term that will not commute with $\sigma(t)$, as it is non-commuting terms in the Hamiltonian which generate quantum fluctuations and allow for tunneling. For a real Ising spin system, we would introduce a transverse field term, but we are not able to do so with a soft spin. We thus follow other works on quantum spin glasses which introduce a kinetic term, $\dot{\sigma}^2/2g$, in lieu of a transverse field term [112].

The second term in Eq. F.1 is a double-well potential of the form $V[\sigma] = (V/2)(\sigma - \mathrm{sgn}(\sigma))^2$ or $V[\sigma] = (V/4)(\sigma^2 - 1)^2$; i.e., a piece-wise quadratic potential or a quartic potential. Both choices are characterized by a potential strength V. The function $\mathrm{sgn}(x)$ is the signum function, which returns the sign of x. Both choices have their advantages and disadvantages. The quartic potential is smooth and easier to work with both analytically and numerically, but will introduce high-order terms into the action that we must neglect in a semi-classical approximation in order to make progress. The piece-wise potential will not force us to neglect any terms, but is not suitable for the numerical analyses to be described in section F.6. Plots of the two choices of potential are shown in Fig. F.1.

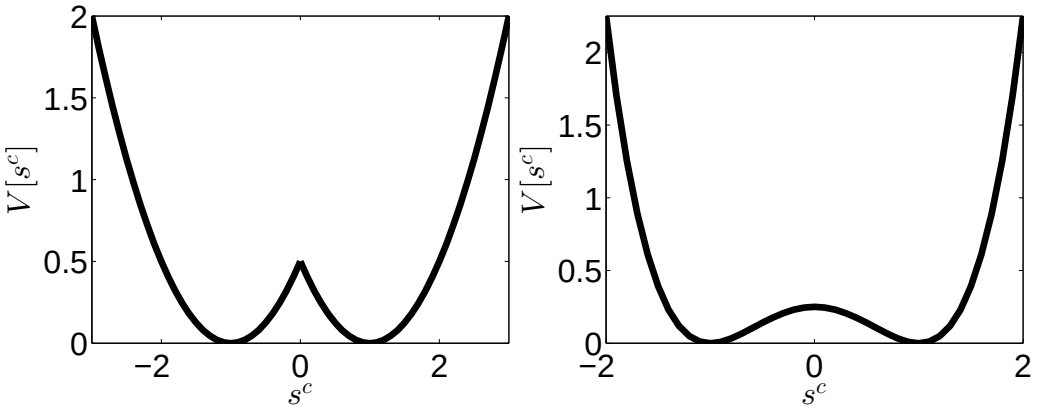

(a) $V(s^c) = (s^c - \mathrm{sgn}(s^c))^2$ (b) $V(s^c) = ((s^c)^2 - 1)^2$

Figure F.1: Plots of two choices of double-well potential which localize the soft-spin to values nears $s^c = \pm 1$. (a) The piecewise quadratic potential. (b) The quartic potential. The advantages and disadvantages of each form are discussed in the main text. Here, s^c is the classical component of the spin field, defined precisely in Sec. F.3.

The third term in Eq. F.1, $H(t)\sigma(t)$, is a simple driving term that couples the spin to the external field $H(t)$. Given that there is only one spin, any random field terms can be absorbed into $H(t)$.

The fourth term, $\sigma(t)\sum_{i=1}^{N_b} C_i x_i$, is a coupling between the spin and the harmonic oscillator bath. We have chosen a linear coupling, though more general couplings could also be considered [112].

The last sum in Eq. F.1 is the Hamiltonian of the harmonic oscillator bath. In deriving the effective action of the system, we will take the number of oscillators to ∞. In order to have a well-behaved thermodynamic limit, we will have to specify the frequency spectrum of the oscillators. Ideally, the spectrum would scale as ω^α, where $\alpha = 1$, $\alpha < 1$ and $\alpha > 1$ correspond to Ohmic, sub-Ohmic, and super-Ohmic dissipation, respectively [112]. However, the frequency spectrum cannot support arbitrarily large frequencies, and must be cutoff at some frequency Λ to have a sensible thermodynamic limit. A typical choice is to impose a spectrum [112]

$$I(\omega) = \frac{\gamma}{\pi}\omega\left(\frac{\omega}{\Lambda}\right)^{\alpha-1}\exp\left(-\frac{|\omega|}{\Lambda}\right), \tag{F.2}$$

where γ sets the strength of dissipation from the spin system to the bath. In this work I study only the case of Ohmic dissipation, $\alpha = 1$, as it is the simplest case and allows for many of the following calculations to be done analytically (e.g., calculating forms of the noise and dissipation kernels, $\nu(t)$ and $\eta(t)$, respectively, to be introduced below, is more difficult for sub- or super-Ohmic dissipation).

F.2.1 Connection to other spin-boson models

Before I present the effective action of this model, I should comment on the name, the "soft-spin boson model". The case of a single (hard) spin (or two-level system) coupled to a bath of harmonic oscillators is not a new problem, and several variations of the problem have been previously studied [113–118]. See Ref. [113] for a review of the initial work on two level systems coupled to a bath. Refs. [114] and [115] in particular study the driven spin-boson model using real two-level spins. The authors do not appear to study hysteresis, and instead focus on calculating the probability that the spin remains in its initial state at later times. One could perhaps adapt their results to study hysteresis; however, the soft-spin approach developed in this chapter is designed to be scaled up to study a lattice of spins. A lattice of interacting spins is much more difficult to study if we use true hard (two-level) spins rather than the continuous spins studied here.

Nonetheless, because the model I study in this appendix is effectively a dissipate two-state system, I have thus adopted the name "soft-spin boson model" and applied it to this model of a soft-spin coupled to an oscillator bath. The purpose of this study will be to determine whether or not the hysteresis loop shrinks as the temperature is increased relative to the sweeprate, as predicted by the model of Appendix E. Although the predictions of Appendix E are ostensibly for a lattice of spins, I believe the soft-spin boson model is a good simple system for understanding the qualitative dynamics of a full lattice model, as the average value of $\sigma(t)$ at any give time is analogous to the magnetization of a lattice model. The single-spin model, however, will fail to capture any critical properties of the lattice model, which require a thermodynamically large spin system.

F.3 Soft-spin boson model effective action

I now present the effective action for the soft-spin boson model. The details of how to derive the action are given in Appendix G, in which it is done for N spins. Note that, for technical reasons made clear in Appendix G, the spin $\sigma(t)$ has been replaced with two fields, $s^c(t)$ and $s^q(t)$, which represent the classical and quantum contributions to the spin field. The ultimate quantities of interest in this model are the averages $\langle s^c(\tau)\rangle$ and $\langle s^c(\tau)s^c(\tau')\rangle$ - i.e., the average classical spin field value, which is analogous to the magnetization, and the two-point correlation function of the value of the spin at different times during its dynamics. Using a path integral formalism with the effective action S_{eff}, below, we can derive equations of motion for these averages.

The effective action is

$$\begin{aligned}\frac{i}{\kappa}\mathcal{S}_{eff} &= -\frac{1}{2}\int_{-\infty}^{\infty} d\tau d\tau' s^q(\tau)[2\kappa\nu(\tau-\tau')]s^q(\tau') \\ &\quad +i\int_{-\infty}^{\infty} d\tau s^q(\tau)\left[-m^{-1}\partial_\tau^2 s^c(\tau)+\int_{-\infty}^{\infty} d\tau'\mu(\tau-\tau')s^c(\tau')+H(\tau)-\frac{\partial V[s^c(\tau)]}{\partial s^c(\tau)}\right]. \quad \text{(F.3)}\end{aligned}$$

Here, κ, τ, τ', and m are non-dimensionalized constants and parameters given by $\kappa = \hbar/\gamma$, $\tau = (V/\gamma)t$ (and similarly for τ'), and $m = \gamma g/V$. The functions $\mu(\tau)$ and $\nu(\tau)$ are the dissipation and noise kernels, respectively. They are given by

$$\mu(\tau) = \int_0^{\infty} dx\ \tilde{I}(x)\sin(x\tau) \quad \text{(F.4)}$$

and

$$\nu(\tau) = \int_0^{\infty} dx\ \tilde{I}(x)\coth\left(\frac{\beta V\kappa x}{2}\right)\cos(x\tau). \quad \text{(F.5)}$$

The function $\tilde{I}(x)$ is a non-dimensionalized version of Eq. (F.2), $I(x) = \gamma\tilde{I}(x)$. Note that these integrals would not converge if we did not set a frequency cutoff for the spectrum $\tilde{I}(x)$. The parameter β is the usual inverse temperature, $\beta = 1/k_BT$. The functions $\mu(\tau)$ and $\nu(\tau)$ take special forms in the classical ($\kappa \propto \hbar \to 0$) and zero-temperature ($\beta \to \infty$) limits. We will discuss these later in sections F.6 and F.8.

As written, Eq. (F.3) appears to be quadratic in $s^q(\tau)$, the quantum contribution to the spin field. This is only true if the potential V is the piece-wise quadratic potential or if we neglected terms of order $(s^q)^3$ or higher produced by the quartic choice of the potential. From this point forward, we will assume that if we are using the quartic potential, all terms of order higher than quadratic have been discarded (amounting to a semi-classical approximation [119]).

As we are only considering terms quadratic in the field $s^q(\tau)$, we could now complete the square in the action, as preparation for computing averages such as $\langle s^c(\tau)\rangle$ or $\langle s^c(\tau)s^c(\tau')\rangle$. However, we are going to take a slightly different approach which amounts to the same thing in the end, but will make clear the connection between these averages and stochastic differential equations.

F.4 Computing averages from the path integral formalism

Suppose we want to calculate the average of some quantity $\mathcal{O}$. Some quantities of interest experimentally or in simulations could be $s^c(\tau)$, $s^q(\tau)$, $s^c(\tau)s^q(\tau')$, etc. In a path integral formalism, we would compute this average as [120]

$$\langle \mathcal{O} \rangle = \frac{\int \mathcal{D}s^c \mathcal{D}s^q \ \mathcal{O} \exp\left[-\frac{1}{2}\int d\tau d\tau' s^q(\tau) A(\tau-\tau') s^q(\tau') + i\int d\tau B(\tau) s^q(\tau)\right]}{\int \mathcal{D}s^c \mathcal{D}s^q \exp\left[-\frac{1}{2}\int d\tau d\tau' s^q(\tau) A(\tau-\tau') s^q(\tau') + i\int d\tau B(\tau) s^q(\tau)\right]}, \tag{F.6}$$

where $A(\tau-\tau')$ represents the quadratic coupling kernel (equal to $2\kappa\nu(\tau-\tau')$ in our model) and $B(\tau)$ contains terms dependent on the classical spin field, $s^c(\tau)$. In full,

$$B(\tau) = -m^{-1}\partial_\tau^2 s^c(\tau) + \int_{-\infty}^{\infty} d\tau' \mu(\tau-\tau') s^c(\tau') - \frac{\partial V[s^c(\tau)]}{\partial s^c(\tau)} + H(\tau). \tag{F.7}$$

Because we have neglected quantum field terms terms of order $(s^q)^3$ or higher [119], the effective action is quadratic in $s^q(\tau)$, so we could attempt to compute these integrals by completing the square in $s^q(\tau)$. However, to make a connection to stochastic differential equations, we will instead introduce a field $\zeta(\tau)$ by a Hubbard-Stratonovich transformation [121–123]. This will make our action linear in *both* s^c and s^q, at the expense of introducing a term quadratic in our new field $\zeta(\tau)$.

If we assume that the kernel $A(\tau-\tau')$ has a symmetric inverse $A^{-1}(\tau,\tau')$, then we may write [120]

$$\exp\left[-\frac{1}{2}\int d\tau d\tau' \ s^q(\tau) A(\tau,\tau') s^q(\tau')\right] \propto \int \mathcal{D}\zeta \exp\left[-\frac{1}{2}\int d\tau d\tau' \zeta(\tau) A^{-1}(\tau,\tau')\zeta(\tau') - i\int d\tau \zeta(\tau) s^q(\tau)\right]. \tag{F.8}$$

As promised, the transformation has rendered our action linear in s^q. Our average is hence

$$\langle \mathcal{O} \rangle = \frac{\int \mathcal{D}\zeta \mathcal{D}s^c \mathcal{D}s^q \ \mathcal{O} \exp\left[-\frac{1}{2}\int d\tau d\tau' \zeta(\tau) A^{-1}(\tau,\tau')\zeta(\tau') + i\int d\tau (B(\tau)-\zeta(\tau)) s^q(\tau)\right]}{\int \mathcal{D}\zeta \mathcal{D}s^c \mathcal{D}s^q \exp\left[-\frac{1}{2}\int d\tau d\tau' \zeta(\tau) A^{-1}(\tau,\tau')\zeta(\tau') + i\int d\tau (B(\tau)-\zeta(\tau)) s^q(\tau)\right]}. \tag{F.9}$$

Note that the proportionality factor from the Hubbard-Stratonovich transformation cancels out from the numerator and denominator. It is now quite easy to calculate averages.

For example, let $\mathcal{O} = s^q(\tau)$. Integration over s^q is analogous to a Fourier integral $\int dx \ x \exp(ikx)$, and will yield a functional delta function derivative, "$\delta'(B(\tau)-\zeta(\tau))$". Because the rest of in the integrand is independent of s^c, doing the s^c integral will result in zero, giving $\langle s^q(\tau)\rangle = 0$. If, on the other hand, we

choose $\mathcal{O} = s^c(\tau)$, then integrating over s^q first yields a delta function $\delta(B(\tau) - \zeta(\tau))$, giving

$$\langle s^c(\tau)\rangle = \frac{\int \mathcal{D}\zeta \mathcal{D}s^c s^c(\tau) e^{-\frac{1}{2}\int d\tau d\tau' \zeta(\tau) A^{-1}(\tau,\tau')\zeta(\tau')} \delta(B(\tau) - \zeta(\tau))}{\int \mathcal{D}\zeta \mathcal{D}s^c e^{-\frac{1}{2}\int d\tau d\tau' \zeta(\tau) A^{-1}(\tau,\tau')\zeta(\tau')} \delta(B(\tau) - \zeta(\tau))}. \tag{F.10}$$

In performing the s^c integral, the delta function forces $s^c(\tau)$ to be the solution of $B(\tau) - \zeta(\tau)$; i.e., $s^c(\tau)$ must satisfy the equation

$$m^{-1}\partial_\tau^2 s^c(\tau) - \int_{-\infty}^{\infty} d\tau' \mu(\tau - \tau') s^c(\tau') + \frac{\partial V[s^c(\tau)]}{\partial s^c(\tau)} + \zeta(\tau) = H(\tau). \tag{F.11}$$

Doing the final integration over the auxiliary field ζ means that $\langle s^c(\tau)\rangle$ is the solution of Eq. (F.11) averaged over ζ. We can show that ζ is in fact random noise term, meaning Eq. (F.11) is a stochastic equation for $s^c(\tau)$. I will show later that this equation indeed reduces in a certain limit to a purely differential equation. First, I demonstrate that $\zeta(\tau)$ can be interpreted as a random noise term by calculating its average and two-point correlation.

To calculate the average, we can take $\mathcal{O} = \zeta(\tau)$ [1]. Integrating over $s^q(\tau)$ gives a delta function $\zeta(\tau) = B(\tau)$. We can then change variables from $s^c(\tau)$ to $B(\tau)$. This should only introduce a constant Jacobian[2], which will cancel out of the equation. We can then integrate over $B(\tau)$ to find $\langle\zeta\rangle = \langle B\rangle = 0$. Similarly, if we take $\mathcal{O} = \zeta(\tau_1)\zeta(\tau_2)$, the delta function again forces $\zeta = B$, giving a quadratic action for $B(\tau)$. Changing variables from $s^c(\tau)$ to $B(\tau)$ again and performing the integrals, and we find $\langle\zeta(\tau_1)\zeta(\tau_2)\rangle = \langle B(\tau_1)B(\tau_2)\rangle = A(\tau_1 - \tau_2)$. That is, $\zeta(\tau)$ is a random noise term with zero average and correlation function $A(\tau_1 - \tau_2)$.

F.5 The adiabatic limit

At this point, it is useful to take a step back and consider a simpler case: the noiseless (zero temperature, classical), adiabatic limit. Thus far we have been implicitly assuming that $H(\tau)$ is increased at a finite, non-infinitesimal rate. For the moment, we will suppose instead that it is increased adiabatically. The noiseless limit is achieved by first taking the classical limit $\kappa \to 0$ ($\hbar \to 0$), and then setting the temperature to zero. We must take the classical first, as taking the temperature to zero first will leave us with temporally-correlated

[1] Although we originally wrote the equation for $\langle\mathcal{O}\rangle$ before introducing ζ, we could have introduced ζ earlier, so it is no problem to do this.

[2] This is not obvious, and in fact I have not rigorously proven it to be the case. However, Kleinert [119] shows that the Jacobian for a similar system is indeed constant, and so I assume that the result will also hold for my system. It seems like one should be able to prove the result by a similar time-slicing argument as used by Kleinert. See also Appendix G, in which I calculate the averages in a similar manner, without introducing $\zeta(\tau)$. I further discuss some of these issues then.

quantum noise that does not reduce to a delta function (i.e., white noise) as $\kappa \to 0$.

The result is that the spin, $s^c(\tau)$, is dragged along by the slowly increasing magnetic field $H(\tau)$, such that

$$(s^c(\tau))^3 - s^c(\tau) = \frac{H(\tau)}{V}, \tag{F.12}$$

where we have assumed we are using the quartic potential, $V[s^c] = (V/4)((s^c)^2 - 1)^2$, which gives rise to the $(s^c)^3$ term. Eq. (F.12) can be derived from Eq. (F.11) by neglecting the $\partial_\tau^2 s^c$ and $\int d\tau' \mu(\tau - \tau') s^c(\tau')$ terms, which is valid in the noiseless, over-damped limit.

If we consider H as a function of s^c and plot this equation, we find we have a cubic equation with three zeros and the asymptotic behaviors $H \to \pm\infty$ as $s^c \to \pm\infty$. A graph of s^c as a function of H is then achieved by mirroring this plot over the $H = s^c$ line. However, in doing so there will be a region in the center of the plot that now corresponds to an unstable state, as shown in Fig. F.2. If we start the system off at $H = -\infty$ and increase it, $s^c(\tau)$ will start at $-\infty$ and increase until it reaches the point at which $\partial s^c / \partial H = \infty$ (corresponding to the maximum of the $H(s^c)$ curve. Because $s^c(H)$ must remain a function, it cannot turn back, and so must jump up to the stable solution above it, before it continues to increase. The same thing occurs if we start with $H = +\infty$ and decrease the field: we eventually reach a field, dubbed the coercive field, at which the solution becomes unstable to the branch solution below it, and we get another jump. Our solution for s^c thus exhibits hysteresis, as expected for the classical, zero temperature system.

The question we want to answer now is, what happens when we add back in the noise (thermal or quantum)? In particular, if we average $s^c(\tau)$ over the noise, what does the resulting $\langle s^c \rangle$ vs. H curve look like? Suppose we take the temperature to be nonzero, $T \neq 0$ [3], but stay in the adiabatic limit. The noise has no associated timescale. Because we are in the adiabatic limit, the system spends an extraordinary long time at any field H - long enough for essentially any sized fluctuation to occur. This means that at any point on the s^c vs. H curve the system will have enough time to "nucleate" a fluctuation that knocks the spin up past the unstable branch of the hysteresis curve, sending it to the upper hysteresis branch well before the coercive field would do so. The size of the fluctuation needed to knock the spin into one metastable state from the other depends on which state the spin is initially in, except at $H = 0$, at which point we expect the rate at which a spin is knocked into the lower branch from the upper branch is equal to the rate at which a

[3] Or $\kappa \neq 0$

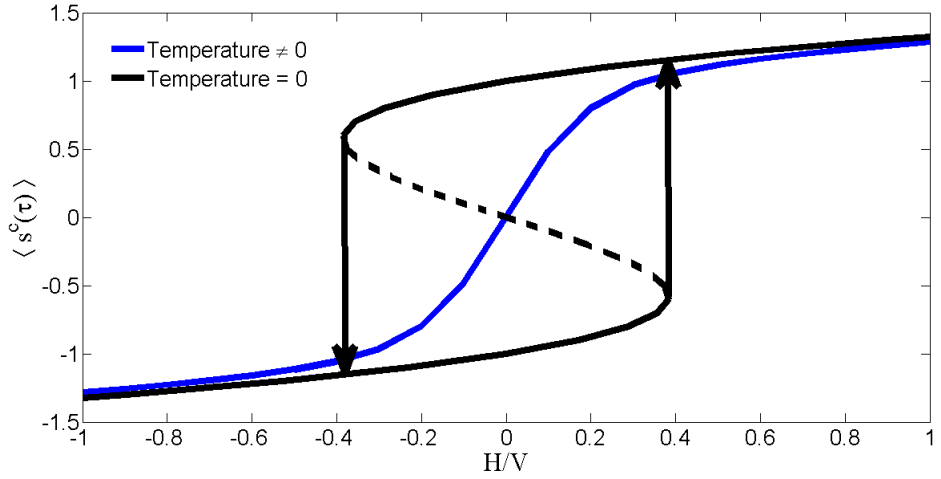

Figure F.2: The average value of the soft-spin (the "magnetization", for simplicity), $\langle s^c(\tau)\rangle$, in the adiabatic limit ($\tilde{\Omega} \to 0$). If temperature is taken to zero before the sweeprate $\tilde{\Omega}$, the magnetization exhibits hysteresis as a function of the applied magnetic field H (black curve). The zero-temperature curve is solved for exactly by inverting Eq. (F.12). The dashed portion of the curve represents the unstable part of the hysteresis curve: if the magnetic field is initially negative (positive), then at the turn-around point the magnetization will jump along the arrow to the higher (lower) branch. However, if the temperature in the system is non-zero, then hysteresis is entirely eliminated if the sweeprate is adiabatic (blue curve). This indicates that at non-zero temperatures and adiabatic sweeprates, the spin equilibrates with the oscillator bath. The equilibrium curve is computed using Eq. (F.16).

spin is knocked into the upper branch from the lower branch. At any other point where the two metastable states coexist, one branch is more favored than the other because the size of fluctuations needed to knock into the other state are different in the different directions. Hence, if we average over all realizations of this experiment, we expect the average curve $\langle s^c\rangle$ to exhibit no hysteresis: there is only a single, smooth curve, as seen in Fig. F.2. This indicates that the spin has equilibrated with the oscillator bath.

Accordingly, we expect that we need a non-infinitesimal sweep-rate $\tilde{\Omega}$ in order to observe any hysteresis in $\langle s^c\rangle$ in the presence of noise. Note that any single observation s^c over the course of a closed magnetic field sweep will exhibit hysteresis; it's the hysteresis in the noise-averaged s^c curve that will be washed out.

So, what we would ultimately like to understand is the competition between the sweep-rate $\tilde{\Omega}$ and the noise. A finite sweep-rate will require consideration of the derivative and integral terms in Eq. (F.11). Studying this problem in general is difficult. I will thus first study the pure-thermal problem, which is amenable to some analytic analyses, but which we will ultimately still need to solve numerically. I will also discuss the pure-quantum problem and the mixed quantum and thermal problem, though these problems

have not yet been resolved.

F.6 The classical thermal soft-spin boson model

In the classical limit, $\kappa \to 0$ ($\hbar \to 0$), we can safely take the frequency cutoff of the bath spectrum to $\Lambda \to \infty$. In these limits, the dissipation and noise kernels take on particularly simple forms:

$$\lim_{\Lambda\to\infty} \lim_{\kappa\to 0} \mu(\tau) = \delta'(\tau)$$

and

$$\lim_{\Lambda\to\infty} \lim_{\kappa\to 0} 2\kappa\nu(\tau) = 4k_B T\delta(\tau).$$

Because the noise kernel reduces to a delta function, the field $\zeta(\tau)$ has become uncorrelated white noise. Similarly, because the dissipation kernel has reduced to the derivative of a Dirac delta function, the term $\int d\tau' \mu(\tau - \tau') s^c(\tau')$ reduces to a simple time derivative. If we neglect the inertial term in Eq. (F.11), our equation of motion for the classical spin field $s^c(\tau)$ becomes

$$\frac{ds^c(\tau)}{d\tau} - \frac{\partial V[s^c(\tau)]}{\partial s^c(\tau)} + H(\tau) = -\zeta(\tau). \tag{F.13}$$

This is a stochastic differential equation for $s^c(\tau)$. Written in formal, rigorous notation, it reads

$$ds^c_\tau = \left[-\frac{\partial V[s^c(\tau)]}{\partial s^c(\tau)} + H(\tau)\right] d\tau - \sqrt{4k_B T} dW_\tau, \tag{F.14}$$

where dW_τ is a Brownian white noise process with $dW_\tau^2 = d\tau$. (i.e., W_τ is a normalized noise term, such that the $4k_BT$ appears explicitly in the stochastic differential equation). I assume that the stochastic differential equation is written in the Ito interpretation [4].

Because our stochastic differential equation is driven (due to the $H(\tau)$ term), solving it analytically is difficult, if not impossible. A numerical approach is more appropriate. If we directly numerically integrate Eq. (F.14) for several sets of normally distributed random numbers for dW_τ, we could then average the resulting solutions to construct $\langle s^c(\tau)\rangle$, a numerical estimate of the path integral average. We could similarly

[4] It is this interpretation that Kleinert [119] uses to show that the Jacobian determinant in the path integral is constant, so we assume the same interpretation here for consistency.

numerically calculate the two-point correlation function $\langle s^c(\tau)s^c(\tau')\rangle$. An Euler integration is sufficient for this purpose.

However, we can actually do better than this. It is a well-know result that stochastic differential equations of the form of Eq. (F.14) can be mapped to a partial differential equation for the *entire distribution* function $\rho(s^c,\tau)$ of the values that s^c takes on at time τ. From the distribution function, we could then compute any moment of $s^c(\tau)$. However, to use this mapping we must restrict ourselves to smooth potentials, meaning we will choose the quartic double well potential $V[s^c] = (V/4)((s^c)^2-1)^2$ in the following. (Direct numerical integration of Eq. (F.14) does have the advantage that we may use either the quartic or piecewise quadratic forms of $V[s^c]$).

The partial differential equation that Eq. (F.14) can be mapped to is

$$\frac{\partial\rho(x,\tau)}{\partial\tau} = -\frac{\partial}{\partial x}\left(\left\{-\frac{\partial V(x,\tau)}{\partial x} + H(\tau)\right\}\rho(x,\tau)\right) + \sigma^2\frac{\partial^2\rho(x,\tau)}{\partial x^2}, \tag{F.15}$$

where $\sigma^2 = 4k_BT$ and we write $x = s^c(\tau)$ for brevity. This is an example of a Fokker-Planck equation (which is formally equivalent to the Schrodinger equation). Again, due to the explicit time dependence of the equation, it is very difficult to solve this equation analytically. A multi-scale approximation method may give some analytical results, but for simplicity we will solve this equation numerically.

However, first, we consider the steady state solution in the adiabatic limit ($\tilde{\Omega}\to 0$), as we will use its form for the initial boundary data in our numerical solution of Eq. (F.15).

In the adiabatic limit, $\partial\rho/\partial\tau = 0$, and we can integrate Eq. (F.15) over x. The integration constant is zero, as ρ and its derivative must vanish as $x\to\infty$. This gives a simple equation to solve,

$$\sigma^2\frac{\partial}{\partial x}\rho_{ss}(x) = -\left(x^3 - x - H_0\right)\rho_{ss}(x),$$

where $\rho_{ss}(x)$ is the steady state solution. This equation is easily integrated to obtain

$$\rho_{ss}(x) \propto \exp\left[-\frac{x^4/4 - x^2/2 - H_0x}{\sigma^2}\right], \tag{F.16}$$

where the constant of proportionality is given by the integral

$$\int_{-\infty}^{\infty} dx\ \exp\left[-\frac{x^4/4 - x^2/2 - H_0x}{\sigma^2}\right].$$

In our numerical solution, we cannot solve the equation over the entire real line in the time domain or the position (spin) domain. We will instead have to solve it on a domain $[-T, T] \times [-X, X]$, for some large time T and largest position X. We will need to approximate the solution to Eq. (F.15) on the $-T$ boundary. We will do so using Eq. (F.16), making the replacement $H_0 \to H_0 - \Omega T$. This will not produce a perfect numerically accurate solution near $\tau = -T$, but as long as the bulk of the approximate boundary solution's area occurs within $[-X, X]$, it will provide a decent solution at later times.

Eq. (F.15) is a diffusion-type partial differential equation. In order to numerically integrate this and generate a numerically stable solution, it is best to use a Crank-Nicholson method [124]. We discuss the numerical solution below.

F.6.1 Crank-Nicholson numerical solution of the Fokker-Planck equation for the probability density of the value of the spin s^c at time τ

The Crank-Nicholson method is a numerically unconditionally stable method for solving diffusion-type partial differential equations of the form

$$\frac{\partial u}{\partial \tau} = F(\tau, x, \partial_x u, \partial_x^2 u),$$

for a function $u(x, t)$. Numerical stability comes at a price: the Crank-Nicholson method is implicit, meaning the solution $u(x, t)$ at future time-steps depends on both on itself and the value at the current time-step, which will require us to solve a simple matrix equation at each time step of the solution. Fortunately, this can be done relatively efficiently, as will be described below.

The Crank-Nicholson method uses a central-difference approximation scheme, wherein we discretize the time derivative as

$$\frac{\partial u}{\partial \tau} \to \frac{u_i^{n+1} - u_i^n}{\Delta \tau} = \frac{1}{2}\left[F_i^{n+1}((n+1)\Delta\tau, x, \partial_x u, \partial_x^2 u) + F_i^n(n\Delta\tau, x, \partial_x u, \partial_x^2 u)\right],$$

where the index i is the index of the position coordinate (i.e., $x = i\Delta x$, for some position-step Δx) and n is the time index, with Δt the time-step. As such, $u_i^n = u(i\Delta x, n\Delta t)$. For a numerically stable solution without oscillations, we want the time step $\Delta t < \mathcal{O}(\Delta x^2)$ [124].

In our case, the function $F(\tau, x, \partial_x u, \partial_x^2 u)$ is

$$F(\tau, x, \partial_x u, \partial_x^2 u) = \frac{\partial}{\partial x}\left[\left(x^3 - x - H(\tau)\right) u(x,\tau)\right] + \sigma^2 \frac{\partial^2}{\partial x^2} u(x,\tau).$$

Similar to the time derivative central-difference approximation, the first order spatial derivative term in Eq. (F.15) becomes

$$\frac{\partial}{\partial x}\left[\left(x^3 - x - H(\tau)\right) u(x,t)\right] \to \frac{1}{4\Delta x}\left[V_{i+1}^{n+1} u_{i+1}^{n+1} - V_{i-1}^{n+1} u_{i-1}^{n+1} + V_{i+1}^{n} u_{i-1}^{n} - V_{i-1}^{n} u_{i-1}^{n}\right],$$

where

$$V_i^n = -(i\Delta x)^3 + (i\Delta x) + H_0 + \tilde{\Omega} n \Delta\tau.$$

Similarly, the second derivative term in Eq. (F.15) becomes

$$\sigma^2 \frac{\partial^2}{\partial x^2} u(x,\tau) \to \sigma^2 \frac{1}{2\Delta x^2}\left[u_{i+1}^{n+1} - 2u_i^{n+1} + u_{i-1}^{n+1} + u_{i+1}^{n} - 2u_i^{n} + u_{i-1}^{n}\right].$$

Putting all of this together, our partial differential equation, Eq. (F.15), can be rewritten as

$$\begin{aligned} u_i^{n+1} - u_i^n &= -\frac{\Delta\tau}{4\Delta x}\left[V_{i+1}^{n+1} u_{i+1}^{n+1} - V_{i-1}^{n+1} u_{i-1}^{n+1} + V_{i+1}^{n} u_{i-1}^{n} - V_{i-1}^{n} u_{i-1}^{n}\right] \\ &\quad + \frac{\sigma^2 \Delta\tau}{2\Delta x^2}\left[u_{i+1}^{n+1} - 2u_i^{n+1} + u_{i-1}^{n+1} + u_{i+1}^{n} - 2u_i^{n} + u_{i-1}^{n}\right]. \end{aligned} \tag{F.17}$$

Rearranging, and writing $\lambda = \sigma^2 \Delta\tau / (2\Delta x^2)$ and $\alpha = \Delta\tau / (4\Delta x)$, we can write this as

$$(-\lambda + \alpha V_{i+1}^{n+1}) u_{i+1}^{n+1} + (1 + 2\lambda) u_i^{n+1} + (-\lambda - \alpha V_{i-1}^{n+1}) u_{i-1}^{n+1} = (\lambda - \alpha V_{i+1}^{n}) u_{i+1}^{n} + (1 - 2\lambda) u_i^{n} + (\lambda + \alpha V_{i-1}^{n}) u_{i-1}^{n}. \tag{F.18}$$

This is a tri-diagonal matrix equation for u_{i-1}^{n+1}, u_i^{n+1} and u_{i+1}^{n+1} in terms of the values at the previous time-steps, u_{i-1}^{n}, u_i^{n} and u_{i+1}^{n}. This can be solved relatively easily using the tri-diagonal matrix algorithm. A simple implementation in Matlab can be found online [5].

We are now prepared to numerically solve Eq. (F.15).

[5] See `http://en.wikipedia.org/wiki/Tridiagonal_matrix_algorithm`

F.7 Results

We solve Eq. (F.15) with a time-step of $\Delta\tau = 0.001$ and a position-step of $\Delta x = 0.02$. Our total time is $T_{max} = 3000$ and our max position is $X_{max} = 250$. We will solve the system for a number of variances σ^2 (which are proportional to the temperature) and sweep-rates $\tilde{\Omega}$. For simplicity, we will set $H_0 = 0$.

Two plots of the probability density $\rho(s^c, \tau)$ - the probability density for observing the spin with value within $[s^c, s^c + ds^c]$ at time τ, for finite temperature and finite sweeprate $\tilde{\Omega}$. For an upward sweep ($\tilde{\Omega} > 0$), for two values of temperature, which is proportional to σ^2, are given in Fig. F.3. The density at the higher temperature exhibits a wider spread of values of $s^c(\tau)$ that are likely to be observed. In both plots the transition from one of the potential wells into the other is clearly visible.

We can find the path-integral average, $\langle s^c(\tau) \rangle$, by computing $\int_{-\infty}^{\infty} ds^c \; s^c \rho(s^c, \tau)$ numerically. As expected, the resulting averages are different if we initialize $\tilde{\Omega} > 0$ (spin down initially) or $\tilde{\Omega} < 0$ (spin up initially); i.e., the average spin value exhibits hysteresis! Furthermore, the width and height of the hysteresis loop decrease as the temperature is increased relative to the sweeprate, $\tilde{\Omega}$. This qualitatively confirms the predictions of Appendix E. In Fig. F.4, below, we plot the hysteresis loops for $\sigma^2 = 0.16$ versus $\sigma^2 = 10.24$. (Recall that σ^2 is proportional to the temperature). Both loops are performed with a sweeprate of $\tilde{\Omega} = 4$. As seen in the figure, the higher temperature hysteresis loop is smaller than the lower temperature loop, indicating that it is closer to equilibrium.

Although our simulations agree qualitatively with the predictions of the scaling theory presented in Appendix E, we do not expect the actual scaling form predictions to hold in our simulations. This is because the scaling theory predictions apply to a lattice spin system in the thermodynamic limit. Here, I have only modeled a single spin, which is much less than the infinite number of spins required to be in the thermodynamic limit! To quantitatively check the scaling theory predictions with a simulation, we thus need to start with a lattice model. The preliminary formulation of such a model is given in Appendix G.

F.8 Quantum noise

Finally, to end this appendix, I will briefly discuss the case of quantum noise. I will focus on the zero temperature case for simplicity, though the same issues arise in the finite temperature case. Unfortunately, the quantum case is much less tractable than the thermal noise case. This is because, in the present formalism we are using, the quantum noise kernel is much different than the thermal noise kernel. Notably,

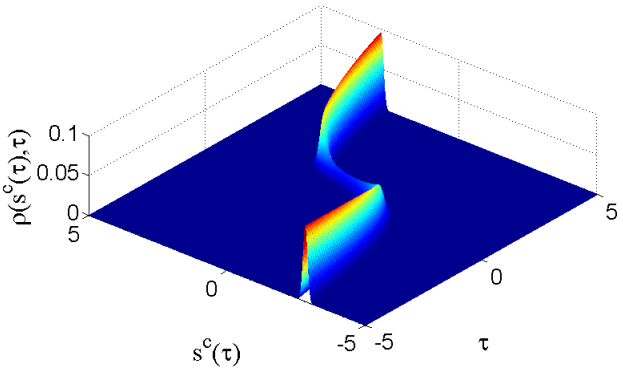

(a) $\sigma^2 = 0.16$

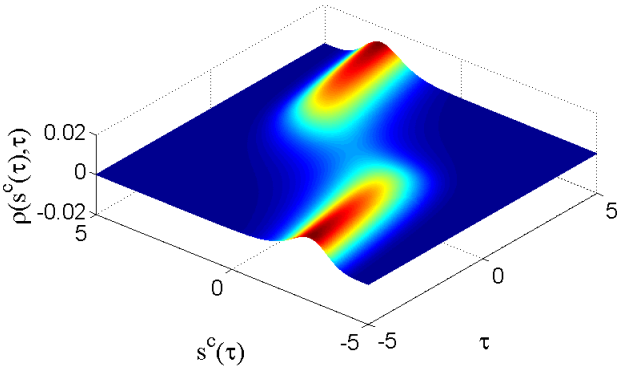

(b) $\sigma^2 = 10.24$

Figure F.3: Plots of the probability density $\rho(s^c, \tau)$, for observing the value of s^c at time τ. The spin begins in the negative well of the double-well potential (set by initializing the system with $\tilde{\Omega} > 0$) and evolves forward in time, eventually transitioning to being most likely in the positive well. In this simulation, I set $\tilde{\Omega} = 4$.

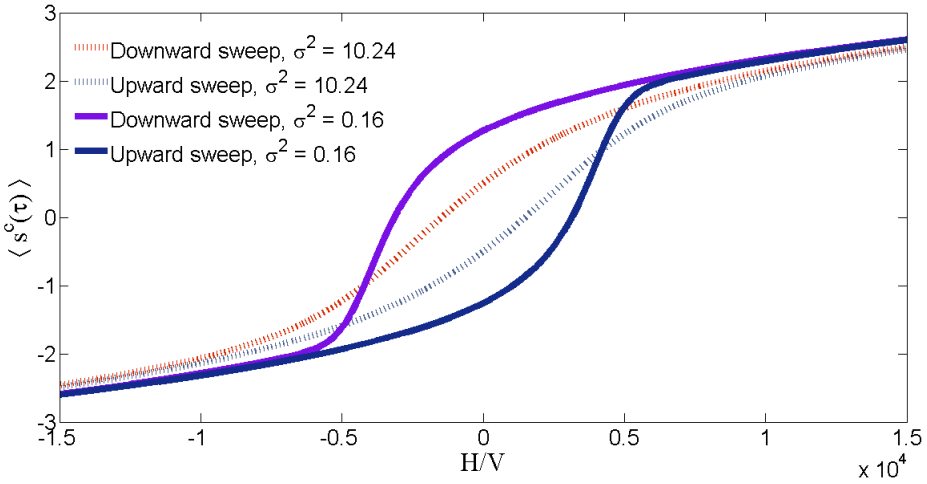

Figure F.4: Hysteresis in the average spin value $\langle s^c(\tau)\rangle$, which is analogous to the magnetization in a lattice spin model. As expected, not only is hysteresis observed, but the size of the hysteresis loop shrinks, in qualitative agreement with the scaling theory presented in Appendix E. In these simulations, $|\tilde{\Omega}| = 4$.

the quantum noise correlations are temporally *long range*, with a component that decays as $1/(\tau - \tau')^2$ at long time differences $\tau - \tau'$. There is no limit other than $\hbar \to 0$ in which the correlations reduce to white noise. The long range correlations introduce numerous severe complications:

1. In the memoryless bath limit ($\Lambda \to \infty$), $\nu(\tau - \tau')$ develops a singular term, $-1/(\tau - \tau')^2$. While the quadratic term in the action, $\int d\tau d\tau' \; s^q(\tau)\nu(\tau - \tau')s^q(\tau') = \int d\tau d\tau' \; s^q(\tau)s^q(\tau')/(\tau - \tau')^2$, can be evaluated as $\int d\tau d\tau' \; (s^q(\tau) - s^q(\tau'))^2/(\tau - \tau')$ as a principal value integral, doing so makes our action non-Gaussian, making computations more difficult. Furthermore, numerical simulations with a singular correlation kernel are not well behaved, suggesting we should not take the memoryless bath limit if we intend on doing numerics. However, it is only in the memoryless bath limit that the dissipation kernel $\mu(\tau - \tau')$ tends to $\delta'(\tau - \tau')$. Thus, if we do not take the memoryless bath limit, we will have a term $\int d\tau' \; \mu(\tau - \tau')s^c(\tau')$ in our equation of motion for $s^c(\tau)$, rather than the first derivative term $-\partial_\tau s^c(\tau)$. This will make numerical solutions much more difficult, as we must solve a stochastic integro-differential equation, rather than a simpler stochastic differential equation.

2. Because the equation of motion is a stochastic integro-differential equation, numerical solution is not simple, as the equation is not local and requires global knowledge of the solution through the integral kernel term $\int d\tau' \mu(\tau - \tau')s^c(\tau')$.

3. Long range correlations are in general a difficult subject, and are not treated in depth by many sources, either analytically or numerically. Analytically, long range correlations prevent a mapping from the stochastic equation of motion to a Fokker-Planck-like equation. This means we must solve the equation of motion itself for different instances of the correlated noise, and average over the solutions. However, correlated noise trains cannot be produced on the fly, meaning we must produce the noise-vector in advance and use a fixed time-step method for numerically solving the stochastic equation.

For these reasons, I will presently leave the treatment of quantum noise in the soft-spin boson model as work to be pursued further in the future.

Appendix G

Developing a quantum random field Ising model

G.1 Introduction

In the previous appendix, I discussed a model of a single spin in contact with a bath of harmonic oscillators in thermal equilibrium. One of the goals of that model was to gain a qualitative understanding of the microscopic physics behind the competition between sweeprate and thermal (or quantum) fluctuations on the non-equilibrium evolution of the spin system, as described by the phenomenological scaling theory presented in Appendix E. The single-spin model qualitatively captures the shrinking of the hysteresis loop as the temperature is increased and the spin equilibrates; however, because there is only a single spin, we cannot quantitatively compare the results to the scaling theory predictions of Appendix E, which are valid only for a thermodynamically large system.

To this end, we would like to consider a lattice of interacting spins. As in the single-spin model, we will introduce thermal and/or quantum fluctuations by coupling the lattice to a bath of harmonic oscillators. This model will essentially be an extension of the classical, zero-temperature model previously studied by Dahmen [59, 125].

Ultimately, we would like to understand the sweeprate-fluctuation competition in this lattice model, and compare the quantitative results to the scaling theory predictions of Appendix E. However, to study this competition, the single-component soft-spins used in the single-spin model of Appendix F may not be appropriate. In the mean field model in the thermodynamic limit, the barriers to equilibration are expected to be infinitely high. To get around these barriers, we may need to study $O(m)$ spins, where m is the number of components of the spins. However, as the formalism to study these spins is quite involved, we will first study the single-component soft-spin lattice. The extension to m-component spins will be left for future work, but will be discussed briefly in section G.5.

In developing the lattice model of single-component soft-spins, I encountered many difficulties, which

also appear in the soft-spin boson model discussed in Appendix F. In fact, the soft-spin boson model was originally developed as an offshoot of the lattice model, intended as a simpler case in which I could more easily study these difficulties [1]. In particular, treating the quantum fluctuations is quite difficult at present. Further difficulties are introduced by the couplings to other spins. In particular, the mean field equations of motion are non-linear, and generally difficult to solve analytically, which impedes the analysis of the model. As a result, the work presented in this chapter is a preliminary foray into the random field Ising model with thermal or quantum fluctuations, and is not complete. It is primarily included in this thesis for posterity, so that I or future students may build off these notes and see to the model's completion in the future.

Development of the model and appendix outline

Before jumping into the details of the model and the subsequent calculations, I would like to give the reader an overview of the development of the model, as a way to motivate the sections of this appendix.

Karin Dahmen, my advisor, original studied the classical, zero-temperature soft-spin random field Ising model (RFIM) using the Martin-Siggia-Rose formalism [59,125] , a set of path integral techniques. I noticed that this formalism was very similar to a formalism my undergraduate research advisor, Malcolm Kennett, had used in his thesis [126] to study a non-equilibrium model of disordered spin-glass dynamics. The technique Kennett used, the Closed-Time-Path or Schwinger-Keldysh formalism, actually reduces to the Martin-Siggia-Rose formalism in the classical ($\hbar \to 0$) limit. It thus appeared to me that I should be able to use the Schwinger-Keldysh formalism to introduce quantum and thermal fluctuations into the random field Ising model and study the effects of these fluctuations on the critical properties and hysteresis in the random field Ising model. Recent experimental realizations of the random field Ising model have studied thermal and quantum features of the model [81,111,127,128], which motivated the development of a quantum RFIM.

I thus decided to develop the quantum RFIM using the Schwinger-Keldysh formalism. Many of the calculations closely followed the calculations done by Dahmen for the classical, zero-temperature model [59,125], due to the close connection between the Schwinger-Keldysh formalism and the Martin-Siggia-Rose formalism. To help familiarize the reader with these techniques, I will briefly discuss them in section G.2. In section G.3, I present the set up of the model using the Schwinger-Keldysh formalism, and proceed to follow Dahmen in expanding the model around the saddle-points of the action (i.e., the mean field expansion). Due

[1] Because the soft-spin boson model only features a single spin, the energy barriers to equilibration will not be infinitely high, unlike the barriers in the infinitely-large mean field lattice model. The soft-spin boson model thus also allowed us to more easily study the sweeprate-fluctuation competition predicted by the scaling theory of Appendix E.

to difficulties encountered while studying the model, I sought to study a simpler version of it in order to better understand the physics. Instead of a lattice of spins, my advisor suggested I focus on the single-spin problem. The result was the soft-spin boson model, introduced in Appendix F. The soft-spin boson model follows as a special case of the lattice model presented here, so the calculations presented in this chapter will fill in the details left out of the previous appendix.

The notes in this appendix go so far as setting up the expansion of the effective action about the mean field solutions. The mean field solutions and some of the expansion coefficients are defined in terms of the solutions of certain integro-differential equations which are extremely not trivial to solve and analyze. Nevertheless, I hope the notes will be of use in the future.

G.2 The Martin-Siggia-Rose and Schwinger-Keldysh formalisms for non-equilibrium, disordered systems

G.2.1 The Martin-Siggia-Rose functional

The Martin-Siggia-Rose formalism was developed to study non-equilibrium, disordered statistical models using a path integral formalism. One of the advantages of this formalism is that disorder averages can be done directly over the generating functional (i.e., the "partition function"). In other formalisms, disorder averages must be done over the log of the generating functional, leading to introducing "replicas" which are harder to work with.

The basic idea of the Martin-Siggia-Rose formalism is to take an equation of motion for a statistical system - for example, an equation of the form $\dot{\phi}_k - F(t, \{\phi_j\}) = 0$, for some set of fields ϕ_j, $j = 1, \ldots, N$ - and introduce a path integral functional

$$\mathcal{Z} = 1 = \int \mathcal{D}\phi \prod_{k=1}^{N} \delta\left(\dot{\phi}_k - F(t, \{\phi_j\})\right).$$

The functional $\mathcal{Z}$ is normalized to 1, and the path-integral Dirac delta function enforces the equation of motion for the fields ϕ_j. The path integral measure is $\int \mathcal{D}\phi \equiv \prod_{j=1}^{N} \int d\phi_j$. By using the Fourier decomposition of the Dirac delta function (and neglecting any infinite constants of proportionality), we can write

$$\mathcal{Z} \propto \int \mathcal{D}\phi \mathcal{D}\hat{\phi} \ \exp\left[i \int dt \ \sum_k \hat{\phi}_k \left(\dot{\phi}_k - F(t, \{\phi_j\}) \right) \right],$$

where we have introduced a set of auxiliary fields $\hat{\phi}_j$, for $j = 1, \ldots, N$. In this form, we can now perform the usual path integral manipulations on our fields ϕ_j and $\hat{\phi}_j$.

As an example, the Hamiltonian for the soft-spin random field Ising model studied by Dahmen [59, 125] is

$$\mathcal{H} = -\sum_{i,j} J_{ij} s_i s_j - \sum_i (H(t) + h_i) s_i + \sum_i V[s_i], \tag{G.1}$$

for a potential $V[s_i] = \frac{V}{2}(s_i - \mathrm{sgn}(s_i))^2$, where $\mathrm{sgn}(s_i)$ returns the sign of s_i. (Recall that the meaning of a "soft" spin is that it takes on any real value from $(-\infty, \infty)$). To study relaxational dynamics, the equation of motion for the soft spins is taken to be

$$\dot{s}_i = -\frac{\delta \mathcal{H}}{\delta s_i},$$

giving the path integral functional

$$\mathcal{Z} \propto \int \mathcal{D}s \mathcal{D}\hat{s} \exp\left[i \int dt \ \sum_i \hat{s}_i \left\{ \dot{s}_i - \sum_j J_{ij} s_j - (H(t) + h_i) s_i + \frac{\delta V[s_i]}{\delta s_i} \right\} \right]. \tag{G.2}$$

This is the starting point for the renormalization group analysis performed by Dahmen [59, 125]. I will later show that the quantum RFIM I introduce reduces to Eq. (G.2) in the classical ($\hbar \to 0$) limit.

G.2.2 The Schwinger-Keldysh path integral

The Keldysh path integral functional is similar to the Martin-Siggia-Rose in that it is automatically normalized to 1, though for (superficially) different reasons. Keldysh realized that the generating functional could be written as the probability for going from some state a, to a state b, then back again to a. If traveling from state a to b covered all of the available state space, then this probability must be 1. That is, the generating function can be written $\mathcal{Z} = |\langle \psi_b | \psi_a \rangle|^2 = \langle \psi_b | \psi_a \rangle \langle \psi_b | \psi_a \rangle^* = 1$, for some transition amplitude $\langle \psi_b | \psi_a \rangle$ from state a to b. As the transition amplitudes can be written as path integrals,

$$\langle \psi_b | \psi_a \rangle = \exp\left[\frac{i}{\hbar} S[\psi]\right],$$

then

$$\mathcal{Z} = \langle \psi_b | \psi_a \rangle \langle \psi_b | \psi_a \rangle^* = \exp\left[\frac{i}{\hbar} S[\psi^+]\right] \exp\left[-\frac{i}{\hbar} S[\psi^-]\right] = \exp\left[\frac{i}{\hbar}\left(S[\psi^+] - S[\psi^-]\right)\right];$$

the cost of writing the path integral in this manner is that the state variable, ψ (which may be a vector of fields), has been duplicated, resulting in two fields, ψ^+ and ψ^-. If we write the actions as integrals over some Lagrangian L,

$$S[\psi^+] - S[\psi^-] = \int_{t_0}^{t_f} dt\ L[\psi^+] - \int_{t_0}^{t_f} dt\ L[\psi^-],$$

we can combine the two time integrals into a single closed contour integral, where the field ψ^+ exists on the forward in time contour from t_0 to t_f and the field ψ^- exists on the backward contour from t_f to t_0. This is where the alternative name of this method, the "Closed Time Path Method", originates.

This construction results in a partition functional $\mathcal{Z}$ that is already normalized, as in the Martin-Siggia-Rose case, meaning we can do disorder averages directly over the functional (as long as the initial state of the system is not correlated with the disorder [112]). However, in this construction we can also deal with quantum fields. The price we paid, however, was a doubling of the degrees of freedom in our system. On the other hand, to develop the Martin-Siggia-Rose functional, an additional set of fields had to be introduced, which also doubled the number of fields to be dealt with (although in a somewhat trivial way). In fact, it turns out that in the classical limit, linear combinations of the fields ψ^+ and ψ^- reduce to the classical fields ϕ_k and $\hat{\phi}_k$. I will demonstrate this later with the quantum RFIM fields.

The Schwinger-Keldysh path integral also provides an easy way to couple a bath to the system, as the bath terms simply appear in the action of the total path integral. The bath terms can be integrated out, as in a Caldeira-Leggett or Feynman-Vernon formalism, resulting in effective non-local interactions between the system variables that give rise to dissipative and noise. In the quantum RFIM, I am interested in the system dynamics, rather than the bath dynamics, so I will integrate out the bath variables.

This will serve as my *very* brief introduction to the Martin-Siggia-Rose and Schwinger-Keldysh methods. Rather than give a lengthy overview of the techniques, I prefer to demonstrate them as I construct the model. For more detailed discussions or examples of the Martin-Siggia-Rose method, see Refs. [129–133]. For more

discussion or examples of the Schwinger-Keldysh method, see Refs. [112, 119, 134, 135].

For studying disordered quantum spin or rotor models specifically, the paper "Real-time dynamics of quantum glassy systems" by Cugliandolo and Lozano [112] is an excellent introduction. In fact, the set up of the quantum RFIM, as described in the following section, closely follows the path laid out by Cugliandolo and Lozano in their paper. They focus on the p-spin spherical model, for which the $p = 2$ case which is similar to the soft-spin model, although in their model the disorder is in the spin exchange coupling bonds J_{ij} and there are no random fields at each site. Furthermore, rather than introduce a potential $V[s_i]$ to keep the soft-spins constrained to be near ± 1, they impose a spherical constraint, requiring $\sum_k s_k^2 = N$, where N is the number of spins on the lattice. This similarly constrains the spins to tend to be near ± 1. I could have similarly used a spherical constraint in developing the quantum RFIM. However, in equilibrium the spherical model is known to produce pathological critical exponents below mean field theory [136]. Because the critical properties of the model are of interest to us, I decided to introduce a potential well, as Dahmen did [59, 125]. This also makes it easier to compare at each step the calculation to Dahmen's classical, zero temperature calculation.

Without further ado, I will introduce the model for the quantum random field Ising model in the next section, and proceed to calculate the saddle-point equations of the action. Expanding around the saddle-point solutions corresponds to an expansion about mean field theory, which I perform in section G.4.

G.3 Setting up the formalism for the quantum random field Ising model

In this (lengthy) section, I will go through the development of the Schwinger-Keldysh path integral formalism for the quantum random field Ising model. This will include a discussion of the bath reservoir, averaging over the random fields, and a change of variables to a set of more "natural" variables which can be interpreted as classical and quantum components of the spin field. I will end this section by showing that the Schwinger-Keldysh formalism for the quantum RFIM reduces to the Martin-Siggia-Rose formalism for the zero-temperature, classical RFIM studied by Dahmen [59, 125].

As given in Cugliandolo and Lozano [112], the generating functional for the doubled-degree of freedom system is

$$\mathcal{Z}[\xi^+,\xi^-] = \int \mathcal{D}\sigma^{\pm}\ \exp\left[\frac{i}{\hbar}\left(S_{sys}[\sigma^+] - S_{sys}[\sigma^-] + S_T[\sigma^+,\sigma^-] + \sum_i \int dt\ \xi_i^+\sigma_i^+ - \sum_i \int dt\ \xi_i^-\sigma_i^-\right)\right],$$

where $\sigma = (\sigma_1, \sigma_2, \ldots, \sigma_N)$, and each sigma may take real values between $-\infty < \sigma < \infty$. The measure $\mathcal{D}\sigma^{\pm}$ is shorthand for $\prod_i \mathcal{D}\sigma_i^+(t)\mathcal{D}\sigma_i^-(t)$. The ξ are source terms, which can be used to compute averages or correlation functions. I will omit in the following.

The action $S_{sys}[\sigma]$ is the system action (on either the upper or lower branch), which contains information about the spins and their interactions which each other. The action $S_T[\sigma^+,\sigma^-]$ is the bath action, which arises by integrating out the harmonic oscillator bath variables. The integration results in the upper-time-branch fields σ^+ coupled with the lower-time-branch fields σ^-; furthermore, the couplings occur at different times. The bath action is thus non-local in time.

I describe the details of these actions in the next two subsections.

G.3.1 System action

The action of the system is

$$S_{sys}[\sigma] = \int_{-\infty}^{\infty} dt\ \left[\sum_i \frac{\dot{\sigma}_i^2}{2g} - \sum_i V[\sigma_i(t)] + \frac{1}{2}\sum_{i=1,j=1}^{N} J_{ij}\sigma_i\sigma_j + \sum_i (H(t)+h_i)\sigma_i\right].$$

This action corresponds to the Hamiltonian of Eq. (G.1), with the exception that an additional kinetic term, $\dot{\sigma}_i^2/2g$, has been added. The significance of this term will be discussed below. First, I will review the meaning of all the terms in the action.

The spins, denoted by σ_i, interact via a coupling term J_{ij}. The coupling could be long-range, short range, anisotropic, etc. For now, I will not specify its form, but in following Dahmen [59, 125] I will later take it to be a simple long range, isotropic coupling in the mean field approximation.

The spins are exposed to a global longitudinal field $H(t) = H_0 + \Omega t$, where H_0 is the value of the magnetic field at time t = 0 and Ω is the rate at which the field is increased. We will take this rate to be rather slow compared to the dissipation timescale γ, defined in the next subsection in which I discuss the bath action $S_T[\sigma^+,\sigma^-]$.

Each spin experiences a random local field h_i. These fields are drawn from a Gaussian distribution, as

in the classical RFIM:

$$\rho(h_i) = \frac{1}{\sqrt{2\pi}R} \exp\left(-\frac{h_i^2}{2R^2}\right).$$

The parameter R, the "disorder", is the width of the distribution and characterizes the energy scale associated with the disordering of the system.

Because we are using soft spins, which take any value on the real line, rather than hard spins which only point up and down, we need some way to define "spin up" and "spin down" in our system to make it more like the hard spin RFIM, in which spins take only discrete values ± 1. The solution is to introduce a double-well potential such that the minima correspond to $\sigma = \pm 1$. Then, spins in the lower well are considered "spin down", while those in the upper minimum are "spin up". The potential is chosen to be

$$V[\sigma_i] = (V/2)(\sigma_i - \mathrm{sgn}(\sigma_i))^2, \tag{G.3}$$

where $\mathrm{sgn}(\sigma_i)$ returns the sign of s_i, as before. This ensures that the σ variables stay close to ± 1, just like the actual hard-spin Ising variables. A spin-flip for the soft-spins is defined to be a spin moving from the minimum of one potential well to the other. In the classical soft-spin RFIM, this piece-wise potential is the appropriate double-well potential to use, as it is the potential produced under coarse-graining. However, there are situations in our upcoming analysis for which a smooth potential is more desirable; hence, we will also consider using a quartic potential,

$$V[\sigma] = \frac{V}{4}(\sigma^2 - 1)^2, \tag{G.4}$$

when convenient. In the classical Martin-Siggia-Rose formalism, the choice of smooth versus piecewise potential did not alter the static critical exponents, but did change some dynamical exponents (the critical exponents associated with time-varying quantities) [59].

We would like the system to initializing start off with all spins point "down" - that is, in the lower well. We achieve this by choosing the initial time to be $t_0 = -\infty$, such that $H(t_0) = -\infty$. In this case, no matter the strength of the random fields, all spins will point down. It is actually not immediately obvious that we can make this choice in the Schwinger-Keldysh formalism. Cugliandolo and Lozano note that for the spin glass system they study, choosing $t_0 = -\infty$ would allow their system to equilibrate, preventing them from studying the non-equilibrium dynamics [112]. However, this is only a concern in the model Cugliandolo

and Lozano study because they are interested in the non-equilibrium relaxation dynamics of the spin glass, whereas in the quantum RFIM model there is an external driving field which can prevent the system from equilibrating. For this reason, it should not be a problem to take $t_0 = -\infty$.

Finally, I discuss the present of the kinetic energy term, $\dot{\sigma}_i^2/2g$, which does not appear in the classical version of the model. This term is introduced because it is proportional to the momentum of σ_i, which of course does not commute with σ_i and thus introduces quantum fluctuations in the spin system. If we were working with a hard spin Ising model, we could include quantum fluctuations in the model by introducing a transverse field term $\Gamma \sum_i \sigma_i^x$, which would commute with spins σ_i^z aligned along the z direction. Because we are using soft-spins, it is not obvious how to introduce such a transverse field term to the problem in order to generate tunneling between metastable states. (Even if we used m-component spins, they would still commute with each other). So, in order to produce quantum fluctuations in our system, I follow Cugliandolo and Lozano by introducing a kinetic term with parameter g, which roughly speaking controls the strength of quantum fluctuations. This term does add inertia to our system; however, we will assume the parameters are constrained in such a way that the dissipative dynamics, rather than the inertial dynamics, dominate the system's behavior.

G.3.2 Bath action

In order to introduce dissipative dynamics to the system, the system is coupled to a bath of harmonic oscillators. The Lagrangian of the bath and the coupling to the spin system is

$$L_{bath} = \sum_{k=1}^{N_b} \left[\frac{1}{2} M_k \dot{x}_k^2 - M_k \omega_k^2 x_k \right] - \sum_{i,k} C_{ik} \sigma_i x_k,$$

where x_k is the position of the kth oscillator, N_b is the number of harmonic oscillators (taken to ∞), M_k is the mass of the kth oscillator, ω_k is the frequency of the kth oscillator and C_{ik} denotes the strength of the coupling between spin i and oscillator k.

Because we are not interested in the dynamics of the bath, we integrate out the oscillator variables. If we assume the oscillators are in equilibrium at inverse temperature β, then we can define the $S_T[\sigma^+, \sigma^-]$ via

$$\exp\left[\frac{i}{\hbar} S_T[\sigma^+, \sigma^-]\right] \propto \int \mathcal{D}x^+ \mathcal{D}x^- \langle x^+ | \hat{\rho}(t_0) | x^- \rangle \exp\left[\frac{i}{\hbar} \int_{t_0}^{t_f} dt\ L_{bath}\right],$$

where $\langle x^+|\hat{\rho}(t_0)|x^-\rangle$ is the matrix element of the density matrix between harmonic oscillators at the initial time t_0, which we again take to be $t_0 = -\infty$. For a bath of harmonic oscillators initially in equilibrium, the density matrix is simply the Boltzmann weight at inverse temperature β.

The result of integrating out the bath variables produces an effective Feynman-Vernon term of the form [112]

$$S_T[\sigma^+,\sigma^-] = -\int dt \int dt' \, \{[\sigma^+(t)-\sigma^-(t)]\eta(t-t')[\sigma^+(t')+\sigma^-(t')]+i[\sigma^+(t)-\sigma^-(t)]\nu(t-t')[\sigma^+(t')-\sigma^-(t')]\}. \tag{G.5}$$

This action couples both spins on different time contours and of different times. Hence, it is a non-local coupling.

The noise and dissipative kernels ν and η are given by

$$\nu(t-t') = \int_0^\infty d\omega I(\omega)\coth\left(\frac{\beta\hbar\omega}{2}\right)\cos[\omega(t-t')], \tag{G.6}$$

and

$$\eta(t-t') = -\Theta(t-t')\int_0^\infty d\omega \; I(\omega)\sin[\omega(t-t')], \tag{G.7}$$

where $\Theta(\tau-\tau')$ is the Heaviside step function.

The function $I(\omega)$ is the spectral density of the bath, given by

$$I(\omega) = \sum_{k=1}^{N_b}\delta(\omega-\omega_k)\frac{(\sum_i C_{ik})^2}{2M_k\omega_k}. \tag{G.8}$$

In the thermodynamic limit of the bath reservoir, the density of oscillator frequencies approaches a continuous density, allowing us to replace this function by a smooth function. Ideally, we want $I(\omega) \sim \omega^\alpha$, but this will not give convergent integrals for ν and η. As such, we need to impose a frequency cutoff, Λ, for the spectrum of the bath. Specifically, we will choose the spectrum to be

$$I(\omega) = \frac{\gamma}{\pi}\omega\left(\frac{\omega}{\Lambda}\right)^{\alpha-1}\exp\left(-\frac{|\omega|}{\Lambda}\right). \tag{G.9}$$

As mentioned in Appendix F, $\alpha < 1$, $\alpha = 1$, and $\alpha > 1$ correspond to the cases of sub-Ohmic, Ohmic, and

super-Ohmic dissipation. In this work, I focus only on the case of Ohmic dissipation.

I have now assembled the necessary pieces for studying the quantum random field Ising model. However, before proceeding further, I will take some time to non-dimensionalize the model, so that we will deal in only dimensionless parameters.

G.3.3 Non-dimensionalization of time and energy scales

I have mentioned that the Schwinger-Keldysh path integral will reduce to the Martin-Siggia-Rose path integral in the classical limit, $\hbar \to 0$. Similarly, to compare to the classical, zero-temperature RFIM model by Dahmen, we would also like to be able to take the zero temperature limit. It is important to note that the order of these limits matters: taking the zero-temperature before the classical limit will result in persistent noise fluctuations.

To be able to sensibly take the classical or zero-temperature limits, we should take care to properly non-dimensionalize our variables. It turns out the problem has a natural action scale, γ, which sets the dissipation scales. The typical energy-scale in the problem will be some characteristic spin-spin coupling J, from which we can construct a time-scale γ/J. We non-dimensionalize all the timescales in the problem by this timescale, which will give us a dimensionless parameter $\kappa = \hbar/\gamma$ which we can take to zero to recover the classical limit. (If we try to non-dimensionalize the time in terms of some other timescale, we will find we cannot take a proper dimensionless limit to recover the classical action; hence, γ/J is the proper timescale to normalize by).

We thus non-dimensionalize by changing variables in the time integrals to $\tau = (J/\gamma)t$ and the frequency integrals in the noise and dissipation kernels $\omega = (\gamma/J)x$. Similarly, the magnetic field sweeprate is written in dimensionless form as $\tilde{\Omega} = (\gamma/J^2)\Omega$.

Non-dimensionalizing the system-action is simple, and we find

$$\frac{i}{\hbar}\mathcal{S}_{sys} = i\frac{\gamma}{\hbar}\sum_i \int_{-\infty}^{\infty} d\tau \left\{ \frac{1}{2m}\frac{\partial^2 \sigma_i}{\partial \tau^2} + \frac{1}{2}\sum_j J^{-1} J_{ij}\sigma_i\sigma_j + (H(\tau)/J + h_i/J)\sigma_i - J^{-1}V[\sigma_i] \right\},$$

where we have defined the dimensionless (inverse) mass

$$m = \frac{\gamma g}{J}.$$

We similarly change time variables to non-dimensionalize the bath action. The two time integrals give factors of $(\gamma/J)^2$ for both kernels, which will be canceled out by changing variables in the frequency integral in each kernel:

$$\left(\frac{\gamma}{\hbar}\right)^2 \nu(t-t') = \gamma\left(\frac{\gamma}{\hbar}\right)^2\left(\frac{\hbar}{\gamma}\right)^2 \int_0^\infty dx \tilde{I}(x) \coth\left(\frac{\beta J \kappa x}{2}\right)\cos[x(\tau-\tau')] \equiv \gamma\nu(\tau-\tau'),$$

and

$$\left(\frac{\gamma}{\hbar}\right)^2 \eta(t-t') = -\gamma\left(\frac{\gamma}{\hbar}\right)^2\left(\frac{\hbar}{\gamma}\right)^2 \Theta(\tau-\tau') \int_0^\infty dx\ \tilde{I}(x)\sin[x(\tau-\tau')] \equiv \gamma\eta(\tau-\tau'),$$

where we have also removed the dimensions from spectrum: $\tilde{I}(x) = \gamma I(\omega)$, giving an extra factor of γ out front overall, and such that $\tilde{I}(x)$ is given by

$$\tilde{I}(x) = \frac{1}{\pi} x \exp\left(-\frac{|x|}{X}\right), \tag{G.10}$$

where the factor γ/J is absorbed into the frequency cutoff: $\Lambda = (J/\gamma)X$.

The full bath action is then

$$\frac{i}{\hbar}S_T[\sigma^+,\sigma^-] =$$
$$\frac{\gamma}{i\hbar}\int d\tau d\tau'\ \{[\sigma^+(\tau)-\sigma^-(\tau)]\eta(\tau-\tau')[\sigma^+(\tau')+\sigma^-(\tau')] + i[\sigma^+(\tau)-\sigma^-(\tau)]\nu(\tau-\tau')[\sigma^+(\tau')-\sigma^-(\tau')]\}.$$

As we can see, there is a factor $\gamma/\hbar$ out front of the non-dimensionalized bath action as well. This is why we chose to normalize by the dissipation parameter. We set

$$\frac{1}{\kappa} = \frac{\gamma}{\hbar},$$

which is our dimensionless parameter which controls how close the system is to being classical.

For the remainder of the calculations, we will set $J = 1$ to ease the notation.

G.3.4 Limits of the dissipation and noise kernels

Before discussing the random field averages, I first want to discuss the limits of the noise and dissipation kernels in various limits. Many of the limiting forms listed here are given in Ref. [112], though I make some

additional observations. As I am working only with Ohmic dissipation, this is the only case I consider here.

The evaluation of the dissipative kernel $\eta(\tau)$ can be done exactly, and for finite cutoff X is

$$\eta(\tau) = \frac{1}{\pi}\Theta(\tau)\frac{d}{d\tau}\left(\frac{X}{1+(X\tau)^2}\right). \tag{G.11}$$

Of great interest is the "memoryless bath limit", $X \to \infty$ ($\Lambda \to \infty$). In that limit, the dissipative kernel becomes

$$\lim_{X\to\infty}\ \eta(\tau) = \Theta(\tau)\delta'(\tau). \tag{G.12}$$

It is this kernel which gives rise to the first derivative term in the mean field equations of motion (to be discussed later, but the same result appeared in the purely thermal soft-spin boson model in Appendix F).

The noise kernel is more complicated because it depends on both temperature and the quantum fluctuations (through κ). I used Mathematica to calculate the result for finite cutoff (assuming τ is real and all other parameters are positive):

$$\nu(\tau) = \frac{1}{\pi}\left[-X^2\frac{1-(X\tau)^2}{(1+(X\tau)^2)^2} + \frac{\psi^{(1)}\left(\frac{1-iX\tau}{2aX}\right)+\psi^{(1)}\left(\frac{1+iX\tau}{2aX}\right)}{4a^2}\right], \tag{G.13}$$

where $a = \beta\kappa/2$ and $\psi^{(m)}(z)$ is the mth polygamma function, defined as the $(m+1)$th derivative of $\log\Gamma(z)$, where $\Gamma(z) = \int_0^\infty dt\ t^{z-1}\exp(-t)$ is the usual Gamma function.

Taking the $a \to \infty$ limit (corresponding to $\beta \to \infty$, the zero-temperature limit), Mathematica gives

$$\lim_{\beta\to\infty}\nu(\tau) = \frac{1}{\pi}X^2\frac{1-(X\tau)^2}{(1+(X\tau)^2)^2}, \tag{G.14}$$

which is the same limit that Cugliandolo and Lozano get by taking the zero temperature limit in the integral form.

Taking the memoryless bath limit, $X \to \infty$, gives

$$\lim_{X\to\infty}\lim_{\beta\to\infty}\nu(\tau) = -\frac{1}{\pi}\frac{1}{\tau^2}, \tag{G.15}$$

which is a strongly singular kernel. Because the power of the singularity is even, it is not clear that even a principal value exists.

However, it can be shown that [2]

$$\lim_{X\to\infty}\frac{1}{\pi}\int_{-\infty}^{\infty}d\tau\int_{-\infty}^{\infty}d\tau'\ f(\tau)\left[X^2\frac{1-(X(\tau-\tau'))^2}{(1+(X(\tau-\tau'))^2)^2}\right]f(\tau')=\frac{1}{2}\int_{-\infty}^{\infty}d\tau\int_{-\infty}^{\infty}d\tau'\ \frac{(f(\tau)-f(\tau'))^2}{(\tau-\tau')^2},$$

which is well defined at $\tau=\tau'$. Because the noise kernel will appear in the action in an integral of this form, we could thus get around the singularity. However, the price we would pay is that our action would no longer be quadratic, making calculations difficult. For these reasons, I will leave $\nu(\tau)$ with a finite cutoff until all calculations are done and it may safely be taken to be infinite (if possible).

Note that the zero-temperature quantum kernel is not a delta-function, as we might have otherwise expected. The quantum fluctuations introduce noise correlations, which is qualitatively different than the thermal fluctuations. It would be very interesting to see if the noise correlations ultimately have any effect on the critical properties of the model.

If we instead the classical limit, $\kappa\to 0$ ($\hbar\to 0$), first, we find

$$\lim_{\kappa\to 0}\ \kappa\nu(\tau)\to\frac{2k_BT}{\pi}\frac{X}{1+(X\tau)^2},$$

(the extra κ on the left hand side comes from the action), which tends to a delta function as the cutoff is sent to infinity:

$$\lim_{X\to\infty}\ \lim_{\kappa\to 0}\ \kappa\nu(\tau)=2\frac{k_BT}{\pi}\delta(\tau),$$

which is what is expected for classical, uncorrelated thermal noise of temperature T.

G.3.5 Random field averaging

As explained earlier, one of the advantages of the Schwinger-Keldysh or Martin-Siggia-Rose path integral methods is the ease with which quenched disorder is treated. In typical path integral treatments, or equilibrium statistical mechanics, averages over quenched disorder must be done at the level of the free energy; i.e., the logarithm of the partition function. Such averages are typically quite difficult to do, so a work-around called the "replica trick", which makes use of the identity $\log Z=\lim_{n\to 0}(Z^n-1)/n$. I will not go into

[2] See exercise 6.10 of Ref. [97], which asks the reader to prove the identity.

the details of the replica trick here; rather, I will merely note that because the Schwinger-Keldysh and Martin-Siggia-Rose path integrals are automatically normalized, the averages can be done directly over the partition function(al) - at least so long as the disorder is uncorrelated with the initial state of the system. This is indeed the case for the random field Ising model, as we initialize the system with a magnetic field so strongly negative that all of the spins will point down, no matter the distribution of the random fields.

Though I will not make much use of the disorder-averaged partition functional in this appendix, I will go through the average over the random fields. It turns out that the overall form of the action does not change much - basically, the disorder average amounts to a modification of the noise kernel, $\nu(\tau - \tau')$.

Because we chose a Gaussian disorder distribution, the disorder average will be quite easy to do; it will essentially amount to completing the square. The integral we must do is

$$\prod_{i=1}^{N} \int_{-\infty}^{\infty} dh_i \frac{1}{\sqrt{2\pi}R} \exp\left(-\frac{h_i^2}{2R^2} + \frac{i}{\kappa} \underbrace{\int_{-\infty}^{\infty} d\tau \, \{\sigma^+(\tau) - \sigma^-(\tau)\}}_{\equiv \Delta\sigma} h_i \right).$$

Completing the square gives

$$\prod_{i=1}^{N} \exp\left(\frac{i}{\hbar} \int_{-\infty}^{\infty} d\tau \int_{-\infty}^{\infty} d\tau' \, (\sigma^+(\tau) - \sigma^-(\tau)) \frac{iR^2}{2\kappa} (\sigma^+(\tau') - \sigma^-(\tau)) \right).$$

This term can be absorbed into the bath action, giving an effective noise kernel $\tilde{\nu}(\tau - \tau') = -\frac{R^2}{2\kappa} + \nu(\tau - \tau')$. So, the disorder-averaged functional is

$$\begin{aligned} \overline{\mathcal{Z}} \;=\; & \int \mathcal{D}\sigma^{\pm} \, \exp\left[\frac{i}{\kappa} \left(\int_{-\infty}^{\infty} d\tau \, \sum_i \left[\frac{(\dot{\sigma}_i^+)^2}{2m} + \frac{1}{2} \sum_j J_{ij} \sigma_i^+ \sigma_j^+ + H(\tau) \sigma_i^+ \right] \right. \right. \\ & - \int_{-\infty}^{\infty} d\tau \, \sum_i \left[\frac{(\dot{\sigma}_i^-)^2}{2m} + \frac{1}{2} \sum_j J_{ij} \sigma_i^- \sigma_j^- + H(\tau) \sigma_i^- \right] \\ & \left. \left. - \int_{-\infty}^{\infty} d\tau \, \sum_i (V[\sigma_i^+(\tau)] - V[\sigma_i^-(\tau)] + \tilde{S}_T[\sigma_i^+, \sigma_i^-] \right) \right], \end{aligned} \tag{G.16}$$

where $\tilde{S}_T[\sigma^+, \sigma^-]$ is the non-local effective bath action with $\nu(\tau - \tau')$ replaced by $\tilde{\nu}(\tau - \tau')$.

We can easily switch between the disorder-averaged functional and the non-averaged functional by restoring $\tilde{S}_T \to S_T$ ($\tilde{\nu}(\tau - \tau') \to \nu(\tau - \tau')$) and $H(\tau) \to H(\tau) + h_i$ in Eq. (G.17). For the following manipulations

below, I will use the disorder-averaged functional, but in Sec. G.4 I will return to using the non-averaged functional.

G.3.6 Notation compactification

The action is becoming rather unwieldy to write down, so I will follow Cugliandolo and Lozano in writing the quadratic part of the action in a compact form by defining an operator $O_2^{\alpha\beta}(t,t')$, with the indexes $\alpha,\beta = +/-$, giving

$$\begin{aligned}\overline{\mathcal{Z}} &= \int \mathcal{D}\sigma^{\pm}\ \exp\left[\frac{i}{\kappa}\left(-\frac{1}{2}\sum_i \int d\tau \int d\tau'\ \sigma_i^{\alpha}(\tau) O^{\alpha,\beta}(\tau,\tau')\sigma_i^{\beta}(\tau')\right.\right. \\ &+ \int d\tau \left[\frac{1}{2}\sum_{i,j} J_{ij}\sigma_i^{+}\sigma_j^{+} + \sum_i H(\tau)\sigma_i^{+} - \frac{1}{2}\sum_{i,j} J_{ij}\sigma_i^{-}\sigma_j^{-} - \sum_i H(\tau)\sigma_i^{-}\right] \\ &\left.\left. - \int d\tau\ \sum_i (V[\sigma_i^{+}(\tau)] - V[\sigma_i^{-}(\tau)])\right)\right].\end{aligned} \tag{G.17}$$

The operator components are

$$O_2^{++}(\tau,\tau') = \frac{1}{m}\left(\frac{\partial}{\partial\tau}\right)^2 \delta(\tau-\tau') - 2i\tilde{\nu}(\tau-\tau'),$$

$$O_2^{+-}(\tau,\tau') = 2\eta(\tau-\tau') + 2i\tilde{\nu}(\tau-\tau'),$$

$$O_2^{-+}(\tau,\tau') = -2\eta(\tau-\tau') + 2i\tilde{\nu}(\tau-\tau'),$$

$$O_2^{--}(\tau,\tau') = -\frac{1}{m}\left(\frac{\partial}{\partial\tau}\right)^2 \delta(\tau-\tau') - 2i\tilde{\nu}(\tau-\tau').$$

I do not include any possible quadratic terms from the potential $V[\sigma]$ in the operator notation. This is because, at this point, I have yet not needed to specify which potential I am using, and I wish to keep the notation general until I need to choose a potential.

G.3.7 Rotation to Classical and Quantum Variables

It will now be convenient to perform a rotation of the $\sigma^{\pm}$ variables into new variables that correspond to the classical and quantum spin variables (in the sense that as $\hbar \to 0$, one variable becomes the spin in

the classical Martin-Siggia-Rose formalism and the other becomes the auxiliary variable $\hat{s}$ introduced when writing the Dirac delta function as an exponential).

The rotation, as used in Ref. [112], is

$$\sigma_i^+(\tau) = s_i^c(\tau) + \frac{\kappa}{2} s_i^q(\tau),$$

$$\sigma_i^-(\tau) = s_i^c(\tau) - \frac{\kappa}{2} s_i^q(\tau).$$

The reverse rotation from the new variables $s^c(\tau)$ and $s^q(\tau)$ to the old variables is

$$s_i^c(\tau) = \frac{\sigma_i^+(\tau) + \sigma_i^-(\tau)}{2},$$

$$s_i^q(\tau) = \frac{\sigma_i^+(\tau) - \sigma_i^-(\tau)}{\kappa}.$$

The fields $s_i^c(\tau)$ carry a superscript c because they are the "classical" spin fields - that is, in the classical $\kappa \to 0$ limit, the $s_i^c(\tau)$ become the spin field $s_i(\tau)$ in the Martin-Siggia-Rose formalism. Similarly, the fields $s_i^q(\tau)$ carry a superscript q to denote that they are the "quantum" spin fields. In the classical limit, the $s_i^q(\tau)$ become the auxiliary fields $\hat{s}_i(\tau)$ of the Martin-Siggia-Rose formalism.

I will now rewrite the action in terms of these new fields. I will do the transformation in pieces.

First, let's transform the quadratic term, $\sigma_i^\alpha(\tau) O^{\alpha\beta}(\tau,\tau')\sigma_i^\beta(\tau')$. Inserting the rotation, we may write the quadratic term as $s_i^\alpha(\tau)(G_0^{-1})^{\alpha\beta}(\tau,\tau')s_i^\beta(\tau')$, where now $\alpha, \beta = c$ or q, and

$$(G_0^{-1})^{cc} = O^{++} + O^{+-} + O^{-+} + O^{--} = 0,$$

$$(G_0^{-1})^{cq} = \frac{\kappa}{2}(O^{++} - O^{+-} + O^{-+} - O^{--}) = \frac{\kappa}{2}\left(\frac{2}{m}\partial_\tau^2\delta(\tau-\tau') - 4\eta(\tau-\tau')\right),$$

$$(G_0^{-1})^{qc} = \frac{\kappa}{2}(O^{++} + O^{+-} - O^{-+} - O^{--}) = \frac{\kappa}{2}\left(\frac{2}{m}\partial_\tau^2\delta(\tau-\tau') + 4\eta(\tau-\tau')\right),$$

$$(G_0^{-1})^{qq} = \left(\frac{\kappa}{2}\right)^2 (O^{++} - O^{+-} - O^{-+} + O^{--}) = -8i\left(\frac{\kappa}{2}\right)^2 \tilde{\nu}(\tau-\tau').$$

We perform the rotation on the $J_{ij}\sigma_i^+\sigma_j^+ - J_{ij}\sigma_i^-\sigma_j^-$ terms and find

$$\sigma_i^\alpha\sigma_j^\alpha = s_i^c s_j^c + \alpha\frac{\kappa}{2}(s_i^c s_j^q + s_j^c s_i^q) + \left(\frac{\kappa}{2}\right)^2 s_i^q s_j^q;$$

since the $\alpha = \pm$ terms are subtracted, only the cross term survives, giving

$$J_{ij}\kappa(s_i^c s_j^q + s_j^c s_i^q) = 2\kappa J_{ij} s_j^c s_i^q,$$

where we have assumed that $J_{ij} = J_{ji}$ to condense the expression.

The linear term is $H(\tau)(\sigma_i^+ - \sigma_i^-)$, which reduces to $\kappa H(\tau) s_i^q(\tau)$. There is no general form for the potential term $V[\sigma^+] - V[\sigma^-]$; however, if $V[\sigma]$ is differentiable, then in the limit as $\kappa \to 0$, we may write

$$V[s^c + (\kappa/2)s^q] - V[s^c - (\kappa/2)s^q] = \kappa s^q \frac{\delta V[s^c(\tau)]}{\delta s^c(\tau)} + \mathcal{O}(\kappa^2).$$

In the action all terms are multiplied by a factor of i/κ. As $\kappa \to 0$, only the first term survives, giving

$$\lim_{\kappa\to 0} \frac{i}{\kappa} \left(V[s^c + (\kappa/2)s^q] - V[s^c + (\kappa/2)s^q]\right) = i s^q \frac{\delta V[s^c(\tau)]}{\delta s^c(\tau)}, \tag{G.18}$$

which is the potential term in the Martin-Siggia-Rose formalism. In fact, it turns out that for the piece-wise quadratic potential, this approximation holds exactly. To see this, suppose we can formally expand V in a power series in κ:

$$V[s^c + (\kappa/2)s^q] - V[s^c - (\kappa/2)s^q] = 2\sum_{n=0}^{\infty} \frac{\delta^{2n+1} V[s^c]}{\delta (s^c)^{2n+1}} \left(\frac{\kappa}{2} s^q\right)^{2n+1},$$

where the even terms vanish.

If we treat the derivatives of $V[s]$ for $s < 0$ and $s > 0$ separately, we avoid differentiating the signum function, which would produce delta functions. In doing the derivative piece-wise, all of the derivatives are quite simple. In fact, since the potential is piecewise quadratic, only the first derivative contributes to the expansion of $V[s^c + (\kappa/2)s^q] - V[s^c - (\kappa/2)s^q]$. Hence, we may write

$$V\left[s^c(\tau) + \frac{\kappa}{2} s^q(\tau)\right] - V\left[s^c(\tau) - \frac{\kappa}{2} s^q(\tau)\right] = 2\frac{\delta V[s^c(\tau)]}{\delta s^c(\tau)} \frac{\kappa}{2} s^q(\tau),$$

where

$$\frac{\delta V[s^c(\tau)]}{\delta s^c(\tau)} = \begin{cases} V(s^c(\tau) - 1), & s^c(\tau) > 0 \\ V(s^c(\tau) + 1), & s^c(\tau) < 0 \end{cases}$$

Though this is a rather formal, non-rigorous, argument, it will give the correct results in the classical case, so I will assume it to hold true in future calculations. In any event, if my readers are not satisfied with the argument, they may use the quartic potential, instead.

For the quartic potential, we can write down $V[\sigma^+] - V[\sigma^-]$ in terms of s^c and s^q rather easily:

$$V[\sigma^+] - V[\sigma^-] = 4V\left(\frac{\kappa}{2}(s^c)^3 s^q - \frac{\kappa}{2}s^c s^q + \left(\frac{\kappa}{2}\right)^3 s^c (s^q)^3\right).$$

In the classical limit, this contributes $is^q[2V((s^c)^2 - 1)s^c]$ to the action, which is the derivative of the potential, as expected. In the quantum case, however, there is an additional term $\left(\frac{\kappa}{2}\right)^3 s^c(s^q)^3$, which is cubic in κs^q. This term makes analytic calculations difficult, as it is higher order than quadratic (and not of even degree). In fact, it is common to suppose that the quantum fluctuations in the system are in some sense "small", which translates into $\kappa s^q \ll 1$, such that we can neglect the cubic term. This is a semi-classical approximation [119], which I will adopt. In doing so, for *both* the quadratic and quartic potentials, we may use Eq. (G.18). For the remainder of this appendix, I will thus assume that Eq. (G.18) holds.

The partition functional, in terms of the classical and quantum variables $s^c(\tau)$ and $s^q(\tau)$, is then

$$\begin{aligned}\overline{\mathcal{Z}} &= \int \mathcal{D}s^c \mathcal{D}s^q \, \exp\left[\frac{i}{\kappa}\left(-\frac{1}{2}\sum_i \int_{-\infty}^{\infty} d\tau \int_{-\infty}^{\infty} d\tau' \; s_i^\alpha(\tau)(G_0^{-1})^{\alpha,\beta}(\tau,\tau')s_i^\beta(\tau')\right.\right. \\ &\left.\left. + \kappa \int_{-\infty}^{\infty} d\tau \left[\sum_{i,j} J_{ij} s_j^c s_i^q + \sum_i H(\tau) s_i^q(\tau)\right] - i\kappa \int_{-\infty}^{\infty} d\tau \; \sum_i s_i^q(\tau)\frac{\delta V[s^c]}{\delta s^c}\right)\right].\end{aligned} \tag{G.19}$$

G.3.8 Recovering classical action in the $\hbar \to 0$ limit

Having performed our rotation to the "classical" and "quantum" variables, we can now show that in the $\kappa \to 0$ limit our action reduces to the Martin-Siggia-Rose classical action studied by Dahmen. First, we note that due to the factor of i/κ out front of everything, all terms with a linear factor of κ inside the action will survive. Higher order terms will not. We also note that as $(G_0^{-1})^{cc} = 0$, there will be no terms of order $1/\kappa$ - all of the other $G^{\alpha\beta}$ components contain factors of κ or higher powers. Note, however, that while the dissipative kernel $\eta(t-t')$ is independent of $\hbar$, the noise kernel $\tilde{\nu}(t-t')$ is not, and in fact behaves as $1/\kappa$ as κ tends to zero, so $\lim_{\kappa\to 0}(i/\kappa)(G_0^{-1})^{qq} \neq 0$.

In the classical limit and when the frequency cutoff X tends to infinity the kernels become:

$$4\eta(\tau-\tau') = 4\Theta(\tau-\tau')\delta'(\tau-\tau'),$$

$$2\kappa\tilde{\nu}(\tau-\tau') = -R^2 + 4k_BT\delta(\tau-\tau').$$

Hence, in the classical limit,

$$\frac{i}{\kappa}s^c(\tau)(G_0^{-1})^{cq}s^q(\tau') \to is^c(\tau)\left(\frac{1}{m}\partial_\tau^2\delta(\tau-\tau') - 2\Theta(\tau-\tau')\delta'(\tau-\tau')\right)s^q(\tau'),$$

$$\frac{i}{\kappa}s^q(\tau)(G_0^{-1})^{qc}s^c(\tau') \to is^q(\tau)\left(\frac{1}{m}\partial_\tau^2\delta(\tau-\tau') + 2\Theta(\tau-\tau')\delta'(\tau-\tau')\right)s^c(\tau'),$$

$$\frac{i}{\kappa}s^q(\tau)(G_0^{-1})^{qq}s^q(\tau') \to s^q(\tau)(-R^2 + 4k_BT\delta(\tau-\tau'))s^q(\tau').$$

Combining the first two equations together (being careful with the Heaviside step function) and doing the τ' integrals gives

$$\frac{i}{2\kappa}\int_{-\infty}^{\infty}d\tau\int_{-\infty}^{\infty}d\tau'\left(s^c(\tau)(G_0^{-1})^{cq}s^q(\tau') + s^q(\tau)(G_0^{-1})^{qc}s^c(\tau')\right) = \int_{-\infty}^{\infty}d\tau\ is^q(\tau)\left[(\frac{1}{m}\partial_\tau^2 s^c(\tau) - \frac{\partial s^c(\tau)}{\partial\tau}\right].$$

The quadratic term is

$$\frac{i}{2\kappa}\int_{-\infty}^{\infty}d\tau\ s^q(\tau)(G_0^{-1})^{qq}s^q(\tau') = \int_{-\infty}^{\infty}d\tau\ \left[-R^2s^q(\tau)\left[\int_{-\infty}^{\infty}d\tau' s^q(\tau')\right] + 4k_BT(s^q(\tau))^2\right].$$

As we wish, at the moment, to compare this to the zero-temperature classical theory, so we set $T=0$ above. (Leaving $T>0$ gives a Langevin equation). Our action, then, looks like

$$-i\int_{-\infty}^{\infty}d\tau\sum_i s_i^q(\tau)\left[\frac{1}{m}\frac{\partial^2 s^c(\tau)}{\partial\tau^2} - \frac{\partial s^c(\tau)}{\partial\tau} - \sum_j J_{ij}s_j^c(\tau) - H(\tau) + i\frac{R^2}{2}\int_{-\infty}^{\infty}d\tau'\ s_i^q(\tau') + \frac{\delta V[s^c(\tau)]}{\delta s^c(\tau)}\right].$$

This agrees with the classical result! Hence, we have shown that in the $\kappa\to 0$ limit and at $T=0$ our results reduce to the classical results! In fact, had we not averaged over the random fields, the $i\frac{R^2}{2}\int d\tau'\ s_i^q(\tau')$ term would just be $-h_i$, meaning we could integrate out $s^q(\tau)$ to give

$$\mathcal{Z} = \int \mathcal{D}s^c(\tau)\delta\left(\frac{1}{m}\frac{\partial^2 s^c(\tau)}{\partial\tau^2} - \frac{\partial s^c(\tau)}{\partial\tau} - \sum_j J_{ij}s_j^c(\tau) - H(\tau) - h_i + \frac{\delta V[s^c(\tau)]}{\delta s^c(\tau)}\right);$$

i.e., a delta function which enforces the relaxational equation governing the spin dynamics. We have thus recovered the Martin-Siggia-Rose formalism from the Schwinger-Keldysh formalism! (To be perfectly accurate, the actual classical, zero-temperature equation studied by Dahmen does not have the second derivative, so we remove it by setting $m \to \infty$).

At this point, I have followed Cugliandolo and Lozano [112] as far as I can. The path integral is now in a form that is as close as it can be to the classical, zero-temperature path integral studied by Dahmen. Hence, the calculations will now follow Dahmen's calculations for the soft-spin random field Ising model. I begin by introducing a set of auxiliary fields as a first step towards a saddle-point expansion (which will correspond to an expansion around mean field theory).

G.4 The mean field quantum RFIM

G.4.1 Introducing auxiliary field to decouple the system

In order to expand the action about the saddle-point fields, it is helpful to first decouple the sites by introducing auxiliary fields. Let $z_i(\tau) = \sum_j J_{ij}s_j^c(\tau)$, where we remind the reader that J_{ij} is really divided by J (which we set to 1), so that $z_i(\tau)$ is dimensionless. The reverse transformation is $s_i^c(\tau) = \sum_j J_{ij}^{-1}z_j(\tau)$. To properly change variables, we introduce a path integral over $z(t)$ of a delta-function which enforces the change of variables $s_i^c(\tau) = \sum_j J_{ij}^{-1}z_j(\tau)$. We then express the delta function as an exponential by introducing another field, $\hat{z}_i(\tau)$. We will ignore any Jacobians and other constants, as we do not expect them to affect the dynamics. So, we write

$$1 \propto \int \mathcal{D}z\delta\left(s_i^c(\tau) - \sum_j J_{ij}^{-1}z_j(\tau)\right) \propto \int \mathcal{D}[z\hat{z}]\exp\left[\frac{i}{\kappa}\int_{-\infty}^{\infty} d\tau\ \kappa\hat{z}_i(\tau)\left(s_i^c(\tau) - \sum_j J_{ij}^{-1}z_j(\tau)\right)\right]. \quad \text{(G.20)}$$

By collecting all terms that depend on s^c and s^q together, we can rewrite our functional in the form

$$Z = \int \mathcal{D}[z\hat{z}] \left(\prod_{i=1}^{N} \mathcal{Z}_i[z_i, \hat{z}_i] \right) \exp\left[-\frac{i}{\kappa} \int_{-\infty}^{\infty} d\tau \ \sum_i \kappa \hat{z}_i(\tau) \sum_j J_{ij}^{-1} z_j(\tau) \right],$$

where I have defined the local functionals $\mathcal{Z}_i$ to be

$$\mathcal{Z}_i[z_i, \hat{z}_i] = \int \mathcal{D}[s^c s^q] \exp\left[\frac{i}{\kappa} \mathcal{S}_{loc} \right], \tag{G.21}$$

where the local site-actions $\mathcal{S}_{loc,i}$ are

$$\begin{aligned} \mathcal{S}_{loc} &= -\frac{1}{2} \int_{-\infty}^{\infty} d\tau \int_{-\infty}^{\infty} d\tau' \ s_i^{\alpha}(\tau) (G_0^{-1})^{\alpha,\beta}(\tau,\tau') s_i^{\beta}(\tau') \\ &\quad + \kappa \int_{-\infty}^{\infty} d\tau \left\{ s_i^q(\tau) \left[z_i(\tau) + H(\tau) + h_i - \frac{\delta V[s^c]}{\delta s^c} \right] + \hat{z}_i(\tau) s_i^c(\tau) \right\}. \end{aligned} \tag{G.22}$$

The site-actions are independent due to the decoupling field we introduced.

At this point, I would like to remind the reader that I am using the non-disorder-averaged functional again. I would also like to point out that the local action is entirely *quadratic* in $s^q(\tau)$ [3].

G.4.2 Saddle-point equations

The next step is to find the saddle-points of our action. We vary the total effective action,

$$\frac{i}{\kappa} S_{eff} = \sum_i \left(-\frac{i}{\kappa} \int d\tau \ \kappa \hat{z}_i(\tau) \sum_j J_{ij}^{-1} z_j(\tau) + \ln \mathcal{Z}_i[z_i, \hat{z}_i] \right)$$

with respect to z and $\hat{z}$ to arrive at the saddle-point equations.

First, however, I will define the notion of a "local average",

$$\langle A \rangle_{\ell} = \frac{\int \mathcal{D}[s^c s^q] A \exp\left(\frac{i}{\kappa} \mathcal{S}_{loc} \right)}{\int \mathcal{D}[s^c s^q] \exp\left(\frac{i}{\kappa} \mathcal{S}_{loc} \right)}; \tag{G.23}$$

i.e., this is an average with respect to the local site-action, $\mathcal{S}_{loc,i}$, as a path integral weight.

Varying $\mathcal{S}_{eff}$ with respect to $z_k(\tau'')$, we find

[3] Recall that although the quartic potential introduces a cubic $\kappa(s^q)^3$ term, I have assumed it is negligible. As a result, the action is entirely quadratic in $s^q(\tau)$.

$$\begin{aligned}\frac{i}{\kappa}\frac{\delta\mathcal{S}_{eff}}{\delta z_k(\tau'')} &= \sum_i\left(-\frac{i}{\kappa}\int d\tau\sum_j J_{ij}^{-1}\delta_{jk}\delta(\tau-\tau'')\kappa\hat{z}_i(\tau)+\frac{1}{\mathcal{Z}_i[z_i,\hat{z}_i]}\frac{\delta\mathcal{Z}_i[z_i,\hat{z}_i]}{\delta z_k(\tau'')}\right)\\ &= \sum_i\left(-\frac{i}{\kappa}J_{ik}^{-1}\kappa\hat{z}_i(\tau'')+\frac{1}{\mathcal{Z}_i[z_i,\hat{z}_i]}\int\mathcal{D}[s^cs^q]\left(\frac{i}{\kappa}\int d\tau\ s_i^q(\tau)\kappa\delta_{ik}\delta(\tau-\tau'')\right)\exp\left(\frac{i}{\kappa}\mathcal{S}_{loc}\right)\right).\end{aligned}$$

The last term is just the local average of s^q; hence, we arrive at the equation for the saddle-point function $\hat{z}_k^0(\tau)$,

$$-\frac{i}{\kappa}\sum_i J_{ik}^{-1}\kappa\hat{z}_i^0(\tau'')+i\langle s_k^q(t'')\rangle_{\ell,z^0,\hat{z}^0}=0,$$

or

$$\sum_j J_{ij}^{-1}\hat{z}_j^0(t)=\langle s_i^q(t)\rangle_{\ell,z^0,\hat{z}^0}, \tag{G.24}$$

which is analogous to the saddle-point equation in the classical case.

Varying $mathcalS_{eff}$ with respect to $\hat{z}_k(\tau'')$ gives

$$\begin{aligned}\frac{i}{\kappa}\frac{\delta\mathcal{S}_{eff}}{\delta\hat{z}_k(\tau'')} &= \sum_i\left(-\frac{i}{\kappa}\int dt\sum_j J_{ij}^{-1}\delta_{ik}\delta(\tau-\tau'')\kappa z_j(\tau)+\frac{1}{\mathcal{Z}_i[z_i,\hat{z}_i]}\frac{\delta\mathcal{Z}_i[z_i,\hat{z}_i]}{\delta\hat{z}_k(\tau'')}\right)\\ &= \sum_i\left(-\frac{i}{\kappa}J_{ki}^{-1}z_i(\tau'')+\frac{1}{\mathcal{Z}_i[z_i,\hat{z}_i]}\int\mathcal{D}[s^cs^q]\left(\frac{i}{\kappa}\int d\tau\ s_i^c(\tau)\kappa\delta_{ik}\delta(\tau-\tau'')\right)\exp(stuff)\right).\end{aligned}$$

The saddle point equation for $z_k^0(\tau)$ is thus

$$-\frac{i}{\kappa}\sum_i J_{ki}^{-1}\kappa z_i^0(\tau'')+\frac{i}{\kappa}\kappa\langle s_k^c(\tau'')\rangle_{\ell,z^0,\hat{z}^0}=0,$$

or

$$\sum_j J_{ij}^{-1}z_j^0(\tau)=\langle s_i^c(\tau)\rangle_{\ell,z^0,\hat{z}^0}. \tag{G.25}$$

Again, this is analogous to the classical saddle point equation.

The local averages (G.24) and (G.25) are evaluated at the saddle-point values $\hat{z}_k(\tau)=\hat{z}_k^0(\tau)$ and $z_k(\tau)=z_k^0(\tau)$, meaning these equations must be solved *self consistently* for $\hat{z}_k^0(\tau)$ and $z_k^0(\tau)$. This is not necessarily

an easy task. The classical saddle point solutions are $\langle s_i^q(\tau)\rangle = 0 \Rightarrow \hat{z}_i^0(\tau) = 0$ and $z_i^0(\tau) = M(\tau)$, the magnetization given by the mean field equation of motion for the spins $s_i^c(\tau)$. As we will show below, these will also turn out to be the saddle point solutions for our case, though the equation that the magnetization obeys will contain noise, and it will take much more work to prove these results than in the classical, noiseless case.

G.4.3 Unpacking the operator notation for $\mathcal{S}_{loc,i}$

Before I compute the local averages, it will be useful to unpack the operator notation $s_i^\alpha(\tau)(G_0^{-1})^{\alpha\beta}(\tau,\tau')s_i^\beta(\tau')$ and write the local actions out in full. This unpacking is similar to what I did for the classical case, except the dissipation and noise kernels are no longer trivial.

As before, the term $(G_0^{-1})^{cc} = 0$, so there are no quadratic s^c terms. The cq and qc quadratic terms give

$$\begin{aligned}
&\int_{-\infty}^{\infty} d\tau \int_{-\infty}^{\infty} d\tau' \left[s^c(\tau)(G_0^{-1})^{cq}s^q(\tau') + s^q(\tau)(G_0^{-1})^{cq}s^c(\tau')\right] \\
= \;& \kappa \int_{-\infty}^{\infty} d\tau \int_{-\infty}^{\infty} d\tau' s_i^c(\tau)\left[m^{-1}\partial_\tau^2\delta(\tau-\tau') - 2\eta(\tau-\tau')\right]s_i^q(\tau') \\
+ \;& \kappa \int_{-\infty}^{\infty} d\tau \int_{-\infty}^{\infty} d\tau' s_i^q(\tau)\left[m^{-1}\partial_\tau^2\delta(\tau-\tau') + 2\eta(\tau-\tau')\right]s_i^c(\tau').
\end{aligned}$$

The first terms in each line are the same after integrating over the appropriate time variable. In the second term on the second line we swap the dummy variables τ and τ'. This gives us

$$\begin{aligned}
&\int_{-\infty}^{\infty} d\tau \int_{-\infty}^{\infty} d\tau' \left[s^c(\tau)(G_0^{-1})^{cq}s^q(\tau') + s^q(\tau)(G_0^{-1})^{cq}s^c(\tau')\right] \\
= \;& \frac{2\kappa}{m}\int_{-\infty}^{\infty} d\tau s_i^q(\tau)\partial_\tau^2 s_i^c(\tau) \\
+ \;& 2\kappa \int_{-\infty}^{\infty} d\tau \int_{-\infty}^{\infty} d\tau' s_i^c(\tau)s_i^q(\tau')\left[\eta(\tau'-\tau) - \eta(\tau-\tau')\right].
\end{aligned}$$

The last line can be simplified by noting $\eta(\tau'-\tau) = -\Theta(\tau'-\tau)\mu(\tau'-\tau) = -[1-\Theta(\tau-\tau')]\{-\mu(\tau-\tau')\}$,

using the fact that $\mu(\tau-\tau') \equiv \int_0^\infty dx\ \tilde{I}(x)\sin(\tau-\tau')$ is odd. Hence, we find $\eta(\tau'-\tau)-\eta(\tau-\tau') = \mu(\tau-\tau')$.

The cq and qc terms thus give, after multiplying by the factor of $-1/2$ we neglected above,

$$-\kappa\int_{-\infty}^{\infty} d\tau s_i^q(\tau)\left[m^{-1}\partial_\tau^2 s_i^c(\tau) - \int_{-\infty}^{\infty} d\tau'\mu(\tau-\tau')s_i^c(\tau')\right].$$

The purely quantum term, qq, is

$$-\frac{1}{2}\int_{-\infty}^{\infty} d\tau\int_{-\infty}^{\infty} d\tau' s_i^q(\tau)\left\{-8i\left(\frac{\kappa}{2}\right)^2\nu(\tau-\tau')\right\}s_i^q(\tau') = i\kappa^2\int_{-\infty}^{\infty} d\tau\int_{-\infty}^{\infty} d\tau' s_i^q(\tau)\nu(\tau-\tau')s_i^q(\tau'),$$

and I again remind the reader that for the purposes of finding the saddle points I have not done the disorder-average and so the kernel ν is just the regular noise kernel.

Putting everything together, we find that the local action is

$$\begin{aligned}\frac{i}{\kappa}\mathcal{S}_{loc,i} &= -\frac{1}{2}\int_{-\infty}^{\infty} d\tau\int_{-\infty}^{\infty} d\tau' s_i^q(\tau)[2\kappa\nu(\tau-\tau')]s_i^q(\tau') \\ &\quad +i\int_{-\infty}^{\infty} d\tau s_i^q(\tau)\left[-m^{-1}\partial_\tau^2 s_i^c(\tau) + \int_{-\infty}^{\infty} d\tau'\mu(\tau-\tau')s_i^c(\tau') + z_i(\tau) + H(\tau) + h_i - \frac{\delta V[s_i^c(\tau)]}{\delta s_i^c(\tau)}\right] \\ &\quad +i\int_{-\infty}^{\infty} d\tau\hat{z}_i(\tau)s_i^c(\tau). \end{aligned} \tag{G.26}$$

As is now explicitly apparent, this is quadratic in $s_i^q(\tau)$, and we can complete the square to evaluate certain local averages. I will complete the square in the next subsection before moving on to computing the local averages of interest, Eqs. (G.24) and (G.25).

G.4.4 Completing the square in s^q

In Appendix F, rather than complete the square in $s^q(\tau)$, I introduced a new field $\zeta(\tau)$ using a Hubbard-Stratonovich transformation. I could do the same here, but I wish to show this alternate method, as promised in Appendix F.

To simplify notation while I complete the square, let $A(\tau-\tau') \equiv 2\kappa\nu(\tau-\tau')$ and

$$B_i(\tau) \equiv \left[-m^{-1}\partial_\tau^2 s_i^c(\tau) + \int_{-\infty}^{\infty} d\tau'\mu(\tau-\tau')s_i^c(\tau') + z_i(\tau) + H(\tau) + h_i - \frac{\delta V[s_i^c(\tau)]}{\delta s_i^c(\tau)}\right].$$

Note that $B_i(\tau)$ depends functionally on $s_i^c(\tau)$.

The part of the local action relevant to completing the square is

$$-\frac{1}{2}\int_{-\infty}^{\infty} d\tau \int_{-\infty}^{\infty} d\tau' s_i^q(\tau) A(\tau-\tau') s_i^q(\tau') + i\int_{-\infty}^{\infty} d\tau B_i(\tau) s_i^q(\tau).$$

Suppose that the function $A(\tau-\tau)$ has inverse $A^{-1}(\tau,\tau')$, such that

$$\int_{-\infty}^{\infty} d\tau' A^{-1}(\tau,\tau')A(\tau'-\tau'') = \int_{-\infty}^{\infty} d\tau' A(\tau-\tau')A^{-1}(\tau',\tau'') = \delta(\tau-\tau').$$

We then make the change of variables

$$s_i^q(\tau) = y_i(\tau) + i\int_{-\infty}^{\infty} d\tau' A^{-1}(\tau,\tau')B_i(\tau').$$

As this is just a constant shift, the Jacobian will be a 1. (The shift is constant as far as $s_i^q(\tau)$ is concerned, even though the shift depends on $s_i^c(\tau)$). Inserting this change of variables into the quadratic term gives

$$\begin{aligned}
& -\frac{1}{2}\int d\tau \int d\tau' \left\{ y_i(\tau) + i\int d\tau'' A^{-1}(\tau,\tau'')B_i(\tau'') \right\} A(\tau-\tau') \left\{ y_i(\tau) + i\int d\tau''' A^{-1}(\tau,\tau''')B_i(\tau''') \right\} \\
= \; & -\frac{1}{2}\int d\tau \int d\tau' \{ y_i(\tau)A(\tau-\tau')y_i(\tau') \\
& + iy_i(\tau)A(\tau-\tau')\int d\tau''' A^{-1}(\tau',\tau''')B_i(\tau''') + i\int d\tau'' A^{-1}(\tau,\tau'')B_i(\tau'')A(\tau-\tau')y_i(\tau') \\
& - \int d\tau'' \int d\tau''' A^{-1}(\tau,\tau'')B_i(\tau'')A(\tau-\tau')A^{-1}(\tau',\tau''')B_i(\tau''') \Big\},
\end{aligned}$$

where all integrals run from $-\infty$ to ∞.

In order for the terms on the second line to combine and cancel with terms from the $\int_{-\infty}^{\infty} d\tau B_i(\tau)s_i^q(\tau)$, we need to assume that $A^{-1}(\tau,\tau') = A^{-1}(\tau',\tau)$, i.e., A^{-1} is a symmetric kernel. Because A is a symmetric kernel, we expect this to indeed be the case. We can hence write

$$
\begin{aligned}
& -\frac{1}{2}\int d\tau \int d\tau' \left\{ y_i(\tau) + i\int d\tau'' A^{-1}(\tau,\tau'')B_i(\tau'')\right\} A(\tau-\tau') \left\{ y_i(\tau) + i\int d\tau''' A^{-1}(\tau,\tau''')B_i(\tau''')\right\} \\
= \; & -\frac{1}{2}\int d\tau \int d\tau' y_i(\tau)A(\tau-\tau')y_i(\tau') \\
& -\frac{i}{2}\int d\tau \int d\tau''' y_i(\tau)\delta(\tau-\tau''')B_i(\tau''') - \frac{i}{2}\int d\tau'' \int d\tau' B_i(\tau'')\delta(\tau''-\tau')y_i(\tau') \\
& +\frac{1}{2}\int d\tau'' \int d\tau''' A^{-1}(\tau,\tau'')B_i(\tau'')\delta(\tau-\tau''')B_i(\tau''') \\
= \; & -\frac{1}{2}\int d\tau \int d\tau' y_i(\tau)A(\tau-\tau')y_i(\tau') \\
& -i\int d\tau B_i(\tau)y_i(\tau) \\
& +\frac{1}{2}\int d\tau \int d\tau' B_i(\tau')A^{-1}(\tau,\tau')B_i(\tau'),
\end{aligned}
$$

where all integrals run from $-\infty$ to ∞.e The linear term $i\int_{-\infty}^{\infty} d\tau B_i(\tau)s_i^q(\tau)$ becomes

$$
\begin{aligned}
i\int_{-\infty}^{\infty} d\tau B_i(\tau)s_i^q(\tau) &= i\int_{-\infty}^{\infty} d\tau B_i(\tau)\left[y_i(\tau) + i\int_{-\infty}^{\infty} d\tau' A^{-1}(\tau,\tau')B_i(\tau')\right] \\
&= i\int_{-\infty}^{\infty} d\tau B_i(\tau)y_i(\tau) - \int_{-\infty}^{\infty} d\tau \int_{-\infty}^{\infty} d\tau' B_i(\tau)A^{-1}(\tau,\tau')B_i(\tau').
\end{aligned}
$$

Adding this to the quadratic terms gives a transformed action of

$$
-\frac{1}{2}\int_{-\infty}^{\infty} d\tau \int_{-\infty}^{\infty} d\tau' y_i(\tau)A(\tau-\tau')y_i(\tau') - \frac{1}{2}\int_{-\infty}^{\infty} d\tau \int_{-\infty}^{\infty} d\tau' B_i(\tau)A^{-1}(\tau,\tau')B_i(\tau').
$$

With this, we can now attempt to do the local average integrals, which we will cover in the next subsection.

G.4.5 Computing the local averages

The local average of some quantity $\mathcal{O}$ is given by

$$
\langle \mathcal{O} \rangle = \frac{\int \mathcal{D}s_i^c \mathcal{D}y_i \; \mathcal{O} \exp\left[-\frac{1}{2}\int d\tau d\tau' y_i(\tau)A(\tau-\tau')y_i(\tau') - \frac{1}{2}\int d\tau d\tau' B_i(\tau)A^{-1}(\tau,\tau')B_i(\tau') + i\int d\tau \hat{z}_i(\tau)s_i^c(\tau)\right]}{\int \mathcal{D}s_i^c \mathcal{D}y_i \exp\left[-\frac{1}{2}\int d\tau d\tau' y_i(\tau)A(\tau-\tau')y_i(\tau') - \frac{1}{2}\int d\tau d\tau' B_i(\tau)A^{-1}(\tau,\tau')B_i(\tau') + i\int d\tau \hat{z}_i(\tau)s_i^c(\tau)\right]}. \tag{G.27}
$$

All τ or τ' integrals have limits of $-\infty$ to ∞, as usual. Recall that $B_i(\tau)$ contains $s_i^c(\tau)$, and so terms

containing $B_i(\tau)$ cannot be pulled out of the $s^c(\tau)$ integrals.

In the denominator, we can evaluate

$$\int \mathcal{D}y_i(\tau) \exp\left[-\frac{1}{2}\int_{-\infty}^{\infty} d\tau \int_{-\infty}^{\infty} d\tau' y_i(\tau) A(\tau-\tau') y_i(\tau')\right] \propto \frac{1}{\sqrt{\det(A(\tau-\tau'))}}.$$

The determinant of $A(\tau-\tau')$ is likely infinite; however, this term will typically be canceled by an identical term in the numerator. If $\mathcal{O}$ in the numerator is independent of $s_i^q(\tau)$ then the y integrals in the numerator and denominator will cancel out exactly.

Now, consider the case that $\mathcal{O} = s_i^q(\tau) = y_i(\tau) + i\int_{-\infty}^{\infty} d\tau' A^{-1}(\tau,\tau') B_i(\tau')$. The second term is independent of $y_i(\tau)$, and so the y integral will evaluate to the same factor as in the denominator and cancel out. The first term is just y, and so the functional integral will evaluate to zero, leaving

$$\langle s_i^q(\tau)\rangle = i\frac{\int \mathcal{D}s_i^q(\tau) \int d\tau A^{-1}(\tau,\tau') B_i(\tau') \exp\left[-\frac{1}{2}\int d\tau \int d\tau' B_i(\tau) A^{-1}(\tau,\tau') B_i(\tau') + i\int d\tau \hat{z}_i(\tau) s_i^c(\tau)\right]}{\int \mathcal{D}s_i^q(\tau) \exp\left[-\frac{1}{2}\int d\tau \int d\tau' B_i(\tau) A^{-1}(\tau,\tau') B_i(\tau') + i\int d\tau \hat{z}_i(\tau) s_i^c(\tau)\right]}.$$

It may be possible to evaluate this by expanding B out in terms of $s_i^c(\tau)$, but instead, I will use the fact that based on the classical case (and similar calculations in other models), we expect the saddle point solution for $\hat{z}_i(\tau)$ to be $\hat{z}_i^0(\tau) = 0$. Let's enter this into the average above and show that the result is indeed zero. Because $\hat{z}_i^0(\tau) \propto \langle s_i^q(\tau)\rangle$, this will demonstrate that $\hat{z}_i^0(\tau) = 0$ is indeed the self-consistent mean field solution.

By eliminating the $\hat{z}_i s_i^c$ term, the integrand is now only in terms of B. Now, let's formally change variables from $s_i^c(\tau)$ to $B_i(\tau)$. The resulting Jacobian will be

$$\mathcal{D}s_i^c(\tau) \to \mathcal{D}B_i(\tau) \left[\det\left(\frac{\delta B_i(\tau)}{\delta s_k^c(\tau')}\right)\right]^{-1}.$$

The derivative is

$$\frac{\delta B_i(\tau)}{\delta s_i^c(\tau')} = -m^{-1}\partial_\tau^2 \delta(\tau-\tau') + \int_{-\infty}^{\infty} d\tau'' \mu(\tau-\tau'')\delta(\tau''-\tau') - \frac{\delta}{\delta s_i^c(\tau')}\left[\frac{\delta V[s^c(\tau)]}{\delta s^c(\tau)}\right].$$

It is not obvious as to whether or not the determinant of this matrix depends on $B_i(\tau)$ through $s_i^c(\tau)$. In fact, a similar issue is encountered in the book by Kleinert, Ref. [119]. Kleinert performs a similar change of variables for a general potential,

$$B_{Klein}(t) = \frac{M}{2}\ddot{x}(t) - \frac{M\gamma}{2}\dot{x}(t) - V'(x(t)).$$

Kleinert shows that by choosing the time slicing of the time axis in a particular way one can make the discretized Jacobian matrix lower triangular with ones along the diagonal, such that the determinant is C^{N+1} for C some constant involving M, γ and the time slice interval ϵ. This is entirely independent of the potential $V(x)$, and so the determinant cancels out of the average. The argument does not appear to depend on the potential being a continuous function, which means this would work if we choose the piece-wise quadratic potential.

The primary difference between Kleinert's example and our case is that the presence of the $\mu(\tau - \tau')$ term in our change of variables cannot be made lower triangular, except in the limit that the memory of the thermal bath tends to zero, $X \to \infty$, in which case $\mu(\tau - \tau') \to \delta'(\tau - \tau')$ and then we can indeed make the determinant in our problem lower triangular, and by the same argument our determinant cancels out. Recall, however, that the reason I have not taken the $X \to \infty$ limit is that the kernel $A(\tau, \tau')$ develops a singular piece in this limit. This singularity goes as $1/(\tau - \tau')^2$, as so generally cannot be removed by taking the principal value when integrated over. Because of this we do not wish to take the memoryless bath limit until the end of the calculation. Then again, Kleinert has the same noise kernel in his example, and does not seem to worry about the singularity (only commenting that it can be treated as a principal value calculation), and so perhaps this is not an issue.

Encouraged by Kleinert's results, I will assume that for large but finite X the determinant is at least approximately constant, if not actually constant, and we assume it approximates cancels out and will neglect the determinant. This gives

$$\langle s_i^q(\tau)\rangle = i\frac{\int \mathcal{D}B_i(\tau) \int_{-\infty}^{\infty} d\tau' A^{-1}(\tau,\tau')B_i(\tau') \exp\left[-\frac{1}{2}\int_{-\infty}^{\infty} d\tau \int_{-\infty}^{\infty} d\tau' B_i(\tau)A^{-1}(\tau,\tau')B_i(\tau')\right]}{\int \mathcal{D}B_i(\tau) \exp\left[-\frac{1}{2}\int_{-\infty}^{\infty} d\tau \int_{-\infty}^{\infty} d\tau' B_i(\tau)A^{-1}(\tau,\tau')B_i(\tau')\right]}.$$

We (assume we) can swap the regular $d\tau'$ integral with the path integral, and find that $\langle s_i^q(\tau)\rangle = \int_{-\infty}^{\infty} d\tau' A^{-1}(\tau,\tau')\langle B_i(\tau')\rangle$; however, the average over B is just a Gaussian integral, and so is zero. Hence, we have demonstrated that the mean field self-consistent solution for $\hat{z}_i(\tau)$ is indeed

$$\hat{z}_i^0(\tau) = 0,$$

as expected.

The average over $s_i^c(\tau)$ (with $\hat{z}_i^0(\tau) = 0$ inserted) is

$$\langle s_i^c(\tau)\rangle = \frac{\int \mathcal{D}s_i^c(\tau) s_i^c(\tau) \exp\left[-\frac{1}{2}\int_{-\infty}^{\infty} d\tau \int_{-\infty}^{\infty} d\tau' B_i[s_i^c](\tau) A^{-1}(\tau,\tau') B_i[s_i^c](\tau')\right]}{\int \mathcal{D}s_i^c(\tau) \exp\left[-\frac{1}{2}\int_{-\infty}^{\infty} d\tau \int_{-\infty}^{\infty} d\tau' B_i[s_i^c](\tau) A^{-1}(\tau,\tau') B_i[s_i^c](\tau')\right]},$$

where we have explicitly noted that $B_i(\tau)$ is a functional of $s_i^c(\tau)$. If we change variables from $s_i^c(\tau)$ to $B_i(\tau)$ again, we have

$$\langle s_i^c(\tau)\rangle = \frac{\int \mathcal{D}B_i(\tau) s_i^c[B_i](\tau) \exp\left[-\frac{1}{2}\int_{-\infty}^{\infty} d\tau \int_{-\infty}^{\infty} d\tau' B_i(\tau) A^{-1}(\tau,\tau') B_i(\tau')\right]}{\int \mathcal{D}B_i(\tau) \exp\left[-\frac{1}{2}\int_{-\infty}^{\infty} d\tau \int_{-\infty}^{\infty} d\tau' B_i(\tau) A^{-1}(\tau,\tau') B_i(\tau')\right]},$$

where $s_i^c[B_i](\tau)$ is now a functional of $B_i(\tau)$, determined by solving the equation

$$B_i(\tau) = -m^{-1}\partial_\tau^2 s_i^c(\tau) + \int_{-\infty}^{\infty} d\tau' \mu(\tau-\tau') s_i^c(\tau') - \frac{\delta V[s^c(\tau)]}{\delta s^c(\tau)} + C(\tau),$$

where $C(\tau) = z_i(\tau) + H(\tau) + h_i$.

Rather than try to solve this equation directly, let's average over it. Because $\langle B(\tau)\rangle = 0$, we have

$$0 = -m^{-1}\partial_\tau^2 \langle s_i^c(\tau)\rangle + \int_{-\infty}^{\infty} d\tau' \mu(\tau-\tau')\langle s_i^c(\tau')\rangle - \left\langle \frac{\delta V[s^c(\tau)]}{\delta s^c(\tau)} \right\rangle + z_i^0(\tau) + H(\tau) + h_i;$$

i.e., the mean field solution $z^0(\tau)$ is determined self consistently by solving the above equation for $\langle s_i^c(\tau)\rangle$. However, this equation is still not easy to solve, as the average over the potential term contains terms nonlinear in $s^c(\tau)$: either $\mathrm{sgn}(s^c(\tau)$ if we use the piece-wise quadratic potential, or $(s^c(\tau))^3$ if we use the quartic potential. Both terms are difficult to work with, and the equation would either have to be solved numerically or with some approximation scheme. Note that this equation reduces to the equation of motion for the average of the single soft-spin in the soft-spin boson model of Appendix F, for which $z_i^0(\tau) = 0$, due to there being no other spins.

Despite the fact that we cannot easily solve this equation, we will nonetheless assume that there is *some* solution, $z_i^0(\tau) = M_c(\tau)$, where we furthermore assume the solution will be the same for all sites i. We can

then formally expand our action about this solution. The resulting expansion will enable us to organize the action into quadratic terms and higher, where the quadratic terms represent the mean field theory and the higher order terms represent corrections. I will show in the next section that the structure of this expansion has the same form as in the classical, zero-temperature case, although some of the expansion coefficients are different.

G.4.6 Expansion about the saddle point solutions

To expand the action about the saddle point solutions, I introduce new fields $\phi_i(\tau) = z_i(\tau) - z_i^0(\tau) = z_i(\tau) - M_c(\tau)$ and $\hat{\phi}_i(\tau) = \hat{z}_i(\tau) - \hat{z}_i^0(\tau) = \hat{z}_i(\tau)$. The generating functional becomes

$$Z = \int \mathcal{D}[\phi(\tau)\hat{\phi}(\tau)] e^{-i\int d\tau \sum_{ij} \hat{\phi}_i(\tau) J_{ij}^{-1} \phi_j(\tau) + \sum_i \left\{ \ln \mathcal{Z}_i[\phi_i(\tau) + M_c(\tau), \hat{\phi}_i(\tau)] - i\int d\tau \hat{\phi}_i(\tau) M_c(\tau) \right\}},$$

where I have used $\sum_j J_{ij}^{-1} = 1$ (in our chosen units of $J = 1$). The τ integrals run from $-\infty$ to ∞. We expand the second term in our action about the new saddle points $\phi = \hat{\phi} = 0$,

$$\begin{aligned} & \ln \mathcal{Z}_i[\phi_i(\tau) + M_c(\tau), \hat{\phi}_i(\tau)] - i\int_{-\infty}^{\infty} d\tau \hat{\phi}_i(\tau) M_c(\tau) \\ = & \sum_{m,n=0}^{\infty} \frac{1}{m!n!} \int_{-\infty}^{\infty} d\tau_1 \ldots d\tau_{m+n} u_{mn}(\tau_1 \ldots \tau_{m+n}) \hat{\phi}_i(\tau_1) \ldots \hat{\phi}_i(\tau_m) \phi_i(\tau_{m+1}) \ldots \phi_i(\tau_{m+n}), \end{aligned}$$

where

$$\begin{aligned} & u_{mn}(\tau_1 \ldots \tau_{m+n}) \\ = & \frac{\delta}{\delta\phi_i(\tau_{m+n})} \cdots \frac{\delta}{\delta\phi_i(\tau_{m+1})} \frac{\delta}{\delta\hat{\phi}_i(\tau_m)} \cdots \frac{\delta}{\delta\hat{\phi}_i(\tau_1)} \left[\ln \mathcal{Z}_i[\phi_i(\tau) + M_c(\tau), \hat{\phi}_i(\tau)] - i\int d\tau \hat{\phi}_i(\tau) M_c(\tau) \right] \Bigg|_{\phi=\hat{\phi}=0} \end{aligned} \quad \text{(G.28)}$$

It is not hard to show that the u_{mn} coefficients are simply related to $m+n$-point correlation functions between $s_i^q(\tau)$ and $s^c(\tau)$, for $m+n \geq 2$. (The coefficients u_{10} and u_{01} are zero by construction.) For example, the quadratic coefficients are $u_{02} = -\langle s_i^q(\tau_1) s_i^q(\tau_2) \rangle = 0$, $u_{11} = -\langle s_i^q(\tau_1) s_i^c(\tau_2) \rangle$, and $u_{20} = -\langle s_i^c(\tau_1) s_i^c(\tau_2) \rangle$. Calculating these correlation functions, however, is not easy in the presence of noise. Even in the classical, noiseless case, calculating these coefficients is quite involved, and was done primarily in the adiabatic limit

[125]. I will not attempt to go so far as to calculate the correlation functions here. However, I will set up some calculations for the quadratic terms, which could yield to a hierarchy approximation scheme for calculating the u_{mn}.

Note that the following calculations make use of the inverse of the noise kernel, $A^{-1}(\tau_1 - \tau_2)$. In the noiseless limit, $A(\tau_1 - \tau_2) = 0$, so the following calculations cannot be brought back to the classical limit; another method would need to be used in order to recover the classical limit at the end of these calculations.

The coefficient u_{02}

First, let's consider u_{02}, which I have claimed to be zero. According to Eq. (G.28), to calculate u_{02}, we act on the local functional with two derivatives of the field ϕ. These derivatives will bring down two factors of $i \int d\tau s_i^q(\tau)$, giving

$$u_{02}(\tau_1, \tau_2) = -\langle s_i^q(\tau_1) s_i^q(\tau_2) \rangle_\ell,$$

where the average is again a local average. We will show that this turns out to be zero. If we change variables again to $s_i^q(\tau) = y_i(\tau) + i \int_{-\infty}^{\infty} d\tau' A^{-1}(\tau, \tau') B_i(\tau)$, we get

$$\begin{aligned} \langle s_i^q(\tau_1) s_i^q(\tau_2) \rangle &= \langle y_i(\tau_1) y_i(\tau_2) \rangle + i \int_{-\infty}^{\infty} d\tau' A^{-1}(\tau_1, \tau') \langle y_i(\tau_2) B_i(\tau') \rangle + i \int_{-\infty}^{\infty} d\tau' A^{-1}(\tau_2, \tau') \langle y_i(\tau_1) B_i(\tau') \rangle \\ &\quad - \int_{-\infty}^{\infty} d\tau' \int_{-\infty}^{\infty} d\tau'' A^{-1}(\tau_1, \tau') A^{-1}(\tau_2, \tau'') \langle B_i(\tau') B_i(\tau'') \rangle. \end{aligned}$$

The cross terms vanish because the local functional is separable into a Gaussian in y and a Gaussian in B, for which the averages are both zero. For the quadratic averages, since the averages are Gaussian, we have $\langle y_i(\tau_1) y_i(\tau_2) \rangle = A^{-1}(\tau_1, \tau_2)$ and $\langle B_i(\tau_1) B_i(\tau_2) \rangle = A(\tau_1, \tau_2)$.

Plugging all of these in gives

$$\begin{aligned} -u_{02}(\tau_1, \tau_2) &= A^{-1}(\tau_1, \tau_2) - \int_{-\infty}^{\infty} d\tau' \int_{-\infty}^{\infty} d\tau'' A^{-1}(\tau_1, \tau') A^{-1}(\tau_2, \tau'') A(\tau', \tau'') \\ &= A^{-1}(\tau_1, \tau_2) - \int_{-\infty}^{\infty} d\tau' A^{-1}(\tau_1, \tau') \delta(\tau' - \tau_2) \\ &= A^{-1}(\tau_1, \tau_2) - A^{-1}(\tau_1, \tau_2) \\ &= 0. \end{aligned}$$

This result means there is no $\phi(\tau)\phi(\tau')$ term in the action, which is true in the classical case as well.

The coefficient u_{11}

We now consider the coefficient $u_{11}(\tau_1, \tau_2)$. This is formed by taking a derivative of the local functional with respect to ϕ and another with respect to $\hat{\phi}$. The ϕ derivative brings down a factor of $is_i^q(\tau_1)$ again (and also kills the $\hat{\phi}M_c$ term), while the $\hat{\phi}$ derivative brings down a factor of $is_i^c(\tau_2)$. Changing variables to $s_i^q(\tau) = y_i(\tau) + i\int_{-\infty}^{\infty} d\tau' A^{-1}(\tau, \tau')B_i(\tau)$ once more, the term linear in y will vanish, leaving

$$-\langle s_i^q(\tau_1)s_i^c(\tau_2)\rangle = i\int_{-\infty}^{\infty} d\tau' A^{-1}(\tau_1, \tau')\langle B_i(\tau')s_i^c(\tau_2)\rangle.$$

Because $s_i^c(\tau)$ depends functionally on $B_i(\tau)$ in a nontrivial way, we cannot easily write down the average $\langle B_i(\tau')s_i^c(\tau_2)\rangle$. What we can do, however, is develop a differential equation for it. We do so by taking the equation relating B and s^c:

$$B_i(\tau_1) = -m^{-1}\partial_{\tau_1}^2 s_i^c(\tau_1) + \int_{-\infty}^{\infty} d\tau'' \mu(\tau_1 - \tau'')s_i^c(\tau'') - \frac{\delta V[s^c(\tau)]}{\delta s^c(\tau)} + C_i(\tau_1).$$

We multiply this equation by $B_i(\tau')$ and take the average. Let $v_{11}(\tau, \tau') = \langle s_i^c(\tau)B_i(\tau')\rangle$. Then, we have

$$A(\tau_1, \tau') = -m^{-1}\partial_{\tau_1}^2 v_{11}(\tau_1, \tau') + \int_{-\infty}^{\infty} d\tau'' \mu(\tau_1 - \tau'')v_{11}(\tau'', \tau') - \left\langle \frac{\delta V[s_i^c(\tau_1)]}{\delta s_i^c(\tau_1)} B_i(\tau') \right\rangle. \tag{G.29}$$

Note that we can write down this equation because the operators, e.g., ∂_τ^2, only act on one of the time indexes, so because we have two-time functions the operators don't affect the factor of $B_i(\tau')$ that we multiplied the equation by. The obvious difficulty with the resulting equation is the term $\left\langle \frac{\delta V[s_i^c(\tau_1)]}{\delta s_i^c(\tau_1)} B_i(\tau') \right\rangle$. Both choices of potential - piece-wise quadratic or quartic - will produce a factor of $v_{11}(\tau_1, \tau')$, as they both contain a term linear in $s_i^c(\tau)$. However, both potentials also contain a nonlinear term, resulting in either $\langle \mathrm{sgn}(s_i^c(\tau_1)B_i(\tau')\rangle$ or $\langle (s^c(\tau_1))^3 B_i(\tau')\rangle$. Both averages are difficult to compute, and an approximation scheme may be necessary to do so. For example, for the cubic non-linearity, equations for averages over powers of $s_i^c(\tau)$ may be developed. These equations will always be linked to averages over even higher order powers, but by truncating the hierarchy at some level, we may be able to solve for $v_{11}(\tau, \tau')$ approximately. In any event, we can formally write

$$u_{11}(\tau_1, \tau_2) = -i \int_{-\infty}^{\infty} d\tau' A^{-1}(\tau_2, \tau') v_{11}(\tau_1, \tau'). \tag{G.30}$$

The factor of i in this equation may seem odd, but it should not pose a problem. In Ref. [125], $\hat{\phi}_i$ is redefined to absorb a factor of i; as the u_{11} coefficient enters the action with one factor of $\hat{\phi}_i$, the imaginary unit i can be eliminated with such a redefinition.

The coefficient u_{20}

Finally, we will derive an equation for the last quadratic term. The two $\hat{\phi}$ derivatives bring down two factors of is_i^c, giving $u_{20} = -\langle s^c(\tau_1) s^c(\tau_2) \rangle$. We proceed similarly to the previous coefficient calculation, starting with the equation

$$B_i(\tau_1) = -m^{-1} \partial_{\tau_1}^2 s_i^c(\tau_1) + \int_{-\infty}^{\infty} d\tau'' \mu(\tau_1 - \tau'') s_i^c(\tau'') - \frac{\delta V[s_i^c(\tau_1)}{\delta s_i^c(\tau_1)} + C_i(\tau_1).$$

We multiply this by $s_i^c(\tau_2)$ and take the average. We find

$$\begin{aligned} & v_{11}(\tau_1, \tau_2) \\ = \; & m^{-1} \partial_{\tau_1}^2 u_{20}(\tau_1, \tau_2) - \int d\tau'' \mu(\tau_1 - \tau'') u_{20}(\tau'', \tau_2) \\ & - \left\langle \frac{\delta V[s_i^c(\tau_1)}{\delta s^c(\tau_1)} s_i^c(\tau_2) \right\rangle + [M_c(\tau_1) + H(\tau_1) + h_i] \langle s_i^c(\tau_2) \rangle. \end{aligned}$$

This equation depends on the function $v_{11}(\tau_1, \tau_2)$ that we must calculate for u_{11}, and it also depends directly on $\langle s_i^c(\tau_2) \rangle = M_c(\tau_2)$, as well as external field and mean field magnetization. There is again a problematic term $\left\langle \frac{\delta V[s_i^c(\tau_1)}{\delta s^c(\tau_1)} s_i^c(\tau_2) \right\rangle$, which we must develop a scheme for approximating.

Note: this term also depends on h_i, as we have not assumed we have averaged over the random fields yet. If we had averaged over the random fields, that amounts to formally setting all $h_i = 0$ and adding a term $-R^2/\kappa$ to $A(\tau, \tau')$.

This is as far as I have come with these calculations. It is not clear if the approximation schemes I have suggested will bear fruit, but hopefully they or other methods will be useful for whomever tackles this problem in the future.

G.5 Future directions: Extension to m-component spins

In the previous subsection, the equations I developed were fully time-dependent. In Ref. [125], the coefficients u_{11} and u_{20}, as well as some higher order coefficients, were calculated in the adiabatic limit. In principle, one could perhaps perform a similar calculation here; however, in the presence of the noise terms, it is not clear what the result would be, or if it would even be meaningful. Physically, we expect the noise terms should cause the system to equilibrate in the adiabatic limit. However, in mean field theory, we expect the barriers to equilibration to be infinite, suggesting that the noise is irrelevant in the above calculations - perhaps even in the technical renormalization group sense. Should this be the case, then it is not clear that one can meaningfully study the competition between the sweeprate $\tilde{\Omega}$ and noise-induced equilibration, even for $\tilde{\Omega} > 0$. Some modification to the model may be necessary.

One such modification, as I mentioned earlier, would be to consider multiple-component spins. Because such spins can be perturbed in multiple directions with relatively little energy cost, it may be possible for them to surpass the energy barriers to equilibration. In such a model, then, we could meaningfully study the sweeprate-noise competition.

A classical, zero temperature random field Ising model with multi-component spins has previously been studied in Ref. [61]. The formalism is a simple extension of that in Ref. [125] (though done in a slightly different way), so switching to multiple-component spins may amount, at a superficial level, to merely adding some more indexes to keep track of during our calculations. Unfortunately, many of the other problems encountered here will persist in the multi-component model, so there is still quite a long way to go before the quantum random field Ising model can be solved. Hopefully, with these notes as a foundation, future studies of the quantum random field Ising model will be successful.

References

[1] J. P. Sethna, K. A. Dahmen, and C. R. Myers. Crackling noise. *Nature*, 410:242–250, Mar 2001.

[2] Nir Friedman, Shinya Ito, Braden A. W. Brinkman, Masanori Shimono, R. E. Lee DeVille, Karin A. Dahmen, John M. Beggs, and Thomas C. Butler. Universal critical dynamics in high resolution neuronal avalanche data. *Phys. Rev. Lett.*, 108:208102, May 2012.

[3] Karin A. Dahmen, Yehuda Ben-Zion, and Jonathan T. Uhl. Micromechanical model for deformation in solids with universal predictions for stress-strain curves and slip avalanches. *Phys. Rev. Lett.*, 102:175501, Apr 2009.

[4] Karin A. Dahmen, Yehuda Ben-Zion, and Jonahtan T. Uhl. A simple analytic theory for the statistics of avalanches in sheared granular materials. *Nature Physics*, 7:554–557, 2011.

[5] K. A. Dahmen and Y. Ben-Zion. *Physics of Jerky Motion in Slowly Driven Magnetic and Earthquake Fault Systems*. Springer, 2010.

[6] Daniel S. Fisher, Karin Dahmen, Sharad Ramanathan, and Yehuda Ben-Zion. Statistics of earthquakes in simple models of heterogeneous faults. *Phys. Rev. Lett.*, 78:4885–4888, Jun 1997.

[7] Nicholas W. Hayman, Lucie Duclou, Kate L. Foco, and Karen E. Daniels. Granular controls on periodicity of stick-slip events: Kinematics and force-chains in an experimental fault. *Pure and Applied Geophysics*, 168(12):2239–2257, 2011.

[8] Troy Shinbrot, Nam H. Kim, and N. Nirmal Thyagu. Electrostatic precursors to granular slip events. *Proceedings of the National Academy of Sciences*, 109(27):10806–10810, 2012.

[9] Georgios Tsekenis, Nigel Goldenfeld, and Karin A. Dahmen. Dislocations jam at any density. *Phys. Rev. Lett.*, 106:105501, Mar 2011.

[10] J. Fineberg, E. Sharon, and G. Cohen. Crack front waves in dynamic fracture. *International Journal of Fracture*, 119(3):247–261, 2003.

[11] S. Zapperi. Current challenges for statistical physics in fracture and plasticity. *The European Physical Journal B*, 85(9):1–12, 2012.

[12] Mikko J. Alava, Phani K. V. V. Nukala, and Stefano Zapperi. Statistical models of fracture. *Advances in Physics*, 55(3-4):349–476, 2006.

[13] D. Sornette and L. Knopoff. The paradox of the expected time until the next earthquake. *Bulletin of the Seismological Society of America*, 87(4):789–798, 1997.

[14] Bettina P. Allmann and Peter M. Shearer. Global variations of stress drop for moderate to large earthquakes. *Journal of Geophysical Research: Solid Earth*, 114(B1), 2009.

[15] Tom Parsons and Eric L. Geist. Were global $M \geq 8.3$ earthquake time intervals random between 1900 and 2011? *Bulletin of the Seismological Society of America*, 102(4):1583–1592, 2012.

[16] M. Bottiglieri, L. de Arcangelis, C. Godano, and E. Lippiello. Multiple-time scaling and universal behavior of the earthquake interevent time distribution. *Phys. Rev. Lett.*, 104:158501, Apr 2010.

[17] Jörn Davidsen and Grzegorz Kwiatek. Earthquake interevent time distribution for induced micro-, nano-, and picoseismicity. *Phys. Rev. Lett.*, 110:068501, Feb 2013.

[18] Tomohiro Hasumi, Takuma Akimoto, and Yoji Aizawa. The Weibull-log Weibull distribution for interoccurrence times of earthquakes. *Physica A: Statistical Mechanics and its Applications*, 388(4):491 – 498, 2009.

[19] Dionissios T. Hristopulos and Vasiliki Mouslopoulou. Strength statistics and the distribution of earthquake interevent times. *Physica A: Statistical Mechanics and its Applications*, 392(3):485 – 496, 2013.

[20] Mark V. Matthews, William L. Ellsworth, and Paul A. Reasenberg. A Brownian model for recurrent earthquakes. *Bulletin of the Seismological Society of America*, 92(6):2233–2250, 2002.

[21] Gleb Yakovlev, Donald L. Turcotte, John B. Rundle, and Paul B. Rundle. Simulation-based distributions of earthquake recurrence times on the San Andreas fault system. *Bulletin of the Seismological Society of America*, 96(6):1995–2007, 2006.

[22] Braden A. W. Brinkman, Michael P. LeBlanc, Yehuda Ben-Zion, Jonathan T. Uhl, and Karin A. Dahmen. A probabilistic model for the distribution of waiting times between large slips in frictional media. *To be submitted*, 2013.

[23] Braden A. W. Brinkman, Michael P. LeBlanc, Yehuda Ben-Zion, Jonathan T. Uhl, and Karin A. Dahmen. Control of large failures in frictional stick-slip systems subjected to periodic shear stresses. *To be submitted*, 2013.

[24] Braden A. W. Brinkman, Michael P. LeBlanc, Yehuda Ben-Zion, Jonathan T. Uhl, and Karin A. Dahmen. Forecasting large earthquakes using small-quake tidal correlations. *Submitted*, 2013.

[25] P. Dayan and L.E. Abbott. *Theoretical Neuroscience: Computational and Mathematical Modeling of Neural Systems*. The MIT Press, 2005.

[26] Yehuda Ben-Zion and James R. Rice. Earthquake failure sequences along a cellular fault zone in a three-dimensional elastic solid containing asperity and nonasperity regions. *Journal of Geophysical Research: Solid Earth*, 98(B8):14109–14131, 1993.

[27] Yehuda Ben-Zion. Stress, slip, and earthquakes in models of complex single-fault systems incorporating brittle and creep deformations. *Journal of Geophysical Research: Solid Earth*, 101(B3):5677–5706, 1996.

[28] Yehuda Ben-Zion. Episodic tremor and slip on a frictional interface with critical zero weakening in elastic solid. *Geophysical Journal International*, 189(2):1159–1168, 2012.

[29] Per Bak, Kim Christensen, Leon Danon, and Tim Scanlon. Unified scaling law for earthquakes. *Phys. Rev. Lett.*, 88:178501, Apr 2002.

[30] Álvaro Corral. Long-term clustering, scaling, and universality in the temporal occurrence of earthquakes. *Phys. Rev. Lett.*, 92:108501, Mar 2004.

[31] Álvaro Corral. Universal local versus unified global scaling laws in the statistics of seismicity. *Physica A: Statistical Mechanics and its Applications*, 340(4):590 – 597, 2004. Complexity and Criticality: in memory of Per Bak (1947–2002).

[32] Álvaro Corral. Local distributions and rate fluctuations in a unified scaling law for earthquakes. *Phys. Rev. E*, 68:035102, Sep 2003.

[33] Zdeněk P. Bažant, Jia-Liang Le, and Martin Z. Bažant. Scaling of strength and lifetime probability distributions of quasibrittle structures based on atomistic fracture mechanics. *Proceedings of the National Academy of Sciences*, 106(28):11484–11489, 2009.

[34] David A. Lockner and Nick M. Beeler. Premonitory slip and tidal triggering of earthquakes. *Journal of Geophysical Research: Solid Earth*, 104(B9):20133–20151, 1999.

[35] N. M. Beeler and D. A. Lockner. Why earthquakes correlate weakly with the solid earth tides: Effects of periodic stress on the rate and probability of earthquake occurrence. *Journal of Geophysical Research: Solid Earth*, 108(B8), 2003.

[36] Heather M. Savage and Chris Marone. Effects of shear velocity oscillations on stick-slip behavior in laboratory experiments. *Journal of Geophysical Research: Solid Earth*, 112(B2), 2007.

[37] Heather M. Savage and Chris Marone. Potential for earthquake triggering from transient deformations. *Journal of Geophysical Research: Solid Earth*, 113(B5), 2008.

[38] Rosario Capozza, Shmuel M. Rubinstein, Itay Barel, Michael Urbakh, and Jay Fineberg. Stabilizing stick-slip friction. *Phys. Rev. Lett.*, 107:024301, Jul 2011.

[39] James H. Dieterich. Modeling of rock friction: 1. Experimental results and constitutive equations. *Journal of Geophysical Research: Solid Earth*, 84(B5):2161–2168, 1979.

[40] James H. Dieterich. Modeling of rock friction: 2. Simulation of preseismic slip. *Journal of Geophysical Research: Solid Earth*, 84(B5):2169–2175, 1979.

[41] James H. Dieterich. Nucleation and triggering of earthquake slip: effect of periodic stresses. *Tectonophysics*, 144:127 – 139, 1987.

[42] James Dieterich. A constitutive law for rate of earthquake production and its application to earthquake clustering. *Journal of Geophysical Research: Solid Earth*, 99(B2):2601–2618, 1994.

[43] Paul A. Rydelek and Lotte Hass. On estimating the amount of blasts in seismic catalogs with Schuster's method. *Bulletin of the Seismological Society of America*, 84(4):1256–1259, 1994.

[44] Bridget Smith-Konter and David Sandwell. Stress evolution of the San Andreas fault system: Recurrence interval versus locking depth. *Geophysical Research Letters*, 36(13), 2009.

[45] Yehuda Ben-Zion. Collective behavior of earthquakes and faults: Continuum-discrete transitions, progressive evolutionary changes, and different dynamic regimes. *Reviews of Geophysics*, 46(4), 2008.

[46] Elizabeth S. Cochran, John E. Vidale, and Sachiko Tanaka. Earth tides can trigger shallow thrust fault earthquakes. *Science*, 306(5699):1164–1166, 2004.

[47] S. Hartzell and T. Heaton. The fortnightly tide and the tidal triggering of earthquakes. *Bulletin of the Seismological Society of America*, 79:1282–1286, 1989.

[48] John E. Vidale, Duncan Carr Agnew, Malcolm J. S. Johnston, and David H. Oppenheimer. Absence of earthquake correlation with earth tides: An indication of high preseismic fault stress rate. *Journal of Geophysical Research: Solid Earth*, 103(B10):24567–24572, 1998.

[49] Sachiko Tanaka. Tidal triggering of earthquakes precursory to the recent Sumatra megathrust earthquakes of 26 December 2004 (M_w 9.0), 28 March 2005 (M_w 8.6), and 12 September 2007 (M_w 8.5). *Geophysical Research Letters*, 37(2), 2010.

[50] Sachiko Tanaka. Tidal triggering of earthquakes prior to the 2011 Tohoku-Oki earthquake (m_w 9.1). *Geophysical Research Letters*, 39(7), 2012.

[51] Peter M. Shearer, Germn A. Prieto, and Egill Hauksson. Comprehensive analysis of earthquake source spectra in southern california. *Journal of Geophysical Research: Solid Earth*, 111(B6), 2006.

[52] P. A. Johnson, H. Savage, M. Knuth, J. Gomberg, and C. Marone. Effects of acoustic waves on stick-slip in granular media and implications for earthquakes. *Nature Publishing Group*, 451:57–60, 2007.

[53] P. A. Johnson. Nonlinear acoustic/seismic waves in earthquake processes. *International Symposium on Nonlinear Acoustics*, 2012.

[54] Braden A. W. Brinkman and Karin A. Dahmen. Tuning coupling: Discrete changes in runaway avalanche sizes in disordered media. *Phys. Rev. E*, 84:041129, Oct 2011.

[55] James P. Sethna, Karin Dahmen, Sivan Kartha, James A. Krumhansl, Bruce W. Roberts, and Joel D. Shore. Hysteresis and hierarchies: Dynamics of disorder-driven first-order phase transformations. *Phys. Rev. Lett.*, 70:3347–3350, May 1993.

[56] Karin Dahmen and James P. Sethna. Hysteresis loop critical exponents in 6-ϵ dimensions. *Phys. Rev. Lett.*, 71:3222–3225, Nov 1993.

[57] Eduard Vives, Jordi Ortín, Lluís Mañosa, Ismael Ràfols, Ramon Pérez-Magrané, and Antoni Planes. Distributions of avalanches in martensitic transformations. *Phys. Rev. Lett.*, 72:1694–1697, Mar 1994.

[58] Olga Perković, Karin Dahmen, and James P. Sethna. Avalanches, Barkhausen noise, and plain old criticality. *Phys. Rev. Lett.*, 75:4528–4531, Dec 1995.

[59] Karin Dahmen and James P. Sethna. Hysteresis, avalanches, and disorder-induced critical scaling: A renormalization-group approach. *Phys. Rev. B*, 53:14872–14905, Jun 1996.

[60] M.C. Kuntz, O. Perkovic, K.A. Dahmen, B.W. Roberts, and J.P. Sethna. Hysteresis, avalanches, and noise. *Computing in Science Engineering*, 1(4):73 –81, Jul/Aug 1999.

[61] Ravá da Silveira and Mehran Kardar. Critical hysteresis for n-component magnets. *Phys. Rev. E*, 59:1355–1367, Feb 1999.

[62] Olga Perković, Karin A. Dahmen, and James P. Sethna. Disorder-induced critical phenomena in hysteresis: Numerical scaling in three and higher dimensions. *Phys. Rev. B*, 59:6106–6119, Mar 1999.

[63] J. Villain. Nonequilibrium "critical" exponents in the random-field Ising model. *Phys. Rev. Lett.*, 52:1543–1546, Apr 1984.

[64] Prabodh Shukla. Exact solution of return hysteresis loops in a one-dimensional random-field Ising model at zero temperature. *Phys. Rev. E*, 62:4725–4729, Oct 2000.

[65] Mikko J. Alava, Vittorio Basso, Francesca Colaiori, Lorenzo Dante, Gianfranco Durin, Alessandro Magni, and Stefano Zapperi. Ground-state optimization and hysteretic demagnetization: The random-field Ising model. *Phys. Rev. B*, 71:064423, Feb 2005.

[66] Dj. Spasojević, S. Janićević, and M. Knežević. Exact results for mean-field zero-temperature random-field Ising model. *EPL (Europhysics Letters)*, 76(5):912, 2006.

[67] Markus Müller and Alessandro Silva. Instanton analysis of hysteresis in the three-dimensional random-field Ising model. *Phys. Rev. Lett.*, 96:117202, Mar 2006.

[68] Yang Liu and Karin A. Dahmen. No-passing rule in the ground state evolution of the random-field Ising model. *Phys. Rev. E*, 76:031106, Sep 2007.

[69] Yang Liu and Karin A. Dahmen. Unexpected universality in static and dynamic avalanches. *Phys. Rev. E*, 79:061124, Jun 2009.

[70] G. Grinstein and J. F. Fernandez. Equilibration of random-field Ising systems. *Phys. Rev. B*, 29:6389–6392, Jun 1984.

[71] A J Bray and M A Moore. Scaling theory of the random-field Ising model. *Journal of Physics C: Solid State Physics*, 18(28):L927, 1985.

[72] Daniel S. Fisher. Scaling and critical slowing down in random-field Ising systems. *Phys. Rev. Lett.*, 56:416–419, Feb 1986.

[73] H. Barkhausen. *Phys. Z.*, 20:401, 1919.

[74] S. S. Wilks. Order statistics. *Bull. Amer. Math. Soc.*, 54:6–50, 1948.

[75] Benedetta Cerruti and Eduard Vives. Correlations in avalanche critical points. *Phys. Rev. E*, 80:011105, Jul 2009.

[76] Matthew C. Kuntz and James P. Sethna. Noise in disordered systems: The power spectrum and dynamic exponents in avalanche models. *Phys. Rev. B*, 62:11699–11708, Nov 2000.

[77] Pierre Cizeau, Stefano Zapperi, Gianfranco Durin, and H. Eugene Stanley. Dynamics of a ferromagnetic domain wall and the Barkhausen effect. *Phys. Rev. Lett.*, 79:4669–4672, Dec 1997.

[78] Stefano Zapperi, Pierre Cizeau, Gianfranco Durin, and H. Eugene Stanley. Dynamics of a ferromagnetic domain wall: Avalanches, depinning transition, and the Barkhausen effect. *Phys. Rev. B*, 58:6353–6366, Sep 1998.

[79] Gianfranco Durin and Stefano Zapperi. Scaling exponents for Barkhausen avalanches in polycrystalline and amorphous ferromagnets. *Phys. Rev. Lett.*, 84:4705–4708, May 2000.

[80] Hong Ji and Mark O. Robbins. Percolative, self-affine, and faceted domain growth in random three-dimensional magnets. *Phys. Rev. B*, 46:14519–14527, Dec 1992.

[81] Moshe Schechter. $LiHo_xY_{1-x}F_4$ as a random-field Ising ferromagnet. *Phys. Rev. B*, 77:020401, Jan 2008.

[82] L.-M. Duan, E. Demler, and M. D. Lukin. Controlling spin exchange interactions of ultracold atoms in optical lattices. *Phys. Rev. Lett.*, 91:090402, Aug 2003.

[83] T. Senthil. Properties of the random-field Ising model in a transverse magnetic field. *Phys. Rev. B*, 57:8375–8380, Apr 1998.

[84] A. Dutta, B. K. Chakrabarti, and R. B. Stinchcombe. Phase transitions in the random field Ising model in the presence of a transverse field. *Journal of Physics A: Mathematical and General*, 29(17):5285, 1996.

[85] K. Ghosh and J.K. Bhattacharjee. The random field Ising model in a transverse field: multicritical point. *Physics Letters A*, 238(23):203 – 205, 1998.

[86] M. P. Lilly and R. B. Hallock. Avalanche behavior in the draining of superfluid helium from the porous material Nuclepore. *Phys. Rev. B*, 64:024516, Jun 2001.

[87] M. P. Lilly, A. H. Wootters, and R. B. Hallock. Avalanches in the draining of nanoporous Nuclepore mediated by the superfluid helium film. *Phys. Rev. B*, 65:104503, Feb 2002.

[88] M. P. Lilly, A. H. Wootters, and R. B. Hallock. Spatially extended avalanches in a hysteretic capillary condensation system: Superfluid ^{4}He in Nuclepore. *Phys. Rev. Lett.*, 77:4222–4225, Nov 1996.

[89] A. H. Wootters and R. B. Hallock. Superfluid avalanches in Nuclepore: Constrained versus free-boundary experiments and simulations. *Phys. Rev. Lett.*, 91:165301, Oct 2003.

[90] M. L. Rosinberg, E. Kierlik, and G. Tarjus. Percolation, depinning, and avalanches in capillary condensation of gases in disordered porous solids. *EPL (Europhysics Letters)*, 62(3):377, 2003.

[91] F. Detcheverry, E. Kierlik, M. L. Rosinberg, and G. Tarjus. Local mean-field study of capillary condensation in silica aerogels. *Phys. Rev. E*, 68:061504, Dec 2003.

[92] David C. Mertens. Population-specific predictions for the finite Kuramoto model and collective synchronization in a system with resonant coupling. *Ph.D. Thesis*, 2011.

[93] Steven H. Strogatz. From Kuramoto to Crawford: exploring the onset of synchronization in populations of coupled oscillators. *Physica D: Nonlinear Phenomena*, 143(14):1 – 20, 2000.

[94] J.M. Sanz-Serna. Markov Chain Monte Carlo and numerical differential equations. Lecture notes, available online at `http://sanzserna.org/pdf/916_cetraro.pdf`, 2011.

[95] W. Feller. *An Introduction to Probability Theory and Its Applications*. Wiley, 1971.

[96] Ch. P. Robert and G. Casella. *Monte Carlo Statistical Methods*. Springer, 2004.

[97] Michael Stone and Paul Goldbart. *Mathematics for Physics: A Guided Tour for Graduate Students*. Cambridge University Press, 2009.

[98] Amit P. Mehta. Higher order spectra and universal shape functions in avalanche models. *Ph.D. Thesis*, 2005.

[99] Daniel S. Fisher. Collective transport in random media: from superconductors to earthquakes. *Physics Reports*, 301(13):113 – 150, 1998.

[100] R. M. Colress, G. H. Gonnet, D. E. G. Hare, D. J. Jeffery, and D. E. Knuth. On the Lambert W function. *Adv. Compt. Math*, 5:329–359, 1996.

[101] Robert A. White. Sweeprate and temperature effects on crackling noise. *Ph.D. Thesis*, 2005.

[102] Braden A. W. Brinkman, Robert A. White, James P. Sethna, Jonathan T. Uhl, Erica Carlson, and Karin A. Dahmen. Temperature effects on hysteresis with crackling noise. *To be submitted to Phys. Rev. Lett.*, 2013.

[103] Alan Middleton and Daniel S. Fisher. Three-dimensional random-field Ising magnet: Interfaces, scaling, and the nature of states. *Phys. Rev. B*, 65:134411, Mar 2002.

[104] Igor F. Lyuksyutov, Thomas Nattermann, and Valery Pokrovsky. Theory of the hysteresis loop in ferromagnets. *Phys. Rev. B*, 59:4260–4272, Feb 1999.

[105] M. Cristina Marchetti and Karin A. Dahmen. Hysteresis in driven disordered systems: from plastic depinning to magnets. *Phys. Rev. B*, 66:214201, Dec 2002.

[106] E. W. Carlson, K. A. Dahmen, E. Fradkin, and S. A. Kivelson. Hysteresis and noise from electronic nematicity in high-temperature superconductors. *Phys. Rev. Lett.*, 96:097003, Mar 2006.

[107] Y. L. Loh, E. W. Carlson, and K. A. Dahmen. Noise predictions for STM in systems with local electron nematic order. *Phys. Rev. B*, 81:224207, Jun 2010.

[108] B. Phillabaum, E. W. Carlson, and K. A. Dahmen. Spatial complexity due to bulk electronic nematicity in a superconducting underdoped cuprate. *Nat. Commun.*, 3:915, Mar 2012.

[109] A. Berger, A. Inomata, J. S. Jiang, J. E. Pearson, S. D. Bader, and Karin Dahmen. Disorder-driven hysteresis-loop criticality in Co/CoO films. *Journal of Applied Physics*, 89(11):7466–7468, 2001.

[110] Jordi Marcos, Eduard Vives, Lluí s Mañosa, Mehmet Acet, Eyüp Duman, Michel Morin, Václav Novák, and Antoni Planes. Disorder-induced critical phenomena in magnetically glassy Cu-Al-Mn alloys. *Phys. Rev. B*, 67:224406, Jun 2003.

[111] D. M. Silevitch, G. Aeppli, and T. F. Rosenbaum. Switchable hardening of a ferromagnet at fixed temperature. *Proceedings of the National Academy of Sciences*, 107(7):2797–2800, 2010.

[112] Leticia F. Cugliandolo and Gustavo Lozano. Real-time nonequilibrium dynamics of quantum glassy systems. *Phys. Rev. B*, 59:915–942, Jan 1999.

[113] A. J. Leggett, S. Chakravarty, A. T. Dorsey, Matthew P. A. Fisher, Anupam Garg, and W. Zwerger. Dynamics of the dissipative two-state system. *Rev. Mod. Phys.*, 59:1–85, Jan 1987.

[114] Peter P. Orth, Adilet Imambekov, and Karyn Le Hur. Nonperturbative stochastic method for driven spin-boson model. *Phys. Rev. B*, 87:014305, Jan 2013.

[115] Peter P. Orth, Adilet Imambekov, and Karyn Le Hur. Universality in dissipative Landau-Zener transitions. *Phys. Rev. A*, 82:032118, Sep 2010.

[116] M Fannes, B Nachtergaele, and A Verbeure. Tunnelling in the equilibrium state of a spin-boson model. *Journal of Physics A: Mathematical and General*, 21(8):1759, 1988.

[117] S. Florens, D. Venturelli, and Narayanan R. Quantum phase transition in the spin boson model. *arXiv.org*, arXiv:1106.2654, 2011.

[118] Stefan Kirchner, Kevin Ingersent, and Qimiao Si. Quantum criticality of the sub-ohmic spin-boson model. *Phys. Rev. B*, 85:075113, Feb 2012.

[119] Hagen Kleinert. *Path Integrals in Quantum Mechanics, Statistics, and Polymer Physics.* World Scientific, 1990.

[120] Lewis H. Ryder. *Quantum Field Theory.* Cambridge University Press, 1996.

[121] J. Hubbard. Calculation of partition functions. *Phys. Rev. Lett.*, 3:77–78, Jul 1959.

[122] H. Kleinert. Hubbard-Stratonovich transformation: Successes, failure, and cure. *Electronic Journal of Theoretical Physics*, 8:57–64, 2011.

[123] Nigel Goldenfeld. *Lectures on Phase Transitions and the Renormalization Group*. Westview Press, 1992.

[124] J. Crank and P. Nicolson. A practical method for numerical evaluation of solutions of partial differential equations of the heat-conduction type. *Advances in Computational Mathematics*, 6(1):207–226, 1996.

[125] Karin A. S. Dahmen. Hysteresis, avalanches, and disorder induced critical scaling: a renormalization group approach. *Ph.D. Thesis*, 1995.

[126] Malcolm P. Kennett. Disorder effects in spin systems: Diluted magnetic semiconductors and the aging dynamics of spin glasses. *Ph.D. Thesis*, 2002.

[127] C. Ancona-Torres, D. M. Silevitch, G. Aeppli, and T. F. Rosenbaum. Quantum and classical glass transitions in $LiHo_xY_{1-x}F_4$. *Phys. Rev. Lett.*, 101:057201, Jul 2008.

[128] D. M. Silevitch, D. Bitko, J. Brooke, S. Ghosh, G. Aeppli, and T. F. Rosenbaum. A ferromagnet in contnuously tunable random field. *Nature Publishing Group*, 448:567–570, 2007.

[129] Carson C. Chow and Michael A. Buice. Path integral methods for stochastic differential equations. *arXiv.org*, arXiv:1009.5966v2, 2012.

[130] R. Phythian. The functional formalism of classical statistical dynamics. *Journal of Physics A: Mathematical and General*, 10(5):777, 1977.

[131] P. C. Martin, E. D. Siggia, and H. A. Rose. Statistical dynamics of classical systems. *Phys. Rev. A*, 8:423–437, Jul 1973.

[132] Onuttom Narayan and Daniel S. Fisher. Dynamics of sliding charge-density waves in 4-ϵ dimensions. *Phys. Rev. Lett.*, 68:3615–3618, Jun 1992.

[133] Onuttom Narayan and Daniel S. Fisher. Critical behavior of sliding charge-density waves in 4-ϵ dimensions. *Phys. Rev. B*, 46:11520–11549, Nov 1992.

[134] J. Rammer and H. Smith. Quantum field-theoretical methods in transport theory of metals. *Rev. Mod. Phys.*, 58:323–359, Apr 1986.

[135] Alex Kamenev and Alex Levchenko. Path integral methods for stochastic differential equations. *arXiv.org*, arXiv:0901.3586v3, 2009.

[136] R. J. Baxter. *Exactly Solved Models in Statistical Mechanics*. Dover Publications, 1982.